UNIVERSITY OF SOUTHAMPTON

FACULTY OF PHYSICS AND ASTRONOMY
Quantum, Light & Matter

Development of Silicon Carbide Photonics for Quantum Technologies

by

Francesco Martini

Thesis for the degree of Doctor of Philosophy

November 2017

UNIVERSITY OF SOUTHAMPTON

ABSTRACT

FACULTY OF PHYSICS AND ASTRONOMY
Quantum, Light & Matter

Doctor of Philosophy

DEVELOPMENT OF SILICON CARBIDE PHOTONICS FOR QUANTUM TECHNOLOGIES

by Francesco Martini

Quantum information sciences offer novel capabilities in the fields of computation, data security and sensing. In order to deliver these improvements, information needs to be encoded in a physical quantum system the realization of which is technologically challenging. Even though several platforms have been proposed for computation, quantum information encoded in nonclassical states of light is going to play a central role since the classical fiber technology already provides an almost ideal transmitting medium. Furthermore, a hybrid approach formed together with solid state emitters could meet the non-trivial requirement needed for quantum computation. In the past ten years, efforts have been placed in integrating the bulky optical components required to manipulate nonclassical states of light, giving birth to the field of quantum photonics. Between all the different materials proposed, 3C silicon carbide (SiC) meets all the complex requirements needed for photonic quantum technologies and the development of essential components to this scope is the main subject of this thesis. The design, fabrication and characterization of small modal-area waveguides, grating couplers and ring resonators made in SiC are reported. Four wave mixing was demonstrated thanks to the small modal volume achieved in the ring resonator and the Kerr coefficient of SiC was retrieved. The realization of photonic crystal cavities is also investigated with the aim to harness quantum emitters. Thanks to the demonstration of coupling between confined and propagating surface waves, SiC is a potential platform for quantum applications in the mid-infrared. Finally, the generation of photon pairs in the near-infrared by means of third order nonlinear process is reported using ring resonators fabricated in silicon nitride.

Contents

List of Figures

List of Tables

Acknowledgements

I have no idea where to begin thanking my supervisor, Alberto Politi, for everything he has done for me during this period. Without him believing in me in the first place four years ago, I would have never had the opportunity to grow as a researcher and as a person. He took the trouble in helping me far beyond what a supervisor should have, especially in the early stages of my PhD. He has always encouraged me even when results struggled to come and his guidance and support have been invaluable. It has been an incredible learning experience to tail after him during this period with thousand questions, that he always found the time to answer.

I would like also to thank Silvia for the several useful advices, for being the best web manager and the only one I could count on to press dinner on the others. Thanks to my group mates, Robert and Ioannis, for all the work made together. I will miss the infinite arguings and conversations with Robert, who has been incredibly supportive throughout the last period.

I had the fortunate opportunity to collaborate with Simone De Liberato, Chris Gubbin and Stefan Maier on the exiting project of SPhP (Chap.7). Working on SiC has requested a tremendous effort from the fabrication point of view and therefore I would like to thank all the technical staff of the Southampon Nanofabrication Center. I acknowledge experimental support from Roman Bruck and Otto Muskens (Chap.3 and 4, respectively).

A lot of amazing people, who have been part of this incredible journey, deserve my gratitude. First of all, I have to thank Paco for being my social spirit guide. Without him I would have never met Lucia, Valentina and Francesca and life could have been much more sadder. I must thank my nerd friend Amy for burning and gaining fat by jogging and binge eating, always together. Thanks to Matteo for all the chess matches and Giacomo for the amazing food adventures. I would like to thank Daniele for all the time spent living together as flatmates. Thanks to my cleanroom buddy, Abdelrahman Al-Attili, for alleviating the struggle during the hours spent fabricating samples.

Finally, I have to thank my family for being supportive in every decision I made. They encouraged me during the tough periods and made me feel close regardless of the kilometers. I would like to thank Marta for accepting my decision to embark this journey despite it meant a lot of time apart. The distance has been sometimes unbearable for both of us and this result is mine as much as hers. She has been always by my side and we have already shared many adventures together. I look forward to a future filled with many more. I would like to dedicate this thesis to my grandmothers.

Chapter 1

Overview on Quantum Photonics and SiC proposal

After a first introduction to the field of quantum technologies, the basic devices needed for photonic quantum information processing are discussed in Sec.1.2. In particular, an overview of the main achievements and properties of the photonic materials suggested so far is discussed in Sec.1.2.4. The nonlinear and quantum optical advantages that motivate the proposal of SiC as material platform for quantum photonics are reported in Sec.1.3. Finally, in Sec.1.4 is presented the organization of this manuscript.

1.1 Introduction to quantum technologies

Over the past several decades, we have witnessed an increasing interest in quantum information sciences[1] which purpose is to harness the intrinsic features of a quantum mechanic system to gain new functionalities and performances in different technological fields. This area of study was triggered from the initial intuition of R. P. Feynman[14], when he envisaged the computational problem deriving from the simulation of a physical system with a classical computer. To solve this problem, Feynman proposed the use of a **quantum computer** that would take advantage of the properties of a quantum system to decrease the requirement of computational resources to a polynomial number instead of an exponential one, like in the classical case. The probabilistic nature of quantum systems is exploited by quantum algorithms to provide speed up in performing specific tasks, where classical computers suffer resources overheads. In addition to benefits in computational velocity, quantum technologies have also found to offer improvements in the field of communication and sensing.

The basic entity composing a quantum computer is the quantum bit (*qubit*) that can assume any value given by the linear combination between the orthogonal states $|0\rangle$ and

$|1\rangle$

$$|\Psi\rangle = \alpha|0\rangle + \beta|1\rangle \tag{1.1}$$

where, by performing a measurement we find the state $|0\rangle$ with probability $|\alpha|^2$ and $|1\rangle$ with probability $|\beta|^2$. This is a crucial difference with the well-defined classical bit where the outcome of a measurement results in definite values of 0 or 1. Since the two probabilities are subjected to $|\alpha|^2 + |\beta|^2 = 1$, Eq.1.1 can be described using

$$|\Psi\rangle = \cos\frac{\theta}{2}|0\rangle + \sin\frac{\theta}{2}e^{i\phi}|1\rangle \tag{1.2}$$

where $0 < \theta < \pi$ and $0 < \phi < 2\pi$ are angles representing a point on the surface of the Bloch sphere (Fig.1.1). The poles of the sphere constitute the vectors of the computational basis and any state inside the sphere is defined as mixed states that can be described with a density matrix, the trace of which is still 1.

In the following of this section, a review of the main fields of study composing the quantum technology area is reported.

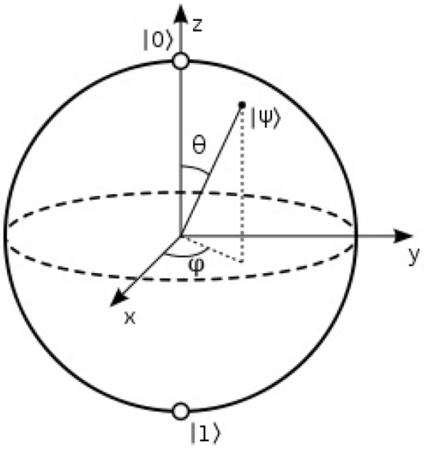

Figure 1.1: The Bloch sphere representing a qubit[1]

Quantum computation The interest on this field has tremendously increased since P. Shor demonstrated in 1994 an algorithm, designed for quantum computers, that would require a polynomial number of steps to factorize any number[15]. This is a major difference with a classical computer where there is no known algorithm able to solve the same problem with a polynomial number of resources. Even though Shor's algorithm is considered a landmark in the subject, Grovers algorithm[16], used to implement an efficient searching of a database, and Deutschs algorithm[17], concerning the evaluation of a binary function, are equally of main interest as provide a speedup compared to classical algorithms (albeit of polynomial size).

Even though different two-level quantum mechanical systems have been proposed to implement the qubit, as described from Eq.1.1, in order to successfully complete any quantum algorithm proposed schemes have to meet the DiVincenzo's criteria[18]:

1. Scalability of the physical system;
2. The ability to initialize the qubits in a defined state;
3. Single- and two-qubits gate operations;
4. A qubit decoherence time much longer than the gate operation time;
5. The ability to measure the state of individual qubits.

These requirements are not trivial to implement on a large number of qubits additionally considering that criteria 2-3 and 4 are in some sense contradictory since the quantum system requires to be both isolated from the environment, otherwise it would be cause of decoherence, and have to perform ondemand gate operations. To date, there is still not a scalable system and even the implementation of a small number of qubits is challenging. This has led to the idea to divide the large quantum computer into a network of small ones with the distances compensated with a transfer of quantum information from each node. The qubits within each node are called *static qubits* and the quantum information exchanged between two quantum computers is carried with *flying qubits*. To implement this scheme, DiVincenzo proposed two additional requirements:

6. The ability to convert stationary qubits in flying qubits, and vice versa;
7. The ability to reliably transfer flying qubits.

Photons are the natural choice to implement flying qubits since their long decoherence time, they hardly interact with each other and the possibility to use the existent fiber network allowing their transmission for long distances. On the other side, static qubits have still to find the technology able to deliver the computational nodes in a semi/scalable manner and to meet the requirements 6 and 7 of DiVincenzo's list.

One of the first system proposed in 1995 to address this problem was based on **cold ions**[19] that can be trapped using laser beams[20]. The qubits are encoded in the excitation states of the atoms and each of them can be initialized and measured separately by resonant laser pulses. The interaction needed to perform two-qubits gate operations can be provided by the repulsive forces, experienced between close ions, resulting in additional vibrational modes[21].

A lot of research has been carried out in order to embed qubits in solid state systems with the aim to improve the scalability. One of the most successful system in terms of decoherence and operation fidelities is based on superconductor (**superconductive qubits**). The quantum state of these qubits are encoded in charges, given by the Cooper's pair, of a superconductive region. By applying electromagnetic pulses across a Josephson junction[22] formed with LC circuits, gate operations are performed by controlling the properties of the superconductive states. The advantage in this technology resides in the opportunity to encode qubits in ordinary electronic designs[23]. In order to have long decoherence, these systems work in challenging temperature of hundreds milli-kelvins and are affected by cross-talk between qubits that ultimately affects the scalability.

Another integrated proposal that has been pursued is based on **quantum dots**, where the quantum information is stored in excitons confined in such as structures or in spin levels[24, 25]. In fact, the three dimensional confinement of the electrons results in atom-like discrete energy levels and operations can be performed, analogously as with cold ions, by resonant optical pulses. Different excitons within a quantum dot can interact by means of Coulomb interaction. This system requires cryogenic temperature but not so deep as the superconductive technology, and the main drawback of quantum dots consists in the random spatial positioning that hampers the development of auxiliary photonic components. Furthermore, the relatively wide size distribution of quantum dots affects the energy levels and results in the so called inhomogeneous broadening. Analogously to this technology, isolated impurities in solid, such as **diamond NV centers**, present an atom-like behaviour that can be exploited for quantum information processing (QIP). The spin levels of these defects can be controlled with RF waves[26, 27] and the quantum state is preserved thanks to a remarkable coherence time. However, spin-spin coupling is challenging and results in difficult two-qubits operations.

Another approach to perform quantum information processing considers the use of non-classical states of light[28]. In this **all-optical** system, operations can be performed with classical optic components meanwhile sources provide the quantum nature required to encode qubits. This technology can be hybridized with solid-state emitters, discussed previously, to harness the advantages deriving from both proposal[29]. Due to the relevance of this topic in this thesis, a more deep treatment is given in the following section.

A lot of physical systems exhibit quantum coherence and therefore have been proposes as qubits, here the most pursued technologies are introduced. For a more complete treatment the reader can refer to Ref.[30, 1].

Quantum communication This field exploits the transmission of a flying qubit between two distant places and, as anticipated before, photons are the undisputed choice for this task. Quantum information can be encoded using different degrees of freedom such as polarization, spatial mode or time[28]. In 1984, the first application exploiting the quantum features of this system gave birth to the field of *quantum key distribution* (QKD)[31] where the transmission of data is made secure from eavesdropping thanks to the non-cloning theorem. The work principle is based on the fact that a measurement performed by an eavesdropper would affect the quantum system giving notice of his/her presence to the parts exchanging the data. Thanks to a low-loss optical fiber network, QKD systems are already commercially available[32] and soon quantum communication might be additionally transmitted using space technologies[33].

Quantum sensing Another branch where quantum features provide improvements over the classical counterpart regards the reduction of uncertainty during a measurement process. Even in this field, non-classical states of light play a central role due to the vast use of systems based on Mach-Zehnder interferometers where the outputs are dependent on the respective phase between the two arms. In the case we use classical inputs, any measurement is hampered by vacuum fluctuation resulting in the *Shot noise* and limiting the sensitivity to $1/\sqrt{N}$, where N is the mean number of photons. The use of either *squeezed* or entangled states as inputs can improve the sensitivity to $1/N$[34]. Between all the applications that are arising in this research, it is worth noting the field of *quantum lithography* that takes advantage of a N-entangled state to reduce the diffraction limit to a value of $\lambda/(2N)$[35], improving the resolution of a factor of $1/N$.

1.2 Quantum photonics

As discussed in the previous section, various approaches are still developed to perform QIP and it is still not possible to determine which technology will be able to successfully and reliably meet all the DiVincenzo's criteria. However, it is clear that non-classical states of light will play a central role in both quantum communication and sensing and a system able to generate as well as manipulate flying qubits will be necessary.
In the last decade, research has been focused on integrating bulky components needed to implement optical qubits and consequently giving birth to *quantum photonics* field[28]. In this section, the focus will be placed on the main devices needed to generate, manipulate and detect single photons even though some parts can be extended, with the due differences, to squeezed states composing the so-called *continuous variable* area.

1.2.1 Sources

The development of ideal photons sources is the main obstacle to photonic quantum computation[36] since, so far, there is not a platform able to deliver on-demand and high-indistinguishable pure single photons. Furthermore, a photons source should be integrated in a scalable way within a photonic circuit and be very bright. A central role in the characterization of a source is played by quantum interference experienced by two indistinguishable photons entering one in each arm of a 50:50 beam splitter: due to Hong Ou Mandel (HOM) effect[37], the probability of detecting one photon at each output arm is null and both photons will instead come out together at the same output port. Therefore, the HOM experiment can be used to define the *indistinguishably* between two photons. This is especially important if we consider photons emitted from two distinct sources or deriving from the same source but in two temporal windows. In order to exhibit HOM interference, the multiphoton probability has to be negligible. This can be characterized by the Hanbury Brown and Twiss interferometer, able to provide the autocorrelation function $g^{(2)}(\tau)$ and therefore to describe the photon statistics emitted by a source. A coherent laser beam has a Poissonian statistics, with an equivalent $g^{(2)}(0) = 1$, meanwhile a super Poissonian one characterizes thermal sources with an equivalent $g^{(2)}(0) = 2$. With $g^{(2)}(0) < 1$, identifying an *antibunched* photon statistics, are defined all the states of light that can not be described classically and the lower $g^{(2)}(0)$ the higher is *purity* of a single photon emitter. This means that for $g^{(2)}(0) = 0$ there is a null probability of multiphoton emission. Finally, the *brightness* simply describes the maximum photon emission rate.

As already mentioned, photons are ideal flying qubit and an essential building block for quantum communication. In order to benefit of the low absorption of optical fiber (Fig.1.2), sources should preferentially emit in the telecom bands where losses can reach the low value of ~0.2dB/km (at 1550nm). For comparison, if operations are moved in the first telecom band at ~800nm, losses increase to more than 2dB/km and therefore severely limiting the maximum communication length. The main solid state emitters produce photons at wavelength shorter than the telecom one and therefore research has been carried out in order to develop quantum transducer[38]. These devices exploit the nonlinear optical properties of photonic waveguides to upconvert photon wavelengths while preserving its quantum footprints. However, these components are still not efficient enough and sources operating in the C-band are still desirable.

Over the years, different approaches have been used to produce single photons. An isolated quantum system, like an atom, is a natural source of antibunched light. Thanks to complex bulky set-up, cold atoms can be used to produce on-demand indistinguishable photons[39] in a deterministic way. However, these systems can not be integrated in photonic platform and provide a slow dynamic, limiting the operation rates. Solid state emitters could provide the same advantages of atoms with the possibility of integrating multiple point sources within the same chip, being conveniently scalable. The presence of the surrounding medium negatively affects emitters by providing two main effects: inhomogeneous broadening, that provides a low HOM visibility between photons deriving from two distinct emitters, and homogeneous linewidth broadening, that causes photons deriving from the same source to be not indistinguishable. Due to the discrete energy levels, the generation of ondemand photons with quantum emitters can be achieved with an excitation pulse that triggers the point source in an exited state and, upon the relaxation of the generated exiton, a photon can be extracted by removing the triggering pulse with spectral filters. In the past decades, a plethora of integrated platforms providing atom-like emitters have been suggested[40] with some showing interesting properties. Here, the focus will be on the most promising ones: quantum dots and fluorescent atomic defects.

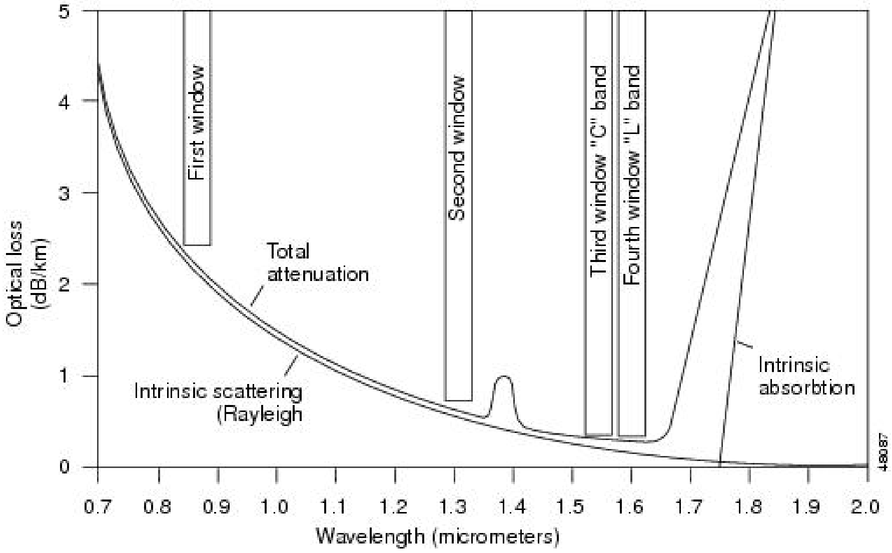

Figure 1.2: Absorption in optical fiber in function of the wavelength. The losses at high frequencies are limited from Rayleigh scattering and, in the UV range, from electronic absorption. In the infrared band, the losses are caused from the intrinsic absorption of vibrational modes, existing in the SiO_2 amorphous structure. The absorption peak around $1.4um$ is due to Si-OH bond that arises from the presence of water inside the fiber. The C-band defines the lowest absorption region, where losses of 0.2 dB/Km are reached[2].

Emitters based on self-assembled InAs/GaAs quantum dots have shown remarkable performances[41, 42, 43, 44, 45, 46] where high brightness, purity and indistinguishably can be achieved. The majority of these results are achieved using photonic components to increase the extraction efficiency that is otherwise challenging due to the high refractive index contrast of III-V compounds. One of the most employed photonic cavity used to exploit quantum dots consists of high-reflective Distributed Bragg Reflector (DBR) and this vertical approach does not allow the fabrication of photonic circuit within the same chip. The main challenges of these sources lie in the emitters inhomogeneity, since two different quantum dots can have very distant emission wavelengths, and random space location. In most cases, photonic components are fabricated only after the emitter location in the wafer plane is identified, hampering the scalability of this platform. Furthermore, due to the inhomogeneous broadening, multiple photons can be only generated using the same source and delay lines that are activated by fast switches. However, this approach is severely affected by losses of these additional photonic components. Other drawbacks of the quantum dot technology reside in the low temperature operation (around 4K) and in the emission in the nearinfrared wavelength band.

Point defects in diamond have been extensively studied over the past two decades since they can operate at room temperature if the defect electronic states are far from the conduction and valence band of the host material. On the contrary to quantum dot, defects can be placed with great accuracy[47] since they can be created by ion implantation using small-aperture masks[48] or with a scanning helium microscope[49]. Recently, positioning of diamond defect have been achieved with strong laser pulses[50]. The most studied defects are the nitrogen-vacancy (NV) and the silicon-vacancy (SiV) that emit at 640nm and 740nm, respectively. Due to their non-zero electronic dipole, NV centers are more affected by the local environment that worsens both homogeneous and inhomogeneous broadening. On the other side, SiV defects are more robust to nearby environment conditions and multiple defects can be grown with similar properties within the same sample[51, 52]. This difference is reflected in the HOM interference between photos coming from remote defects (cooled down to 5K needed to exhibit a sharp zero phonon line) where the SiV case holds a visibility value of 72%[51] against a 66% for the NV case[53]. However, the brightness of the SiV centre in bulk diamond is low due to a low quantum efficiency of the defect[40]. Only the highest crystal-quality diamond exhibits interesting properties of point emitters and this comes in small wafers (2-5mm) of thick monolithic layer, making the scalability of this technology questionable. This is why other crystal impurities in other materials are currently under studies. As it is discussed later in Sec.1.3 and Chap.6, crystal defects in SiC are one promising alternative. Due to the wide interest in the laser industry and a mature technology, rare-earth-ion impurities are well characterized and emit in the visible wavelengths. However, the extremely long coherence time severely limits the operation speed[54, 55].

Another approach to generate single photons takes advantage of the nonlinearity of crystals by a process of parametric fluorescence such as *spontaneous four wave mixing* (SFWM) and spontaneous parametric down conversion (SPDC). Entangled photon pairs can be conveniently produced by these processes and have been used in fundamental quantum optics experiments to test Einstein-Podolsky-Rosen paradox[56] or even to achieve teleportation[57, 58]. Furthermore, SPDC is a cornerstone for the generation and experiments involving squeezed states[59, 60]. The light produced through nonlinear process has a super-Poissonian statistics but single photons can be generated by heralding one of two photons. As it is going to be discussed in Chap.5, the single photon emission is possible only in a low pump condition and imposing a trade-of between brightness and photon purity. Furthermore, this source is intrinsically probabilistic and efforts are currently placed in the development of multiplexing schemes[61] able to provide a near-deterministic photon source. Multiple sources can be easily integrated within the same sample where field confinement boosts the efficiency of nonlinear processes. Furthermore, photons are produced at telecom wavelengths and at room temperature, providing high quantum interference.

1.2.2 Circuits

In the past decade, efforts have been spent in integrating all the photonic devices needed to manipulate photons. In comparison to bulky components used in first experiments of quantum optics, an integrated approach for QIP offers thermal stability, the promise of an easy reconfigurability and scalability, since multiple devices can be integrated within a small sample. Furthermore, integrated optical cavities are essential to increase the emission rate of solid state emitters (through Purcell enhancement) or to boost the nonlinear process required to generate single photons.

Flying qubits can be physically controlled with directional couplers, Mach-Zehnder interferometers and phase shifters, to implement single qubit operations in a reconfigurable way. In order to reach universal quantum computation, a two-qubits gate operation is required and the most common example is the C-NOT gate, where a qubit state is flipped upon the value of a control qubit: if in the state value of the control qubit is $|0\rangle$ the target qubit is left unchanged meanwhile in the case of $|1\rangle$ the target qubit undergoes a NOT logic operation. This is not trivial for optical qubits since the control qubit has to cause a strong nonlinearity able to shift the phase of the target qubit of π. A major breakthrough came in 2001, when it was shown an all-optical way to implement this operation using the nonlinearity provided by the detectors and ancillary photons[62]. However, this scheme is probabilistic and quantum teleportation is required to deterministically perform a C-NOT gate[63]. Another approach to overcome the small linearity at single photon level consists in the use of quantum emitters strongly coupled to an optical cavity[64, 65]. The small modal volume reached in integrated cavities is advantageus to reach strong coupling and high nonlinearities have already been shown with quantum dots[66, 67, 68, 69]. Alternatively, cavity quantum electro dynamic (QED) can be used to efficiently transfer the photon states to spin level of emitters[70, 71, 72], where two-qubit operations might be performed.

Other than logic gates on qubits, photonic circuits need to integrate a series of classical components. In order to implement single photon sources, integrated filters, able to remove a triggering pulse for the quantum emitter case or the strong coherent pump in the nonlinear case, are needed. This task can be particularly challenging if sources are based on SFWM since the pump is spectrally close to the generated photon pairs but promising solution have already been implemented in an integrated way[73]. Reconfigurability of optical circuits, even required for a fine spectral tuning of photonics components, is also desirable. In centrosymetric material, this is at the moment achieved with thermal phase shifters that severely limit the operation speed and are not compatible with superconductive single photon detectors (SSPD), which work at cryogenic temperature. On the other side, fast optical modulations can be achieved through Pockels electro-optic effect of noncentrosymmetric crystals.

1.2.3 Detectors

Until a few years ago, efficient detection of single photons in the telecom band would have been a major challenge since the poor performances of photomultiplier tube and single photon avalanche photodiode made in Ge or InGaAs semiconductors. Single photon detectors are characterized by the *dead time*, that defines the time where the detector is unable to capture an event after the first detection has occurred, by *dark counts*, that are events registered in the absence of an input source, and the *quantum efficiency*, defining the probability of detecting a single photon. Upon a photon detection, the detector emits an electronic signal within a time window, called *jitter*, that is another important parameter. For photonic quantum information processing, the integration of detectors with waveguides would be ideal in order to avoid outcoupling of light in optical fiber that may be inefficient.

Superconductive single photon detector (SSPD) have proven to reach 93% quantum efficiency[74] with reset time of ∼10ns, low time jitter and dark counts. The absorbing layer is a nanowire, usually 80nm wide, made of a thin material that is cooled down right below the critical current. Upon the absorption of a photon, a hotspot is generated causing the rupture of the superconductive regime and generating an electrical signal. The only drawback of this technology lies in the low temperature operation (below 4K), requiring therefore cryogenic systems, and the poor fabrication yield. Photon counting can be achieved by multiplexing conventional detectors[75] and they can be conveniently integrated on top of waveguides[76, 77] without loosing the characteristic performances.

1.2.4 Material platforms

The material platform requires non-trivial characteristics and therefore a lot of technologies have been proposed. Here, I will review some of the main achievements in the principal platforms[78].

Silicon Due to its natural compatibility with the existent semiconductor industry and the advanced development of photonics components driven by classical information processing, the platform based on silicon on insulator (SOI) has been the leading proposal to implement photonic QIP. In fact, in this technology it has been shown almost a full range of photonics components required for QIP[79] and the first quantum devices have already been fabricated using a commercial 45nm complementary metal-oxide semiconductor (CMOS) microelectronic chip[80]. Si offers a high refractive index of 3.6 that allows a deep integration of photonic components and, together with a high $\chi^{(3)}$ susceptibility, efficient photon pairs generation by can be achieved in small modal volume cavities[81, 82, 83] or small cross-section waveguides[84]. The bandgap of 1.12eV allows the generation of photons in the telecom band where efficient gratings couplers can be used to interface optical fibers[85, 86]. However, the bandgap is not wide enough to avoid multiple photon absorption that limits both the generation rate[82] and the signal to noise ratio[87]. A reverse p-i-n junction bias has shown to mitigate the effect of nonlinear absorption in the photon pair generation[88].

The preferred method to encode information is the photon path[89, 84] and the thermo-optic effect is generally used for modulation in QIP. The process speed is severely hampered with this technology and furthermore cannot be combined with low temperature operations required for SSPD. Additionally, nonlinear absorption prevents the use of strong optical beams to achieve modulation with the Kerr effect since free carriers would be generated leading to an increase of propagation losses. By using an electro-optic cladding and slot waveguides, this problem might been solved[90] but this approach has yet to be demonstrated useful for QIP. Another fundamental challenge comes from the probabilistic nature of photons generated with SFWM, which require multiplexing schemes that might be complex to integrate within the same sample.

Silicon Nitride and Silica Other CMOS compatible platforms were investigated initially and the first QIP on a photonic sample was indeed carried out with silica-on-silicon waveguides[91, 92]. This technology benefits of high coupling efficiency with optical fibers and low-birefringence, needed for polarization encoding of photons, can be achieved with a similar technology[93]. Even though silica waveguides have provided a useful tool for proof of concept experiments, the scalability of this platform is hampered by the small refractive index contrast that causes the bending radius of waveguides to be 1000 times bigger than for silicon waveguides. The small nonlinearity requires W-level pump powers to achieve the same photon generation rate of silicon[94] and furthermore the implementation of SSPD is hard on this technology due to a small field overlap with the superconductive medium.

One promising platform that delivers low propagation losses together with a CMOS compatibility is silicon nitride (Si_3N_4) on silica. Thanks to both a moderate field confinement and a third-order nonlinearity, efficient photon pair generation can be achieved with high quality factor ring resonators[95, 96, 97] and advanced photonic circuits for QIP are realized[98]. Even though the amorphous crystal structure does not present a Pockels coefficient, fast modulation might be achieved using the Kerr effect[99] since the wide bandgap prevents multiplephotons absorption that plagues the Si counterpart. However, a defined crystal structure is a prerequisite to achieve high quality sources since Raman gain is spectrally limited to defined wavelengths and the generation of uncorrelated photons can be avoided if the flying qubit wavelengths do not match the Raman ones. This is a main drawback for all source based on SFWM implemented on amorphous materials.

Aluminium Nitride Between all CMOS compatible materials, aluminium nitride (AlN) have risen a growing interest for both classical and quantum applications. Low loss waveguides (0.6dB/cm)[100] can be fabricated starting from an AlN layer deposited by sputtering on top of a silica layer. Instead of being completely amorphous, the layer growth has preferential directions resulting in a non-vanishing $\chi^{(2)}$ nonlinearity[101, 102]. Together with high quality factor ring resonators, efficient photon pairs generation has been demonstrated through a SPDC process[103]. Furthermore, fast electro-optical switches can been realized in this technology[100]. Even though the presence of solid state emitters would be beneficial, this platform represents a promising candidate for an all-optical QIP approach.

Gallium Arsenide The CMOS compatible platforms treated up to now lacks in a solid state emitter that can provide essential resources for QIP (Sec.1.2.1 and 1.2.2). Between the III-V compounds, developments in integrating quantum dots in photonic structures and other essential components for QIP have reached an advanced state in GaAs[104]. Photons emitted can successfully be channelled with almost unitary probability in waveguides[105, 106] representing an ideal integrated photon source. Due to the lack of inversion symmetry, SPDC can be used to produce entangled photons[107, 108] and the high electro-optic coefficient allowed the realization of fast switches[109]. A strong light-matter interaction is provided with photonic crystal cavities where quantum dots can be placed in the middle of the low-modal volume achieved in such as structures. This results in both ondemand single photon generation and a strong single-photon nonlinearity[69]. Other than the low temperature operations, the main drawbacks coincide in the inhomogeneous broadening and the random position of quantum dots, even though progress have been made in addressing these problems[104]. Furthermore, linear losses of photonic circuits are considerably higher than the CMOS compatible materials.

Diamond The wide band-gap of $\sim$5.5eV allows the presence of more than 500 colour centers and most of them are optically active in the visible spectrum. A relatively low phonon population grants the electronic state of defects to persist for long time without phonon-induced relaxation[47]. Exceptional mechanical and thermal properties are available in this material that can be synthesized in high purity thanks to CVD techniques[110, 111]. Even though during the years many defects were isolated singularly, NV and SV center are the most employed for QIP. Thanks to the properties described in Sec.1.2.1, NV centers have shown advanced optical quantum network functionalities that, by employing the spin-photon entanglement[112], have led to the demonstration of quantum teleportation[113] and the loophole-free Bell inequality violation[114]. Even though NV centers can be used for memory[115], SiV centers can be used for ondemand single photon sources due the low inhomogeneity and to create quantum-optical switch[116]. The best quality defects require a crystalline bulk diamond that is not fabrication friendly since the need of free-standing structures[117]. Another approach is to etch a 20μm membrane to a desired thickness[118] that has brought to the demonstration of high quality factor ring resonators (10^6) and efficient non linear frequency conversion[119]. Alternatively, polycrystalline thin films can be grown heteroepitaxially on sacrificial substrate[120]. However, the realization of large-scale single-crystal layer is the main challenge to the scalability of this technology. Furthermore, a lack of Pockels coefficient and auxiliary electronics, that is difficult to integrate on this material[78], are impairing factors to the realization of diamond QIP.

1.3 3C SiC as quantum photonic platform

In the development of new platforms for photonics applications, a lot of interest has grown in 3C Silicon Carbide (SiC) for its unparalleled properties suitable especially for quantum and integrated non-linear optics. The unique properties of 3C Silicon Carbide have risen interest for the possibility of developing integrated quantum and non-linear devices. Its non-centrosymmetric crystal structures grants both third-order and second-order non-linear effects, with a significant $\chi^{(2)}$ susceptibility of 20.4 pm/V[121]. The high refractive index of 2.6, indispensable for deep integration of photonic component and small modal volume in resonators, together with the wide electronic bandgap of 2.3 eV, could allow efficient non-linear optics process, like frequency conversion and non-classical generation of light, without incurring in multiple photon absorption[122]. Furthermore, the high electro-optic coefficient could be used for the fabrication of fast lossless Pockels modulator[123, 124]. 3C SiC thin layers can be grown directly on top of a silicon substrate thanks to a CVD process [125] meanwhile other polytypes need extra fabrication steps (like smartcut process) to create thin layers from thick homoepitaxial crystals[126].

The presence of point defects [127, 128] adds the possibility of implementing a wide range of quantum application (from single photon generation[129, 130] to the engineering of light-matter interaction). Indeed, SiC color centers display features similar to diamonds NV centers[131] with the convenience of near infrared zero phonon line (1100 nm)[132], the possibility of being integrated with semiconductor devices and an easier fabrication technology, more scalable than diamond one. In order to take advantage of all this properties, a fully scalable photonics platform, able to integrate different components, is needed[38]. Due to a small lattice mismatch with niobium nitride[133], SiC could be used to fabricate superconducting detectors with unparalleled signal to noise ratio. The photonic platforms discussed in the previous section are compared with SiC in Tab.1.1, comparing their main features for quantum applications.

The development of photonic structures in this material suffered from the presence of the Si substrate, since its higher refractive index makes the light confinement impossible. The only attempt of waveguiding with high modal-area geometry relied on oxygen implantation[124] or sapphire substrate in order to achieve SiC on insulator[134]. However, sub-μmeter cross-section waveguides benefit of higher confinement, essential for enhancing light-matter interactions and deep integration of optical devices. Moreover, in order to take advantage of the $\chi^{(2)}$ susceptibility and for a vast number of general applications, circular resonators are needed[135, 136, 137, 138]. High-multimode suspended cavities were demonstrated with high quality factor[139, 140], however lacking in the possibility of either engineering the mode dispersion or the coupling with an integrated bus waveguide. Rib waveguides with PECVD SiC have already been realized [141], even with losses less than 1dB/cm [142].

	SSE	NL	PM	PL	TPA	Detector	Waveguide
SOI [143, 144, 79, 145]	-	3×10^{-18} m^2/W	TOPS	0.9 dB/cm	5×10^{-12} m/W	SNSPD	strip Si/SiO_2
Si_3N_4[146, 147, 148, 149]	-	2×10^{-19} m^2/W	TOPS	<1 dB/cm	-	SNSPD	strip Si_3N_4/SiO_2
SiO_2 [150, 151, 152]	-	3×10^{-20} m^2/W	TOPS	<1 dB/cm (low conf.)	-	TES	direct written or Ge:SiO_2/SiO_2
AlN[100, 100, 153, 154]	-	5 pm/V	Pockels	0.6 dB/cm	-	SNSPD	strip AlN/SiO_2
GaAs[155, 104, 6]	QD	90 pm/V	Pockels	3 dB/cm (low conf.)	-	SNSPD	strip GaAs/AlGaAs
Diamond [119, 156, 157]	SiV/NV	8.2×10^{-20} m^2/W	TOPS	0.34 dB/cm	-	SNSPD	free-standing wire or ridge diamond/SiO_2
SiC [128, 121, 123, 124, 133, 11]	Ky5	20 pm/V	Pockels	21 dB/cm	-	SNSPD	Suspended

Table 1.1: Comparison of main features of optical platforms for quantum applications. SSE - Solid state emitter; NL - Nonlinearity value (with red is identified the $\chi^{(2)}$ nonlinearity meanwhile in blue is identified the Kerr nonlinear index); PM - Phase modulation; PL - Propagation losses (at 1550nm); TPA - Two photon absorption (at 1550nm); TOPS thermo-optic phase shifter; TES - Transition edge detector; SNSPD - Superconductive nanowire single photon detector

1.4 Summary of the thesis

As discussed in Sec.1.2.4, the material platforms proposed so far for photonic QIP face challenges deriving from intrinsic material properties or from technological impairments. The outstanding optical characteristics of 3C SiC together with a well-develop semiconductor technology, make this material a promising candidate for nonlinear and quantum photonics. The scope of this work is to harness all optical resources of 3C SiC by developing essential photonic components. Advancements are also achieved in Si_3N_4 that may offer new possibilities in a uncommon spectral range.

The thesis is organized as follow: in Chap.2 efforts required to develop the fabrication procedure of 3C SiC are reported with special emphasis on the realization of suspended waveguides. The design and characterization of sub-μm waveguides, grating couplers and ring resonators, realized with the suspended technology, is reported in Chap.3. The realization of small modal volume cavities facilitates the observation of nonlinear effects, like reported in Chap.4 where the proposal for efficient second harmonic generation is disclosed together with the experimental demonstration of frequency conversion by means of four wave mixing. As reviled in Chap.5, thanks to $\chi^{(3)}$ nonlinearities, correlated photon pairs in Si_3N_4 ring resonators are generated in the nearinfrared band, where competitive semiconductor detectors can be integrated together with thermal phase shifter to realize a complete reconfigurable quantum photonic platform working at room temperature. In order to take advantage of SiC point defects, in Chap.6 is reported our efforts to develop high quality-factor photonic crystal cavities, whose small modal volume is essential to enhance the light-matter interaction and consequently to provide deterministic single photon emitters as well as strong nonlinearities at single photon level. Another interesting feature of this material is exploited in midinfrared wavelengths, where *surface phonon polaritons* (SPhP) propagate at the interface with air and the strong coupling with resonant modes is demonstrated in Chap.7, unfolding the path for polaritonic circuits. Finally, conclusions and perspectives are reported in Chap.8.

Chapter 2

Development of SiC Fabrication

In this chapter I report the process development to produce SiC photonic devices in the Southampton Nanofabrication Centre. The fabrication steps will be used to realize SiC waveguide components, photonic crystals and SPhPRs. For this reason, a study of the SiC dry etch as well as of an appropriate hardmask was performed. Due to the superior complexity in the fabrication of SiC waveguides, the focus is concentrated on their development.

2.1 Etheroepitaxial growth of SiC layer

In addition to the outstanding optical properties described in Sec.1.3, the growth of SiC is of a fundamental interest for many mechanical and chemical properties of this material, useful for the realization of high power electronics as well as sensors[158]. The high production cost of the hexagonal SiC polytypes (4H and 6H), grown homoepitaxially, has motivated the research for a heteroepitaxial-growth technique on top of a silicon substrate, to deposit SiC on an area as large as possible and consequently to reduce the production costs. The cubic structure (3C SiC) is obtained when the bilayer stacking is of the kind ABCABC. . . , resulting in a pure zincblende structure that is more stable at lower temperature with respect to other polytypes. Consequently, 3C SiC can be grown below the Si melting temperature (1410 degC), meaning that the growth of epitaxial 3C SiC films on Si substrates is allowed. Furthermore, Si and 3C SiC have the same cubic symmetry, which implies a relationship of epitaxy usually driven by the orientation of the substrate seed.

The heteroepitaxial growth of SiC on top of Si is technologically challenging due to the high lattice mismatch between these two materials. 3C SiC and Si have a lattice constant of 4.3589Å and 5.4311 Å, respectively, resulting in a lattice mismatch of $\Delta a/a$ of about 19.7%. In order to overcome the lattice mismatch, Nishino et al[159] proposed the use of a multi-step CVD process consisting of three steps (Fig.2.1): a) an etching is performed at 1100 °C using HCl gas flow to clean the Si substrate; b) the Si surface is carbonized at 1360 °C for 2min using C_3H_4 as gas; c) a single crystal is grown at the same temperature of the carbonization step using C_3H_4 and SiH_4 as gas precursors. The carbonization of the Si substrate acts like a buffer layer between Si and SiC since it mitigates the effect of lattice mismatch. During the carbonization, Si atoms out-diffuse to react with the carbon atoms coming from the pyrolytic decomposition of the propane and, as a result, voids are formed in the Si substrate as reported in Fig. 2.2.

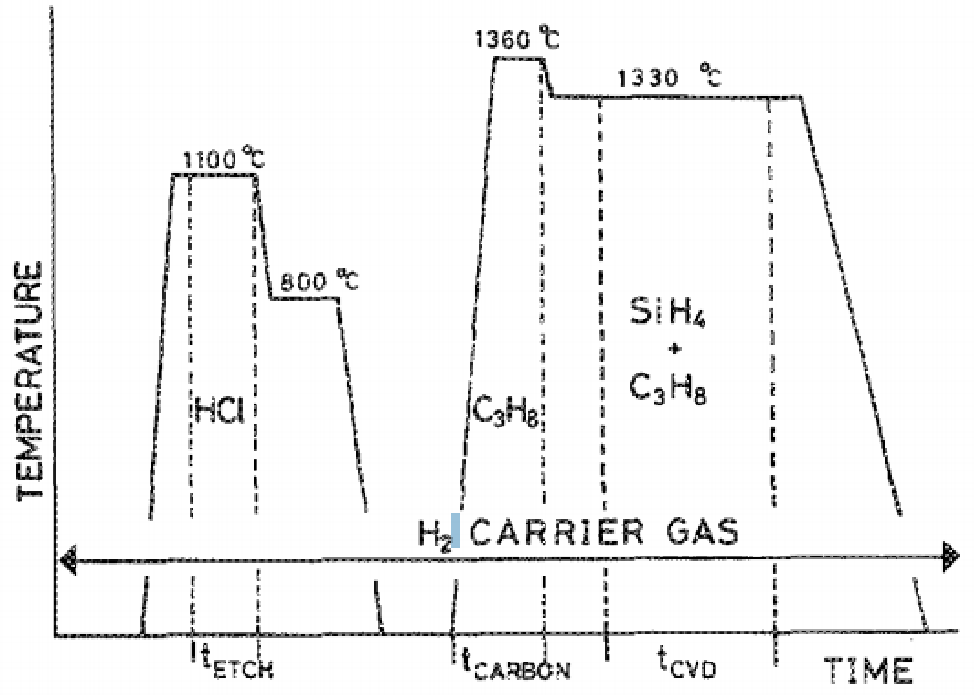

Figure 2.1: Temperature steps for the growth of monocrystalline 3C SiC on top of a Si substrate. With t_{ETCH}, t_{CARBON} and t_{CVD} are indicated the time for surface cleaning, surface carbonization and SiC growth, respectively[3].

The lattice misfit contributes to a residual strain field at the SiC-Si interface that (in order to relieve it) results in high density region of defects in the SiC film, such as stacking faults, microtwins and anti-phase boundaries. This is evident from Fig.2.3, where a cross-section TEM image of a (111)-oriented 3C SiC heteroepitaxially grown on Si shows a dense presence of defects at the interface (darker region). The SiC quality gradually increases with the thickness of the deposited film, eventually leading to a region with low presence of defects (Fig.2.3). In addition, SiC and Si have different thermal expansion coefficients (a mismatch of about 8% is reached at room temperature), causing a tensile strain that results in the bowing of the wafer once it is cooled down after the growth. The amount of bowing is dependent by wafer size, thickness of both 3C SiC film and Si substrate and can lead to the generation of cracks in the epitaxy and in the substrate[158].

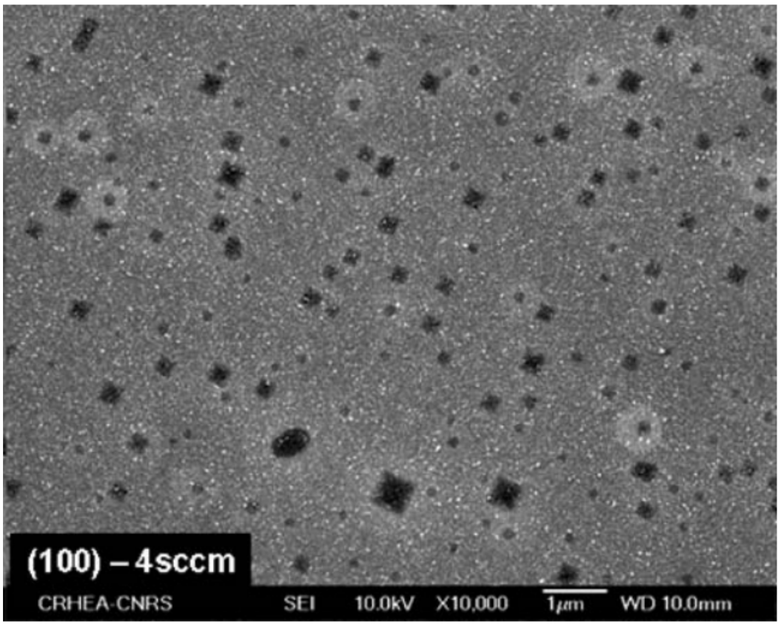

Figure 2.2: SEM picture taken after deposition of a thin layer of (001) 3C SiC[4].

Even though a lot of research has been carried out to use compliance substrates to reduce the presence of stress and voids[160, 161, 162], the multi-CVD technique is the most employed for the heteroepitaxial growth of SiC. For the work carried out in this thesis, I employed a (001)-oriented 3C SiC grown by NOVASIC[163] with the same method developed from Nishino et al. In addition to the polished surface, fundamental for the fabrication of photonic components, the SiC provided by this company has already proven useful to create and observe SiC point defects[164].

2.2 Ellipsometer measurement of SiC layer

Ellipsometry uses a collimated beam to shine the sample surface meanwhile a sensor measures the reflected amplitude. By fitting the polarization change of the beam due to the layer properties, it is possible to retrieve different parameters, like the refractive index n and the material absorption α. The ellipsometer Woolham M-2000, in particular, offers a quick evaluation of layer thickness (mostly transparent dielectrics) and it has been vastly used together with the ICP RIE (*Inductively Coupled Plasma Reactive Ion Etching*) to determine etching rates and selectivities with respect to masks. Moreover, the exact knowledge of the SiC refractive index is a crucial point for the development of linear and nonlinear photonics.
Using the Cauchy model in the transparent window of SiC

$$n(\lambda) = A + \frac{B}{\lambda^2} + \frac{C}{\lambda^4} \tag{2.1}$$

Figure 2.3: Cross-section TEM image showing a (111)-oriented 3C SiC from the interface with the Si to the surface. The darkest part of the image, close to the interface with Si, is due to the large density of defects generated by the heteroepitaxy[5].

is possible to find the coefficients A, B and C describing the material dispersion, as reported in Fig.2.4. The presence of voids in the Si substrate[165, 166, 167], due to the carbonization step done before the heteroepitaxial growth, limits the fit quality to *mean squared error* (MSE) of 10-20. Improvements can be achieved considering a graded layer, to take in account the inhomogeneity of the material as the thickness grows (2.3). As reported in Fig.2.5, where the MSE is plotted in function of percentage change of the A parameter, the absolute minimum corresponds to a variation along the growth direction of 6.8%. If we consider this variation in the A coefficient, the resulting fit provides two refractive indexes for the top and the bottom SiC levels (Fig.2.6).

The introduction of different parameters to describe different layers of the SiC slab can reduce the MSE value of 50%, however the development of a model with fixed Cauchy's values that is able to fit all different points of the wafer and all different thickness, is still to be found.

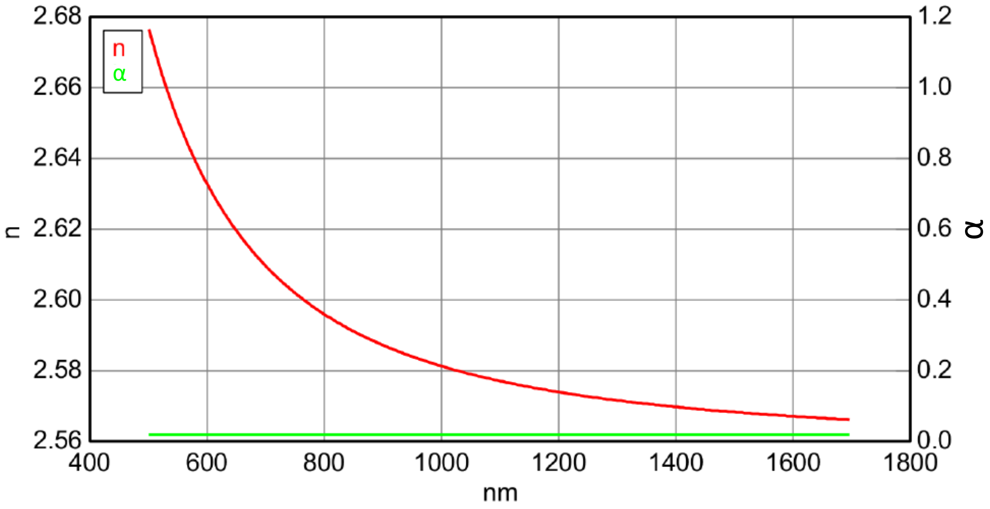

Figure 2.4: Fitted SiC dispersion with $A = 2.559$, $B = 0.01994[\mu m]^2$ and $C = 0.00238[\mu m]^4$. The value of the absorption coefficient is $\alpha = 0.019121/cm$

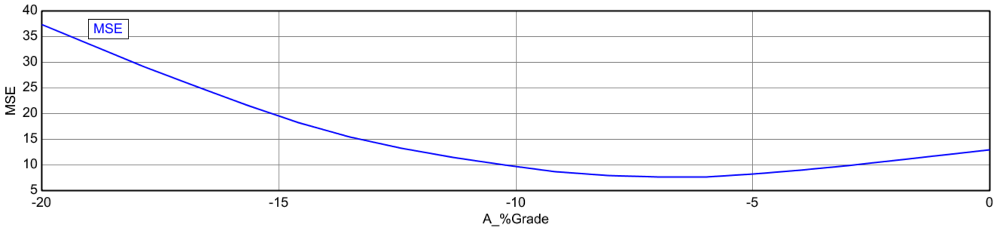

Figure 2.5: The minimum of the MSE corresponds to an inhomogeneity of 6.8%. The grading of the SiC layer is a statistical relevant parameter for the fit since it provides only one absolute minimum of MSE

2.3 Plackett-Burman design for SiC etch

Photonics structures generally require to be patterned by means of lithography tools and anisotropic etches. The latter is not trivial in SiC due to its chemical inertness and robustness against physical etches, like ion sputtering or milling. As a result, SiC is far more etching resistant than many resists or hardmasks from both physical and chemical point of views. The ICP RIE has proven to be able to etch SiC thanks to reactive ions impacting the surface with high energy and providing combined chemical and physical actions. Strong RF sources generate the reactive plasma from gas precursors meanwhile additional RF induction magnetic coils control the plasma density, providing supplementary advantages in term of process control over standard RIE tools. The ICP RIE technology offers great versatility in the choice of the parameters and its potentials in the nanofabrication of SiC has already been widely investigated.
The principal gas mixture employed for the etching of SiC with RIE-based tools consists of SF_6 and O_2, where the ratio of 4:1 (SF_6:O_2) was found to provide high etching rates in different independent studies [168, 169, 170, 171, 172, 173]. The addition of Ar to the

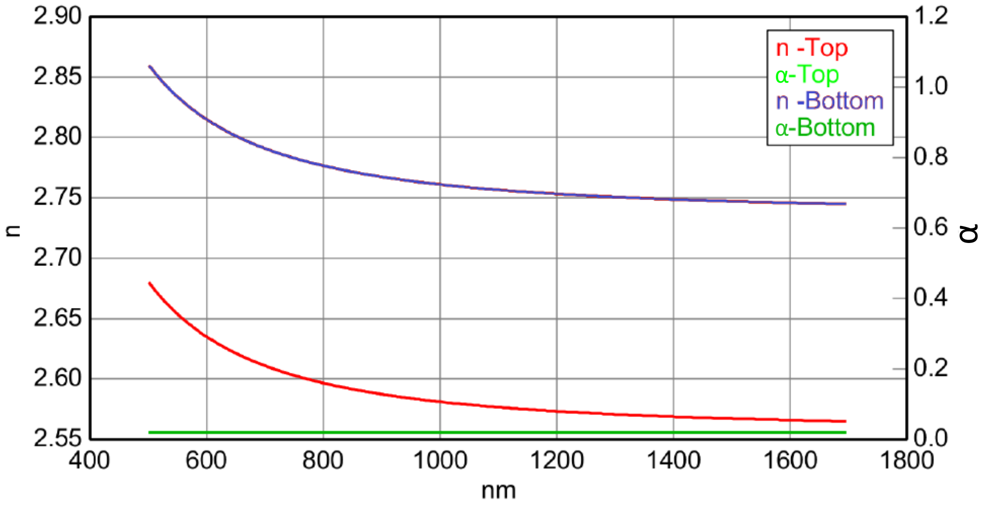

Figure 2.6: New fit made with the SiC slab of 1.2μm divided in 30 layers with different A parameters. In the middle layer, the value of $A = 2.647$, $B = 0.02183[\mu m]^2$ and $C = 0.00224[\mu m]^4$. The inhomogeneity causes two refractive index dispersions for the top and bottom layers while the values of the absorption coefficients are coincident.

SF_6-O_2 mixture was found beneficial to further increase the etching rate [174]. Other fluorine[175] and chlorine[176, 177] based gas precursors were also studied with considerably lower etching performances in term of etching rate and sidewall angle. Photonic crystals realized in SiC were fabricated using SF_6-based gas mixtures[178, 179] meanwhile CHF_3-O2 mixture was used for the realization of ring resonators[140] and CF_4-Ar mixture to fabricate toroids[180]. Since SF_6 is the most used gas for the etching of SiC and was successfully employed to fabricate photonic components[178] in the same material I used in this thesis (provided by NOVASIC), I performed the etch study in the SNC cleanroom by fixing the SF_6 gas flow meanwhile changing its ratio with other gases in the ICP-RIE chamber.

The optimal condition of the etch (most anisotropic etch with an etching rate that allows a controllable depth) is strongly dependent on the exact properties of the plasma and chamber configuration. Consequently it is impossible to transfer the parameters found in literature to the OIPT SYS380 tool made by Oxford Instrument that is available in the SNC facility. The development of a physical model that describes the profiles of distribution of electrons and ions within the plasma inside the ICP-RIE chamber requires computationally expensive numerical simulations. In addition, the plasma modelling is usually subjected to many simplifying assumptions that, together with the complex nature of particle dynamics within the plasma, make the connection between these microscopic models and macroscopic parameters (such as etch rate) difficult to establish[181]. However, empirical approaches can be used to obtain statistical models that describes the etch characteristics in terms of input parameters. This methodology effectively treats the etching process as a black box with input *factors* (gas mixture, plasma energy, pressure, etc.) and output *responses*(etching rate, anisotropy, uniformity, etc.) which connections are described thanks to a set of definite experiments (called *runs*). The process of changing one or more factors in order to observe their effects on one or more responses can be time and cost consuming, especially with a large number of factors. The (statistical) *design of experiments* (DOE) is an efficient procedure for planning experiments so that the data obtained from a limited number of runs can be analysed to yield valid and objective conclusions[182].

The most common empirical model that can be used to fit the experimental data is linear

$$Y = C_0 + \beta_1 X_1 + \beta_2 X_2 + \beta_3 X_3 + \beta_{12} X_1 X_2 + \tag{2.2}$$

$$+ \beta_{13} X_1 X_3 + \beta_{23} X_2 X_3 + \beta_{123} X_1 X_3 X_3 + \text{experimental error} \tag{2.3}$$

where X_s are the main terms, $X_s X_r$ are interaction terms and $X_s X_r X_t$ is a three-way interaction term. The scope of DOE is to determine all the unknown β parameters to address which one is statistically irrelevant ($\beta \simeq 0$) and which one has a significant impact on the output. In order to fully describe Eq.2.2, the *full factorial design* is required for the simultaneous study of the effects that several factors may have on a process. For the linear model described by the full factorial design, the input factors can assume two levels and a design with all possible high/low combinations of all the input factors will require 2^N experimental runs, with N the number of input factors.

For the SiC etch development, I am interested in screening which are the statistical relevant factors between a total of ten factors and the use of a full factorial design would require 2^{10} etches. Instead of varying levels one at a time, it is convenient to change levels simultaneously. In the attempt to find an experimental design where each combination of levels for any pair of factors appears the same number of time, Plackett and Burman[183] described a construction of a very economical design where the total run number is a multiple of four (rather than a power of 2). Therefore, this design is very efficient in the screening process when only main effects are of interest. In fact, the downside of this method is given by the impossibility to distinguish main factors from effects given by the interaction of two factors. The development of this experiment as well as the analysis of the results was carried out with the help of Dr. Owain Clark. In Tab.2.1 twelve different experiments are reported, where the flow of SF_6 was maintained constant in order to study its interaction with other gases. The ranges of the factor composing Tab.2.1 were chosen to effectively encompass the typical values of etch recipes in the ICP RIE tool of the SNC .

These experiments were carried out on 5mm x 5mm chips, with a patterned grating of S1813 positive resist made via optical lithography. The resist thickness was 1.3 μm and the sidewall angle, selectivity and etching rate were measured via a SEM analysis of the cross section, obtained through the cleaving of the chips. The 1st and the 6th etch are reported in Fig.2.7 .(a) and (b) respectively.

Run #	P (mT)	T (°C)	RF (W)	ICP (W)	MC (A)	SF_6 (sccm)	O_2 (sccm)	Ar (sccm)	C_4F_8 (sccm)	TF (sccm)
1	5	15	50	1500	0	50	10	10	10	80
2	5	-5	25	1500	1	50	10	0	40	100
3	5	-5	25	1000	0	50	0	0	10	60
4	15	15	50	1000	1	50	10	0	40	100
5	15	-5	50	1500	0	50	10	0	10	70
6	5	15	50	1000	1	50	0	0	10	60
7	5	-5	50	1500	1	50	0	10	40	100
8	15	15	25	1500	1	50	0	10	10	70
9	5	15	25	1000	0	50	10	10	40	110
10	15	15	25	1500	0	50	0	0	40	90
11	15	-5	25	1000	1	50	10	10	10	80
12	15	-5	50	1000	0	50	0	10	40	100

Table 2.1: Plackett-Burman experiment of design for SiC etch characterization. P: pressure in the chamber; T: plate Temperature; RF: power in the forward capacitors; ICP: Power in the ICP capacitors; MC: magnetic current; SF_6: Sulphur Hexafluoride; O_2: Oxygen; Ar: Argon; C_4F_8: Octafluorocyclobutane; TF: total flow inside the chamber.

In Tab.2.2, the results measured from the etches are showed. These output values were analysed through the software MiniTab, that performs the *analysis of variance* (ANOVA) technique to statistically determine which of the input parameters have the strongest effect on each output we measured. As can be seen from Fig.2.8, the main

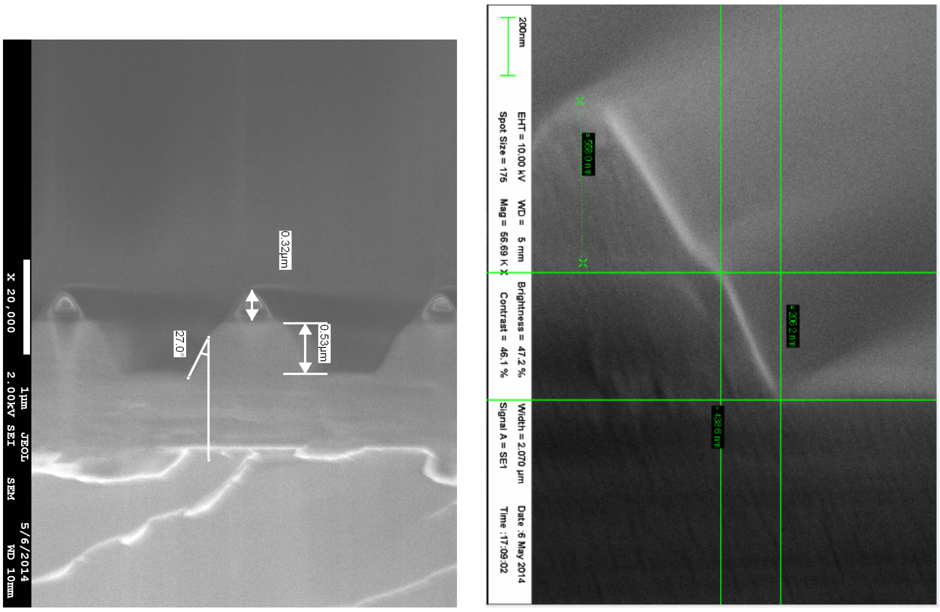

(a) (b)

Figure 2.7: (a) experiment 1; (b) experiment 6. The relative parameters can be found in Tab. 2.1. After the etches, both the samples still presented the resist on top the etched SiC layer. In (a), the Si substrate can be seen

factors to get the most anisotropic etch are the forward power, the ICP power and the pressure. This is also confirmed from the Pareto plot of Fig.2.9 , where the red line in the Pareto plots indicates a level beyond which main factors are statistically significant.

The effects of the inputs on the etching rate are reported in Fig.2.10 and the relative Pareto plot in Fig.2.11. An increase of RF or ICP plasma powers boost the etching rate since the higher energy promotes physical sputtering. On the other side, the presence of C_4F_8 inhibits the chemical reactions and the same effect is provided by lowering the plate temperature. Finally, with pressure is possible to control the amount of chemical reagents in the chamber as well as the physical etch. We believed that a smaller amount

Run (#)	SA(°)	ER SiC (nm/min)	ER S1813 (nm/min)	Selectivity
1	64.7	261	500	0.52
2	54.3	86	200	0.43
3	42.7	117	290	0.40
4	44.2	97	250	0.39
5	64.8	175	400	0.44
6	70.2	224	370	0.61
7	71.4	165	420	0.39
8	49.5	127	320	0.40
9	/	/	/	/
10	55.3	70	185	0.38
11	39.9	75	193	0.39
12	42.6	80	165	0.49

Table 2.2: Results of Plackett-Burman experiment. SA: sidewall angle; ER: etching rate

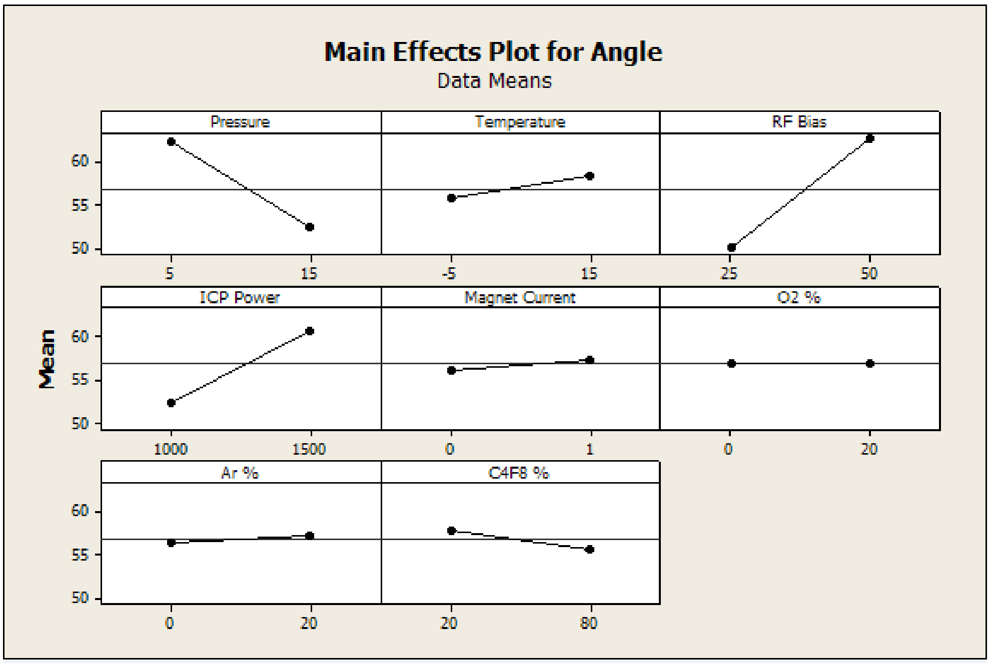

Figure 2.8: Effects of the inputs on the sidewall angle

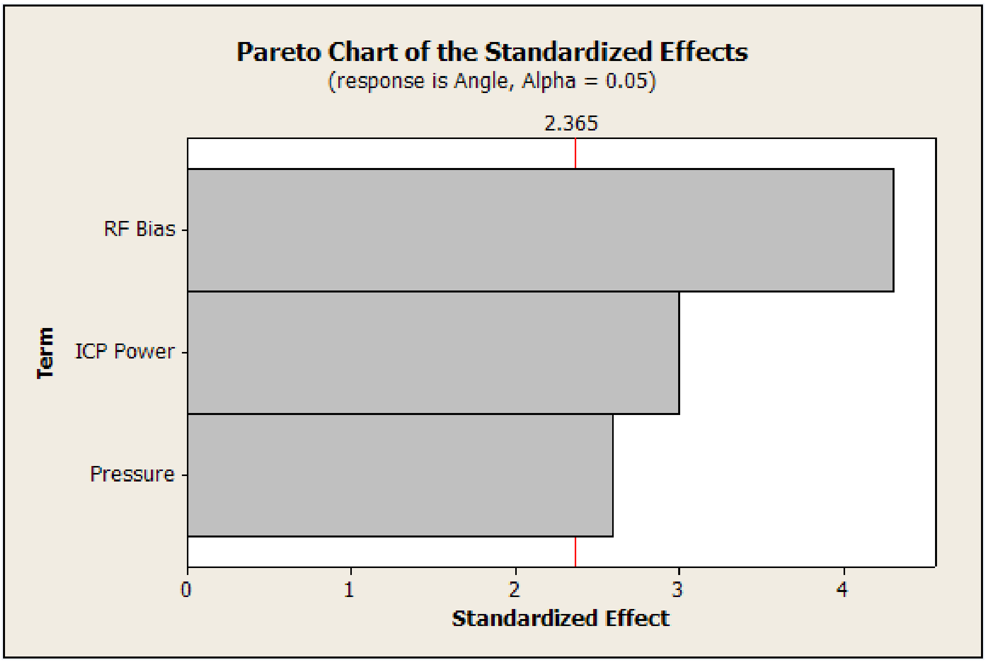

Figure 2.9: Pareto plots for the effects of the inputs on the sidewall angle

of precursors could increase the physical sputtering of SiC since the increased line of sight allows a higher ion acceleration before impacting the SiC layer. On the other side, we observed a decrease of etching rates at pressures below 5mTorr since in this condition the process is limited by the amount of reagents.

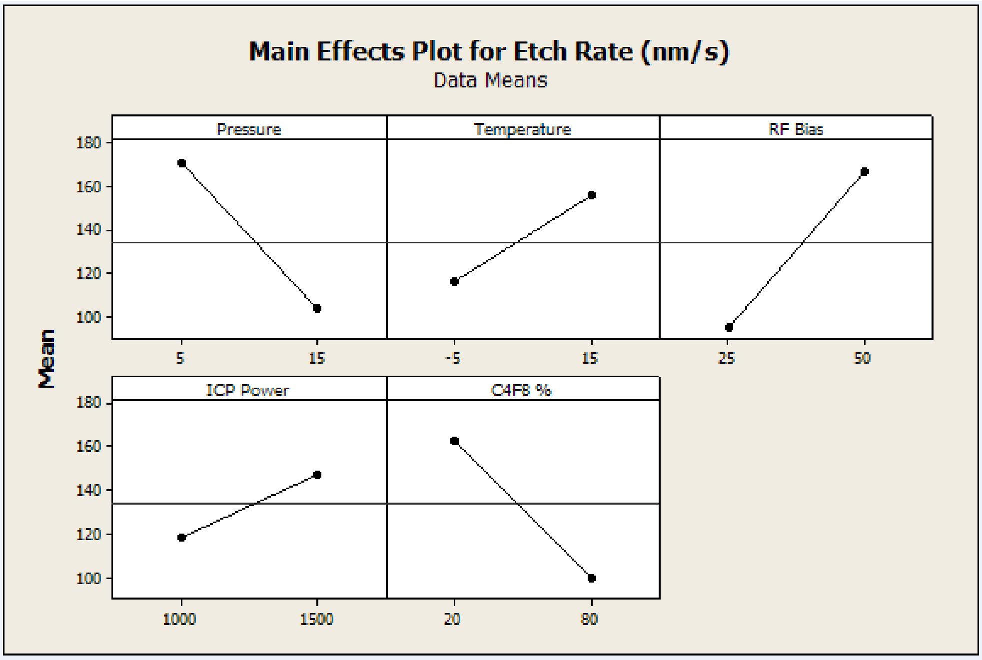

Figure 2.10: Effects of the inputs to the etching rate

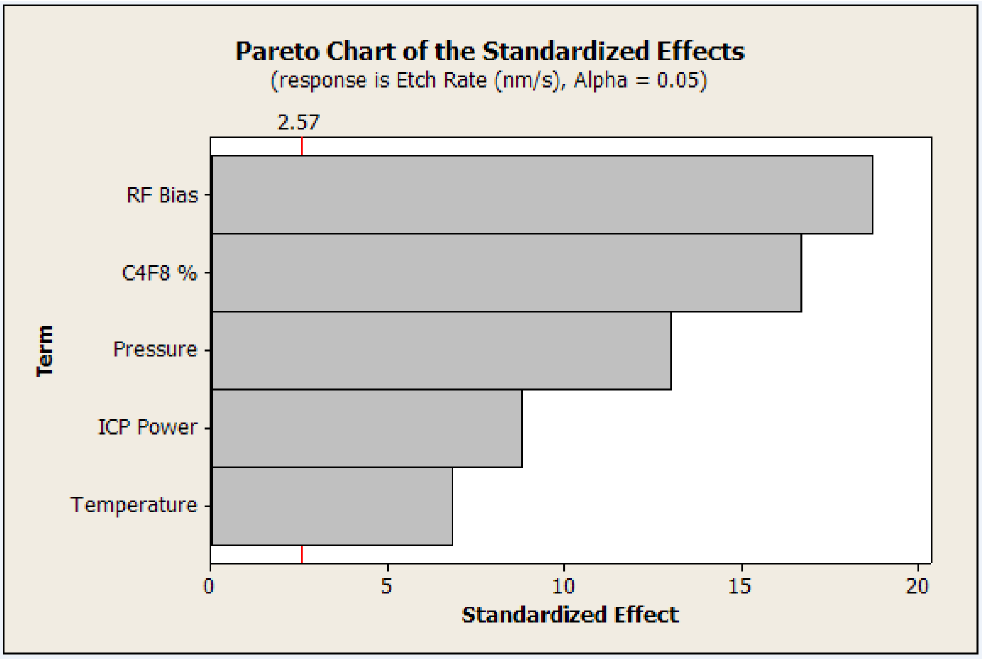

Figure 2.11: Pareto plots for the effects of the inputs on the etching rate

2.4 Process workflow

The waveguide cross-section is showed in Fig.2.13 and the process step list used to fabricate it is reported in Fig.2.12. Unlike the previous works, here we are going to remove the Si substrate under the SiC waveguide by the use of xenon difluoride (XeF_2). This gas can reach the substrate through a series of holes of 1.6μm diameter, appositely made on the SiC slab along the sides of the waveguides ($\sim 7\mu$m of distances) with a repetition of one every 6μm. In this way, the photonic structures are suspended in air thanks to a membrane and a high refractive index contrast is reached.

So far, only micrometer rib waveguides were realized in SiC, where the related transverse mode fields were not able to reach a tight confinement. Even if a large mode reduces the losses since the scattering due to the roughness decreases, the mode is less concentrated in the waveguide leading to less efficient non-linear effects.

2.5 Hardmask and process definition

The high-energy SiC etch performed with the ICP RIE can not be used only with electron beam resists since these offer a limited etching resistance and they generally come in low thickness to attain high resolutions in patterning. The ratio between the mask and SiC etching rates defines the *selectivity* of one particular etch and high values are desired to achieve anisotropic and deep etches. The photonics layout is transferred from an electron beam resist to a sacrificial middle layer (called *hardmask*) with a dry etch and

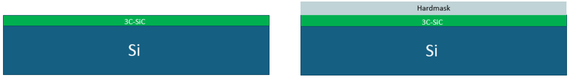

(a) 400nm SiC layer (b) Hardmask deposition

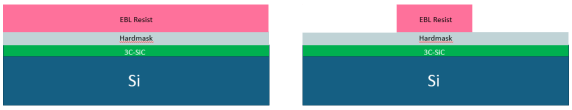

(c) EBL-resist deposition (d) Waveguides pattern

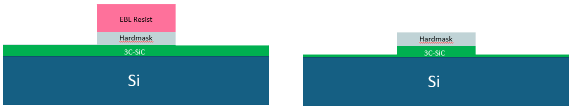

(e) Hardmask etch (f) SiC etch

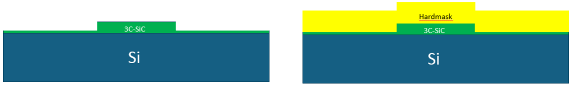

(g) Hardmask removal (h) Hardmask deposition

(i) EBL resist deposition (j) Holes pattern

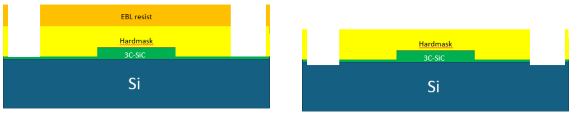

(k) Hardmask etch (l) SiC holes

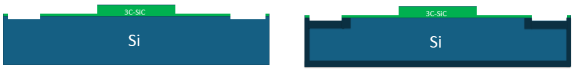

(m) Hardmask removal (n) Si oxidation

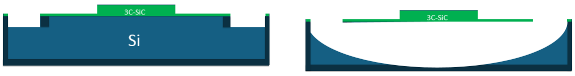

(o) SiO_2 dry etch (p) XeF_2 etch

Figure 2.12: Workflow for the fabrication of SiC suspended waveguides

then a second one patterns the SiC taking advantage of superior etching resistance of the hardmask, able to stand the etch for the time needed to reach the desired depth in SiC. In the following, different hardmasks are employed to find which one is able to deliver vertical sidewall, low roughness and the desired etch depth of SiC. Even though etches are aimed to fabricate waveguides, some results coming from realized photonic crystal samples as well as SPhPR pillars are used for the process analysis.

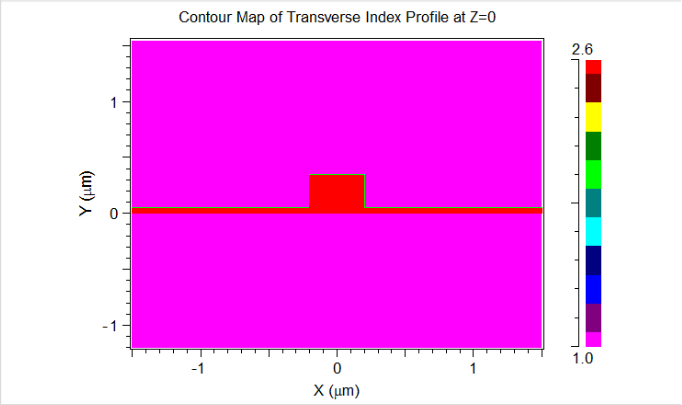

Figure 2.13: Structure of the suspended SiC waveguide (400nm width, slab of 50nm and total thickness of 400nm)

2.5.1 Nickel hardmask

Thanks to the results from the Plankett Burman DOE, we developed the anisotropic etch for SiC in the OIPT SYS380 reactor, using 800 W of ICP power, 280 W of forward power, 0.7 mT of pressure , 5 sccm of SF_6 flow, 2 sccm Ar flow and 20°C of plate temperature. The etching rate was ∼150nm/min with a high selectivity for Chromium (Cr) and Nickel (Ni), and below one for SiO_2. In Fig.2.14 is reported the cross section of SiC grooves etched with the anisotropic recipe, where the sidewall angle of the structures was better than 86°. For the etch of Fig.2.14, we employed Ni as hardmask deposited by electron beam deposition and using a lift-off process. Unfortunately, the Ni etch is difficult to perform with an electron beam resist and the lift-off technique is not suited for photonics processing due to the high roughness.

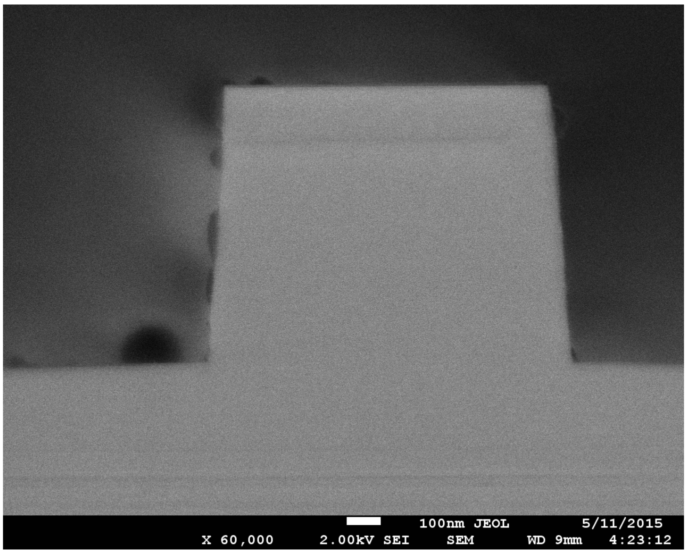

Figure 2.14: SiC etched with 800 W of ICP power, 280 W of forward power, 0.7 mT of pressure , 5 sccm of SF_6 flow, 2 sccm Ar flow and 20°C of plate temperature. A Ni hardmask deposited by lift-off was used for the etch

2.5.2 Chromium hardmask

Another hardmask able to stand with high selectivity over the powerful anisotropic SiC etch described in the previous section is Cr that, differing from Ni, can be successfully dry etched using chlorine gas precursors. In order to define the 400nm-width waveguide we employed 30nm of HSQ as negative electron beam resist, which offers high selectivity with chlorine-based etches and high lithography resolution. The pattern in the resist was transferred to the Cr hardmask of 60nm thickness (deposited with electron beam deposition) thanks to the ICP RIE. The etch lasted ten minutes with the following parameters: 2000 W of ICP power, 25 W of RF forward power, 16 mT of pressure, 50 sccm of Cl_2 flow and 20 sccm O_2 flow. The selectivity of the Cr etch and HSQ was measured to be greater than 20:1.
With all the process steps characterized, the first SiC sample patterned with electron beam lithography was made and in Fig.2.15.(a) is showed the top view of the waveguide while in Fig.2.15.(b) is reported the 35° angled view of the etched sidewall of the SiC. The top view of the waveguide shows a problem of shrinking of the Cr hardmask during the etch of SiC, due to the behaviour of the HSQ during the Cr etch. This effect was further investigated in the fabrication of pillars in SiC, where in Fig.2.16.(a) was used a 100nm-etched Cr hardmask (prepared in the same way as for the waveguide) and in Fig.2.16.(b) it was used the same thickness of Cr deposited by lift-off (the conditions of etching for the SiC were equal for both the samples).

Increasing the forward power from 25W to 75W of the Cr etch solved the shrinking problem and consequently the waveguide showed in Fig.2.17.(a) was realized. Although the good verticality of the etched sidewall (Fig.2.17.(b)), the waveguides presented an excessive roughness due to the grain size of the Cr film. Furthermore, the conditions of low pressure and high power of the SiC etch resulted in an uncontrollable etching rate since the gauge of the tool chamber is not accurate at this pressure level. An increase of

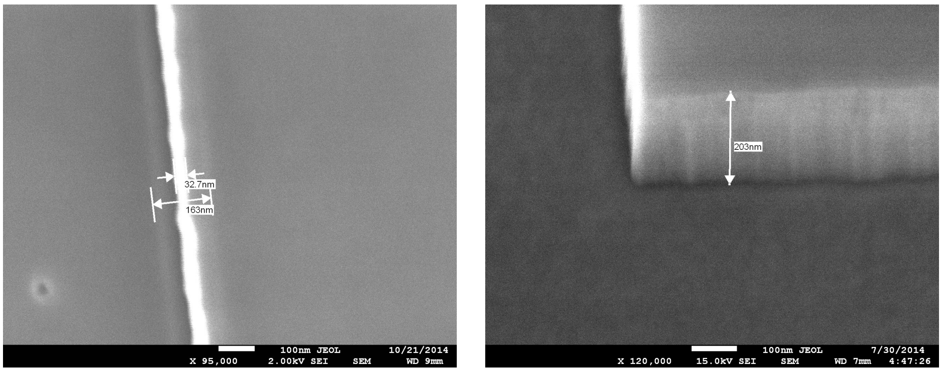

(a) (b)

Figure 2.15: (a) top view of the realized waveguide with the Cr hardmask ; (b) 35° view of the etched mark in SiC.

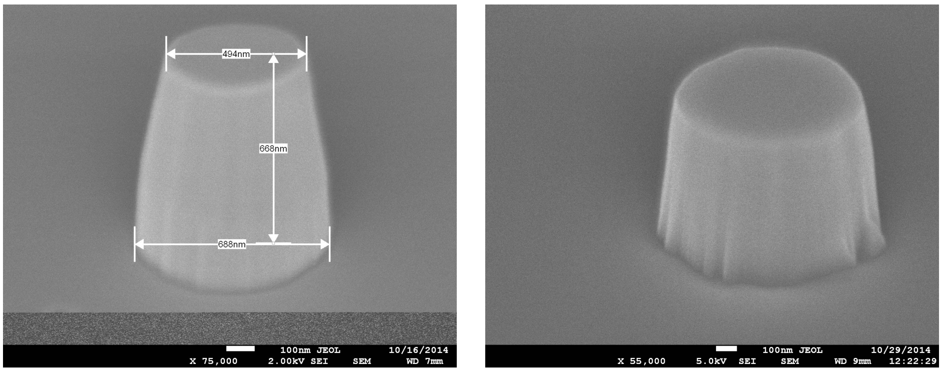

(a) (b)

Figure 2.16: (a) SiC pillars made with an etched Cr hardmask patterned with HSQ ; (b) SiC pillars made with a Cr hardmask deposited by lift-off. In the left figure is possible to see a change in the sidewall slope due to the shrinking of the etched hardmask.

pressure would have led to higher etching rates, undesirable to control the etch depth.

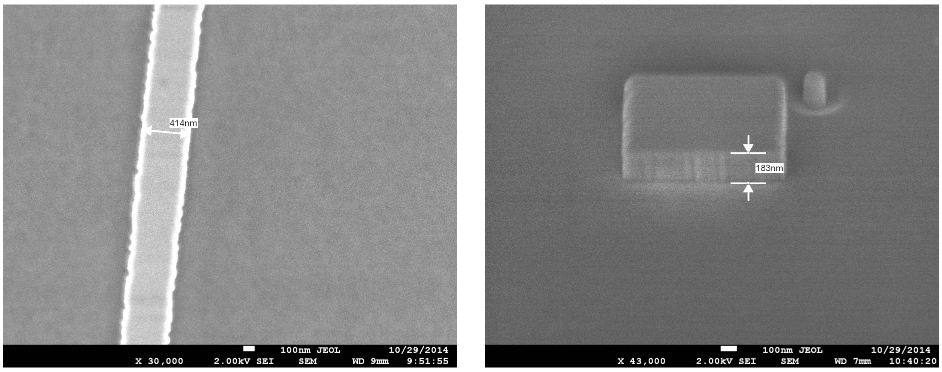

(a) (b)

Figure 2.17: (a) top view of the realized waveguide with Cr hardmask ; (b) 60° view of the etched sidewall in SiC.

2.5.3 Silica hardmask

In order to reduce the roughness with the respect to the one provided from a Cr layer, we decided to try SiO_2 as hardmask that is amorphous, widely used in photonic processing and could be thermally grown directly from the SiC layer. SiO_2 was etched by RIE Plasmalab 80 Plus made by Oxfor Instrument with a forward power of 200 W, a pressure of 30mT, 38 sccm of Ar and 12 sccm of CHF_3. This choice imposed the use of another electron beam resist since HSQ has selectivity below unity for the SiO_2 etch and the maximum thickness is not enough to endure the SiC etch. We decided to use 270nm CSAR 62 positive electron beam resist that offers the same advantage of the well known ZEP but at a cheaper price. The selectivity between CSAR 62 and SiO_2 was measured between 0.8 to 1 (for the PECVD and for the thermal SiO_2, respectively).

The SiC etch was changed in 100W forward power, 1000W ICP power, 3mT of pressure, 20sccm of $SiCl_4$ and 5sccm of O_2. Although the sidewall verticality is 80°, this etch has the advantage of a slower etching rate (100nm/min) and the use of a chlorine based chemistry increases the selectivity with the SiO_2 mask (etching rate 48nm/min). Furthermore, the higher pressure is more controllable by the gauge and improves the stability of the plasma. These characteristics increase the repeatability of the process and make this etch more suitable for the waveguides fabrication.

In Fig.2.18.(a) is showed the top view of a waveguide made with a hardmask of 200nm of SiO_2 deposited by Oxford Instrument PECVD 100 Plasma Pro (pressure 1000mT, SiH_4 10sccm, N_2 80sccm, 20W forward power, NH_3 1000sccm and 350°C plate temperature). As shown in Fig.2.18.(b), the sidewall roughness is affected by the quality of the SiO_2 hardmask that looks inhomogeneous and composed by "grains" instead of being an amorphous continuous layer. Furthermore, the insulating properties of the SiO_2 hardmask produced a trenching effect in the SiC layer (Fig.2.19), imposing the fabrication of a thicker SiC membrane (100nm instead of 50nm).

The poor SiO_2 layer quality results in rough SiC sidewalls and additional steps, aimed to improve both the hardmask quality and its sidewall roughness, are needed and in the next paragraphs some tests are reported:

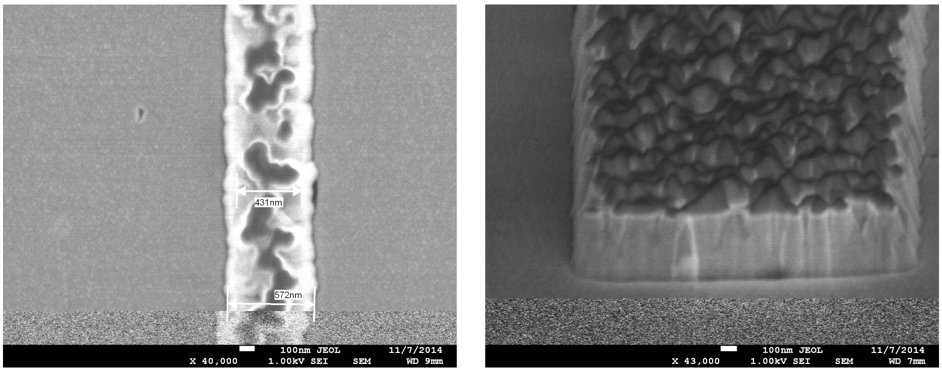

(a)

(b)

Figure 2.18: (a) top view of the realized waveguide with PECVD SiO_2; (b) 60° view of the etched sidewall of the mark. Both the images were taken with the SiO_2 layer still on top

Wet etch Since a rough surface is chemically more active than a smooth one, an isotropic process can decrease the roughness of the SiO_2 sidewall. A partial improvement was indeed seen using a buffered hydroflouric acid (BHF) carried out after the dry etch. In Fig.2.20.(a) is shown the cleaved SiO_2 hardmask before the effect of 5s in HF 48%, whose effects are reported in Fig.2.20.(b) .

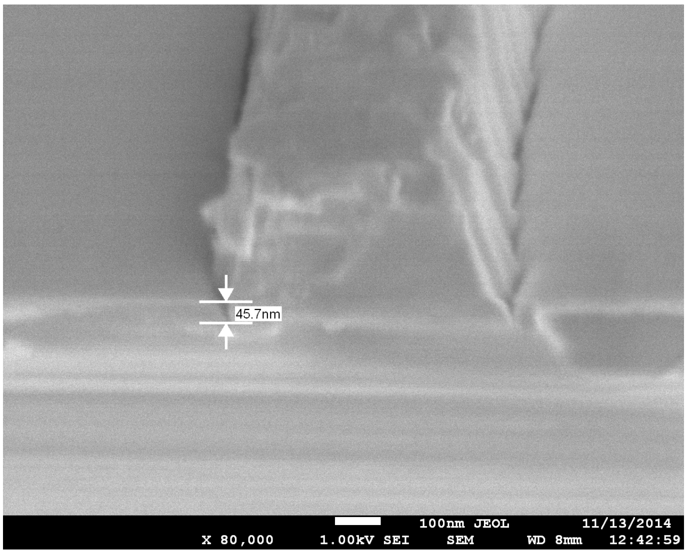

Figure 2.19: 60° view of the cleaved waveguide showing the trenching effect

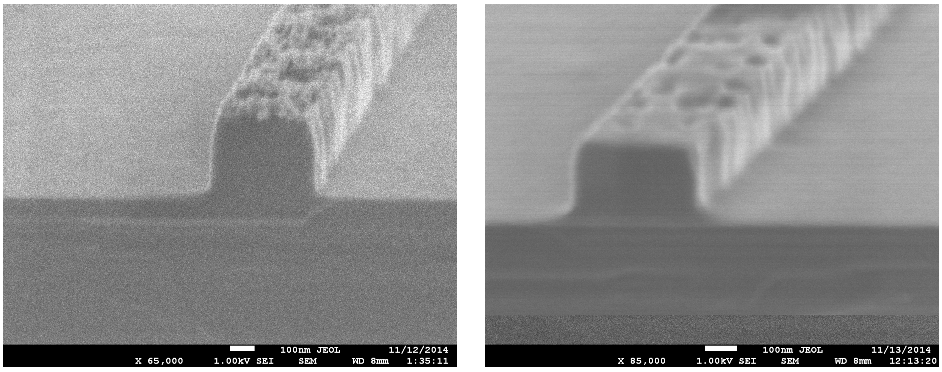

(a)

(b)

Figure 2.20: 60° of cleaved SiO_2 hardmask (a) before the HF etch and (b) after the HF etch

Annealing and sputtering deposition In order to improve the quality of the SiO_2 film, we tried a step of annealing at 850°C for 10 minutes (Fig.2.21.(a)) after the deposition by PECVD. The resulted SiC waveguide has roughness smaller than the one of waveguide without the annealing step reported in Fig. 2.19. A similar result in term of roughness can be achieved by the use of sputtered SiO_2 as hardmask (Fig.2.21.(b)).

ICP RIE etch In Fig.2.22 is reported an etched hole for the access of the XF_2 to the Si substrate in order to make the undercut (see Fig.2.23.(b)). In figure is possible to compare the straight etched line made in SiC (derived from the use of a positive resist and after the etching by RIE of the SiO_2 hardamask), with the curved line made using a SiO_2 layer etched by ICP RIE OIPT SYS380 (100W forward power, 1500W ICP, 10mT of pressure, C_4F_8 40 sccm, O_2 15 sccm and 15°C of temperature). Even if the layer of

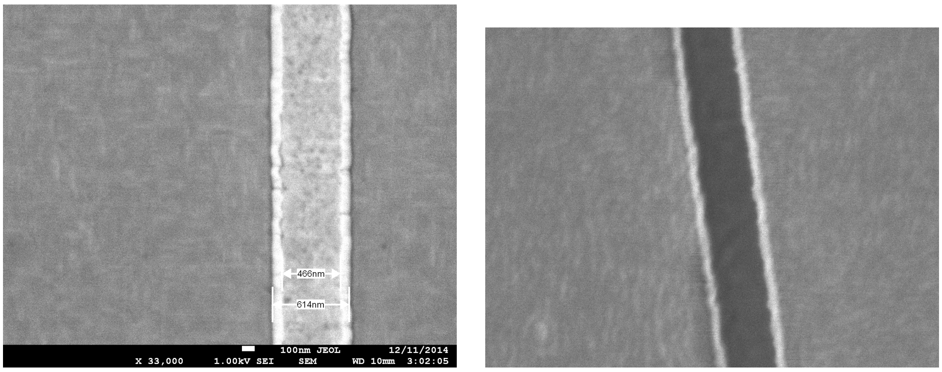

(a) (b)

Figure 2.21: Top view of SiC etched waveguide using (a) annealed SiO_2 (b) sputtered SiO_2. Both the images are taken after the hardmask removal.

SiO_2 used to make the holes was not annealed, the roughness is decreased due to the different etches. The waveguide resulted from the use of the ICP RIE etching of the SiO_2 hardmask is showed in Fig.2.23.(a).

First waveguide completion After the waveguide fabrication, a second step of electron beam lithography was carried out in order to make the holes in the membrane along the waveguide, creating the access points for the XeF_2 gas to etch the Si substrate underneath and creating the suspended waveguide (Fig.2.23.(b)). This step was accomplished using 200nm of SiO_2 hardmask under 220nm of positive electron beam resist CSAR 62, to remove 100nm of SiC from the membrane. Before the XeF_2 etching step, the chip was lapped (to remove the imperfection on the edge due to the inhomogeneous spinning of the resist at the sample edges) and chemical mechanical polished. These two steps were made in order to have a better optical coupling between the waveguide end-face and the lensed fiber. As it is reported in Chap.3, the preferred method to couple light with an optical fiber is going to be grating couplers. In this case, the depth of the SiC etching during the second step is optimal for maximizing the coupling efficiency and always enough to etch through the SiC membrane to reach the Si substrate in the holes positions. However, in the rest of this paragraph, the steps required to complete the waveguide with side couplers are described.

In order to prevent the gas to access from the sides of the chip creating a fragile suspended membrane along the sample edges, the chip was oxidised at 850°C for 10min to create 10nm of thermal SiO_2 on the substrate sidewall and dry etched in RIE, allowing the gas to access only from the holes. In Fig.2.24.(a) is showed the etch of the Si substrate trough the holes after seven steps of 30s at 1T of XeF_2. The inhomogeneous etch of the Si (Fig.2.23.(b)) produces a strong light scattering, allowing the waveguide to be seen even with a stereoscopic microscope mounted on top of the waveguide measuring setup.

After 20μm are removed from the Si substrate by the XeF_2, the waveguide is completed as is shown in Fig.2.25 (a) and (b), where the polished end face is shown. In the second figure is still possible to see the partial film of SiO_2 under the waveguide. To reduce the losses due to the scattering [142], we also carried out a wet oxidation step[184] at 1000°C for three hours and we removed the generated oxide. This step has grown 30nm of SiO_2 corresponding to 15nm of SiC. The effects of the wet oxidation on the waveguide of Fig.2.25 is depicted in Fig.2.26, where is possible to see the presence of defect lines on the surface (the wet SiC oxidization happens preferentially in the defects sites). The defects number increases exponentially as the thickness of the SiC film decreases [158], as it is illustrated in Fig.2.26.(a) where the presence of defects on

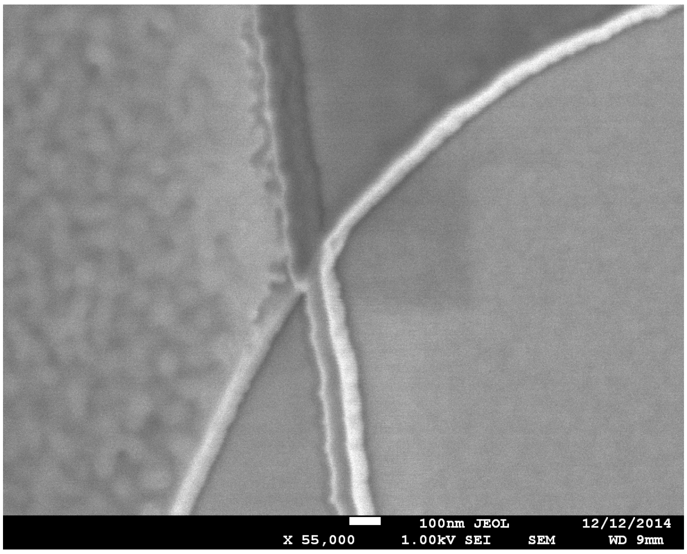

Figure 2.22: Top view of a hole made in SiC for the access of XeF_2 to the Si substrate by ICP RIE etched SiO_2, with an etched SiC straight line made by RIE etched SiO_2

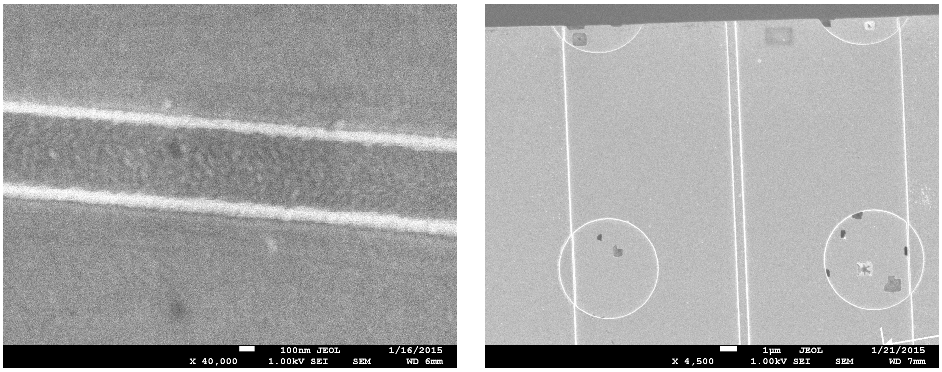

(a) (b)

Figure 2.23: (a) Top view of SiC waveguide made by ICP RIE etch of SiO_2 hardmask; (b) Top view of a hole in the membrane along the waveguide for the access of XeF_2 made in SiC

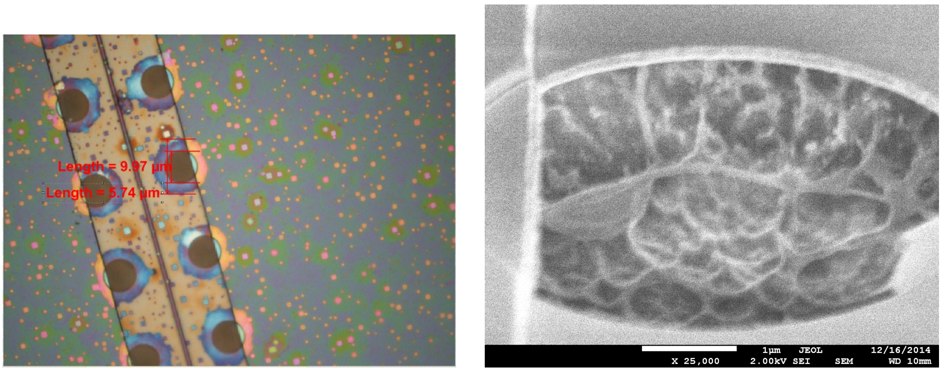

(a)

(b)

Figure 2.24: (a) Optical-microscope image of an etching of the Si substrate by the XeF_2; (b) 60° SEM image of the etching of the XeF_2

the waveguide (400nm thick) is less than on the membrane (100nm thick). The stress of the oxidation and the subsequent SiO_2 removal by wet etch, caused the breakage of the membrane (Fig.2.26.(b)). These results suggest to carry out a dry oxidation step, followed by a vapour HF removal of the SiO_2.

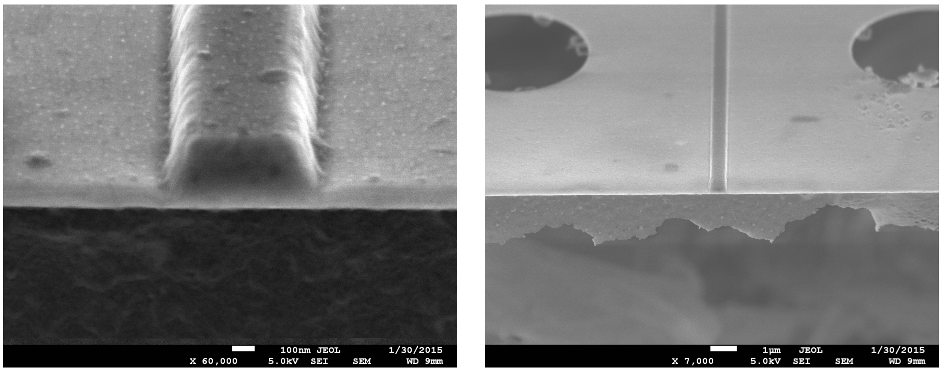

(a)

(b)

Figure 2.25: (a) Polished face of the waveguide after all process steps; (b) SiO_2 membrane under the waveguide

Thermal SiO_2 as hardmask Up to now, the poor quality of the deposited SiO_2 was one of the main reasons to cause the high roughness of SiC structures. The best SiO_2 quality from both homogeneity and stoichiometry point of view can be achieved by oxidizing directly the SiC layer. The dry oxidation of the SiC requires temperatures above 1000°C [185] and the use of the furnaces room in the *Integrated Photonic Cleanroom* allowed us to characterize the thermal growth of SiO_2, using a tube furnace at 1100°C. The comparison of the quality of the SiO_2 films on SiC is reported in Fig.2.27, where in figure (a) was used 200nm of standard PECVD SiO_2 and in (b) 190nm of thermally

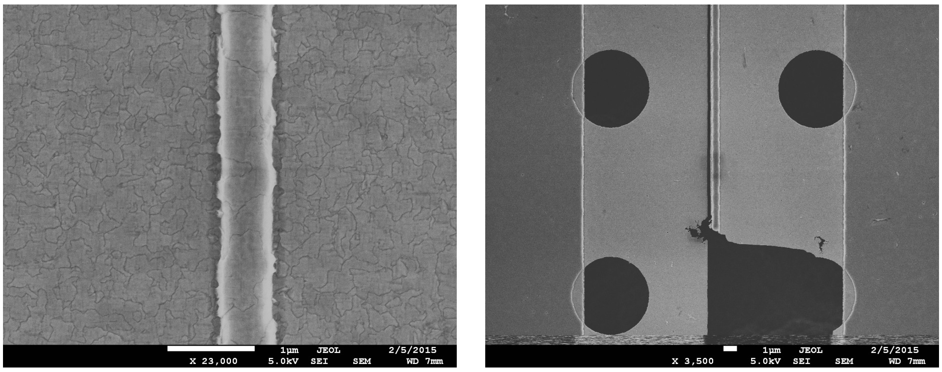

(a) (b)

Figure 2.26: Effects of the wet oxidation on SiC; (a) revealing the presence of imperfections at the low thickness; (b) breakage of the membrane due to the stress of this step

grown SiO_2 at 1100°C for 8 hours and 35min, to fabricate a photonic crystal cavity. The improvement given by the thermal SiO_2 is promising for the fabrication of low loss SiC waveguide, although the quality of the sidewall results rough after the SiC etching (Fig.2.28.(a)). This problem could derive from the high power of the SiC etch.

2.5.4 Aluminium hardmask

So far, the best result from the roughness point of view is given by the use of an Aluminium (Al) hardmask. Unlike Cr, the ICP-RIE etch of Al (150W RF, 800W ICP, 5mt pressure, 40sccm HBr, 10sccm Cl_2 and 50°C of temperature) results in smooth sidewall as reported in Fig.2.28.(b), where it is possible to see under the SiC the Si substrate. This hardmask shows a selectivity greater than 8 using the anisotropic etch of SiC developed with the Plankett Burman DOE. As depicted in the figure, the downside of this technology is the presence of residues on the bottom of the etched surface that are difficult to remove and a low verticality due to the shrinking of the Al mask during the SiC etch.

The shrinking problem deriving from the use of the powerful anisotropic etch and the Al hardmask (Fig.2.28.b) can be solved by the use of a lower RF power during the SiC etch (130 W). By carefully tailoring the time of etching and by keeping the CSAR 62 after the Al etch, anisotropic sidewall can be reached in close structures like photonic crystal (Fig.2.30(a)). The same etch performed in open structures, like waveguides, resulted in a sidewall angle of $\sim 80°$, as reported in Fig.2.30(b). The presence of residues (Fig.2.28.b) were attributed to the oxidization of the Al and to the inhomogeneous etch in air due to the presence of Cl_2 on the resist sidewall after the Al etch. In order to prevent oxidization, 5nm of Titanium (Ti) were deposited right after the Al deposition by electron beam evaporation. The residues Cl_2 molecules were nullified using a short C_4F_8 RIE plasma right after the Al etch. The high RF power could have taken part in

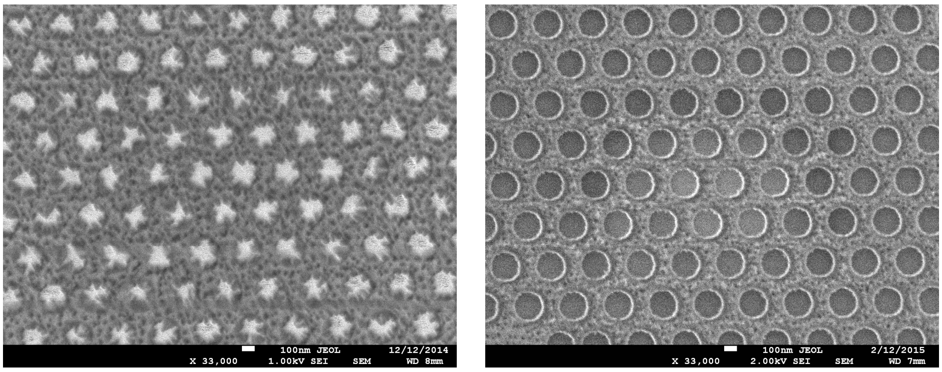

(a) (b)

Figure 2.27: RIE etch of photonic crystal in (a) PECVD SiO_2 and (b) thermal SiO_2. Both the films were grown on SiC and patterned with 220nm of CSAR62

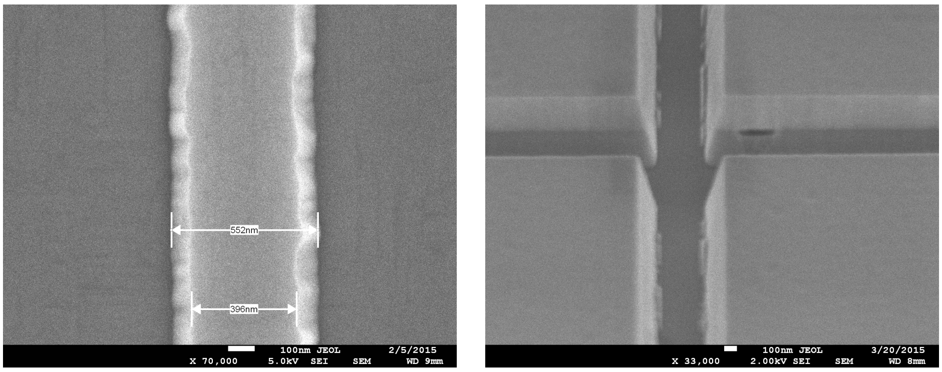

(a) (b)

Figure 2.28: (a) SiC waveguide using 200nm of thermal SiO_2 (b) 45° view of SiC etch using 100nm of Al hardmask.

the formation of residues as depicted in Fig.2.29. The SF_6 molecules impacting the mask with high energy, due to the high forward power and low pressure (that increases the line of sight of the molecules before hitting each other), caused a sputtering process of Al that was partially rideposited on the SiC sidewall. The reduction of RF power together with the removal of the Ar chemistry, contributed to the elimination of the residues that were present at the end of the process. An extensive wet etch in HF ensured that all the remaining residues were dissolved.

2.6 Conclusions

Due to the high selectivity and reasonably smooth sidewall, the use of Al hardmask with the reduced forward power during the ICP etch allowed the realization of anisotropic holes for photonic crystals and relatively low roughness for waveguides. Furthermore,

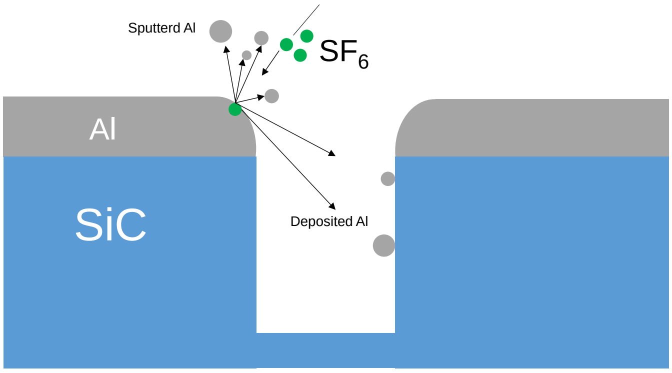

Figure 2.29: Process of Al sputtering and redeposition on the SiC sidewall due to the high power of the SiC etch

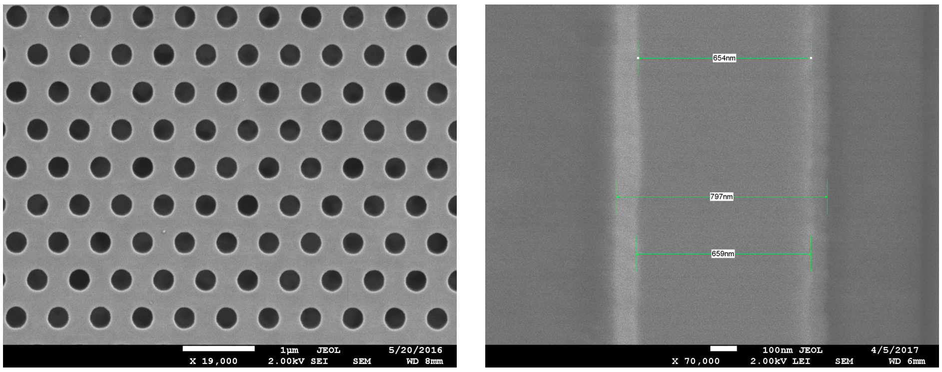

(a)

(b)

Figure 2.30: (a) Photonic crystal fabricated using 130 W forward power, 900 W ICP, 1 mT chamber pressure and SF$_6$ gas. 100nm of Al was used as hardmask and 5nm Ti were deposited on top to prevent the oxidation of the Al hardmask. (b) Same process for the SiC waveguides fabrication

the drop in verticality for the waveguide does not affect the guiding properties. This etch conditions were used for the realization of photonic crystal cavities and waveguides, meanwhile the powerful etch deriving from the Plackett-Burman DOE was used together with Ni hardmask for the realization of the SPhPRs samples. In the latter, Ni offered high selectivity for the extensive SiC etch and the powerful etch granted high verticality even in open-space structures(Fig.2.14).

Chapter 3

SiC Linear Photonics

In this chapter, it is reported the work made to design and characterize linear components fabricated in 3C SiC. In the first section, some general notions are introduced including a preface of light confinement in dielectric media, derived from a ray optics treatment together with the concept of total internal reflection. We report the mode solution of the multi-mode (MM) and single-mode (SM) waveguide structures realized in 3C SiC using the fabrication described in Chap.2. Since ring resonators play a central role in this thesis (Chaps.4 and 5), in Sec.3.2 the ring behaviour is analysed in function of its physical parameters. Furthermore, the method used to retrieve the propagation losses from the measured quality factor is described. The components for coupling to SiC waveguides are evaluated in Sec.3.3, where we show the disadvantages of an edge-coupling system based on waveguide tapering over the grating coupler approach. The suspended grating couplers, ring resonators and waveguides are characterized in the last section of this chapter. Part of the results reported here have been published in Ref.[11].

3.1 Light confinement in dielectric media

Light propagating in a homogeneous medium is subjected to diffraction, where the initial field cross-section will spread as it propagates in the material. However, optical fields can be confined and routed thanks to the employment of a higher refractive index dielectric (*core*) with the respect to the surrounding medium (*cladding*). In this case, the beam inside the core can be trapped due to total internal reflection (TIR), that is a direct consequence of the Snell's law and reflection law

$$n_1 \sin(\theta_1) = n_2 \sin(\theta_2) \tag{3.1}$$

$$\theta_1 = \Psi_r \tag{3.2}$$

where the first relates the trajectories (described from the angles) of a refracted beam to the incidence angle θ_1 of a beam travelling through the interface of two media of different refractive indexes (Fig.3.1). At the interface, the beam will be also reflected back with the same incidence angle (Eq.3.2).

Considering a wave propagating from a higher refractive index region to a lower refractive index one, there is an incident angle

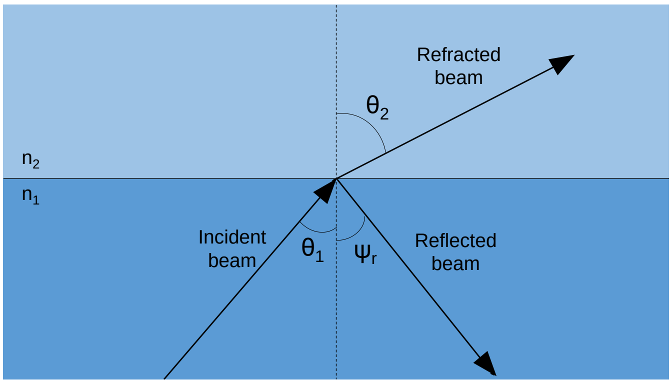

Figure 3.1: The incident beam crossing the interface of two media with different refractive indexes with an angle θ_1 is refracted with an angle θ_2 (Snell's law) and reflected with $\Psi_r = \theta_1$

$$\theta_c = \sin^{-1}\left(\frac{n_2}{n_1}\right) \tag{3.3}$$

in which $\sin(\theta_2) = 1$ and no light will be refracted in the lower index material. For all the angles greater than θ_c, the power of an incident beam will be totally reflected.

For the structure of Fig.3.2.(a), where n_1 is greater than n_2, the light injected in the core region with an angle greater than θ_c is subjected to the TIR at both interfaces. However, not all waves subjected to TIR can constitute a mode of the structure. The mode of the structure must have a well defined field amplitude at each point in space and in time and a unique propagation constant β [6]. The wave propagating in the structure of Fig.3.2.(a) can be written as

$$E(x, y, z) = E_0(x) \exp[i(\omega\, t - \beta\, z - h\, x)] \tag{3.4}$$

where $E_0(x)$ is the field profile along the structure, ω is the angular frequency, β is the propagation constant of the guided mode and h is the transverse propagation constant. In the distance Δx, the phase accumulated from the field will be

$$\phi_{tot} = \omega\, \Delta t - \beta\, \Delta z - 2h\, d + 2\phi_r \tag{3.5}$$

where d is the waveguide thickness. The phase shift ϕ_r derives from the Fresnel equation for the reflected and transmitted amplitudes at the interface between two transparent media. In the s polarization, the amplitude of a beam encountering an interface between two medium is changed following

$$r_s = \frac{n_1 \cos\theta_1 - n_2 \cos\theta_2}{n_1 \cos\theta_1 + n_2 \cos\theta_2} \tag{3.6}$$

where, in TIR, θ_2 becomes complex. In order for β to be the propagation constant of a mode of the structure, the extra transverse phase shift must be equal to a multiple of 2π

$$-2h\,d + 2\phi_r = 2m\pi \tag{3.7}$$

where m denotes the TE_m and TM_m modes of the structure. Following the development reported in reference[6], ϕ_r can be linked directly to

$$h = \sqrt{(n_1\,k_0)^2 - \beta^2} \tag{3.8}$$

$$q = \sqrt{\beta^2 - (n_2\,k_0)^2} \tag{3.9}$$

where q describes the exponential decay of the mode in the cladding while h the sinusoidal behaviour of the amplitude in the core

$$E_m = \begin{cases} A\text{sin}(h\,x) + B\text{cos}(h\,x) & \text{if } |x| < d/2 \\ C\text{exp}(-q\,x) & \text{if } x > d/2 \\ D\text{exp}(q\,x) & \text{if } x < d/2 \end{cases} \tag{3.10}$$

with A, B, C and D constants to be derived from the boundary conditions. Thanks to Eq.3.7, h and q can be calculated considering

$$\phi = \begin{cases} 2\text{tan}^{-1}\left(\frac{q}{h}\right) & \text{for TE modes} \\ 2\text{tan}^{-1}\left(\frac{n_1^2 q}{n_2^2 h}\right) & \text{for TM modes} \end{cases} \tag{3.11}$$

The fundamental mode corresponds to $m = 0$ and it is always present for the TE case. For bigger refractive index n_1 or thicker core, the structure supports higher order modes, each corresponding to a different input angle (Fig.3.2.b). The mode angles are always in TIR and greater value of m corresponds to angles approaching the critical angle. The propagation constant β is instead bigger for the fundamental mode and smaller for the highest order mode, since the effective refractive index

$$n_{eff} = \frac{\beta_m}{k_0} \tag{3.12}$$

approaches to the clading value n_2. For a confined mode n_{eff} is always between n_1 and n_2.

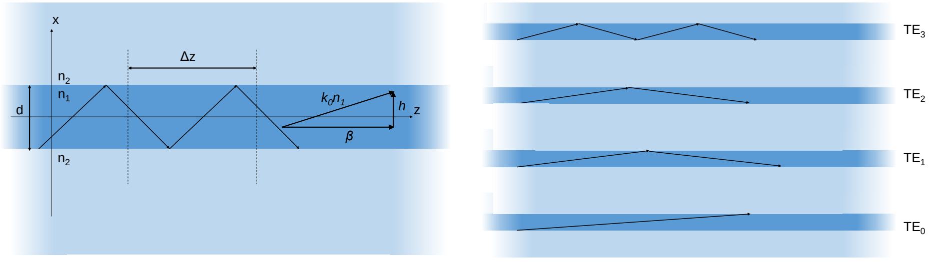

(a) (b)

Figure 3.2: (a) Light trapped by total internal reflection in the core of a waveguide. b) Different modes propagating at different incident angles

3.1.1 Mode Solver

The ray treatment can be used only for slab waveguides and step-index fiber to determine the propagation constant. However, this method does not provide any insight of the field distribution inside the structure. The field described in Eq.3.10 can be used as solution of the Maxwell's equation for the regions composing the structure of an infinite slab waveguide (Fig.3.2)

$$\nabla \cdot \mathbf{D} = \rho \tag{3.13}$$

$$\nabla \times \mathbf{E} = \frac{\partial \mathbf{B}}{\partial t} \tag{3.14}$$

$$\nabla \cdot \mathbf{B} = 0 \tag{3.15}$$

$$\nabla \times \mathbf{H} = \mathbf{J} + \frac{\partial \mathbf{D}}{\partial t} \tag{3.16}$$

together with the constitutive equations

$$\mathbf{B} = \mu_0 \mathbf{H} + \mathbf{M} \tag{3.17}$$

$$\mathbf{D} = \epsilon_0 \mathbf{E} + \mathbf{P} \tag{3.18}$$

where **B** is the magnetic flux density, **H** is the magnetic field, **D** is the displacement vector and **E** is the electric field. For nonmagnetic materials, the magnetization field **M** is zero and, for the purpose of this thesis, both the current density **J** and the charge density ρ will be zero. In Eq.eqs. (3.17) and (3.18), μ_0 is the vacuum permeability and ϵ_0 is the vacuum permittivity.

The electric polarization **P** describes the induced electric dipoles moment of a material subjected to an electric field. In this chapter, we will consider only the case of linear dependence of the polarization vector with the respect to the electric field

$$\mathbf{P} = \epsilon_0 \chi^{(1)} \mathbf{E} \tag{3.19}$$

where $\chi^{(1)}$ is the linear susceptibility and it is linked to the refractive index of the medium

$$n = \sqrt{(1+\chi^{(1)})\mu_r} \tag{3.20}$$

with μ_r the relative permeability and for the considered materials is equal to 1.
For high-confinement two-dimensional channel waveguides (or in general more complex structures) there is no analytical solution to eqs. (3.13) to (3.16) describing the field distribution in the guiding region. Only approximated analytical approach, like the *effective index theory*, can be used when the difference of refractive index between core and cladding is small. For the general case, numerical solvers are needed.
In order to calculate the mode of SiC waveguides, we employed the software *Lumerical Mode Solution* which uses the *finite difference method* (FDM) as numerical solver. Provided a uniform rectangular grid (Yee's mesh [186]) that subdivides the structure in cells (Fig.3.3), the FDM discretizes the partial differential eqs. (3.13) to (3.18) for each grid point where the spatial increments are given by mesh resolution. The discretized equations can be gathered in a matrix form[187] whose eigenvalues correspond to the propagation constants and the solutions of the problem. In this way, the solver provides the field distribution and the propagation constant. The FDM accuracy relies on the refinement of the mesh.

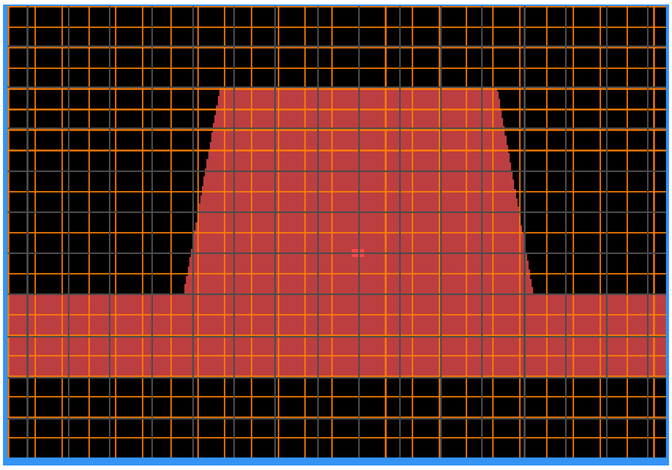

Figure 3.3: Coarse Yee's mesh of the suspended SiC waveguide

3.1.2 SiC mode solutions and waveguide engineering

The high refractive index of SiC is fully exploited by our technology using air as cladding and sub-μm cross-section of the waveguides. A mode analysis of the structures is performed for the fundamental TE mode, reported in Fig. 3.4, showing effective index n_{eff} of 1.88 (SM) and 2.25 (MM) for 480x400 nm and 670x700 nm sizes, respectively. The modes were calculated using the refractive index dispersion reported in Fig. 2.4 and the high n_{eff} values of both structures are evidence of a thigh light confinement, essential for integrating photonics components in a small area and achieving the minimum modal volume in resonators.

The possibility of engineering the waveguide dimensions for the MM waveguides can improve the propagation losses by diminishing the roughness scattering thanks to a major confinement of the mode inside the core material and a consequent reduction of the field at the SiC-air boundaries. This is shown in Fig.3.5, where is reported the distributions of the electric field norm $E_n(x)$ taken at half of the waveguide total thickness for the first TE mode, where the black line show the case of a 400nm-thick waveguide meanwhile the red line reports the 700nm-thick case. The dashed lines represent the position of SiC-air boundaries, where the roughness deriving from the fabrication could cause scattering losses (see Sec.3.1.3). As expected, by increasing the waveguide dimensions (both thickness and width), the electric field at the SiC-air boundary is reduced with the respect of the smaller waveguide. The field at the boundary can be plotted as function of the waveguide width (Fig.3.6) for different thickness. For 700nm and 900nm thickness (black and blue line, respectively), the electric fields have similar values for almost all the waveguide widths, meaning that the waveguide thickness does not contribute to the lateral field distribution for values larger than 700nm. This is not true for the 400nm case (red line), where the electric field at the boundary is always greater than the thicker cases. For large widths, the electric field diminishes as the waveguide width increases for all the thickness reported in Fig.3.6.

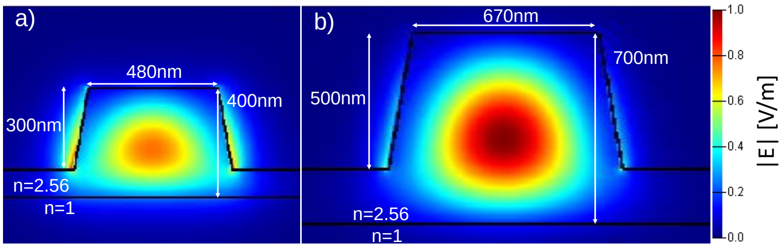

Figure 3.4: Normalized electric field intensity for the first TE mode in SM (a) and MM (b) waveguides.

The reduction of the field at the waveguide boundaries that can be achieved by increasing the waveguide dimensions comes at the cost of higher order modes, like reported in Fig. 3.7 where the effective index of modes are plotted for 700nm-thick (Fig. 3.7.a) and 900nm-thick (Fig. 3.7.b) waveguides as function of the width. The n_{eff} difference between the fundamental and higher order modes of the MM waveguide (Fig.3.4.b) is wide enough such that cross-mode field leakage is avoided, especially in small-radii bending of waveguides.

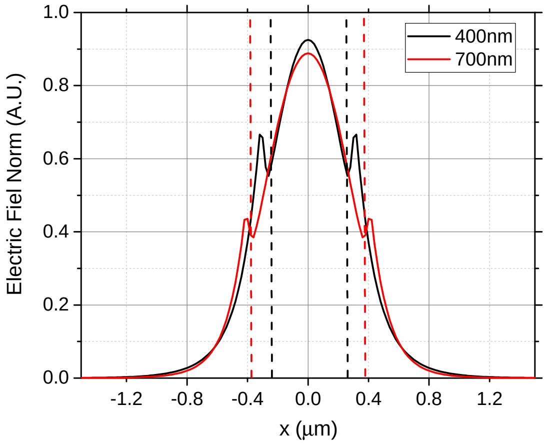

Figure 3.5: First TE-mode distribution of the electric field norm $E_n(x)$ simulated at half of the waveguide total thickness. Red line shows $E_n(x)$ for 700nm thickness meanwhile the black line reports the 400nm case. Dashed lines represent the SiC-air boundaries of the waveguides in the 700nm (red) and 400nm (black) thickness case.

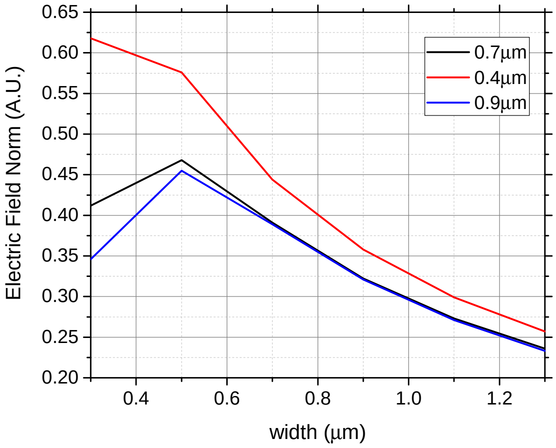

Figure 3.6: Electric field norm for the first TE mode at the SiC-air boundaries at half thickness in function of the waveguide width. The thicknesses considered in the simulation are 400nm (red line), 700nm (black line) and 900nm (blue line)

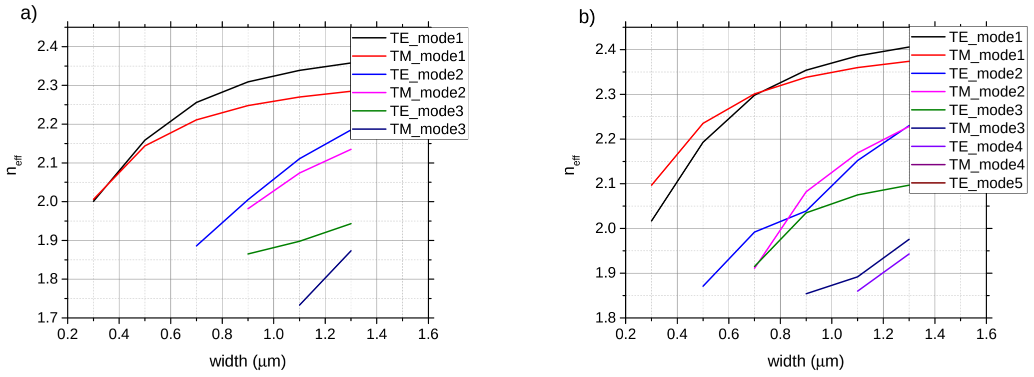

(a) (b)

Figure 3.7: Effective index of modes as function of the waveguide width for a) 700nm and b) 900nm thick waveguides.

3.1.3 Losses in waveguides

When light propagates in a waveguide for a distance Δz, the electric field amplitude is attenuated by a factor

$$a = e^{-\frac{\alpha}{2}\Delta z} \tag{3.21}$$

where α is the power loss coefficient and it is mesured in $[1/cm]$. The absortion coefficient can be decomposed in three different factors

$$\alpha = \alpha_b + \alpha_s + \alpha_m \tag{3.22}$$

where α_b describes the losses deriving from the waveguide bending, α_s accounts for the scattering of the field due to the roughness and α_m is the bulk material loss.

The presence of dislocations, impurities and crystal boundaries can cause absorption in the bulk material. The light emitted outside the waveguide from this inhomogeneity results in an imaginary component of the refractive index and consequently in the exponential decay described by Eq.3.21.

The fabrication of sub-μm waveguides requires the pattering of a mask. Although the high resolution of the lithography tools, patterned resists and subsequent etching provide a non-negligible sidewall roughness ζ at the interface between cladding and core. The top and the bottom interfaces, instead, usually do not contribute significantly to scattering losses since the chemical mechanical polishing provides a roughness level on the order of angstroms. The scattering losses can be described using[188, 189]

$$\alpha_s = \frac{\zeta^2 k_0^2 h}{\beta} \cdot \frac{E_s^2}{\int E^2 dxy} \cdot \Delta n^2 \tag{3.23}$$

where Δn is the refractive index difference between core and cladding meanwhile E_s represents the electric field of the mode at the core/cladding interface. The integral $\int E^2 dxy$, where $E(x,y)$ is the mode electric field, is extended over all the waveguide cross-section such that the term $E_s^2 / \int E^2 dxy$ is the normalized electric field intensity at the core/cladding interface. In order to minimize α_s, fabrication techniques have been developed to reduce ζ[190, 191, 192]. In order to decrease the field portion at the interface and increase the propagation constant, multimode waveguides can be used to reduce α_s[193].

When a mode propagates in a bent waveguide (Fig.3.8.a) it is subjected to two kind of losses. The first is the mode mismatch at the interface between the straight and bent waveguide while the second is given by a field leakage in radiative modes during the propagation in the bent waveguide. In fact, the equivalent refractive index of the structure depends on the radius of curvature R[6]:

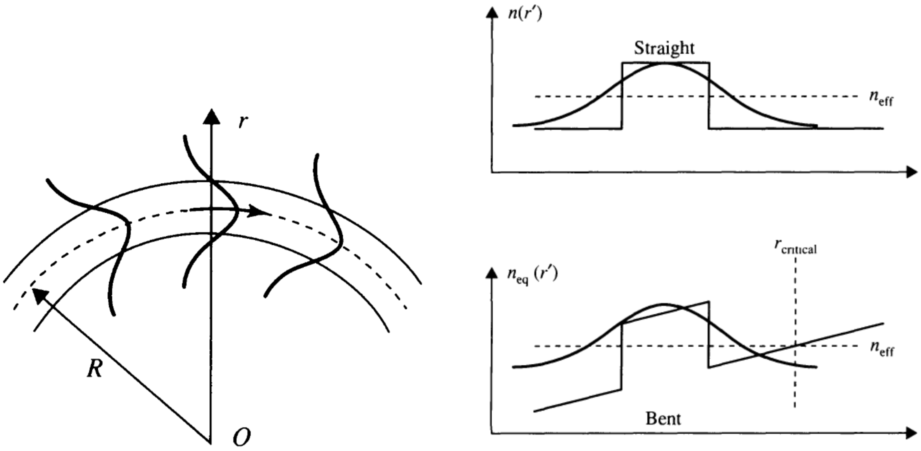

(a) (b)

Figure 3.8: (a) bending of a waveguide; (b) change of the equivalent refractive index during the bending[6]

$$n_{eq}(r') = n(r')\left(1 + \frac{r'}{R}\cos(\phi')\right) \tag{3.24}$$

where r' is the radial distance with the respect to the waveguide center and ϕ' is the azimuthal angle from the plane perpendicular to the propagation. The radial dipendence of the refractive index can be physically explained assuming that the mode inside the waveguide keeps the same field profile as it propagates. To do so, the outer field portion must propagates with a smaller propagation constant (and higher phase velocity) with the respect to the inner portion of the field, that travels for a smaller distance. As depicted in Fig.3.8.(b), at a critical radius, the propagation constant is below the one correspondent to the cladding refractive index and the field starts to leak[194, 188] following

$$\alpha_b = K \exp(-B\,r) \qquad \text{where} \tag{3.25}$$

$$B = \beta(2\,\Delta n_{eff}/n_{eff})^{3/2} \tag{3.26}$$

where K depends on the waveguide thickness and refractive indexes of the core and cladding), Δn_{eff} is the difference between n_{eff} and the cladding refractive index. Therefore, the higher Δn_{eff} the higher is the possibility to reduce the size of photonic components without deteriorating the bending losses.

3.2 Ring Resonators

Ring resonators are a key component for a vast range of applications[136, 137, 195] since the provide size reduction of photonic devices and a boost in nonlinear optical effects due to the field enhancement experienced inside the cavity. As we will see later in this dissertation, ring resonators were used to retrieve the propagation losses of SiC waveguides, for frequency conversion in SiC (Chap.4) and for the generation of nonclassical state of light in Si_3N_4 (Chap.5).

Rings are made by bending the waveguide back to itself and forming a close path, like showed in Fig.3.9. The advantage of such a cavity is the ability to control the field coupling between the ring and the bus waveguide by just changing the gap during the lithography step. Referring to Fig.3.9, we can analyze this component using the matrix formalism[196, 197] describing the coupler

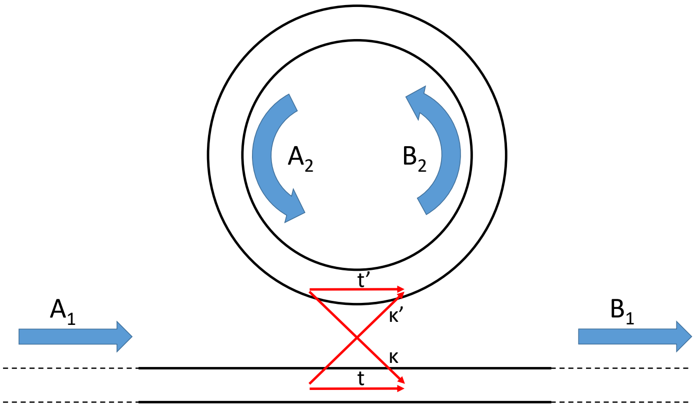

Figure 3.9: Scheme of a ring resonator of radius R coupled to a straight waveguide.

$$\begin{vmatrix} B_1 \\ B_2 \end{vmatrix} = \begin{vmatrix} t & \kappa \\ \kappa' & -t' \end{vmatrix} \begin{vmatrix} A_1 \\ A_2 \end{vmatrix} \tag{3.27}$$

where A_1 and B_1 are the beam amplitudes of the field at the input and output of the resonator, respectively, while B_2 is the field coupled to the ring thanks to the cross coupling coefficient κ and with t is indicated the straight-through field transmission. The matrix in Eq.3.27 is unitary

$$|t|^2 + |\kappa|^2 = 1 \tag{3.28}$$

and, by propagating in the ring resonator of radius R, the coupled field B_2 acquires a phase θ so that

$$A_2 = B_2\, a \exp(i\theta) \tag{3.29}$$

with

$$\theta = \beta\, L = n_{eff} \frac{2\pi}{\lambda} 2\pi\, R \tag{3.30}$$

where the dependence of n_{eff} to the wavelength has been omitted for simplicity in the notation and the attenuation a is defined as in Eq.3.21, with $\Delta z = L$ the circumference of the ring. Using Eq.3.27 and 3.29 we can derive

$$\frac{B_1}{A_1} = \frac{-a + t\exp(-i\theta)}{-a\, t' + exp(-i\theta)} \tag{3.31}$$

$$\frac{A_2}{A_1} = \frac{-a\, \kappa'}{-a\, t' + exp(-i\theta)} \tag{3.32}$$

with the normalized power straight-through transmission

$$\left|\frac{B_1}{A_1}\right|^2 = \frac{a^2 + t^2\ - 2atcos\theta}{1 + a^2t^2\ - 2a\, tcos\theta} \tag{3.33}$$

and circulating power coefficient

$$\left|\frac{A_2}{A_1}\right|^2 = \frac{a(1-t^2)}{1 + a^2t^2\ - 2a\, tcos\theta)} \tag{3.34}$$

At some wavelengths there is no phase difference between A_2 and B_2 and the input field is on resonance with the ring resonator. Considering Eq.3.30, this is equivalent to the case of $\theta = 2m\pi$, with m integer. The resonances λ_0 correspond to difference values of m

$$\lambda_0 = n_{eff}(\lambda_0)\frac{L}{m} \tag{3.35}$$

and the distance between two following resonances corresponding to m and $m+1$ is defined the *free spectral range* (FSR)

$$FSR = \lambda_{m+1} - \lambda_m \simeq \frac{\lambda_m^2}{n_g(\lambda_m)L} \tag{3.36}$$

where we used the definition of *group index* n_g

$$n_g(\lambda) = n_{eff}(\lambda) - \lambda \frac{\partial n_{eff}(\lambda)}{\partial \lambda} \tag{3.37}$$

that takes in account the small change of n_{eff} between two consecutive resonances. Using Eq.3.33, it is possible to retrieve another important spectral characteristic of the ring resonator named the *full width half maximum* ($\Delta\lambda$)

$$\Delta\lambda = \frac{(1 - ta)\lambda_0^2}{\pi n_g L \sqrt{at}} \tag{3.38}$$

where again we made use of the dispersion of the effective index (3.37).
When the input field is on resonance with the ring resonators, the circulating power coefficient of Eq.3.34 reaches its maximum

$$\left|\frac{A_2}{A_1}\right|^2 = \frac{a(1 - t^2)}{(1 - at)^2} \tag{3.39}$$

meanwhile the straight-through transmission reaches its minimum

$$\left|\frac{B_1}{A_1}\right|^2 = \frac{(a - t)^2}{(1 - a\,t)^2} \tag{3.40}$$

By tuning the coupling between the bus waveguide and the ring resonator is possible to reach the particular condition $a = t$. This is called *critical coupling condition* and it is reached when the coupled power to the ring is equal to the round trip losses. The destructive interference at the output causes the straight-through transmission to be zero, meanwhile the intra-cavity field to be the maximum.
Once the light is trapped inside the cavity, the field can be either out-coupled in the bus waveguide or lost due to the propagation losses (Eq.3.22). This behaviour is characterized by the *quality factor* Q that physically describes the number of field oscillations before the power inside the cavity is depleted by $1/e$[198]

$$Q = \frac{\omega \mathcal{E}}{P} \tag{3.41}$$

where $\mathcal{E}$ is the energy stored, ω is the angular frequency and P is the dissipated energy $P = \partial\mathcal{E}/\partial t$. For optical cavities the Q factor relates to the spectral sharpness defined by $\Delta\lambda$

$$Q = \frac{\lambda_0}{\Delta\lambda} \tag{3.42}$$

and can be experimentally measured by a transmission scan to reconstruct the Lorentzian deep of Eq.3.33. The retrieved Q is function of the power loss in the ring due to propagation losses and the coupling to the bus waveguide, and it is defined as *loaded* quality factor (Q_L)

$$Q_L = \frac{\pi n_g L \sqrt{at}}{(1 - ta)\lambda_0} \tag{3.43}$$

from Eq.3.38 and 3.42. If the ring resonator is completely un-coupled to the bus waveguide, the value of t becomes zero and the Q factor depends just on the propagation losses a. We define in this case the *intrisinc quality factor* (Q_I)

$$Q_I = \frac{\pi n_g L \sqrt{a}}{(1 - a)\lambda_0} \tag{3.44}$$

The intrinsic and loaded quality factors are linked by

$$\frac{1}{Q_I} = \frac{1}{Q_L} - \frac{1}{Q_C} \tag{3.45}$$

where the value of Q_C depends on the coupling conditions

$$Q_C = \begin{cases} \frac{2Q_L}{1-\sqrt{T_{min}}} & \text{for} \quad a < t \\ \frac{2Q_L}{1+\sqrt{T_{min}}} & \text{for} \quad a > t \end{cases} \tag{3.46}$$

The first case in Eq.3.46 is called under-coupled condition and defines the event in which the cross-coupling coefficient κ is smaller than the internal loss $\sqrt{1-a^2}$. On the other side, the over-coupled condition refers to the opposite case ($a > t$) in which $\kappa > \sqrt{1-a^2}$. The value T_{min} in Eq.3.46 corresponds to the transmission when the field is resonant with the cavity. In critical coupling $T_{min} = 0$ and, since $Q_I = 2\,Q_L$, we can extract the propagation losses α from a transmission scan. However, we are interested in retrieving the propagation losses in the most general case $T_{min} \neq 0$, where from a transmission correspond two values of a (Eq.3.46). In order to understand if a measured ring is in under-coupled or over-coupled condition, it is necessary to disentangle the value of a from the value of t[198]. In this thesis, we fabricated multiple rings with different coupling conditions by sweeping the gap values between rings and bus waveguides. By going from a ring with a small gap to a ring with an increased gap, we go from an over-coupled condition to an under-coupled condition and at the same time the loaded quality factor increases. The drawback of this analysis lies on the assumption that all the rings have the same propagation losses.

In a high Q-factor cavity the optical power is boosted due to a constructive interference of the field. This is a direct consequence of the light trapping experienced inside the cavity and can be expressed by the finesse ($\mathcal{F}$)

$$\mathcal{F} = \frac{FSR}{\Delta\lambda} = \frac{\pi\sqrt{t\,a}}{1 - t\,a} \tag{3.47}$$

that is the number of round trip inside the cavity before the energy is reduced of a factor $1/e$ times 2π. In the case of critical coupling ($a = t$), we have

$$\mathcal{F} = \frac{\pi\, a}{1 - a^2} \approx \frac{2\pi}{\alpha L} \tag{3.48}$$

where the second equality holds in low loss regime[199] ($\alpha \simeq 1$). In most applications it is required a high finesse in order to enhance the power intensity inside the ring. For the same propagation losses, this can be achieved by reducing the ring radius as showed in Eq.3.48.

3.3 Fiber Coupling Optimization

High field confinements in waveguides represent a problem for coupling light from an optical fiber due to a small field overlap between the two modes that would cause high insertion losses. In order to overcome this problem, mode converters can minimize the modal mismatch in edge-coupling systems[200, 201] showing high CE but requiring further processes (as dicing and polishing, that compromise the throughput of the process), in general combined with lensed fibers. Alternatively, grating couplers are one of the most used component in silicon photonics since they can be integrated in different parts of the chip (thanks to the vertical coupling) with a higher spatial tolerance in the alignment. Gratings remove the need of polishing steps often used to maximize performances in edge-coupling systems and can be easily scaled to couple tens of waveguides using standard v-grove fiber arrays.

The versatility of our technology offers the possibility to use both techniques by slightly changing the process list in order to insert the polishing step in case of edge coupling. Since edge-coupling system can offer high CE, we present some simulations to evaluate the coupling between a lensed fiber and the waveguide. However, due to the resulting design requirements, the additional fabrication steps and the lower CE, the preferred component for out-coupling light is the grating coupler and in Sec.3.3.2 we present its parameters optimization.

3.3.1 Edge coupling

Edge-coupling techniques require that the input or output fiber is accurately aligned in all directions with the photonic waveguide. In this way, provided a close proximity between the two guided modes, the light scattered from the end-face of the waveguide is coupled directly to the fiber mode. The efficiency of the process depends on two factors: the mode overlap and the effective index mismatch.

The mode overlap can be computed directly with the software *Lumerical*, where it calculates

$$overlap = \left| \mathrm{Re}\left[\frac{\int \mathbf{E}_1 \times \mathbf{H}_2^* \, dS \cdot \int \mathbf{E}_2 \times \mathbf{H}_1^* \, dS}{\int \mathbf{E}_1 \times \mathbf{H}_1^* \, dS} \right] \frac{1}{\mathrm{Re}\left[\int \mathbf{E}_2 \times \mathbf{H}_2^* \, dS\right]} \right| \tag{3.49}$$

in which $\mathbf{E}_i$ and $\mathbf{H}_i$ are the electric and magnetic vectors with i defining the fiber and waveguide modes.

Due to a tight confinement given by the high index contrast between the SiC waveguide and the air cladding, a lensed fiber is considered in this analysis in order to achieve higher CE. The lensed fiber provides a mode waist of $\sim 2\,\mu m$ that is, compared to normal single mode fibers, about five times smaller (Fig.3.10).

By sweeping the waveguide width, the mode overlap can be changed as reported in Fig.3.11. The maximum overlap is achieved with a waveguide width of $\sim 100nm$ meaning that a mode converter is needed to adiabatically change the dimension of Fig.3.4(a) to inverse taper of Fig.3.12.(a). If the width changes along the propagation direction is slow enough, the mode converter can have negligible excess losses.

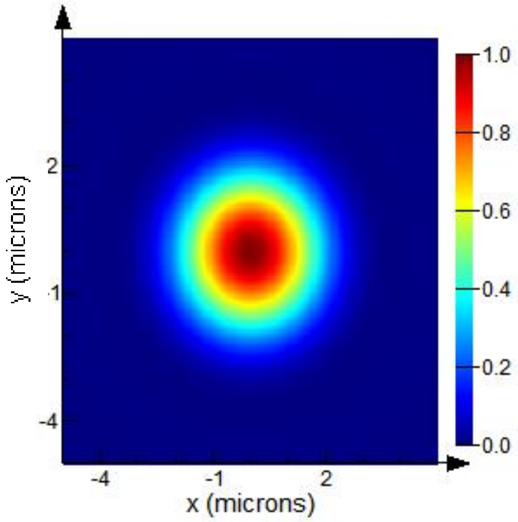

Figure 3.10: Normalized electric field intensity for the TE mode of the lensed fiber.

A good CE can also be obtained by increasing the width of the waveguide. For the mode of Fig.3.12.(b), the overlap is $\sim 16\%$. The dip in overlap depicted in Fig.3.11 corresponds to the case where the field is optimally confined in the structure. Besides the mode overlap, the coupling efficiency is also dependent by the index mismatch between the tapered waveguide and the fiber: in case the two effective refractive indexes are equal there is no light reflection at the end. This can even be seen in the ray optics picture since the more the numerical aperture of the fiber is equal to the waveguide one, the higher the CE is.

The fabrication of an inverse tapered waveguide of 100nm imposes some lithography and etching challenges. Furthermore, the expected CE is considerably lower than the one simulated for apodized grating coupler.

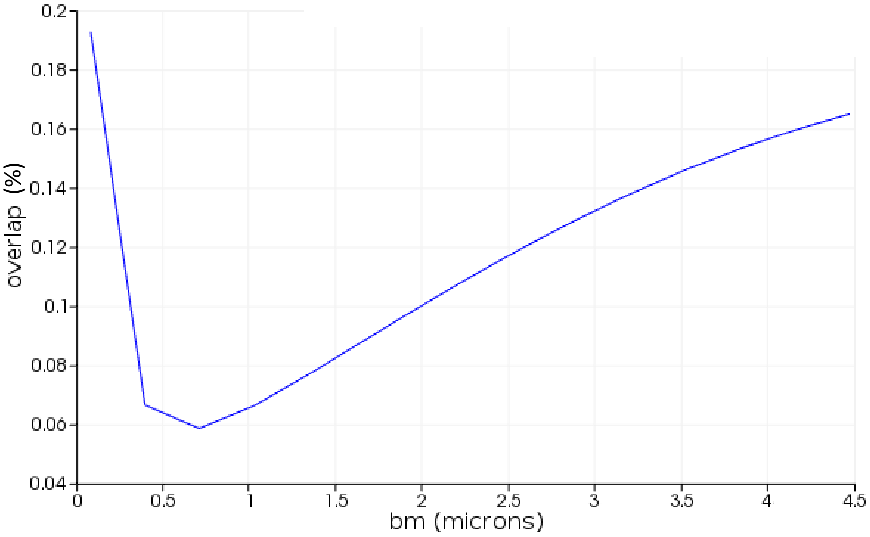

Figure 3.11: Overlap between the first TE mode Fig.3.12 and the lensed fiber mode Fig.3.10 at different waveguide width.

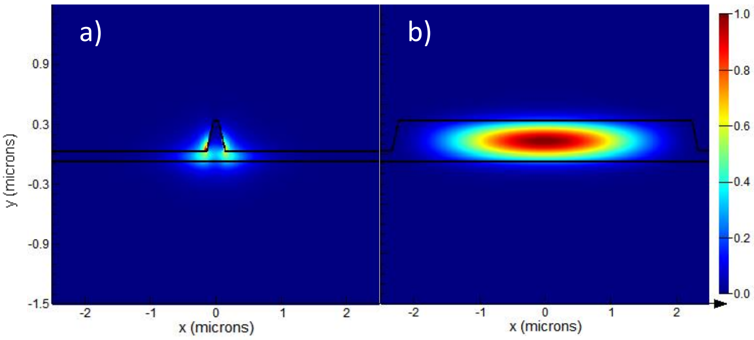

Figure 3.12: Normalized electric field intensity for the first TE mode of the in-versed(a) and normal(b) tapered waveguides.

3.3.2 Grating Coupler Optimization

When a beam, propagating inside a waveguide, encounters a section in which the refractive index is changed periodically, the field is scattered preferentially in the direction angle θ described by the Bragg's condition

$$\sin\theta = \frac{n_{eff} - m\lambda/p}{n_{clad}} \tag{3.50}$$

where n_{eff} is the effective index characterizing the periodic section, n_{clad} is the refractive index of the cladding, p is the period and λ is the free-space wavelength. In Eq.3.50, m is an integer describing the scattering order and usually, in order to have just one scattering angle, it is fixed at one by the grating design. The scattered light can be gathered by a single mode fiber, inclined at the angle that matches the scattering angle

θ. With reference to Fig.3.13.(a),the CE between grating and waveguide can be divided in three factors[202, 86]

$$\eta = \frac{P_{fib}}{P_w} = \eta_{rad} \cdot \eta_{dir} \cdot \eta_{ov} \tag{3.51}$$

where η_{rad} accounts for the radiation efficiency that is affected by the power reflection at the grating (P_r) and the remaining power after the grating (P_t)

$$\eta_{rad} = \frac{P_{in} - P_t - P_r}{P_{in}} = 1 - R - T \tag{3.52}$$

The reflection coefficient $R = P_r/P_{in}$ can be minimized if the refractive index change at the interface between waveguide and grating is not too abrupt meanwhile the transmission $T = P_t/P_{in}$ can be reduced to zero if the number of scattering elements is high enough.

The light at the grating can be either scattered toward the fiber, with power P_{up}, or scattered toward the substrate, with power P_{down}. This efficiency is described with

$$\eta_{dir} = \frac{P_{up}}{P_{up} + P_{down}} \tag{3.53}$$

The maximization of this efficiency requires generally additional fabrication steps to implement efficient back reflectors, like metal layer[86] or distribute Bragg reflector[203], in order to reflect back the light towards the fiber. In SOI technology, the thickness of the layer between the waveguide and the back reflector, called BOX, is chosen such that a constructive interference phenomenon occurs between the reflected and the scattered light. The suspended nature of the SiC photonics does not allow the use of a back reflector and consequently this is a limiting factor for this technology.

In order to have a high coupling efficiency, the spatial distribution of the field has to match along all directions the gaussian distribution of the fiber. In a uniform grating, the envelope of the scattered field propagating along the z direction follows

$$P_s(z) = \exp(-2\gamma\, z) \tag{3.54}$$

with γ is a constant loss per length. This power profile has a mode overlap with the fiber mode that can be calculated using

$$\eta_{ovZ} = \left| \frac{\int (E_{fiber}(z) \cdot E^*_{grating}(z)\,)^2 dz}{\int (E^2_{fiber}(z) dz \cdot \int (E^2_{grating}(z) dz} \right| \tag{3.55}$$

for the z direction, and

$$\eta_{ovY} = \left| \frac{\int (E_{fiber}(y) \cdot E^*_{grating}(y)\,)^2 dy}{\int (E^2_{fiber}(y) dy \cdot \int (E^2_{grating}(y) dy} \right| \tag{3.56}$$

for the y direction, perpendicular to the plane of Fig.3.13.(a). In Eq.3.55 and 3.56, E_{fiber} and $E_{grating}$ are the electric field of the mode of the fiber and scattered from the grating, respectively, along the two directions. The efficiency η_{ovY} can be close to unity if we use a tapered waveguide or focusing grating[204], since, for large width of the waveguide, the field distribution along y of the fundamental mode is similar to the gaussian distribution of the fiber. In addition to η_{ovY} and η_{ovZ}, the efficiency η_{ov} depends on the Fresnel equation for the fiber mode and cladding propagation constants

$$\eta_{ovF} = \frac{4\,\beta_{fiber} \cdot \beta_{clad}}{(\beta_{fiber} + \beta_{clad})^2} \tag{3.57}$$

where, provided the use of a cladding and an index matching oil, the efficiency η_{ovF} can be close to unity. Even if at the moment we have not implemented a cladding different from air, the suspended platform can make use of different upper-cladding materials and consequently increase the efficiency η_{ovF}.

From now on we focus in the optimization od 3C SiC grating couplers, since they best take advantage of the presence of a second step of electron-beam lithography to achieve a higher CE. By implementing the model (Fig. 3.13.a) in a 2D-FTDT simulator, we optimized the grating period, etch depth and filling factor for maximizing the CE from a 8°-tilted single mode fiber injecting TE-polarized light. Fig. 3.13(b) reports the simulated CE versus wavelength for the best period (794 nm and 720 nm for SM and MM waveguide, respectively), etch depth (162 nm and 320 nm for SM and MM waveguide, respectively) and filling factor (0.457 and 0.417 for SM and MM waveguide, respectively). For both structures we considered a sidewall angle of 80°, consistent with our process technology, and a refractive index of 2.6. Despite the lack of a back reflector, often used in SOI technology, the SM grating coupler reaches a high CE of -4.4 dB at 1550 nm and a wide 3 dB bandwidth of 88 nm. On the other side, the uniform grating coupler for the MM platform shows reduced CE of -7.7 dB with the fundamental mode, and a similar bandwidth of 74 nm.

In order to match the spatial distribution of the scattered light from the grating with the gaussian shape of the fiber mode and improve the efficiency η_{ovZ} and η_{rad}, it is possible to optimize the position and size of each post (apodized grating coupler). The parameter space, already composed by the etch depth (ED) and the position of the fiber with respect to the grating coupler (F_{pos}), is increased by two times the number of posts composing the grating coupler: each post i adds a period p_i and a size s_i [Fig. 3.13(a)]. In a similar way to references [85, 86], we developed a four-steps algorithm to optimize the CE: 1) In a first step, we optimize the uniform grating coupler for a given etch depth in order to find the best period p and size s. 2) From the previous step, the algorithm simulates structures sweeping sequentially the value of all s_i for a set of periods close to p for each post i. The parameters are saved only if they perform with a higher CE at 1550 nm than the previous saved solution. The procedure is repeated until the solution converges. 3) In this step, every saved position p_i and sizes s_i are mutated by different

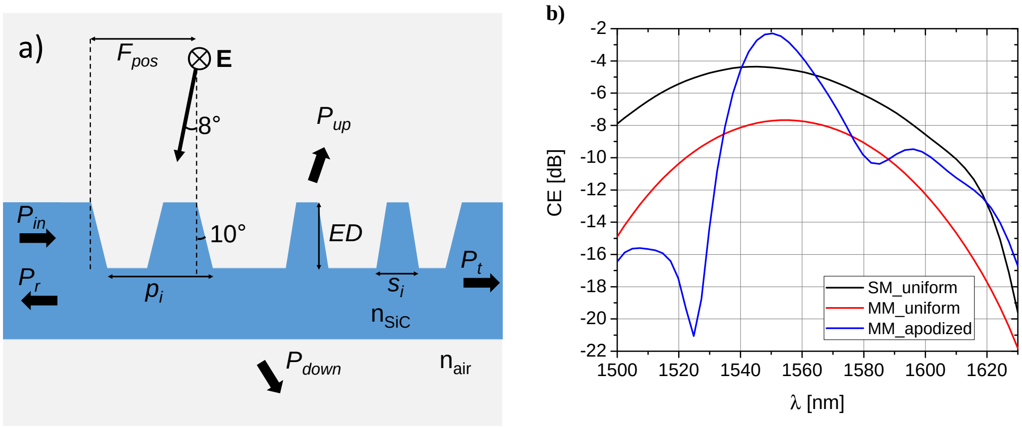

Figure 3.13: (a) Schematic of an apodized grating coupler. (b) Coupling efficiency versus wavelength from 2D-FDTD simulation of grating couplers optimized for SM and MM waveguides.

random values between ±2 nm and the new grating coupler is simulated. Once again, the parameters are saved only if they perform with an higher CE and the procedure is repeated until the solution converges. 4) By changing ED of the grating of 10 nm steps and repeating step 3), it is possible to determine the etch depth that delivers the highest CE. At each step, F_{pos} is swept in order to maximize CE. The optimization can be constrained by process limitations in step 3): for minimum post size of 100 nm and distance between two post of 50 nm, the retrieved post positions and sizes are reported in Table 3.1 for an etch depth of 320nm. This level of constrains does not affect drastically the CE since the reduction from the optimal design lies in a few percent, and makes the designed structure feasible with the fabrication process described below. The simulated CE for MM waveguides is reported in Fig. 3.13 and it improves for the apodized case reaching a value of -2.3 dB at expense of the bandwidth, that reduces to 27 nm. Rather than simply maximizing the CE at 1550 nm, the described algorithm can be used to optimize different figure of merits of the grating depending on the requirements of the photonic device. The complete source code to implement the apodization algorithm in Lumerical, is reported in Appendix B.

3.4 Linear Characterization of SiC Photonics Components

In order to fabricate photonics components in SiC, we developed the fabrication procedure reported extensively in Chap.2. The process steps are resumed in Figs. 3.14(a)-3.14(f) and discussed here for convenience. The SiC layer, heteroepitaxially grown on a Si <001> substrate, is purchased from *NOVASIC* with a chemical-mechanically polished surface. As the first step, the SiC film is thinned down to the desired waveguide thickness (400 nm and 700 nm for SM and MM waveguide, respectively) by dry etching, while a first electron beam lithography step is performed to define the waveguide width

Table 3.1: Positions and sizes resulting from the apodization algorithm for the MM structure, with a refractive index of 2.6 and an etch depth of 320 nm

$1 < i < 10$		$11 < i < 20$	
p_i [nm]	s_i [nm]	p_i [nm]	s_i [nm]
562.2	482.0	824.7	381.8
652.5	233.1	961.7	232.9
791.8	449.8	542.2	492.2
711.0	235.1	688.9	232.9
617.6	472.8	734.0	614.0
793.3	379.4	571.2	308.7
777.3	232.9	947.0	288.4
667.7	609.6	640.6	589.7
812.1	232.9	758.9	616.8
500.1	428.8	516.5	254.2

of 480 nm (SM) and 670 nm (MM) using CSAR62 resist [Fig. 3.14(b)]. The pattern is subsequently transferred to a 100 nm aluminum hardmask by dry etching in order to guarantee sufficient selectivity during the high-power ICP-RIE SiC etch based on fluorine chemistry (SF$_6$), Fig. 3.14(c). The SiC layer is etched 300 nm and 500 nm for SM and MM waveguides, respectively, and a thin SiC membrane is left in order to provide mechanical support once the Si substrate is removed. In a second fabrication flow, both grating coupler grooves and holes in the membrane are patterned by etching the SiC layer for 162 nm (SM) and 320 nm (MM), Figs. 3.14(d) and 3.14(e). The etch depths are chosen to produce the optimum CE for the gratings couplers, while being greater than the membrane thickness, ensuring that the holes expose part of the silicon substrate. In this way, a XeF$_2$ vapor etch can be performed to undercut the Si substrate, suspending the photonics components and generating the maximum refractive index contrast achievable [Fig. 3.14(f)]. Fig. 3.14(g) shows a 45°-tilted SEM picture of a suspended MM ring resonator resulting from the described fabrication flow. The optical-microscope image of the final device is reported in Fig. 3.19(a) and depicts a suspended area of $\sim$40 μm around the waveguides. The extremely high Young's modulus of SiC [205] ensures large suspensions without incurring in the membrane cracks or deformations.

3.4.1 Scattering measurement of straight waveguides

The light propagating inside the waveguide is scattered by roughness at the interface between core and cladding as reported in Eq.3.23. This field leaked from the guiding mode is proportional to the intensity at precise point where it is recorded.

Thanks to an experimental setup composed of magnifying lenses and an InGaAs CCD camera, that absorbs at telecom wavelength, it is possible to record the scattered light in different points of a straight waveguide. In Fig.3.15.(a), the initial scattered light of a

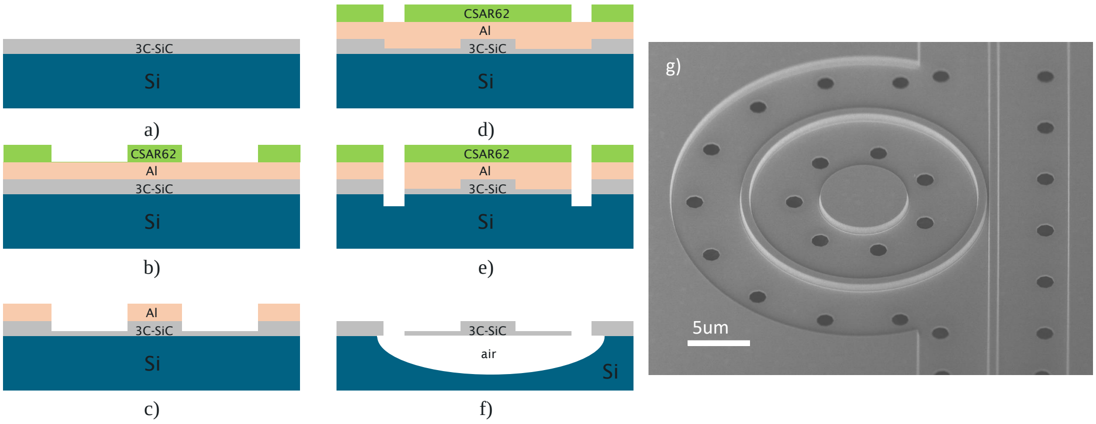

Figure 3.14: Schematic representation of the fabrication process (a)-(f). 45° SEM view of a MM ring resonator (g).

SM waveguide is recorded and, due to propagation losses, the intensity of beam is attenuated as the distance increases from the initial point. This is evident from Fig.3.15.(b), where the distance between the initial point and the recorded point is 0.35cm, resulting in a faint scattered light. The beam was injected in TE polarization thanks to uniform gratings coupled to a single mode fiber.

By averaging the pixel values of the images recorded in different positions, it is possible to retrieve the scattered field intensity. The different intensities are plotted versus the relative distances at which they are recorded in Fig.3.16 where the exponential fit provides a propagation losses of $-(65.8 \pm 5.3)$dB/cm. This measurements were taken with the help of Roman Bruck, that gently lent us his time and setup to perform this characterization.

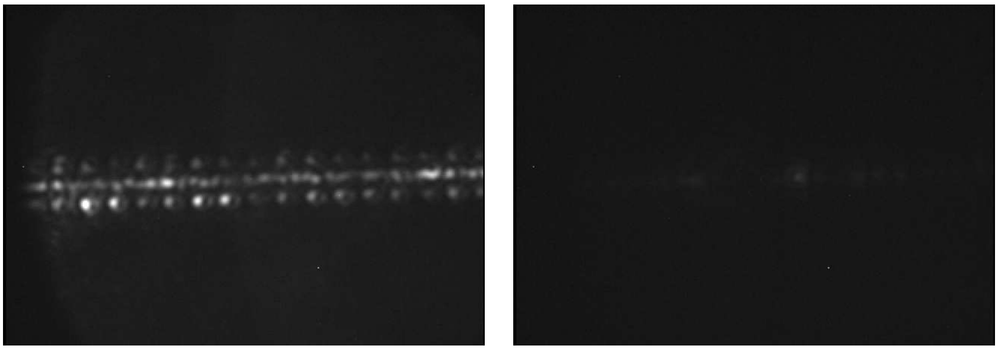
(a) (b)

Figure 3.15: Scattering measurement from a single mode waveguide at the 0cm (a) and after 0.35cm of propagation (b)

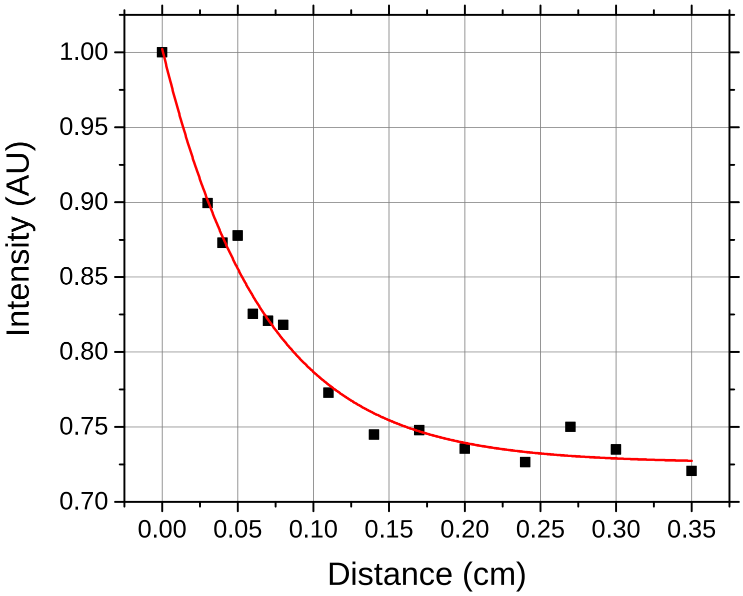

Figure 3.16: Intensity measurements of the scattered light at different propagation distances (black dot) and exponential fit (red curve)

3.4.2 Gratings and rings experimental characterization

To perform a more comprehensive characterization of the fabricated devices, transmission measurements have been performed. The photonics components are characterized in TE polarization using a CW laser (*Santec TSL-510*) tunable across the telecom band (1500-1630 nm) and a polarization-maintaining fiber array. Following the layout of the fabricated optical circuit [Fig. 3.19(a)], light is injected using the uniform grating coupler for the SM waveguide and the apodized grating coupler for the MM waveguide. Both gratings are optimized for the refractive index measured by ellipsometry on the two different wafers used for the fabrication of SM and MM waveguides. In Fig.3.17 is reported the SEM of an apodized grating coupler used to couple light in a MM waveguide. Since the lateral dimension of the grating is 20 μm to maximize the overlap with single mode fibers, mode converters are employed to adiabatically reshape the mode at the grating to the SM and fundamental MM ones. Numerical simulations show conversion loss lower than 0.15 dB for the fabricated length of 800 μm and 490 μm (SM and MM case, respectively). In Fig3.18, the $|S_{12/21}|^2$ parameters describing the transmission of the mode converter ($20\mu m$) are plotted as function of the length of the taper, where the waveguide size is changed linearly along the propagation direction. The fluctuations in the $|S_{12/21}|^2$ values are due to the approximated method used to compute them that makes use of eigen-mode expansion of the structure at different points. This fluctuation can be reduced considerably if the mesh of eigen-mode solver is increased.

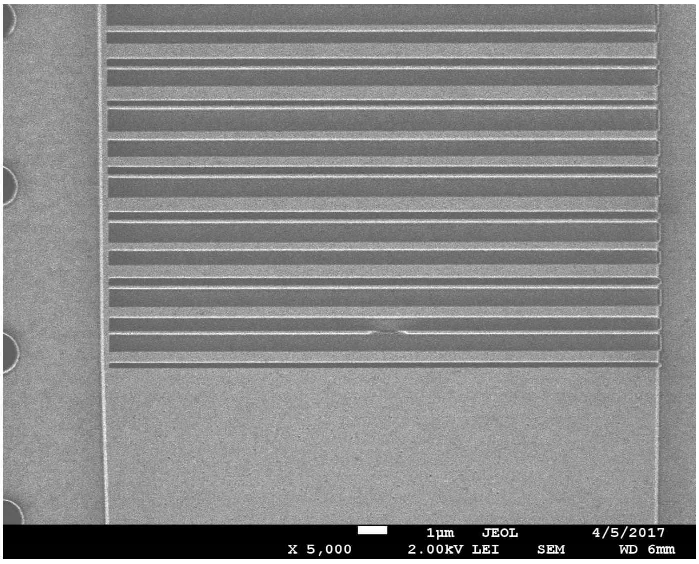

Figure 3.17: SEM of an apodized MM grating coupler

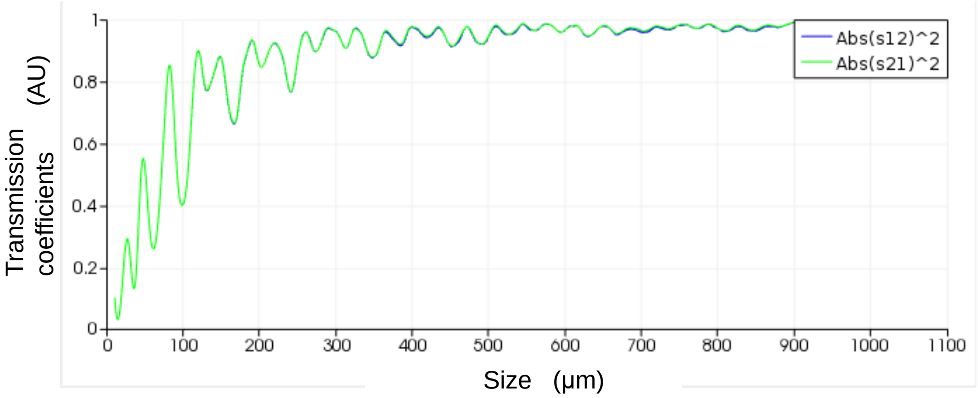

Figure 3.18: Mode converter for the SM case. The $|S_{12/21}|^2$ parameter describes the power coupling from the input to the output of the tapered section as function of the component length

We characterized the performance of the grating couplers by measuring the transmission of SM and MM devices. Since the linear losses calculated below are valid only for the SM (MM) part of the circuit in Fig. 3.19(a), the grating plus tapering sections are characterized as a single coupling component. In Fig. 3.19(b), the total CE for the grating-taper component is reported for both the SM and MM case. The CE is ∼-6 dB (-6.8 dB) at 1500 nm (1527.5 nm) and the half width at half maximum is ∼38 nm (∼18 nm) for the SM (MM) platform. The shift in wavelength of the measured CE compared to the simulation results, is ascribed to fabrication imperfections given by the high etching rate (giving an error on waveguide thickness and *ED* parameter) and a small difference between the actual refractive index of the sample and the one used for simulations. Both effects are amplified by the high refractive index contrast.

Ring resonators provide a direct way to retrieve linear losses of waveguides from the

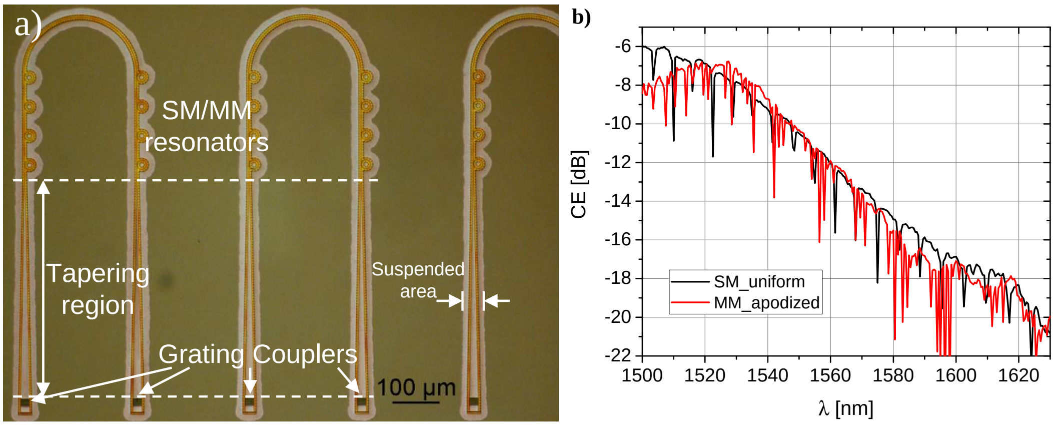

Figure 3.19: Optical microscope image of the sample layout (a). Experimental characterization of fabricated SM and MM grating coupler together with mode converter (b).

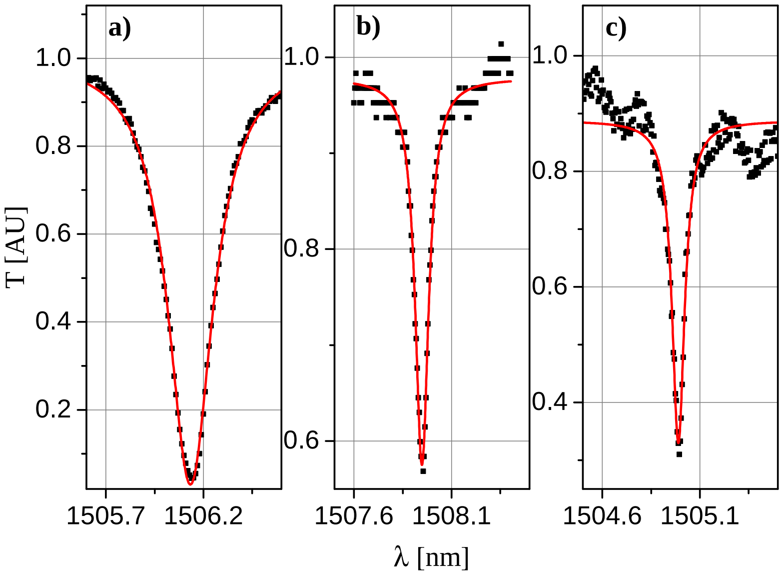

Figure 3.20: Measured high-Q resonance of different ring resonators (black dots) and lorentzian best-fit (red line): 20 μm ring realized with SM waveguide (a), 10 and 20 μm ring realized with MM waveguides (b and c, respectively). All the rings are in the undercoupled condition.

measured quality factor[199]. Thanks to the high confinement, we fabricated ring resonators with small radius of 10 μm (MM) and 20 μm (SM and MM) that are simulated to exhibit small excess bending losses. In the same sample, different gaps between bus waveguides and rings are fabricated in order to tune the coupling strength with the resonators and determine the coupling condition. Fig. 3.20 shows measurements of transmission versus wavelength for a SM-20μm ring [Fig. 3.20(a)], MM-10μm ring [Fig. 3.20(b)] and MM-20μm ring [Fig. 3.20(c)]. For the SM resonance, the intrinsic quality factor is calculated as 9,100 corresponding to linear losses of 58 dB/cm. When the field is more confined inside the material (MM waveguides) the scattering losses reduces and the intrinsic quality factor improves up to 20,000 (25 dB/cm) for the 10 μm ring. This is further shown from Fig. 3.20(c), where the bigger radius decreases the field overlap with the sidewall roughness and the intrinsic quality factor reaches 24,000 (21 dB/cm). Further increasing the radius of the resonator does not provide any significant improvement in the propagation losses. Since the mode intensity at the sidewall is still non-zero for the MM waveguide [Fig. 3.4(b)], it is possible that the reported value of the losses is still not limited by material absorption. The improvements in the losses for the MM structures are also partially explained by the reduction of the field intensity in bottom part of the SiC layer, where the high density of defects generated during the crystal growth increases the material absorption.

The complete losses analysis procedure is reported in Appendix A, where resonance spectra of set of ring resonators (made in the same fabrication run) are reported to extract the linear losses for the 10μm-radius MM, 20μm-radius MM and a 20μm-radius SM case.

3.5 Analysis of scattering losses

The propagation losses of 58 dB/cm (21 dB/cm) for the SM (MM) waveguide are due to the loss mechanisms described in Sec.3.1.3. For the analysis of propagation losses we can neglect the term α_b of Eq.3.22 since the bending losses can be calculated by mean of numerical solvers and ring radii are chosen such that bending losses are negligible. Since it is not trivial to determine the material losses of the suspended SiC film, we can estimate α_m by removing from the total losses the computed scattering losses. As first approximation, we can neglect the scattering due to the top interface since the wafer is chemical-mechanical polished and the roughness is considerably smaller than the one presents on the sidewall. However, we do not have any insight on the roughness of the bottom interface that could be considerably rough due to the SiC growth. Even though the model of scattering losses due to roughness (Eq.3.23) introduced in Sec.3.1.3 relates the losses directly to the field at the boundaries, it does not account for the autocorrelation length L_c that is an important parameter for accurate loss calculations[206, 188]. The top-view image of a MM waveguide reported in Fig.3.21 can be used to estimate the autocorrelation length to be $L_c = 80nm$ and the standard deviation to be $\zeta = 4nm$. According to the model derived from Payne and Lacey[207, 206], it is possible to retrieve the scattering losses due to the lateral sidewall surface roughness to be ~46dB/cm and ~16dB/cm for the SM and MM case, respectively. These values well-match with the experimental results since they explain 30dB/cm out of 37dB/cm improvement in term of propagation losses achieved using a MM structure instead of a SM one. The remaining 7dB/cm that are not explained from the scattering of the waveguide sidewall can be attributed to the use of Al as hardmask that introduces metallic contaminations in the waveguide sidewalls[208]. Additionally, the MM structure presents a mode concentration at the bottom SiC boundary less than the SM case and this could concur to the propagation losses improvement experienced in the MM waveguide. Therefore, the material losses can be estimated to be at maximum 5dB/cm including the losses provided by scattering of the bottom interface.

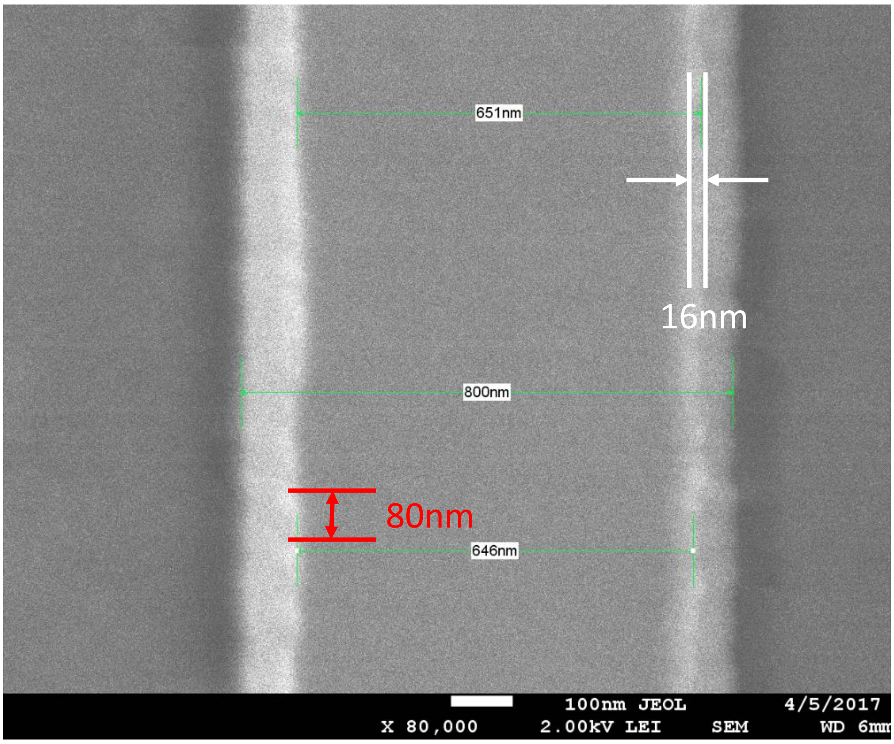

Figure 3.21: SEM images of a MM waveguide (top view) to show the sidewall quality. From the roughness at the edge of the waveguide we can estimate the amplitude and approximate mean distance between the surface fluctuations to be 16nm and 80nm, respectively.

3.6 Conclusion

The presence of a Si substrate, needed for heteroepitaxially growing the crystalline SiC layer, hampered the development of basic photonics components needed for a multitude of optical processes. Thanks to a new fabrication approach, that removes the underlying substrate by employing two steps of electron beam lithography, both SM and MM photonic platforms were realized in a fully scalable manner. This technology can easily be integrated with photonic crystal cavities, a key component for exploiting SiC point defects and low power non-linear interaction, and be extended to other heteroepitaxially grown materials, such as hexagonal SiC films created by electrochemical etching or GaAs membranes. The fabricated couplers show CE around -6 dB when considering grating efficiency and taper propagation loss (in the order of 1-2 dB considering MM propagation losses). This value can be improved using selffocusing gratings [204] that do not require long mode converters, increasing transmission and reducing the footprint of the optical devices. The characterized ring resonators demonstrated high intrinsic quality factors up to 24,000. Even though the reported values of quality factor are sufficient to demonstrate non-linear effects like efficient frequency conversion, improving the propagation losses would open the possibility to use SiC for scalable quantum optical interconnections. Additional steps in the fabrication procedure, including roughness reduction by oxidization or the deposition of a cladding to decrease the high index contrast, could target the scattering loss by reducing the roughness effects and improve the quality factor of the resonators. Furthermore, the use of a non-metal hardmask could improve the propagation losses[208]. The reported results demonstrate a fundamental step in the development of SiC photonics and open the way for the integration of a variety of classical and quantum devices.

Chapter 4

Frequency Conversion in 3C SiC Ring Resonator

The SiC optical properties are ideal for the realization of nonlinear devices, due to the wide bandgap (2.3 eV), the high refractive index (2.6) and the non centrosimmetryc crystal. These features can be fully exploited in integrated structures, where the presence of a tight confinement in the waveguide and in the ring enhances the nonlinear behaviour. The first section of this chapter is dedicated to a brief introduction to optical nonliner process meanwhile, since SiC is non-centrosymmetric, in Sec.4.2 is shortly reported the *second harmonic generation* (SHG) process. In particular, to overcome phase matching problems affecting non-birefringent media, a route toward an efficient process is highlighted.

The *four-wave mixing* (FWM) effect is described in Sec.4.3 together with the enhancement obtained from confined structures. Using the linear photonic components developed in Chap.3, the demonstration of frequency conversion by FWM is reported in the last section of the chapter. Part of the results reported in this chapter have been published in Ref.[13].

4.1 Optical nonlinearities

In Sec.3.1, we introduced the Maxwell's equations and we limited the study to the case of linear dependence of the polarization vector **P** to the electric field **E** (Eq.3.19). In the most general case, the polarization vector has a non-linear power dependence on the electric field and, consequently, the susceptibility χ is function of the electric field. Using the Taylor's expansion, we can write

$$\mathbf{P}_i = \epsilon_0 \left(\sum_j \chi^{(1)}_{ij} \mathbf{E}_j + \sum_{jk} \chi^{(2)}_{ijk} \mathbf{E}_j \mathbf{E}_k + \sum_{jkl} \chi^{(3)}_{ijkl} \mathbf{E}_j \mathbf{E}_k \mathbf{E}_l + \cdots \right) \tag{4.1}$$

where $\chi^{(2)}_{ijk}$ and $\chi^{(3)}_{ijkl}$ are second and third order susceptibility tensors, respectively. The non linear behaviour of the polarization vector can be explained considering the dielectric material as formed by Coulomb dipoles, whose poles are electrons and nucleus. If the electric field is high enough, the potential energy of the dipoles becomes anharmonic and consequently higher order terms are needed to correct the dielectric tensor.

In centrosymmetric materials, the second order susceptibility is zero since in these materials a sign inversion in the applied electric fields $\mathbf{E}_j$ and $\mathbf{E}_k$ corresponds to a sign inversion of the nonlinear polarization vector $\mathbf{P}^{NL}_i$, without changing the amplitude

$$-\mathbf{P}^{NL}_i = -\chi^{(2)}_{ijk}\mathbf{E}_j\mathbf{E}_k = \chi^{(2)}_{ijk}(-\mathbf{E}_j)(-\mathbf{E}_k) \tag{4.2}$$

resulting in a vanishing $\chi^{(2)}_{ijk}$. Furthermore, Pockels effect and piezoelectricity are a consequence of the non-centrosymmetry and consequently all centrosymmetric crystals do not show these effects. With analogous arguments leading to Eq.4.2, it is possible to show that all materials (comprehending gases, liquids and amorphous dielectric) possess $\chi^{(3)}_{ijkl}$.

The nonlinear susceptibilities can roughly be estimated if we consider the Coulomb dipoles approximation and an applied electric field of the same order of magnitude of the characteristic atomic electric field strength[209]

$$E_{at} = \frac{e}{4\pi\epsilon_0 a_0^2} \tag{4.3}$$

where $a_0 = 4\pi\epsilon_0\hbar^2/me^2$ is the Bhor's radius of the hydrogen, with e the electron charge, $\hbar$ the Planck's constant, m the electron mass and ϵ_0 the vacuum permittivity. In this case, considering a non-centrosymmetric crystal, the first correcting factor of the polarization vector deriving from the $\chi^{(2)}_{ijk}$ will be of the same order of magnitude of linear polarization vector $\mathbf{P}_{lin} = \epsilon_0\chi^{(1)}_{ij}\mathbf{E}$. Since $E_{at} = 5.14 \times 10^{11} V/m$ and considering that the linear susceptibility is in the order of one, we have

$$\chi^{(2)}_{ijk} \simeq \chi^{(1)}_{ij}/E_{at} = 1.94 \times 10^{-12} m/V. \tag{4.4}$$

This argument can be extended for the successive susceptibilities appearing in Eq.4.1

$$\chi^{(n+1)} \simeq \chi^{(n)}/E^n_{at} \tag{4.5}$$

and consequently the magnitude of the nonlinear effects due to the second order susceptibility are more than ten orders bigger than the ones due to the $\chi^{(3)}_{ijkl}$.

The wave equation in a nonlinear medium is defined by

$$\nabla^2\mathbf{E} - \frac{n^2}{c^2}\frac{\partial^2\mathbf{E}}{\partial t^2} = \frac{1}{\epsilon_0 c^2}\frac{\partial^2\mathbf{P}^{NL}}{\partial t^2} \tag{4.6}$$

where the nonlinear response of the polarization vector drives the electric field and, in the case of energy conservations, concurs in the coupling of different fields oscillating at different frequencies.

4.2 Second harmonic generation

In the case of second order nonlinearities, the nonlinear polarization vector is composed by

$$\mathbf{P}_i^{NL} = 2\epsilon_0\chi^{(2)}_{ijk}\mathbf{E}_j\mathbf{E}_k \tag{4.7}$$

where, given the point group symmetry $\bar{4}3\text{m}$ of 3C SiC, the second order non linear optical tensor is

$$\chi^{(2)}_{ijk} = \begin{vmatrix} 0 & 0 & 0 & \chi^{(2)}_{xyz} & 0 & 0 \\ 0 & 0 & 0 & 0 & \chi^{(2)}_{yxz} & 0 \\ 0 & 0 & 0 & 0 & 0 & \chi^{(2)}_{zxy} \end{vmatrix} \tag{4.8}$$

with $\chi^{(2)}_{xyz} = \chi^{(2)}_{yxz} = \chi^{(2)}_{zxy}$, where the theoretical value of the susceptibility is 34 pm/V[210]. The coupling equations that can be derived directly from Eq.4.7[6] and Eq.4.1, where **E** is composed by the modes at three different frequencies, can be used to describe different phenomena, like *Sum- and Difference-Frequency Generation* and *Optical Parametric Amplification*. Here we just mention *Second Harmonic Generation* (SHG), where two photons at frequency ω are annihilated to generate one photon at 2ω (Fig.4.1.b). Under the slowly varying amplitude approximation and considering that the pump power at ω is not considerably affected by the SHG process (nondepletion approximation), the coupling equations linking the two fields at different frequencies inside a nonlinear crystal reduces to

$$\frac{\partial E_{2\omega}}{dz} = -i\,\omega\sqrt{\frac{\mu_0}{n^2\epsilon_0}}\epsilon_0\chi^{(2)}E_\omega^2 e^{\Delta kz} \tag{4.9}$$

where

$$\Delta k = k(2\omega) - 2k(\omega) = \frac{2\omega}{c}(n(2\omega) - n(\omega)) \tag{4.10}$$

is the phase mismatch due to the natural dispersion of the crystal. By integrating Eq.4.9 and considering an absent second harmonic field at the beginning of the crystal, we have after a propagation distance L

$$E_{2\omega}(L) = -i\,\omega\sqrt{\frac{\mu_0}{n^2\epsilon_0}}\epsilon_0\chi^{(2)}E_\omega^2\frac{e^{\Delta kL} - 1}{i\Delta kL} \tag{4.11}$$

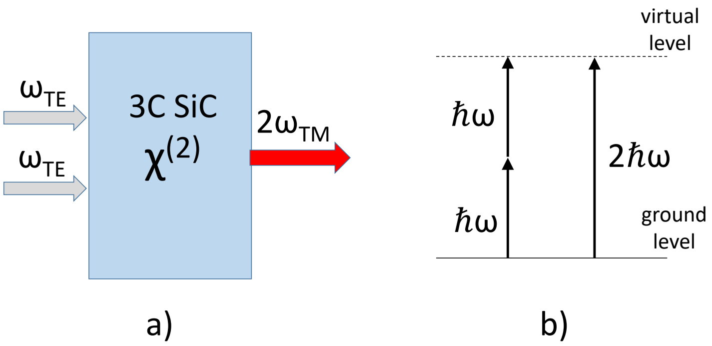

Figure 4.1: a) In SHG, two photons of the pump are converted inside the non-centrosymmetric crystal . b) For energy conservation, the virtual energy level reached by the sum of the two input photons has to match the energy of the output photon.

that can be used to retrieve the efficiency η_{SHG} of the process

$$\eta_{SHG} = \frac{I_{2\omega}}{I_{\omega}} = \frac{2(\omega\epsilon_0\chi^{(2)}L)^2}{n^3}\left(\frac{\mu_0}{\epsilon_0}\right)^{3/2}\frac{\sin^2(\Delta kL/2)}{(\Delta kL/2)^2}I_{\omega} \tag{4.12}$$

The maximum of the efficiency is obtained when

$$k(2\omega) = 2k(\omega) \tag{4.13}$$

called *phase matching condition.* In general, the refractive index of a material increases with ω so, for example, it is possible to realize SHG in birefringence materials, where the polarization of the pump must have at least one component in the plane perpendicular to the polarization of the generated wave.

When the phase matching condition in Eq.4.10 is not satisfied and $\Delta k \neq 0$, a sustained growth of the second harmonic mode is not present and the amplitude sinusoidally oscillates as function of the distance z. In this case, the non-linear interaction can be realized through *Quasi Phase Matching*, where the relative phase difference is corrected using structural periodicity built in the non-linear material [211]. In this way, the generated fields is affected by an inversion of the sign of $\chi^{(2)}(z)$ that leads to a constructive build up of the second harmonic mode along the propagation in the crystal.

4.2.1 SHG in SiC photonic structures

Second order non-linear effects have already been reported in 6-H SiC in an integrated way [212] through the use of photonic crystal nanocavity. In materials with the same point-group symmetry of the 3-C SiC, second harmonic generation with second-order quasi phase-matching has been showed [213, 138] using toroids structures. In fact, by taking advantage of ring resonators (Fig.4.2), we can obtain a modulation of the $\chi^{(2)}$ using the dependence of the non-linear coefficient on θ. The beam propagating for an angle of 90° in the ring experiences an inversion of the domain leading to the second-order quasi phase-matching for a complete round trip in the ring. The quasi phase matching condition results in a reduced value of the nonlinear susceptibility[6]

$$\chi^{(2)}_{qpm} = \frac{2}{\pi}\chi^{(2)}_{bulk} \tag{4.14}$$

meaning that an increased propagation length is needed to have the same conversion efficiency.

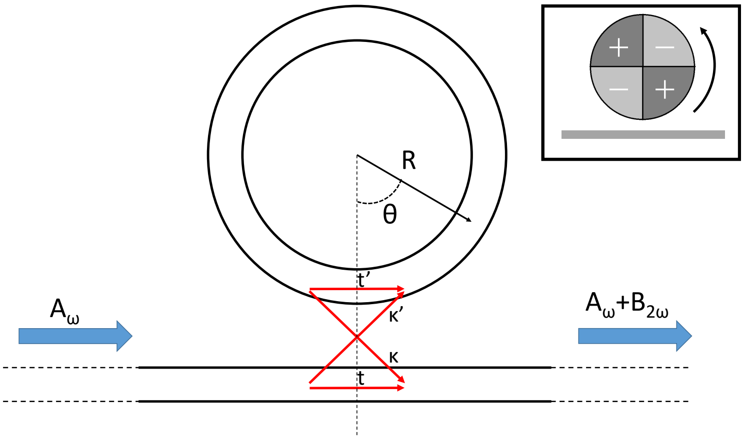

Figure 4.2: Ring resonator for second-order quasi phase matching in $\bar{4}3$m crystal class made using four domain inversions through the propagation of the beam around the $\bar{4}$ axis (<001>)

With this configuration, it is possible to set both the pump and the generated modes on resonance at the condition of

$$\frac{2\pi}{\lambda_{0p}}n_pR = m_p \quad \frac{2\pi}{\lambda_{0s}}n_sR = m_s \tag{4.15}$$

in which the refractive index $n_{p/s}$ are respectively the effective refractive index of the pump and the signal associated to the waveguide mode, $m_{p/s}$ are integers and $\lambda_{0s/p}$ are the pump and second harmonic free space wavelengths, respectively. As reported in Sec.3.2, the maximum field enhancement is reached in critically coupled condition of the ring, resulting in an increase efficiency of the non linear process (Eq.4.12). From the propagation of the beam in the ring, the following phase matching condition is obtained [213]

$$k_p - 2k_s = s\frac{2}{R} \tag{4.16}$$

where $s = \pm1$. Due the use of confined structure, the conversion efficiency depends also on the mode overlap between the generated and pump mode

$$\eta \propto \int_a^b A_s(\varsigma)A_p(\varsigma)d\varsigma \tag{4.17}$$

where a, b are the edges defining the waveguide cross-section, ς is the coordinate transverse to the direction of propagation and $A_{s,p}(\varsigma)$ are the eigenmodes. By looking at the SiC nonlinear tensor (Eq.4.8), the only non vanishing elements can be used to generate a second harmonic TM mode starting from a TE pump, and vice-versa. In this way, it is possible to tune the mode effective indexes by changing the waveguide dimensions in order to aid the phase matching of the process. Nonlinear tensors of some non-centrosymmetric materials require the phase matching between the fundamental and higher order modes, like AlN[214] and GaN[215], resulting in a low mode overlap due to mode orthogonality. This is a disadvantage with the respect to the SiC case, where the use of TE and TM modes with the same parity[216] can result in a high mode overlap. As reported in Ref.[213], the double resonant structure provides high conversion efficiency even considering low Q factors and moderate pump powers without the need of additional fabrication steps usually required in periodically poled structures[217]. When both the fundamental and the second harmonic fields are on resonance with the ring resonator, the maximum efficiency of the nonlinear process is reached since the quasi phase matching condition is fulfilled. Furthermore, both the fundamental field E_ω and the second harmonic $E_{2\omega}$ are enhanced by a factor described from Eq.3.39. As result, the second harmonic conversion efficiency is function of the product of the square of the circulating power coefficient (Eq. 3.39) experienced from the fundamental wave with the circulating power coefficient of the second harmonic wave[218].

4.3 Four wave mixing nonlinear process

Third order nonlinear effects are relevant for a broad variety of optical process in integrated structures, ranging from wavelength conversion[219, 220, 221], amplification[222] and self phase modulation[223] to generation of non-classical state of light[81]. These effects were widely studied in Silicon (Si)[224], due to its high $\chi^{(3)}$ susceptibility and scalability, and Silicon Nitride[148] (Si_3N_4), due to its low propagation loss and wide bandgap. Recently, photonic platform in Aluminium Nitride[225] and Diamond[119] have reached competitive results. Lately, $\chi^{(3)}$ effects were demonstrated in amorphous SiC toroids at telecom wavelengths[226] and in 4H SiC waveguides in the mid infrared wavelengths[126]. Even though numerical predictions are available for 3C SiC $\chi^{(3)}$ susceptibility [227], third order nonlinear effects have not been experimentally demonstrated due to difficulties in fabricating sub-μm photonic components.

The FWM process involves the coupling of four different fields and it is a direct consequence of the nonlinear polarization vector

$$\mathbf{P}_i^{NL} = \epsilon_0 \chi^{(3)}_{ijkl} \mathbf{E}_j \mathbf{E}_k \mathbf{E}_l \tag{4.18}$$

where the tensor $\chi^{(3)}_{ijkl}$ elements determine the coupling strength. Here we focus on the degenerate case where two fields have the same frequency. In this common case, the process is seen as frequency conversion mechanism where a field, referred as *signal* at ω_s, is converted in another field at ω_i, called *idler* (Fig.4.3), even though there is no energy transfer between signal and idler. This mechanism is possible thanks to a strong *pump* field that oscillates at frequency ω_p. The process requires the conservation of the energy and momentum

$$2\omega_p = \omega_s + \omega_i \tag{4.19}$$

$$2k_p = k_s + k_i \tag{4.20}$$

where the second equation is called phase matching condition. In a FWM process, the frequencies of the fields are close to each other and usually the process involves a small change in refractive index. Therefore, the fulfilment of the phase matching condition is less demanding compared to a second order nonlinear process.

In the case of undepleted pump, the nonlinear polarization vector of Eq.4.18 can be used together with the constitutive Eq.4.6 to obtain the coupled amplitude equation

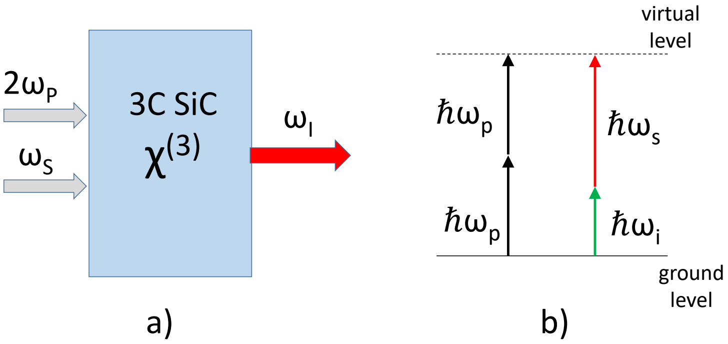

Figure 4.3: a) If a pump and signal waves propagate inside a $\chi^{(3)}$ crystal an idler can be generated, provided the satisfaction of the phase matching condition. b) If the $\chi^{(3)}$ susceptibility is real, the input and output energy are conserved and the process is parametric.

linking the three waves [228, 229, 6]

$$\frac{\partial E_p}{\partial z} = -\frac{\alpha_p}{2}E_p + j\gamma|E_p|^2E_p \tag{4.21}$$

$$\frac{\partial E_s}{\partial z} = -\frac{\alpha_s}{2}E_s + 2j\gamma|E_p|^2E_s + \gamma E_p^2E_i^*e^{-j\Delta kz} \tag{4.22}$$

$$\frac{\partial E_i}{\partial z} = -\frac{\alpha_i}{2}E_i + 2j\gamma|E_p|^2E_i + \gamma E_p^2E_s^*e^{-j\Delta kz} \tag{4.23}$$

where γ is a function of the nonlinear tensor element and describes the nonlinearity of the system. The first term on the right of eqs. (4.21) to (4.22) account the attenuation due to the propagation loss α_n, described before in Sec.3.1.3. The second and third terms account for the *self phase modulation* and *cross phase modulation*, where the $\chi^{(3)}$ nonlinearity causes a phase shift in presence of strong fields. The final term is responsible for the energy transfer between the signal and idler mode and is affected by the phase mismatch

$$\Delta k = 2k_p - (k_s + k_i) \tag{4.24}$$

where we disregarded the phase shift due the pump power that becomes important when the nonlinear process is extend over long distances or if a large bandwidth of the process is required. For the same reasons the second term in Eq.4.22 and 4.23 is neglected. Usually the intensity of the pump is much larger than the other fields and in the case of $|E_s| >> |E_i|$ the power coupling from the idler to the signal in Eq.4.22 can be ignored. In conclusion, the third term of Eq.4.23 is directly responsible for the generation of the idler wave and depends quadratically with respect to the pump field and linearly with the signal field.

4.4 Experimental demonstration of third-order frequency conversion

Optical nonlinearities can be enhanced decreasing the cross-section of waveguides[230], in which the small mode area A_{eff} increases the effective nonlinearity γ of structures

$$\gamma = \frac{n_2\omega_c}{A_{eff}c} \tag{4.25}$$

where ω_c is the pump frequency, c is the speed of light in vacuum and

$$n_2 = \frac{3}{cn^2\epsilon_0}\chi^{(3)}_{iiii} \tag{4.26}$$

is the Kerr coefficient[6] where all the four fields are polarized in the same direction i. Thanks to the tight confinement, efficient frequency conversion was demonstrated in silicon using millimetre long high-confinement waveguides together with a broad conversion bandwidth[221], provided a tailored anomalous group velocity dispersion (GVD) of the structures.

Further improvements in both conversion efficiency and footprint of devices can be achieved implementing ring resonators[220]. When the electromagnetic field is resonant with the cavity, it is subjected to a field enhancement (FE) that, given the nonlinear nature of the process, increases the conversion efficiency η of the nonlinear effects. For a resonator of length L, in which the field is attenuated by a factor $a = \exp(-\alpha L/2)$ for a round trip, the FE is dependent by the field coupling from the bus waveguide to the ring σ, and the transmitted field through the bus waveguide τ (with $\sigma^2 + \tau^2 = 1$), by

$$FE = \left| \frac{\sigma}{1 - \tau \exp(-\alpha L + jkL)} \right| \tag{4.27}$$

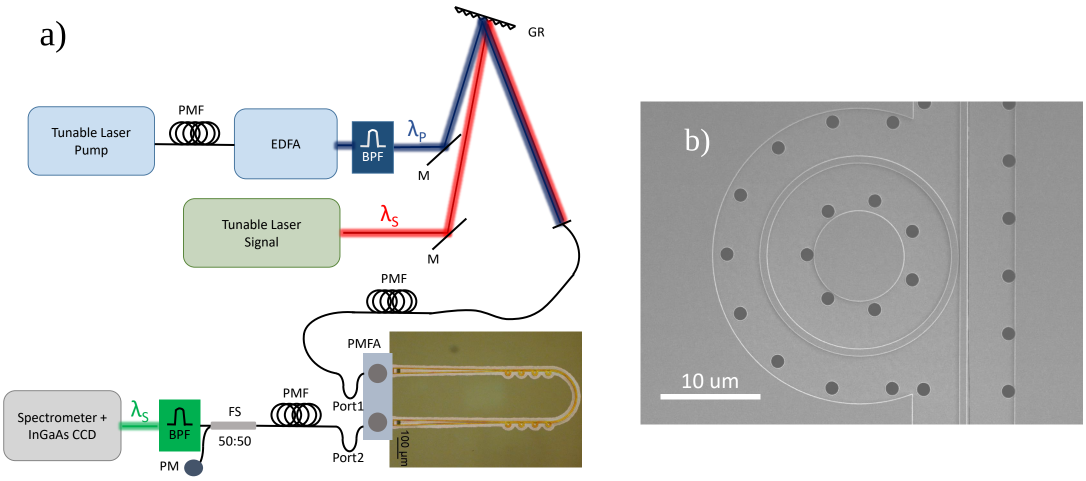

Figure 4.4: a) Experimental setup for the characterization of the FWM process with an optical micrograph of the sample. PMF, Polarization Maintaining Fiber; EDFA, Erbium-Doped Fiber Amplifier; BPF, Band Pass Filter; GR, Grating Reflector; M, Mirror; PMFA, Polarization Maintaining Fiber Array; FS, Fiber Splitter; PM, Power Meter. b) SEM view of the multimode ring resonator.

where k is the wavenumber. The maximum FE is reached when the field wavelength is resonant with the cavity ($kL = 2m\pi$, with m integer) and the resonator is in critical coupling condition ($a = \tau$). Satisfied the previous conditions and in the ideal case of $\sigma << 1$ (low loss regime), the FE can be linked directly to the quality factor (Q) of the cavity

$$FE = \sqrt{\frac{2Q}{k_p L}} \tag{4.28}$$

By looking at Eq.4.25 and 4.28, an increase in the Q factor and a reduction in the modal volume of the resonator correspond to the enhancement of the field inside the photonic structure.

The SiC ring used for this experiment was fabricated as reported in the previous chapter, with a small radius of $10\mu m$ and a multimode structure. The ring was close to a critical coupling condition (Fig.4.6) with a loaded Q of ∼7400. Due to the propagation loss of $36.6dB/cm$, we used the un-approximated model to describe the FWM process[220], in which

$$\eta = |\gamma P_p L'|^2 \; FE_p^4 \; FE_s^2 \; FE_i^2 \tag{4.29}$$

$$L'^2 = L^2 \exp(-\alpha L) \left| \frac{1 - \exp(-\alpha L + j\Delta k L)}{-\alpha L + j\Delta k L} \right|^2 \tag{4.30}$$

where FE_i is the field enhancement (Eq.4.27) for the pump, idler and signal and

$$\Delta k = 2k_p - k_s - k_i \tag{4.31}$$

is the phase mismatch due to the dispersion of the structure. By performing the linear characterization of the sample[199] , we retrieved a FE of 4.37 for the pump and signal, and a reduced value of 4.27 for the idler. Even though the wavelengths of the signal, idler and pump met three successive resonances of the cavity, the phase mismatch accumulated in the $\sim 26nm$ bandwidth caused the difference in FE value for the idler.

The experimental setup used for the characterization of the FWM process is depicted in Fig.4.4.(a) where the pump ($1549.99nm$) and signal ($1563.42nm$) were gathered in the same polarization maintaining fiber using a reflective diffraction grating;, additionally providing more than $-45dB$ noise reduction at the idler frequency. The pump power was increased using a Pritel polarization maintaining erbium-doped fiber amplifier, whose excess noise was filtered using an additional band pass filter. The combined pump and signal waves were injected in the SiC waveguide using a polarization maintaining fiber array and apodized grating couplers (with $\sim -10dB$ coupling efficiency). In the output, the pump and signal were attenuated by the spectrometer and a band pass filter, meanwhile the generated idler intensity was measured with an InGaAs CCD array. A power meter was used to guarantee that the pump and signal were resonant with the ring resonator during the experiment. In Fig.4.4.(b) is reported a SEM view of the multimode SiC ring resonator.

For a pump power of $1.2mW$, the measured idler power at the ring position is reported in Fig.4.5. The red curve represents the idler peak with both signal ($70\mu W$) and pump on resonance, meanwhile the black curve was measured with the signal laser switched off and just the pump on resonance. The power generated when the signal laser is switched off is attributed to Raman gain in the SiC ring resonator and its power dependence is reported in Fig. 4.7.(b).

In crystalline 3C SiC, Raman signals due to the main vibrational modes[231] are expected at $\sim 200nm$ far from the pump wavelength. However, the high density of crystalline defects at the SiC-Si interface[232] might be seen as an amorphous-like region that can

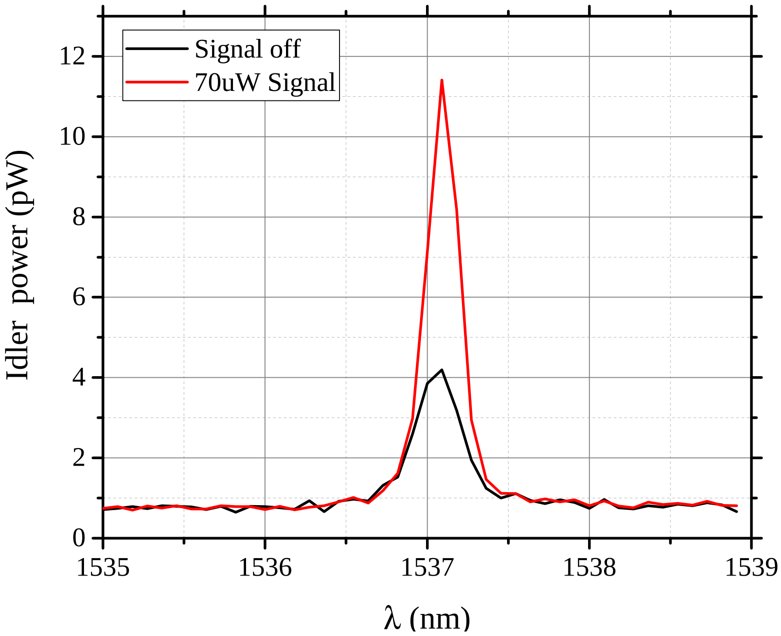

Figure 4.5: Power measured in the idler position for 1.2mW pump power on resonance with and without signal (red and black curve, respectively)

benefit of the FE in the resonator and generate a Raman field.

As depicted in the optical micrograph in Fig.4.4.(a), the sample was designed with eight different ring radius, each with a slightly shifted central resonance. This was made to overcome the fabrication tolerances and deliver one ring with a resonance within the tunability of the pump laser ($\sim 1.5nm$). In Fig.4.6 is reported the transmission spectrum showing all the resonances due to the ring resonators coupled to the same bus waveguide. The pump, signal and idler resonances, that belongs to the same ring resonator and are separated by a free spectral range, are highlighted meanwhile he other resonances shown in the figure result from the presence of other seven ring resonators coupled to the waveguide that do not contribute to the experiment.

In order to determine exactly the losses β between the fiber array and the ring used for the frequency conversion, we performed the experiment twice by inverting the input and output ports of the fiber array. With reference to Fig.4.4.(a), the pump injected inside the sample through the Port 1 (Port2) of the fiber array was attenuated by β_1 (β_2) at the ring position and corresponded to the FWM efficiency η_1 (η_2). Considering T the total transmission between the Port 1 and Port 2, and from Eq.4.29

$$\eta_1/\eta_2 = (\beta_1/\beta_2)^2$$
$$T = \beta_1\beta_2$$

we retrieved the input loss values of $-12.61dB$ and $-6.99dB$. This difference in losses between the two experiments is attributed to propagation losses and inhomogeneities

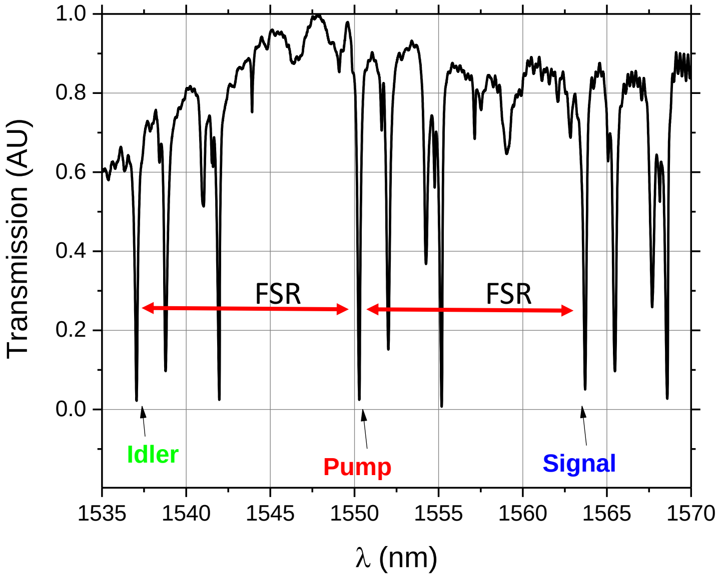

Figure 4.6: Transmission spectra of the sample used for the frequency conversion. In the figure, the pump, signal and idler resonances, that belongs to the same ring resonator and are separated by a free spectral range, are highlighted. The other resonances shown in the figure are due to the presence of other seven ring resonators coupled to the waveguide that do not contribute to the experiment.

deriving from the fabrication process.

The data points of the two experiments are combined together in Fig.4.7 by taking in to account the distinct β values. The FWM gain for different pump powers is reported in Fig.4.7.(a) where the corresponding values of the generated Raman (Fig.4.7.b) were subtracted. By fitting Fig.4.7.(a) with the nonlinear gain of Eq.4.29, we retrieved the nonlinearity of the structure $\gamma = 3.86 \pm 0.03 W^{-1} m^{-1}$. The nonlinear susceptibility can be estimated from Eq.4.25, in which[233]

$$A_{eff} = A_{NL} \iint_{-\infty}^{\infty} S_z \, dxdy \Big/ \iint_{NL} S_z \, dxdy \tag{4.32}$$

with A_{NL} the area of the waveguide cross-section and S_z is the Poynting vector parallel to the propagation direction. Using a mode solver, we calculate $A_{eff} = 0.558(\mu m)^2$, corresponding to $n_2 = (5.31 \pm 0.04) \times 10^{-19} m^2/W$. This value is in partial agreement with the estimated value for bulk crystalline SiC[227] of $4.9 \times 10^{-19} m^2/W$. The absence of a cladding able to participate to the FWM process is accounted in Eq.4.32, where only the field inside the SiC cross-section contributes to the modal area.

The Raman signal of Fig.4.7.(b) is fitted using a linear dependence with the pump power and we estimated a Raman gain in the ring of $(3.8 \pm 0.3) \times 10^{-10} W/W$. To the best of our knowledge, low energy measurements of heteroepitaxially-grown SiC thin films are

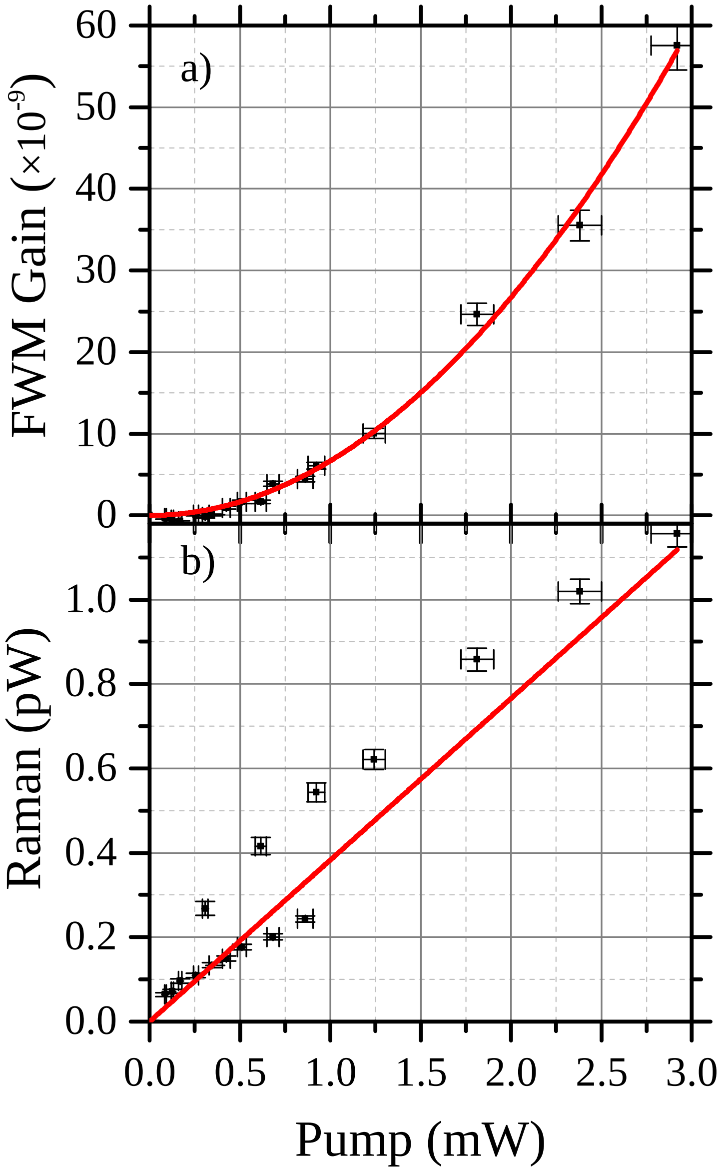

Figure 4.7: a) Experimental FWM gain (black points) and quadratic fit (red line). b) Raman signal generated from the pump power on resonance (black points) and linear fit (red line)

not reported in literature and the in-depth analysis of this effect is left to future works.

4.5 Conclusions

We report the demonstration of frequency conversion by four-wave mixing in 3C SiC ring resonators, fully integrated in an optical circuit composed of grating couplers, bus waveguides and mode converters. The tight confinement provided a high nonlinearity of the structure of $3.86\mathrm{W}^{-1}\mathrm{m}^{-1}$ while the use of the small radius ring resonator enhanced the nonlinear gain of ∼50dB compared to a straight waveguide of the same length. We achieved a conversion efficiency of 72dB at the low pump power of 2.9mW. The absence of two photon absorption at telecom wavelength does not limit the pump intensity, meaning that high conversion efficiencies are possible. The retrieved nonlinear refractive index $\mathrm{n}_2 = (5.31 \pm 0.04)10^{-19} m^2 W^{-1}$ is almost twice the value of $\mathrm{Si_3N_4}$ and comparable to many materials used for nonlinear photonics.

Chapter 5

Near-Infrared twin photon Generation in Si_3N_4 ring resonator

In this chapter I will discuss the photon pair generation in the near-infrared wavelength range in a *silicon nitride* (Si_3N_4) ring resonator. The main part of this work was carried out by Robert Cernansky while my responsibilities were the design of the grating coupler, the definition of etching and lithography parameters for the waveguide fabrication and experimental contribution throughout the project.
In the first section I will briefly introduce the generation of single photon pair by means of *spontaneous four wave mixing* (SFWM) and the characterization of such a source. The results from the optimization of Si_3N_4 grating coupler are discusses in Sec.5.2 meanwhile in the last section the experimental results of the single photon generation are presented.

5.1 Correlated photon pairs generation in ring resonators

In Sec.4.3, we discussed how the third order nonlinearity of the material can be used to generate an idler wave when a pump and signal propagate inside a nonlinear medium. Due to the presence of the signal, the process is often referred as stimulated FWM. The use of optical cavities or long propagation distances can be employed to enhance the efficiency of the process to the point that the pump field generates both signal and idler. In this case, the process is called spontaneous FWM (SFWM) and can be seen as a stimulated FWM effect where the signal is provided by vacuum fluctuations. This process can be used for the generation of correlated photon pairs, essential for applications in quantum technologies. The use of integrated structures can boost the SFWM process due to the enhanced electric field provided in waveguides and ring resonators.

To describe the spontaneous emission of photon pairs, some physical parameters developed in Sec.4.4 can be employed due to the shared nature of the nonlinear process. The complete quantum mechanical treatment of the generation of correlated photon pairs in ring resonator is outside the scope of this chapter and here we will introduce just the essential results developed in Ref.[122, 234].

The generation of the correlated photon pairs comes from the evolution of the squeezing Hamiltonian applied to a coherent pump state[235, 234]

$$|\Psi_{gen}\rangle = e^{\beta C^{\dagger}_{II}}|0\rangle|0\rangle \tag{5.1}$$

where

$$C^{\dagger}_{II} = \frac{1}{2}\int d\omega_s \; d\omega_i \; \phi(\omega_s,\omega_i) a^{\dagger}_s \, a^{\dagger}_i \tag{5.2}$$

contains the bipartite photons wavefunction that, in case of a CW pump, satisfies

$$|\phi(\omega_s,\omega_i)|^2 = \delta(2\omega_p - \omega_i - \omega_s) \tag{5.3}$$

for energy conservation. In Eq.5.1, $|\beta|^2$ represents the generation probability and, for single photon operations, is chosen $|\beta| << 1$. This corresponds to pump the nonlinear process with low power in order to achieve

$$|\Psi_{gen} >= e^{\beta C^{\dagger}_{II}}|0\rangle|0\rangle \approx |0\rangle|0\rangle + \beta|1\rangle|1\rangle \tag{5.4}$$

where we neglect all the following terms $\beta^2, \beta^3 \dots$ deriving from the complete Taylor's series of Eq.5.1.

Since FWM and SFWM share the same nature, even SFWM is subjected to the fulfilment of the phase-matching conditions of Eq.4.19. If we consider a small generation bandwidth, the mode effective index can be considered dispersion-less and the resonances of a ring resonator are equally spaced. Consequently, three resonances are naturally phase matched if we consider symmetric number modes for signal and idler with the respect to the pump. If the pump corresponds to the Nth mode, phase matching is therefore satisfied for an idler in the $(N-m)$th mode and a signal in the $(N+m)$th mode, with N and m integers. The power generated by SFWM from a ring resonator can be written

$$P^{SFWM} = (\gamma L P_p)^2 \, |FE|^6 \frac{\hbar\omega_p v_p}{2L}, \tag{5.5}$$

where v is the group velocity

$$v = \frac{c}{n_g} \tag{5.6}$$

with n_g the group index described in Eq.3.37. In Eq.5.5, $|FE|$ is the field enhancement (Eq.4.27), L the ring circumference and γ the waveguide nonlinearity, all described in

Sec.4.4. From the comparison of SFWM (Eq.5.5) with the classical FWM (Eq.4.29)

$$\frac{P^{SFWM}}{P^{FWM}} = \frac{\hbar\omega_p v_p}{2L|F(\tau)|^2}\frac{1}{P_s} \tag{5.7}$$

we can see that power generated in the stimulated and spontaneous process are equivalent considering a signal power of

$$P_s = \frac{\hbar\omega_p v_p}{2L|F(\tau)|^2} \tag{5.8}$$

Once the linear characterization has been complete, it is possible to calculate the scaling factor from the classical to the spontaneus process (Eq.5.7) and characterizing the quantum process starting from classical FWM.

The number of detected photon pairs (CC) generated from a ring resonator can be calculated from Eq.5.5

$$G_{SFWM} = \frac{P^{SFWM}}{2\hbar\omega_p} = CC\eta_s\eta_i \tag{5.9}$$

where $\eta_{i/s}$ accounts the total losses from the ring resonator to the detector for the idler and signal, respectively. In addition to the presence of losses, other effects such as two photon absorption [87] or Raman [236] can alter the number of coincident photons and an important figure of merit is the *coincidence over accidental* (CAR)[237] ratio

$$CAR = \frac{CC}{AC}, \tag{5.10}$$

where the accidental photons (AC) are the background coincidence, emitted randomly in time. This can be described by

$$AC = R_s R_i \Delta T, \tag{5.11}$$

where

$$R_s = n_s + G_{SFWM}\eta s + dc_s \tag{5.12}$$

$$R_i = n_i + G_{SFWM}\eta i + dc_i \tag{5.13}$$

are the count rate at signal and idler. Other than the generation rate given from Eq.5.9 and the efficiency $\eta_{s/i}$, these are formed by the dark counts of the detector $dc_{s/i}$ and $n_{s/i}$ represents any noise generated by experimental imperfections. The CAR value is strongly affected by the time window ΔT since for a longer time the number of accidental increases[88]. In experiments where $n_s \simeq 0$, the CAR has a well defined power dependence: for low pump powers the CAR is limited by detector dark counts meanwhile for high pump powers the two photon approximation of Eq.5.4 is not satisfied.

5.2 Si_3N_4 grating coupler optimization

The number of photons coincidences measured at the detector depends on how efficiently it is possible to outcouple the generated photons from the sample. In the wavelength range below 1000nm, thanks to the use of silicon as active medium, this problem can be overcome with the integration of single photon avalanche photodiode inside the sample even though the layout complexity increases considerably and, so far, the integration with waveguides has never been demonstrated. Efficient grating coupler can be used additionally to inject the pump power more easily, allowing the use of cost-effective lasers. Using the same tools reported in Sec.3.3.2, I optimized two kinds of Si_3N_4 grating coupler, both surrounded by SiO_2 cladding and index matching oil in order to avoid Fresnel reflection at the fiber end face. The Si_3N_4 refractive index used in the simulation is 2 and can be considered constant for both the wavelengths treated in this section (near-infrared and telecom range). The first scheme consists of an apodized grating coupler where the position and size of each post were optimized using the algorithm developed in Sec.3.3.2. This scheme benefits of the Si substrate that can be used as back reflector and consequently to improve the directionality of the scattered light (Eq.3.53), provided that the BOX thickness allows constructive interference between the reflected and incoming fields (BOX=2.086μm of thermal SiO_2). The CE obtained at 785nm for a waveguide thickness of 400nm is ∼-4 dB that is better than 3 dB with the respect to the optimized uniform grating coupler (Fig.5.2). The etch depth of the grooves is 400nm, allowing the use of one step of electron beam lithography to fabricate the whole optical circuit.
The second scheme takes advantage of the higher refractive index of Si posts realized on top of the Si_3N_4 waveguide, as reported in Fig.5.1, to enhance the light scattering. The Si posts can be fabricated after the realization of the waveguides, by depositing an etch stop layer of SiO_2 (50nm thick) and 200nm of amorphous Si. The size and distance of each post were apodized and can be realized by means of a second electron beam lithography step. Finally, the SiO_2 top cladding can be deposited. Even though silicon absorbs at 785nm, the CE is -1.4dB (Fig.5.2) with a really large 3dB-bandwidth.
The use of Si as grating material to enhance the CE in Si_3N_4 waveguides has never been proposed and I conceived it with the aim to achieve the same CE experienced with Si grating coupler. This design requires only an additional step of electron beam lithography and the presence of an etch stop layer grants a robust fabrication procedure. A similar design was proposed for Si photonics using heteroepitaxially-grown Germanium as grating medium[238]. However, this design requires a total of three electron beam lithography steps, it does not provide an etch stop layer and the CE is lower than the one achieved employing only Si apodized grating coupler[86, 85].

Considering the same waveguide thickness of 400nm, the CE at 1550nm of optimized uniform grating coupler improves compared to 785nm and there is little difference with respect to the apodized case (Fig.5.3). Gratings were also simulated with varying etch

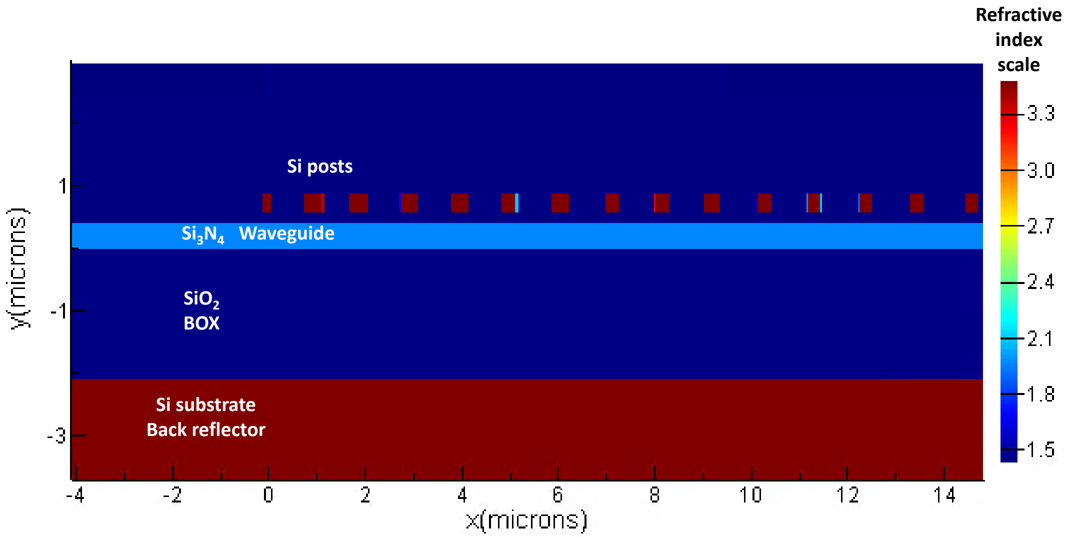

Figure 5.1: Silicon-assisted grating coupler for Si_3N_4 waveguide scheme. The coupler benefits of refractive index Si posts and a silicon back reflector.

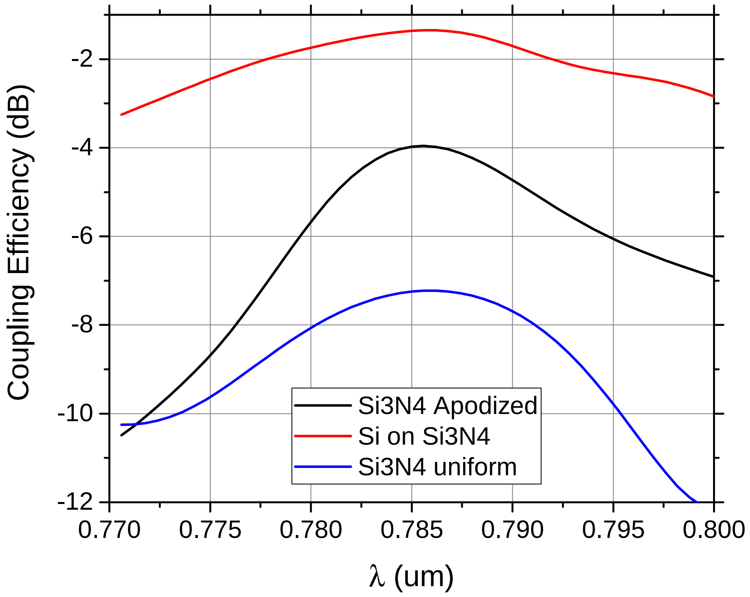

Figure 5.2: Coupling efficiency for different grating couplers at 785nm

depths, providing the highest CE (350nm). The best grating coupler scheme we simulated included a gold back reflector together with the apodized positions and sizes of the posts. In this case, the CE reaches a value of ∼-1dB. Even in the telecom range it is possible to implement the silicon grating coupler scheme of Fig.5.1 by optimizing all the parameters. The etch stop becomes 200nm meanwhile the silicon post thickness increases to 276nm. As reported in Fig.5.3, the CE of this scheme is 0.6dB worse than the apodized grating coupler with gold back reflector.

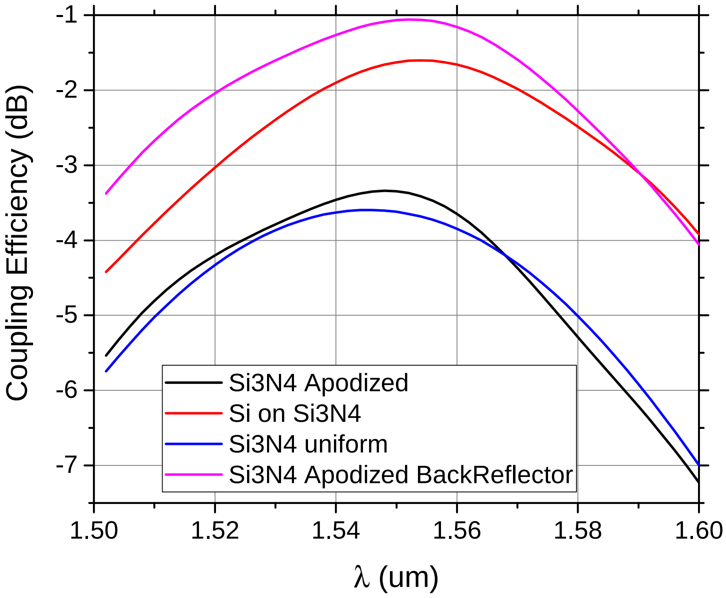

Figure 5.3: Coupling efficiency for different grating couplers at 1550nm

5.3 Experimental results

The development of photonics quantum technologies has relied mainly on Si as material platform[239, 79], due to the high scalability, high refractive index and transparency in the telecom range. This well matched with the need to work at telecom wavelength, where the low loss propagation in silica fiber provided a straightforward platform to implement quantum cryptography[240, 241]. In the telecom wavelengths, due to the lack of competitive semiconductor alternatives, the only efficient platform to detect single photons are superconductive single photon detectors[242] that restrict the temperature operation at a few kelvins. This, however, in the most common case of centrosymmetric materials, conflicts with the use of thermal phase shifters greatly used to change the phase of quantum states, since the termo-optic coefficient decreases at low temperature[243].

If the quantum operations are moved in the nearinfrared wavelengths, it is possible to

use Si as active medium which provides efficient single photon avalanche photodiodes. These detectors are cost-effective, work at room temperature with low dark counts, perform with high efficiency and offer a time resolution of tens of picoseconds[244]. Furthermore, single photons in these wavelengths can be used to interface solid state quantum memories[245, 246] as well as atomic systems[247]. The wide bandgap of Si_3N_4 ($\sim 5eV$)[248] allows operations in nearinfrared without incurring in multiple photons absorption, that limits the generation rate of photons pairs[87]. Furthermore, efficient nonlinear effects have already been demonstrated in Si_3N_4 integrated structures[148, 249] thanks to high Q factor[193] and moderate $\chi^{(3)}$ nonlinearity.
Waveguides in Si_3N_4 are fabricated as reported in Fig.5.4. The Si wafer is oxidized for 2.086 μm in order to form the optimal BOX thickness and to have a high quality bottom cladding. Successively, the Si_3N_4 layer is deposited by PECVD with low contents of SiH_4, to avoid the formation of Si clusters. The waveguides are patterned using electron beam lithography to expose the positive resist CSAR62 and etched with the ICPRIE. A top cladding of SiO_2 is deposited by PECVD usingh TEOS as precursor. Excluding the first wet oxidation step, all the remaining fabrication processes are performed at 350° and therefore, the realization of the Si_3N_4 waveguides is CMOS compatible.
The optical circuit used for the photon pair generation is reported in Fig.5.5.(a) where

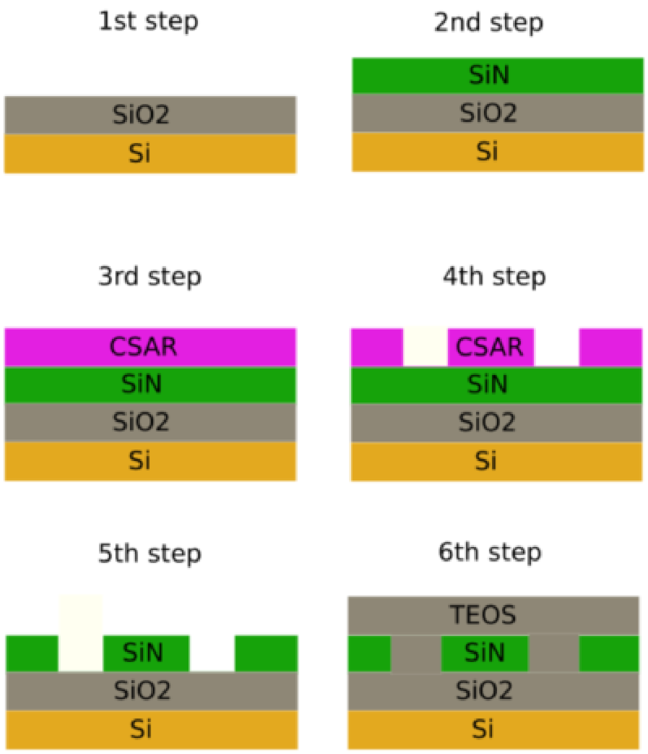

Figure 5.4: Fabrication steps of Si_3N_4 waveguides

in the optical micrograph is possible to see two rings. These rings have slightly different radius in order to ensure that at least one resonance is within the tunability of the pump laser, since the low radius of $19\mu m$ (Fig.5.5.b) provides a FSR of $\sim 2.5nm$. In

Fig.5.5.(d), is reported the transmission measurement of the ring used for the nonlinear process, showing an intrinsic quality factor of 270,000 corresponding to propagation loss of 2.6 dB/cm. The SEM image of Fig.5.5.(c) shows the apodized grating coupler whose simulated CE is reported in Fig.5.2.

The experimental setup used for the coincidence measurements is reported in Fig.5.6 and consists of a first filtering stage, the photon pair generation and the signal and idler photons measurement. The DFB laser at 785nm has a signal to noise ratio of 40 dB and additional noise reduction (60dB) is provided with a reflective diffraction grating. After the filtering, the noise-free pump is coupled to the sample by a high NA objective lens in free space to avoid the use of optical fibers that may introduce Raman photons. The ring resonator provides 11.6 dB attenuation of the pump since the ring is close to critical coupling with the waveguide. The pump and the generated photons are outcoupled with the apodized grating coupler. Finally, the signal (777.5nm) and idler (792.5nm) are separated thanks to a second reflective diffraction grating and the residual pump power is completely removed in both arms thanks to additional band pass filters.

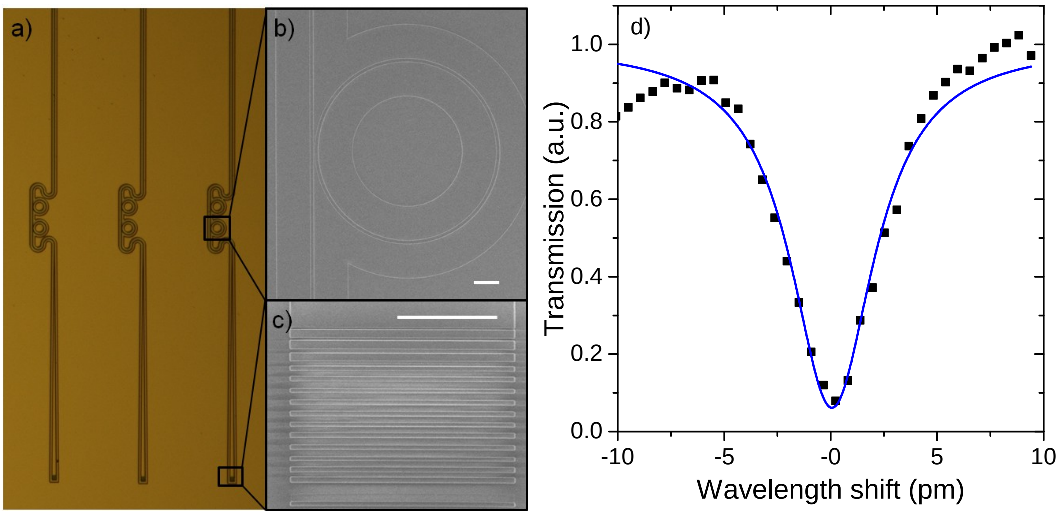

Figure 5.5: a) Optical micrograph of the sample; b) and c) SEM images of the ring resonator and the apodized grating coupler (scale bars of 5 μm). d) Transmission measurement of the undercoupled ring chosen for the photon pair generation, showing an intrinsic quality factor of 270,000.

The silicon avalanche photodiodes used to measure the signal and idler photons are connected to a time-correlated single photon counting electronics to perform coincidence measurements. Whenever two photons in both arms arrive within the same time window, a coincidence count is recorded. The coincidences histogram for a pump power of 1.68mW is reported in Fig.5.7, where it is possible to identify a clear coincidences peak due to the arrival of the generated photons, over a constant background due to accidental photons. The coincidences peak distinguishes in this way the photons deriving from the nonlinear process from the randomly photons caused by noise and the width of the

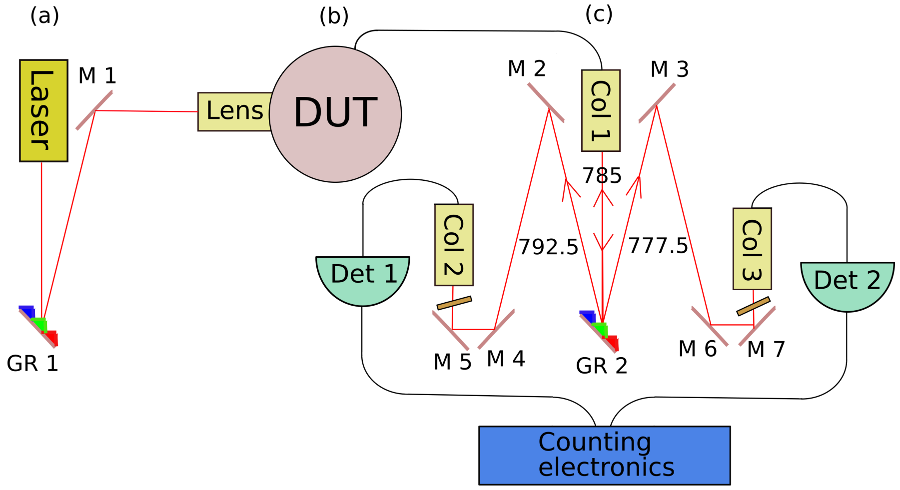

Figure 5.6: Experimental setup for the characterization of the source. On the left is shown the scheme used to filter the excess noise of the pump laser. In the second part the correlated photons are generated and the third part of the setup is used to measure the coincidences.

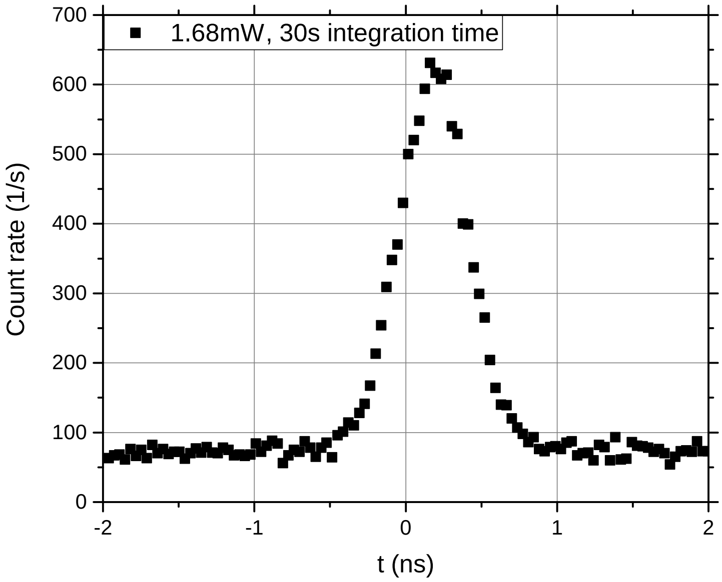

Figure 5.7: Coincidence histogram for 1.68mW pump power. The measurement was integrated for 30s with a time window of ∼1ns.

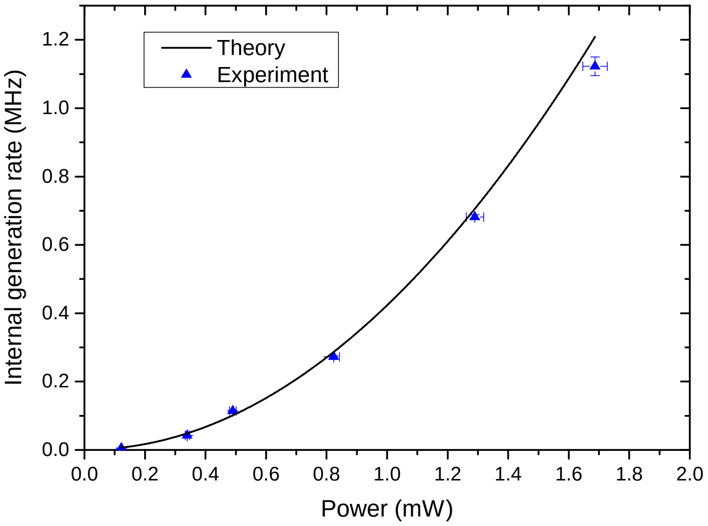

Figure 5.8: The measured count rates for different pump powers considered inside the sample (blue dots). The data is fitted with Eq.5.9 (black line).

peak is due to the time response of the detector (350ps). The signal and idler photons measured at the detectors are subjected to inefficiencies of the setup that decrease the count numbers of 19.4dB and 18 dB, respectively, compared to the numbers initially generated at the ring resonator. In Fig.5.8, it is reported the retrieved generation rate at the ring position versus the pump power. The experimental data (blue dots) follows the quadratic behaviour that is expected from Eq.5.9. The fitting curve (black line), calculated with the common value of the nonlinear susceptibility of Si_3N_4, is in good agreement with the experimental data.

The power dependence of the accidental coincidence is reported in Fig.5.9.(b), where the linear behaviour can be attributed to the presence of spontaneous Raman gain in the Si_3N_4 layer. The coincidences deriving from the Raman photons can not be totally distinguished from the correlated photons generated from SFWM. This affects strongly the measured CAR (Fig.5.9.a), where at low pump powers is mainly limited by the coincidence due to spontaneous Raman generation and dark counts meanwhile at high pump power the multi-photon generation compromises the source. Furthermore, the ring used for this experiment is in undercoupled condition and, even though the transmission is low at resonance (Fig.5.5.(d)), this may affect the heralding efficiency[250].

5.4 Conclusions

In this chapter, the correlated photons pairs generation in the nearinfrared is demonstrated by means of SFWM in CMOS compatible Si_3N_4 ring resonators. The large Q factor granted a maximum generation of ∼1.2 MHz inside the sample at low pump

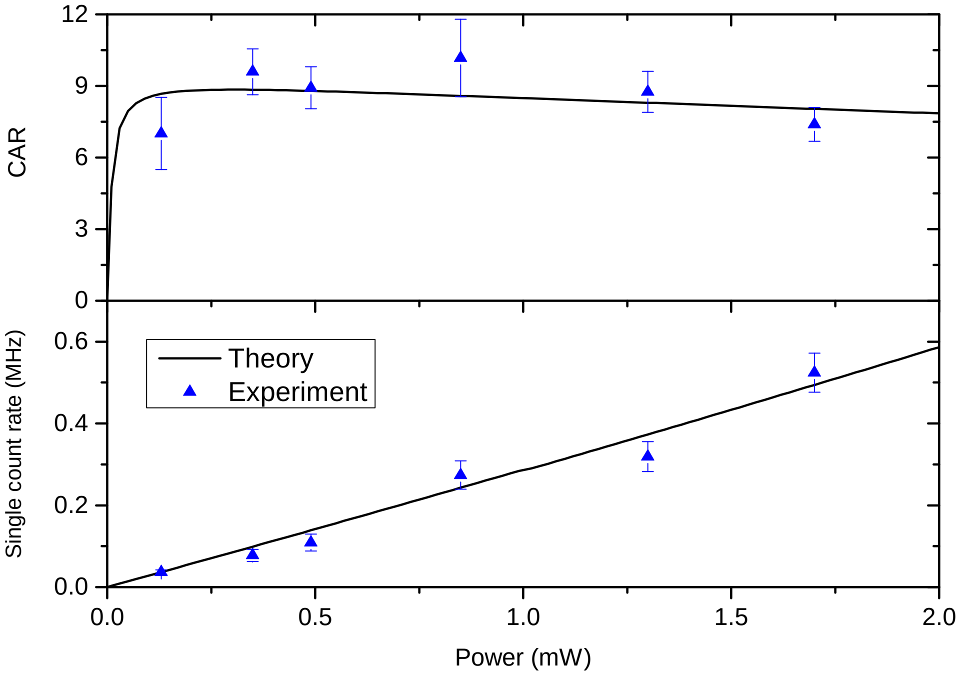

Figure 5.9: a) CAR measurement in function of the pump power (blue dots) and theoretical fit (black line). b) Count rates due to spontaneous Raman of the Si_3N_4 (blue dots) and linear fit (black line). The time window was 36ps.

power of ∼1.6mW meanwhile the highest CAR is measured to be around 10. The high bandgap of Si_3N_4 prevents multiple photons absorption from hampering both CAR and generation rate. However, CAR might be improved by using a different coupling condition for the ring and by placing the idler and signal frequencies in the minimum of the Si_3N_4 Raman gain. This platform could benefit from efficient silicon single photon detectors integrated in the same sample or to interface quantum emitters performing in this wavelength range.

Chapter 6

SiC Photonic Crystal Cavities

In addition to the outstanding nonlinear optical characteristics, SiC offers another essential functionality for quantum technology applications since it implements quantum emitters that can be used as stationary qubit or as on-demand single photon source. In this chapter I am going to introduce briefly the possibilities provided from the integration of these quantum emitters in photonic crystal cavities (Sec.6.1), realized in 3C SiC. My involvement in this project was mainly limited to the substantial fabrication work, deriving from the complexity of SiC processing, meanwhile my colleague Ioannis Chatzopoulos managed all the other aspects concerning the realization and characterization of 3C SiC photonic crystal cavities. In Sec.6.2, some experimental results from the linear characterization are presented.

6.1 Light Matter Interaction

In order to be effective, quantum emitters have to interact efficiently with photons. In fact, optical fields can be used to initialize these two-level atoms in a desired quantum state or to carry out quantum states readout. In more complex systems, photons radiated from an isolated stationary qubit can be used to connect another one, to perform as a quantum node for interconnections or two-qubit gate operations[70]. To enhance the light-atom interaction, the emitter is usually placed inside a high-Q cavity and two different coupling regimes can be achieved: the weak and strong coupling.
The coupling conditions are described using three parameters:

- the cavity decay rate κ, described as

$$\kappa = \frac{1}{\tau_{cav}} \tag{6.1}$$

where τ_{cav} is the time in which the cavity lost $1/e$ photons. By looking at the definition of Q factor we employed in Sec.3.2, we can deduce that the cavity decay rate is dependent on the sharpness of the cavity resonance

$$\kappa = \Delta\omega \tag{6.2}$$

with $\Delta\omega$ the full width half maximum and therefore κ is directly connected to the cavity Q factor, since $Q = \omega/\Delta\omega$, ;

- the non-resonant decay rate γ that describes the amount of photons spontaneously emitted from the qubit. Even though several factors contribute to this parameter, we can imagine that γ increases if the photon absorbed can reach the ground level in a non-radiative manner or by means of vibrational states;

- the atom-photon coupling rate g_0 that describes the strength of the interaction between the emitter and cavity, expressed as

  $$g_0 = \left(\frac{\mu_{12}^2\omega}{2\epsilon_0\hbar V_0}\right)^{1/2} \tag{6.3}$$

  where μ_{12} is the dipole moment and V_0 is the cavity modal volume. In a similar way of Sec.4.4, the light matter interaction is increased as the modal volume of the cavity is reduced.

In the weak coupling regime $g_0 << (\kappa, \gamma)$ and therefore the photon emitted from the qubit is lost in free space before it is able to couple a second time with the qubit within the emitter coherence time. The emission rate is however affected by the cavity that enhances the density of states compared to the free-space value as described by *Purcell's enhancement*

$$F_p = \frac{W_{cav}}{W_{free}} = \frac{3Q(\lambda/n)^3}{4\pi V_0}\xi^2\frac{\Delta\omega_c^2}{4(\omega_0-\omega_c)^2+\Delta\omega_c^2} \tag{6.4}$$

where ξ is field overlap between the cavity and the emitter and $W_{cav/free}$ are the transition rates in the cavity and in free-space, respectively, provided from the Fermi's golden rules. In Eq.6.4, F_p is maximized when the frequency of the cavity mode ω_c and of the emitter ω_0 are resonant, otherwise the Purcell's effect can suppress the spontaneous emission. The Purcell's enhancement can be retrieved by measuring the time decays

$$F_p = \frac{\tau_{cav}}{\tau_{free}} \tag{6.5}$$

and, in the case where $\xi = 1$, it can be maximized by increasing the ratio Q/V_0.
On the other side, the strong coupling regime describes the case where $g_0 >> (\kappa, \gamma)$ and consequently the atom-cavity coupling rate is much faster than the decay rates. The photon emitted by the qubit, since is trapped inside the cavity, is reabsorbed multiple

times by the qubit itself before being radiated in free space. This reversible light-matter interaction is described in the framework of *cavity Quantum Electro Dynamics* (cavity QED) that implements the Jaynes-Cummings model. In this case, the wavefuction of the state describing the system is formed by the superposition between the cavity and photon states. The atom excitation energy and photon energy are not degenerate but new "dressed" states, separated by the Rabi splitting, are formed. For a complete treatment of the light matter interaction, the reader can refer to Ref.[251, 252].

In a similar way of NV center in diamonds, SiC hosts different point defects that can be used as resource for quantum information[253]. One of the most studied defect is called *divacancy* and it is formed by the removal of one Si and C atoms from the crystal structure (inset of Fig.6.1). The photoluminiscence of this emiter is reported in Fig.6.1, where it is possible to distinguish a strong *zero phonon line* (ZPL) at 1.1eV and a wide phonon sideband that extends to the telecom bandwidth. In analogy with diamond NV center, the energy level diagram (Fig.6.2) forms a Λ system where it is possible to take advantage of the auxiliary level A to perform the state readout and initialization. The spin levels also have demonstrated impressive coherence time[254] and their properties were widely studied[255, 128].

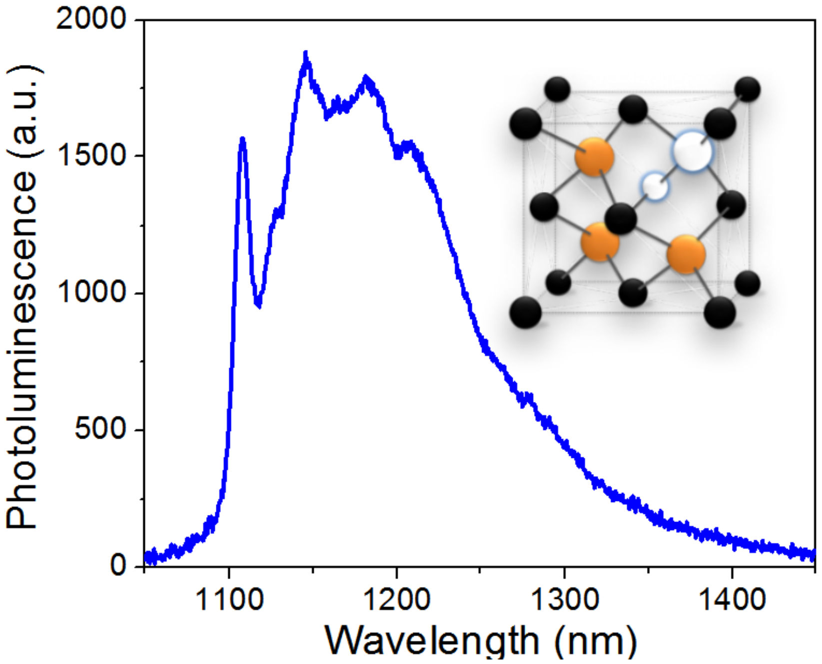

Figure 6.1: Photonluminescence of 3C SiC divacancies defect at 20K. In the inset, the SiC atomic structure in which one Si atom and C atom are missing, forming the quantum emitter.

As we discussed at the beginning of this section, the SiC divancancy needs to be placed inside a cavity with a high Q/V_0 ratio to interact efficiently with an optical beam. Photonic crystal cavities [256, 257] are an excellent solution to this task since they can

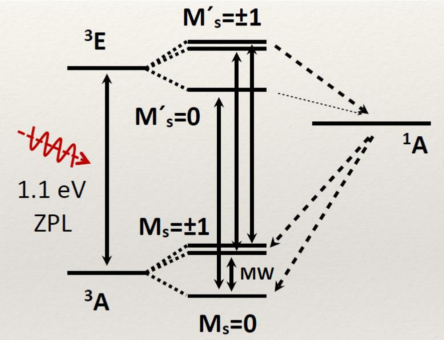

Figure 6.2: Energy level of divancy showing a three-level Λ system with a ZPL at 1.1eV. The spin properties can be used as additional resources for quantum information.

confine the field in a tight volume, comparable with $(\lambda/n)^3$, and can be interfaced with waveguide-based photonics. At the same time, in material with high refractive index, it is generally possible to achieve high quality factors. Photonic crystals are usually fabricated with periodic holes in a dielectric slab to form a periodic perturbation of the refractive index. In analogy with the periodic electronic potential in crystal lattice, where electronic bands are formed as direct expression of the Bloch wavefuctions, even a photonic crystal forms bands were the light propagation is allowed. The frequencies between two photonic bands, called photonic bandgap, define a region where the light propagation is not admitted and consequently the density of states in this region is null. An optical cavity can be formed by removing a number of holes in a photonic crystal structure where the cavity frequency falls in the photonic bandgap of the crystal (Fig.6.3). This generates a mirror-like effect, analogous to the Bragg reflector in optical fiber, and confines the mode in a small volume.

6.2 Realization and characterization of SiC photonic crystal cavities

The long-term aim of this project is to integrate SiC divacancy inside a SiC photonic crystal cavity and to achieve the strong coupling regime. Defects can be implanted with excellent spatial accuracy[128], using an electron beam resist to identify the areas where the defects have to be located. This is a relevant advantage over quantum dots, where the best optical-quality samples are grown randomly on the substrate. Furthermore, SiC divacancies suffer from a reduced inhomogeneous broadening compared to the quantum dot counterpart.

The short-term goal is to develop high Q photonic crystal cavities. This task can be decomposed in the design and fabrication problems. In the case we remove three holes in a 2D photonic crystal slab, we form a L3 cavity whose Q factor can be largely increased

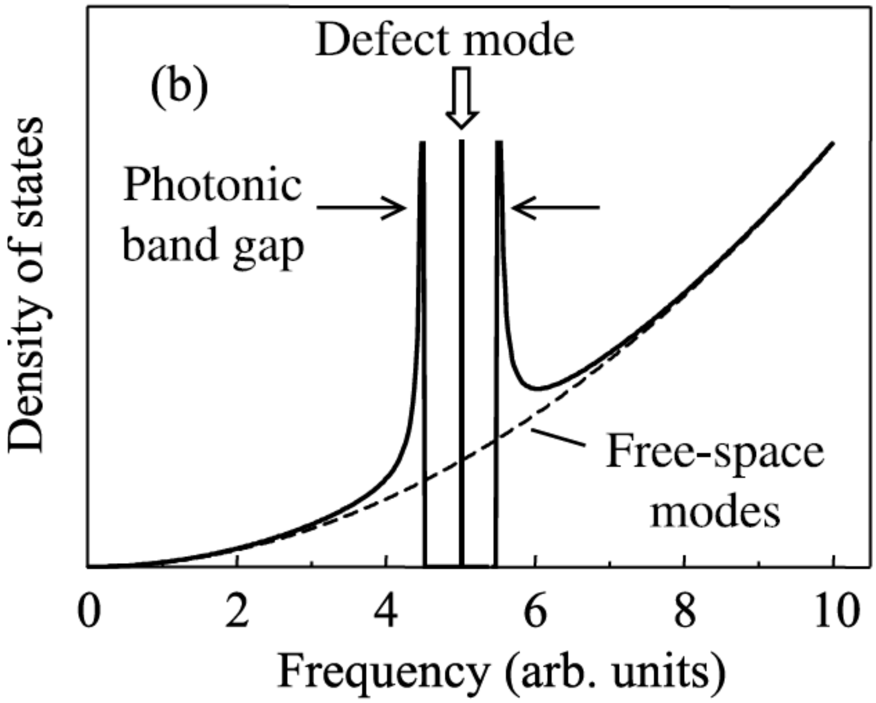

Figure 6.3: Typical density of state of a photonic crystal cavity with missing hole, generating a defect in photonic crystal structure[7].

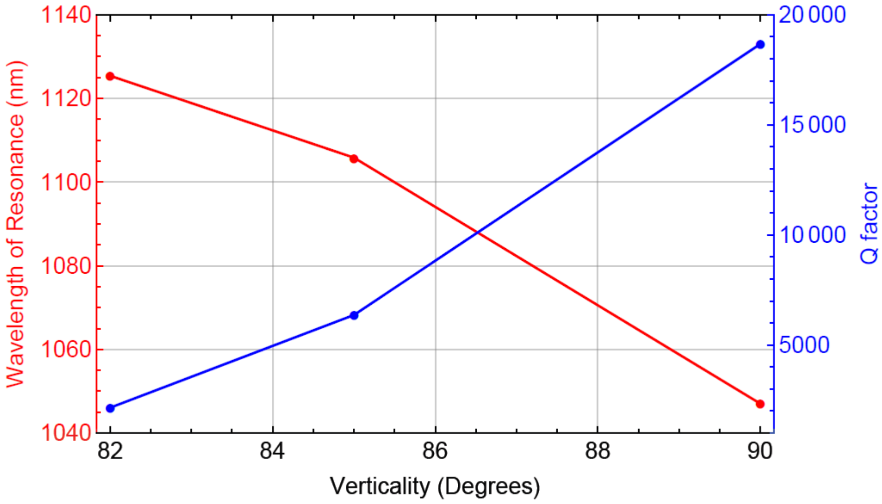

Figure 6.4: Q factor and mode frequency dependence on the sidewall angle.

by shifting and changing the size of the holes nearby the cavity[258]. This has been extensively studied in Si[259] and the optimization of these parameters requires several time-consuming FDTD simulations.

Even though SiC has a higher refractive index than a lot of photonic materials, the fabrication of satisfying cavities has been challenging due to the intrinsic resistance to plasma etching, as discussed in Chap.2. The Q factor is strongly affected by the etch anisotropy[164], as reported in the FDTD simulations of Fig.6.4, where the cavity central frequencies and Q factors are computed as a function of the sidewall angle.

In the Sec.2.5 is reported in detail the SiC fabrication process that, for the photonic crystal cavities, requires to one electron beam lithography step compared with the two needed for suspended waveguides. However, Al hard mask, SiC etch condition, electron beam resist and XeF_2 undercut are equally employed. The need for high verticality required a tailored etch timing in order to prevent the damage by sputtering of the hardmask hole edges, that would deteriorate the holes quality. The reduced plasma power prevented the ri-deposition of Al-hardmask residues on the hole sidewall. In Fig.6.5.(a) is reported a 3C SiC L3 cavity with a shifted position of the holes adjacent to the cavity in order to increment the quality factor. Even though some designs required considerable shrunk holes that could eventually cause a worsening of the etch, the process seems not to be affected by this as showed in Fig.6.5.(b). Additional fabrication results regarding the development of SiC photonic crystal cavities are reported in Appendix C.

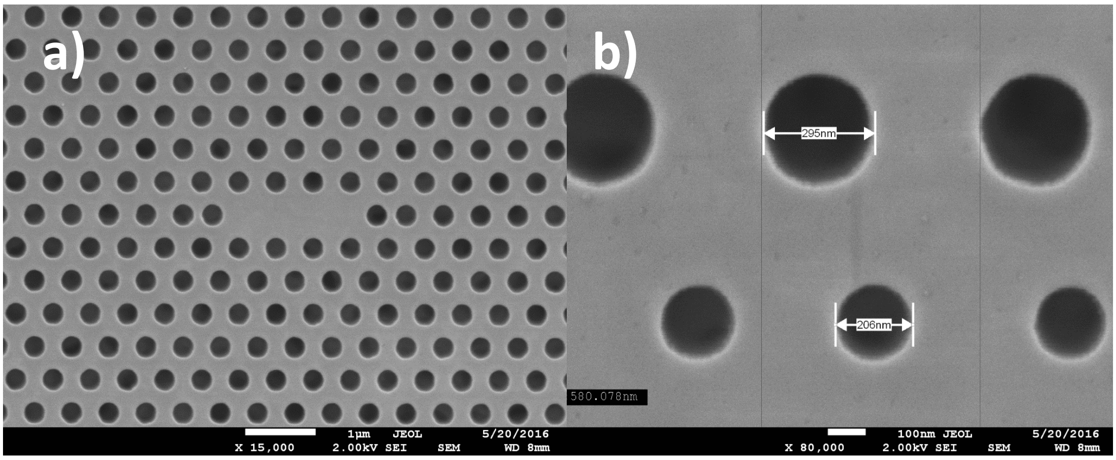

Figure 6.5: a)SEM picture of the realized photonic crystal cavity. b) Particular of the fabricated holes showing a near vertical etch.

The samples were measured with the experimental setup illustrated in Fig.6.6 which consists of a confocal microscope where the broad band source and cavity scattered light are in cross polarization. This allows to separate the light emitted from the cavity from the strong pump thanks to a polarization beam splitter. The source light can be focused on the cavity spatial position thanks to two galvanometric mirrors that accurately scan the sample plane. In Fig.6.7, it is reported the backreflected scattered light as response of the input Gaussian beam that is scanned throughout the sample surface. The mechanism

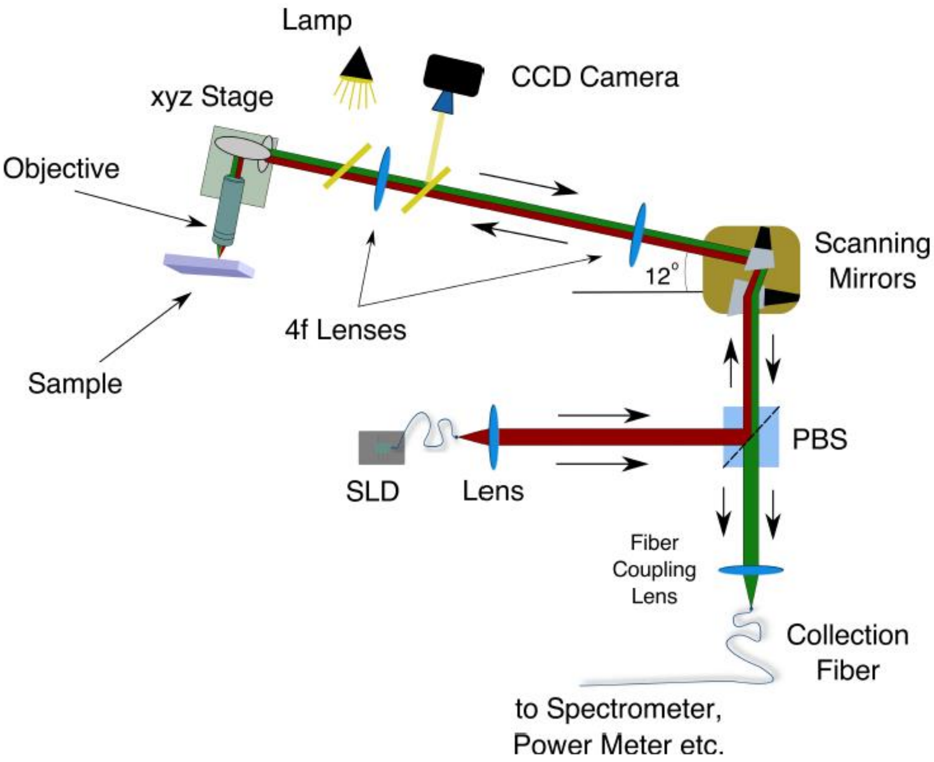

Figure 6.6: Experimental setup for the characterization of photonic crystal cavities.

leading to different scattering intensities, forming the spatial map of Fig.6.7, is caused by the refractive index contrast between the photonic crystal, the cavity and the SiC slab that results in different reflectivities. In this way it is possible to spatially locate the cavity. Once the cavity position is identified, it is possible to spectrally characterize the frequency components thanks to a spectrometer and a cooled InGaAs CCD. The spectral characterization is reported in Fig.6.8 where it is possible to identify a cavity mode at 1145nm with a Q factor of 4138. The Q factor value is the highest reached in 3C SiC and it is promising for the achievement of high Purcell's factors. As it is shown in Fig.6.8, the measurement of sharper resonance peaks is challenging with the current experimental setup since more experimental points are required to accurately fit the Lorentzian shape. Therefore, the experimental setup is going soon to implement a tunable laser which will allow a fine scanning of higher-Q cavities.

6.3 Conclusions

In conclusion, SiC divacancies offer an additional resource for quantum technology applications since they can be used as single photon gun or as computational node for flying qubits, if combined together with a resonant optical cavity. Additionally, spin

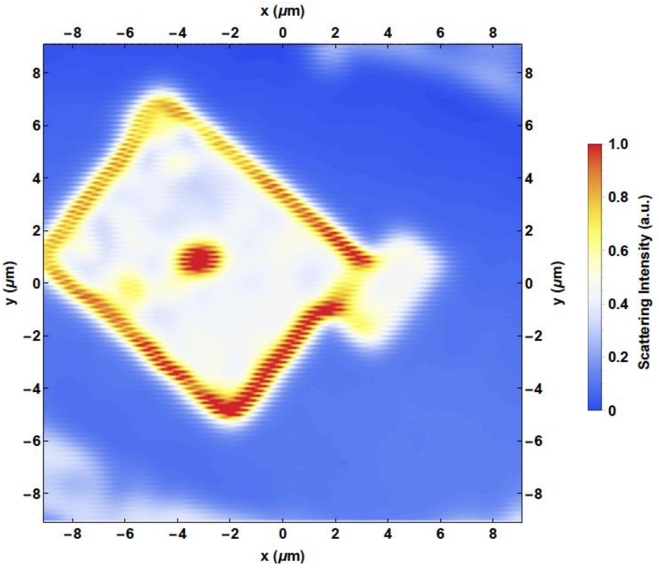

Figure 6.7: Scattering contour plot of the scanned sample.

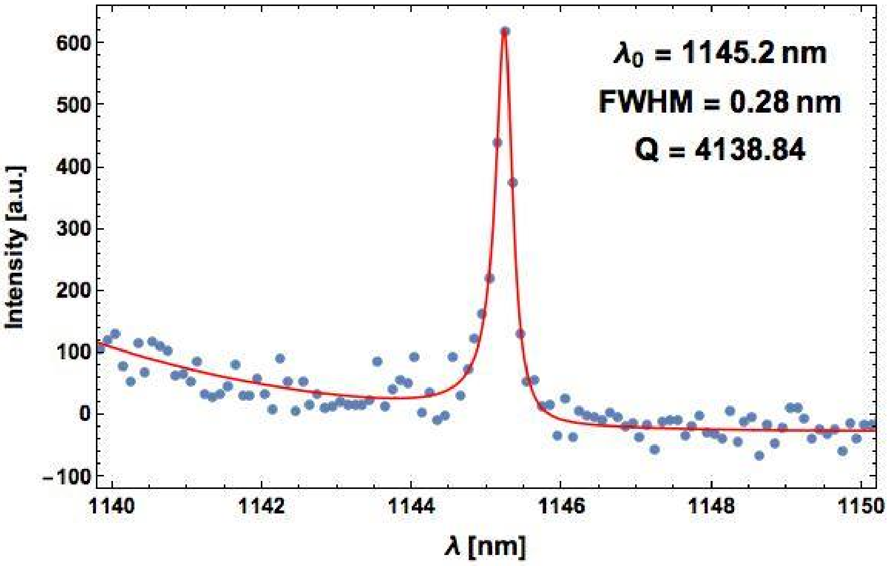

Figure 6.8: Spectral response of the measured cavity mode, showing a mode at 1145nm with a Q of 4138

properties of defects have shown remarkable long coherence time even at room temperature. Here, it is reported our efforts to develop in 3C SiC layer a photonic crystal cavity showing both a high Q factor and a small modal volume, both essential to achieve strong light-matter interaction with defects. In particular, Q factor of these cavities is strongly affected by the etched sidewall angle that was maximized thanks to a precise control of the sample fabrication. Measurements of the realized photonic crystal cavities by a confocal microscope setup provided a maximum Q factor value of ∼4100, that is the highest reported so far in literature for 3C SiC.

Chapter 7

SiC Surface Phonon Polariton Resonator

This chapter is dedicated to the project on Surface Phonon Polariton that was carried out in collaboration with Imperial College of London and the Quantum Theory & Technology Group of University of Southampton. The results reported here have already been published[10]. The involvement in this project consisted in the fabrication of pillar arrays in 3C SiC using a lift-off process and the vertical etch developed in Chap.2.

7.1 Surface Phonon Polariton

In Chap.3 we discussed about the confinement achieved in dielectric waveguides by means of total internal reflection and how it is possible to inject light inside guided modes using the scattering from periodic structures. As we have seen in Chap.4 and 5, small modal volume and high-Q cavities are the prerequisites to achieve efficient nonlinear process. These two parameters are also essential to enhance the radiation from emitters (Chap.6), described conveniently by the Purcell's factor. SiC grants an additional way to provide an exceptionally confined mode exploiting Surphace Phonon Polaritons (SPhP). These waves can propagate at the interface between SiC and air under the same condition characterizing the *Surface Plasmon Polariton* (SPP)[9, 260]

$$\mathrm{Re}(\epsilon_{II}) < 0 \tag{7.1}$$

$$|\mathrm{Re}(\epsilon_{II})| > \mathrm{Re}(\epsilon_I) > 0 \tag{7.2}$$

where $\epsilon_{I/II}$ are the permittivities of the two materials composing the interface and usually $\epsilon_I = 1$ (air). In the case of SPP, the surface waves are associated with coherent oscillations of electrons composing a metal since Eq.7.1 and 7.2 can be satisfied for frequencies below the plasma frequency. Materials that are composed from a partially

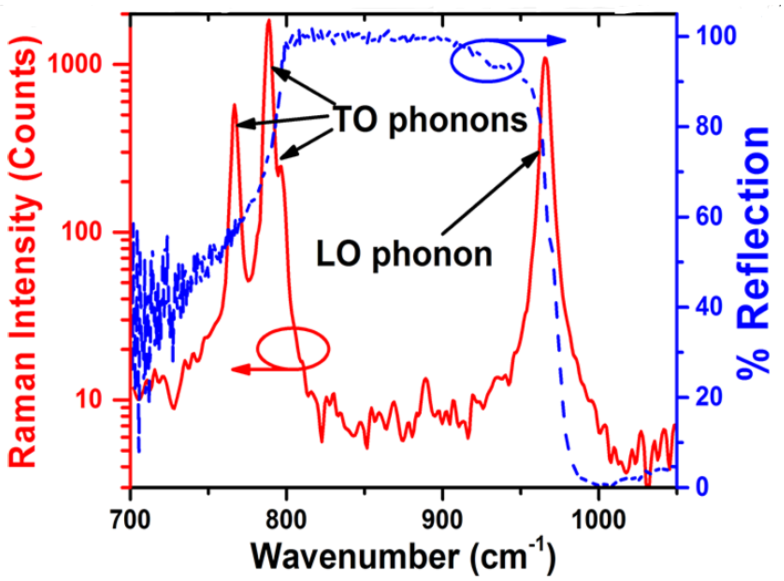

Figure 7.1: Red line represents the Raman scattering form 6H SiC substrate meanwhile the blue line represents the measured reflectivity. The image is taken from Ref.[8]

ionic bonding (referred as *polar dielectrics*) exhibit a similar behaviour in the frequency region between the longitudinal (LO) and transverse (TO) optical phonon modes, called *Reststrahlen Band*. In this case, the surface wave is composed by the coherent oscillations of charged atomic species composing the polar dielectric[8, 261]. Since in this frequency region Eq.7.1 and 7.2 are satisfied, the polar dielectric behaves as a perfect metal and consequently the reflectivity of a wave impinging the surface approaches 100 %. Between TO and LO frequencies, the presence of a negative refractive index induces high reflectivity of the material as represented from the blue dashed line of Fig.7.1, measured for 6H-SiC substrate[8]. The red solid line represents the phonon energies measured by Raman scattering that are overlapped onto the reflection spectrum within the Reststrahlen band. The end of high reflectivity region is achieved when the real part of the permittivity crosses through zero near the LO and TO phonon energies.
The dispersion of the permittivity in this frequency region can be conveniently described with the Lorentz model

$$\epsilon(\omega) = \epsilon_{\text{inf}} \left(1 + \frac{\omega_{LO}^2 - \omega_{TO}^2}{\omega_{TO}^2 - \omega^2 - i\omega\Gamma} \right) \tag{7.3}$$

where $\omega_{LO/TO}$ are the frequencies of the longitudinal and transverse phonon modes, respectively, and Γ accounts for the losses. With ϵ_{inf} is instead indicated the electric permittivity in the visible range. All the parameters for SiC in Eq.7.3 have already been reported in literature[262].

The wave propagates on the surface with a wavevector

$$(k_{sp}) = \frac{\omega}{c}\sqrt{\frac{\epsilon_{II}\epsilon_I}{\epsilon_{II}+\epsilon_I}} \tag{7.4}$$

with ϵ_{II} given from Eq.7.3. This corresponds to the dispersion reported in Fig.7.2, where the real part of the wavevector is plotted as function of the wavelength. The non-radiative part of the SPhP is on the right side of the light line meanwhile the left side is in the light cone, and therefore not guided. The two sides of the dispersion are divided by the discontinuity corresponding to the case of $\epsilon_{II} + \epsilon_I = 0$.

As it is shown from Fig.7.2, the confined modes do not cross the light line and, in order to be exited, require an additional momentum that can be provided with manufactured periodic structures. In a similar way of grating coupler (Sec.3.3.2), it possible to write a Bragg equation that allows the phase matching between the free-space and the SPhP modes[263]

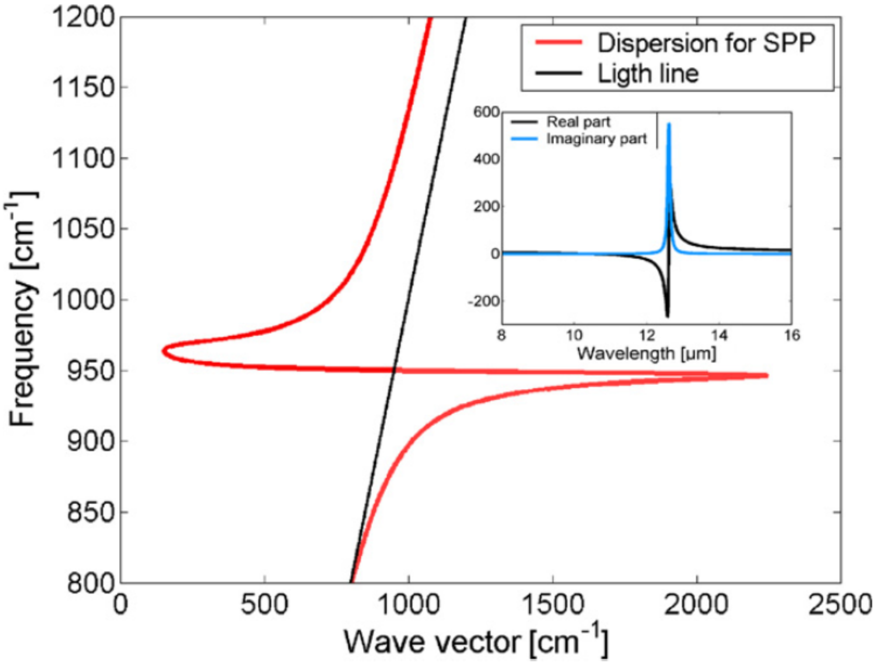

Figure 7.2: Dispersion of the wavevector propagating at the SiC/air interface (red line) and vacuum light line (black line). In the inset the correspondent permittivity is plotted. This picture is taken from Ref.[9]

$$k_{sp} = \frac{\omega}{c}\sin\theta_i + \frac{2\pi}{a}m \tag{7.5}$$

where θ_i is the incident angle, a the period of the structures and m is the diffraction order. The periodic structures have the function of shifting the light cone in frequency of the amount $2\pi m/a$ allowing the coupling with the surface wave.

Even though SPP and SPhP share the same high confinement, the lifetimes of optical phonos is in the picosecond range; orders of magnitude higher than the value for plasmons related to electrons in metal. This substantial difference impacts extremely the optical losses of the surface waves and consequently the development of resonators. In fact, highly localized modes made with SPhP resonators (SPhPR) can reach an equivalent Purcell's factor (Eq.6.4) of 6.4×10^7[8] that is three orders higher than the maximum theoretical Purcell's enhancement achievable with plasmonic structure[264].

7.2 Coupling between resonant and propagating SPhP

The development of a photonic platform based on SPhP requires the coupling between propagating and localized modes, to fully exploit the high field enhancement achieved in these structures.

In order to demonstrate the aforementioned coupling, we realized in a 9.7 μm-thick 3C SiC layer a series of arrays, each composed of 70×70 pillars equally spaced in the $x-y$ directions. Each array was characterized from a specific pitch defining the distance between the pillars, whose designed diameter and height are $1\mu m$ and $0.8\mu m$, respectively. The sample fabrication required an electron beam lithography step to pattern the pillars in a PMMA-MMA bilayer and subsequently the deposition of 120nm Ni hardmask by electron beam deposition. Once the lift-off process was completed, the sample was etched in the ICP RIE using the anisotropic etch developed as result of the Plackett-Burman experiment (Sec.2.3). The Ni hardmask was removed by immersing the sample in FNA acid for 20 minutes. The final pillar height was measured to be 811nm and in Fig.7.3.(c) is reported a SEM picture of a fabricated array.

Even though the realized pillars support a monopolar and transverse dipolar modes[8, 265], from now on we will consider just the monopolar mode whose electric field norm is reported in the inset of Fig.7.3.(b). In an analogous way to Chap.6, the periodicity of the pillar arrays results in Bloch eigenmodes whose dispersion for different pitch dimensions is reported in Fig.7.3.(b). In addition, the different periods of the arrays (between 5 and $7\mu m$) grant the satisfaction of the phase matching condition (Eq.7.5) for different wavevectors and allows consequently the coupling of the free space light with the surface wave. The crossing between the light cone and the propagating surface waves is also represented in Fig.7.3.(a), where the dispersion of the propagating SPhP waves are folded back at different frequencies as they meet the band edges (that are function of the array period) of the first Brillouin zone. Therefore, the arrays work simultaneously as couplers between free space light and propagating SPhP and as resonators. The deep confinement of the localized modes can be deduced from Fig.7.3.(d) where, as comparison, the surface wavelength is shown.

The dispersions of modes of Fig.7.3.(a-b) cross at some frequencies and, provided a non-zero field overlap, the propagating and localized modes couple with each other. In the case of a strong interaction, the dispersions of the two modes splits in two new branches

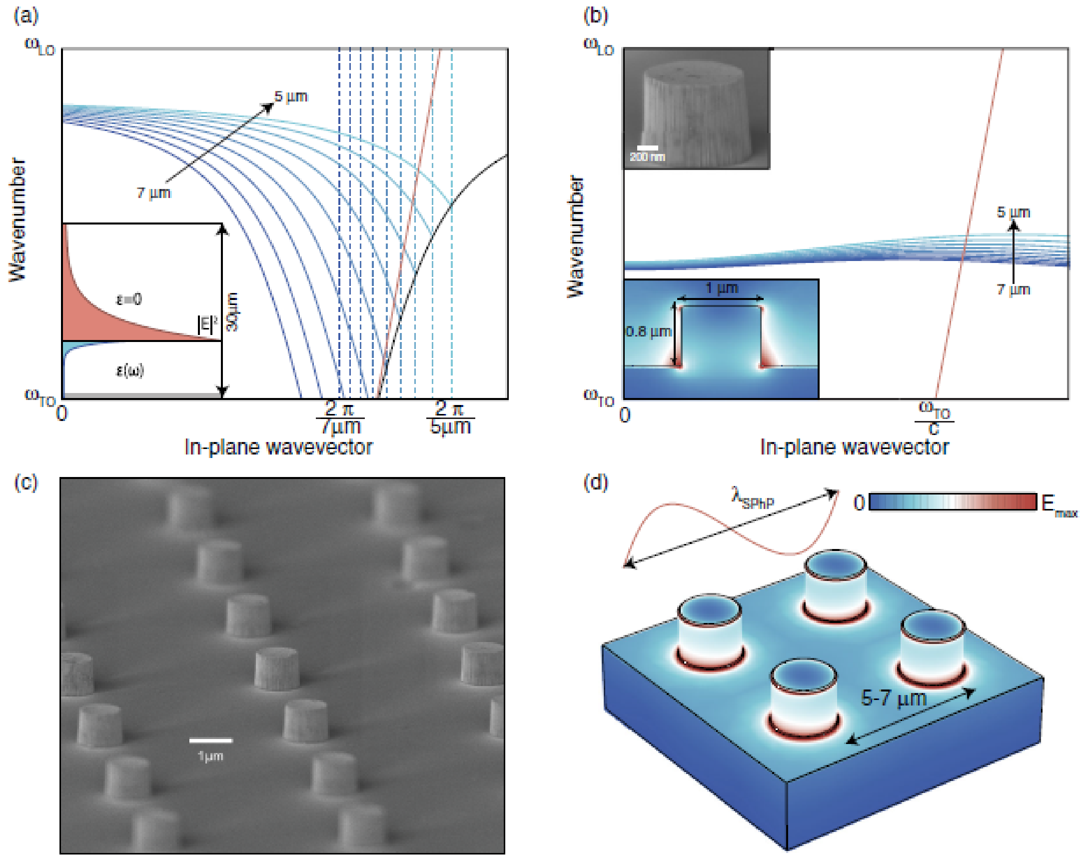

Figure 7.3: a) Dispersion of the propagating SPhP waves (solid blue lines) folded at the edge of first Brillouin zone (dashed lines) depending on the array pitch. The light line (red curve) outlines that the fundamental dispersion of the propagating SPhP (black curve) in non-radiative. In the inset is reported the electric field norm of the propagating surface wave showing that there is approximately no field at the SiC-Si interface (Si substrate is the grey region). b) Dispersion of the Bloch modes associated to the pillar resonators arrays. The insets show a SEM view of the single pillar and a mode cross-section of the electric field. c) SEM picture of the fabricated array of pillars. d) Electric field norm of the pillars modes showing the sub-wavelength nature of the resonator. This whole picture is taken from Ref.[10]

to form the so called *anti-crossing*. The new and old dispersion can be linked together following[10]

$$\omega_q^{\pm} = \frac{\omega_q^m + \omega_q^s \pm \sqrt{(\omega_q^m - \omega_q^s)^2 + 4g_0^2}}{2} \tag{7.6}$$

where g_0 describe the interaction strength, $\omega_q^{\pm}$ are the new frequencies computed from $\omega_q^{m/s}$, the original resonant and surface modes frequencies, respectively. Similarly to what discussed in Chap.6, in order to see strong coupling and hence anti-crossing, the interaction strength has to be greater than the losses of the two modes.

In order to measure the sample, we employed a FTIR microscope in reflectance mode

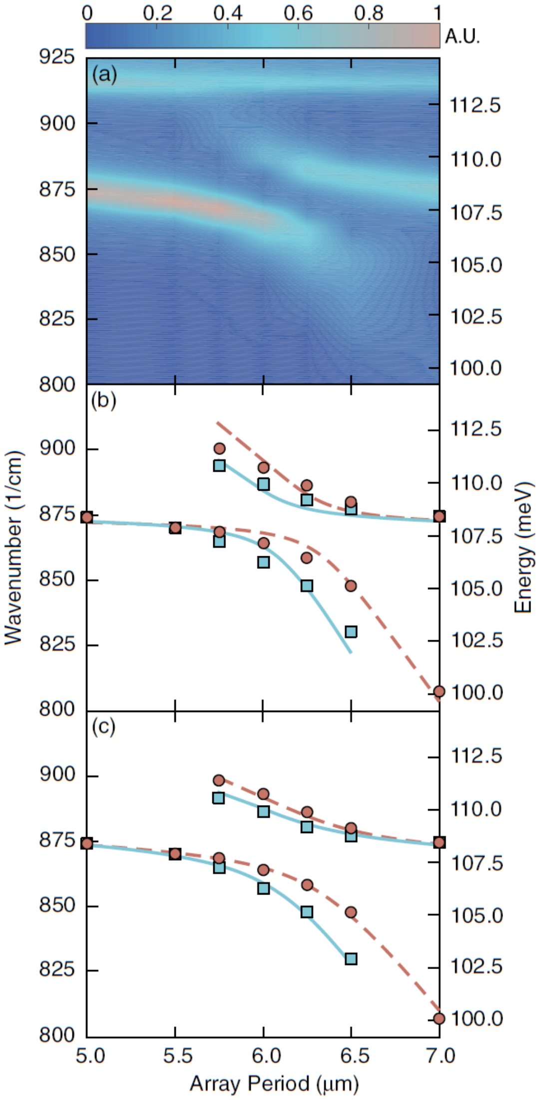

Figure 7.4: a) Measured reflectance map with a FTIR microscopy, showing the two branches composing the anti-crossing and the Transverse dipolar mode. b) The intensity peaks related to the two different angles are extracted: the blue dots represent the larger angle and the red the smaller one. The curves show the fit done considering standard values found in literature for the dielectric constant. c) The parameters describing the dielectric constant are fitted. This picture is taken from Ref.[10]

with the illuminating beam aligned along the principal axis of the resonator arrays. The tool provided illumination of the arrays with two different angles at the same time[10]. The raw reflectance map measured for all the arrays with different periods is reported in Fig.7.4.(a) where it is possible to see the expected anti-crossing and a higher-energy bipolar transverse mode at $\sim 113meV$. The retrieved peak positions composing the top and bottom branches of the anti-crossing, correspond to different angles as reported in Fig.7.4.(b), where the dots are the experimental peaks and the curves represent their fit. The red colour is associated with the smaller angle ($48.54^{\cdot}$, by fitting) meanwhile the blue colour is related to the bigger angle ($55.08^{\cdot}$, by fitting). The small error in the fit (in the order of 1 meV) can be significantly reduced by fitting additionally the dielectric constant parameters and the TO phonon frequency. As reported in Fig.7.4.(c), with just a change of 5% from the standard values found in literature, the anti-crossing is satisfyingly fitted.

7.3 Conclusions

The maximal value of the coupling parameter is $g_0 = 2.55meV$ and, consequently, the energy is exchanged coherently ~ 4 times between the propagating and localized waves before radiating, showing that this platform can be use as a base for coherent circuit[266]. The high Purcell enhancement achieved in SPhP resonators could be used to probe quantum emitters and together with propagative modes paves the way for quantum architectures in the mid-infrared. Furthermore, this platform does not suffer from the limitations of plasmonic circuit since the intrisic losses are orders of magnitude smaller.

Chapter 8

Conclusions and Future Work

The progress of quantum technologies requires new material platforms that satisfy non trivial requirements, including the presence of quantum emitters and of electro-optic effects that, if taken together, considerably narrows down the list of candidates. These prerequisites, together with outstanding optical properties, have raised interest in SiC. The mature fabrication technology offers high quality SiC grown heteroepitaxially on silicon substrates, providing thin layers for device fabrication without requiring extra process steps. Until recently, the presence of the Si substrate hampered the development of a fully scalable 3C SiC photonics needed to integrate nonlinear devices as well as quantum components within the same platform.
One of the basic requirements for the development of low-loss photonics is the fabrication of structures with low sidewall roughness. For 3C SiC, this was accomplished in this thesis by using an Al hardmask, patterned with electron beam lithography, together with a powerful ICP RIE etch, performed with low pressure of the SF_6 precursor in the reactor chamber. The higher refractive index of the Si substrate does not grant the confinement of the electromagnetic field within the SiC layer. Thanks to a second lithography step, access points for a subsequent XeF_2 vapour etches were patterned along all the photonic components together with the grooves for the grating coupler, whose etch depth was optimized to achieve the maximum CE. With this fabrication procedure that suspends all the integrated optical components, waveguides with sub-μm cross-sections, grating couplers and ring resonators were consistently realized for both SM and MM platforms. The devices were characterized using a CW laser tunable across the telecom band and polarization maintaining fiber arrays. The measured coupling efficiency is -6 dB for the uniform SM grating coupler and -6.6 dB for the apodized MM grating coupler, both including losses due to propagation in the tapering region. The half width at half maximum was 38 nm (18 nm) for the SM (MM) platform. The intrinsic quality factor for the SM ring resonators was around 8,700, meanwhile 24,000 was achieved for the 20m MM ring resonators, corresponding to 21 dB/cm propagation loss. This suspended technology could easily be interfaced with photonic crystal cavities which are fundamental

components to exploit SiC quantum emitters. This is the first demonstration of high confinement photonic in 3C SiC and it is essential for the development of a wide range of classical and quantum components.

In order to increase efficiencies in nonlinear processes and for quantum optics interconnections, improvements in the propagation losses are required. This can be achieved in the current suspended technology by implementing extra fabrication steps or by changing the fabrication process. Scattering losses could be diminished by an oxidation step, that would reduce the sidewall roughness. The implementation of a cladding would decrease the refractive index contrast leading to a reduction of the propagation losses and make the sample more robust against the environment at the expenses of bigger bending losses that ultimately affect the dimensions of components. The use of a metal hardmask could introduce metallic contaminations in waveguide sidewalls[208] meaning that a dielectric hardmask, with a drastic change of the fabrication procedures, could be needed to reduce absorption losses. Finally, the crystalline quality of SiC at the boundary with the Si substrate is poor[232] and the realization of SiC on insulators[267] would reduce both material absorption, due to the better quality of the crystal, as well as the scattering losses, due to the use of a bottom oxide cladding. Furthermore, the presence of a BOX layer would improve the grating coupler efficiency.

By taking advantage of the high field enhancement achieved in the rings together with small modal area of the waveguide, in this thesis is demonstrated frequency conversion by means of four wave mixing, measuring for the first time the Kerr nonlinear index of 3C SiC as $\mathrm{n}_2 = (5.31 \pm 0.04)\ 10^{-19}\ \mathrm{m}^2/\mathrm{W}$. The measurement took advantage of an almost critically-coupled ring resonator which Q factor was 7,400 and three consecutive resonances where employed for the signal, idler and pump fields. The spectral distance was given by the ring FSR of 13nm and the pump power at 1550nm was increased using an erbium doped fiber amplifier. At the low pump power of 2.9mW inside the bus waveguide, the conversion gain was -72dB that was not limited by nonlinear absorption due to the wide electronic bandgap of SiC. The measurement of the Kerr nonlinear index of SiC is fundamental for exploiting all $\chi^{(3)}$ effects in this material and is a decisive step forward in the development of 3C SiC nonlinear photonics. The demonstration of $\chi^{(2)}$ effects, such as Pockel modulator and second harmonic generation, could already be achieved with this suspended platform. In particular, efficient SHG could be reached with both the fundamental and the second harmonic fields on resonance with a ring resonator. However, improvements in the fabrication procedure aimed to reduce the propagation losses would benefit nonlinear processes in this material.

Third order nonlinear effects are also fundamental for the generations of correlated photon pairs in centrosymmetric materials. One of the main platforms for classical and nonlinear photonics is provided by using $\mathrm{Si_3N_4}$ waveguides, since they present both a moderate $\chi^{(3)}$ nonlinearity and refractive index together with a CMOS compatible process. These features have already been utilized for efficient single photon generation as well as for complex quantum circuits working at telecom wavelengths. By taking advantage of the wide transparency window in Si_3N_4, in Chap.5 is reported the generation of single photon pairs in the near-infrared window by means of SFWM. The process employed a high-Q factor ring resonator, which radius was 20μm in order to achieve a high field enhancement. The demonstration of a single photon source in the nearinfrared is crucial for the development of an all-optical photonic platform working at room temperature since it can be integrated with Si avalanche single photon detector. Furthermore, this source could be efficiently interfaced with atomic memories once the cavity Q factors are improved. The use of Si as active medium could be beneficial even for the development of a continuous variable platform, since Si photodiodes have high quantum efficiency and nonlinear process can be used to generate squeezed states.

Small modal volume and high Q factor cavities are the main prerequisites to achieve a strong light-matter interaction that is essential to harness SiC quantum emitters. An efficient way to implement cavities showing these features is to create a 2D periodic perturbation of the refractive index through the patterning of holes in the SiC slab, resulting in a spectral band where the light propagation is inhibited. The removal of three holes defines a L3 photonic crystal cavity that is the one fabricated in this thesis. The Q factor of these cavities is severely affected by the etch anisotropy and therefore the process required particular attention during the fabrication. The SiC cavities were analysed with a confocal microscope that scans the sample surface with a wide-spectra beam and the cavity resonances are identified in cross-polarization with a spectrometer. The produced photonic crystal cavities showed Q factors as high as 4,000 at the same wavelength of the ZPL of the divacancy colour center, meaning that strong light matter interaction could be potentially reached once single defects are placed in the middle of cavity centres. Since solid state emitters are affected by the surrounding material condition, improvements in the crystal quality would increase the coherence time as well as the emitters indistinguishably. This could be provided again by the use of SiC on insulator platforms, which better material quality would also benefit the Q factor of the photonic crystal cavities.

Periodic structures were also realized to exploit the coupling between propagating and localized SPhP in the Reststrahlen band, where SiC shows a negative permittivity and, analogously as for plasmonic waves in metal structures, supports a surface wave at the interface with air. Pillars of $1\mu m$ diameter were realized at different pitches in order to couple the propagating surface wave at different wavevector points. Furthermore, resonant cavity modes are sustained in the SiC pillar and the dispersion provided by the array periodic distribution is almost flat in the considered wavelengths. In the spectral positions where the propagating waves and the resonant modes dispersions cross each other, the field is coherently exchanged as demonstrated by the resulting anticrossing dispersion. The achieved strong coupling between a cavity mode with a propagating wave is essential for the realization of polaritonic optical circuits. Furthermore, these SPhP resonators present an incredibly high Purcell's enhancement that could be used for sensing application in the mid-infrared range.

In conclusion, the development of novel platforms for photonic quantum technologies is demonstrated in this thesis. In particular, the unique optical features of 3C SiC are exploited by a new fabrication approach, consisting in the suspension of photonic components, that led to the realization of sub-μm cross-section waveguides, grating couplers and ring resonators. The tight confinement achieved in the cavities was also essential for the demonstration of frequency conversion by four wave mixing and could be exploited in a range of nonlinear and quantum applications. As the presence of quantum emitters in SiC, photonic crystal cavities are also realized with the aim to achieve strong-light matter interactions, fundamental for the development of a scalable photonic quantum platform. Furthermore, the coupling between propagating and localized surface waves are investigated in μm-scale pillar arrays. Finally, the generation of a photon pair source in the nearinfrared wavelengths is reported in Si_3N_4 ring resonators that, if combined with on-chip Si avalanche single photon detectors, could compose a fully integrated photonic platform operating at room temperature.

Appendix A

Analysis of ring resonators for the extraction of linear losses

In order to determine the linear propagation losses from the resonance of a ring resonator, I fabricated a set of waveguides in which the position of the ring with the respect of the bus waveguide was changed. In this way, the trend of loaded quality factor together with the transmission at resonance can be used to determine the coupling condition (undercoupled or overcoupled). This procedure allows to simulate a ring moving from a position close to the waveguide (overcoupled condition) to a position far from the bus waveguide (undercoupled condition), passing through the critical coupling condition where the transmission at resonance is zero. By increasing the ring-waveguide gap, the loaded quality factor increases as described from Eq.3.43 since the transmission t increases.

Fig.A.1, A.2 and A.3 show a set of resonances for a 20μm SM ring resonators, 20μm MM ring resonators and 10μm MM ring resonators, respectively, where the gap is increased (waveguide one has the smallest gap) and each set is realized in the same fabrication run.

The resonances are fitted with a Lorentzian function to determine the $\Delta\lambda$ and the loaded quality factor

$$Q_L = \frac{\lambda_0}{\Delta\lambda} \tag{A.1}$$

Due to the unknown coupling condition, for one value of Q_L corresponds wo different value of intrinsic quality factor Q_I

$$Q_C = \begin{cases} \frac{2Q_L}{1-\sqrt{T_{min}}} & \text{for} \quad a < t \\ \frac{2Q_L}{1+\sqrt{T_{min}}} & \text{for} \quad a > t \end{cases} \tag{A.2}$$

Thanks to

$$Q_I = \frac{\pi n_g L \sqrt{a}}{(1-a)\lambda_0} \tag{A.3}$$

we can extrapolate the attenuation coefficient a from Q_I and by inverting

$$a = e^{-\frac{\alpha}{2}L} \tag{A.4}$$

the propagation losses α. In Eq.A.4, L is the ring circumference meanwhile n_g in Eq.A.3 is the group index, that can be either simulated or measured from the free spectral range from resonance.

The complete analysis of the losses for the set of ring resonators of Fig. A.1, A.2 and A.3 are reported in Tab. A.1, A.2 and A.3, respectively. With the exception of waveguide 1 (Fig.A.3) , all the rings are in undercouled condition.

WG number	Transmission	Q_{loaded}	L_{under} (dB/cm)	L_{over} (dB/cm)
1	0.01	2785	103	84
2	0.002	3098	88	80
3	0.008	3000	95	79
4	0.09	2622	129	69
5	0.25	2189	177	59
6	0.10	3586	95	50
7	0.18	3773	98	40
8	0.52	2177	205	33

Table A.1: Single Mode Ring Resonators (20 μm radius). Losses for overcoupled and undercoupled conditions calculated from the resonances of Fig.A.1. The distance between the bus waveguide and the ring was gradually changed from the smallest gap (waveguide 1) to the biggest (waveguide 8). Values reported in red represent the condition in which the ring should be considered for the exact losses evaluation. Transmission - Normalized transmission at resonance; Q_{loaded} - loaded quality factor; L_{under} - Equivalent linear losses if the ring is in undercoupled condition; L_{over} - Equivalent linear losses if the ring is in overcoupled condition

WG number	Transmission	Q_{loaded}	L_{under} (dB/cm)	L_{over} (dB/cm)
1	0.027	10789	27	20
2	0.082	12024	27	15
3	0.19	12269	30	12
4	0.24	16151	23	8
5	0.37	19282	21	5

Table A.2: Multi Mode Ring Resonators (20 μm radius). Losses for overcoupled and undercoupled conditions calculated from the resonances of Fig.A.2. The distance between the bus waveguide and the ring was gradually changed from the smallest gap (waveguide 1) to the biggest (waveguide 5). Values reported in red represent the condition in which the ring should be considered for the exact losses evaluation. Transmission - Normalized transmission at resonance; Q_{loaded} - loaded quality factor; L_{under} - Equivalent linear losses if the ring is in undercoupled condition; L_{over} - Equivalent linear losses if the ring is in overcoupled condition

WG number	Transmission	Q_{loaded}	L_{under} (dB/cm)	L_{over} (dB/cm)
1	0.06	9507	33	20
2	0.61	11946	38	5
3	0.60	17952	25	3
4	0.82	8461	57	3

Table A.3: Multi Mode Ring Resonators (10 μm radius). Losses for overcoupled and undercoupled conditions calculated from the resonances of Fig.A.3. The distance between the bus waveguide and the ring was gradually changed from the smallest gap (waveguide 1) to the biggest (waveguide 5). Values reported in red represent the condition in which the ring should be considered for the exact losses evaluation. Transmission - Normalized transmission at resonance; Q_{loaded} - loaded quality factor; L_{under} - Equivalent linear losses if the ring is in undercoupled condition; L_{over} - Equivalent linear losses if the ring is in overcoupled condition

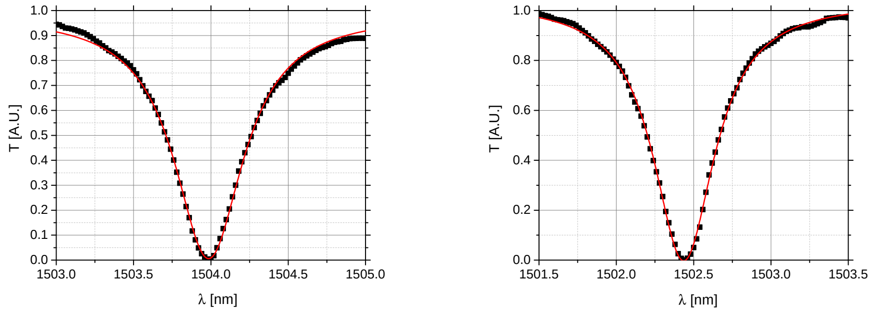

(a) Waveguide 1 (b) Waveguide 2

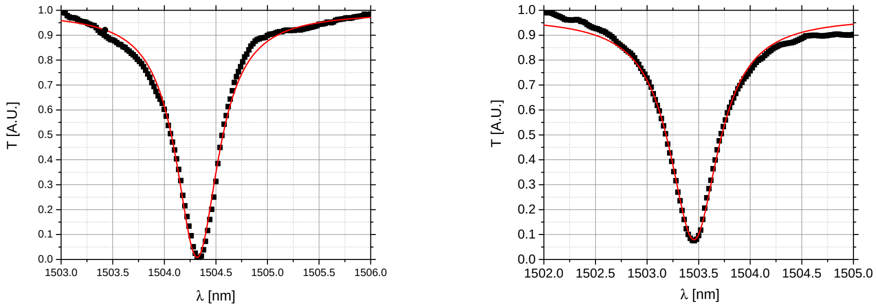

(c) Waveguide 3 (d) Waveguide 4

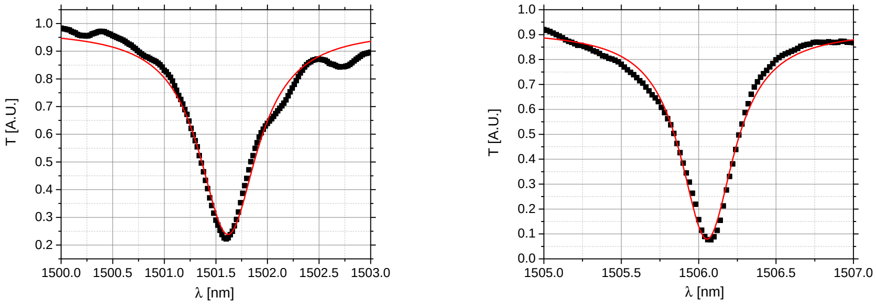

(e) Waveguide 5 (f) Waveguide 6

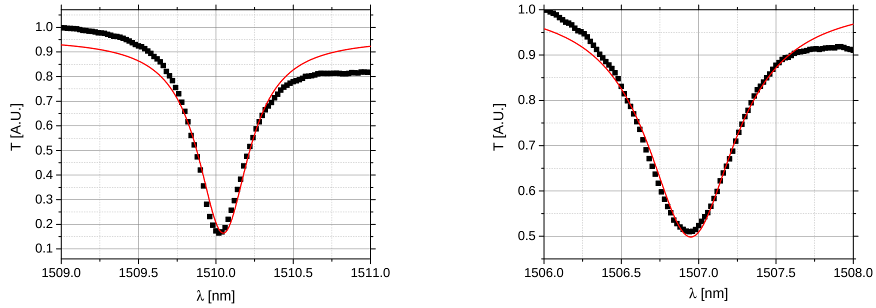

(g) Waveguide 7 (h) Waveguide 8

Figure A.1: Single Mode Ring Resonators (20 μm radius).Resonance spectra of a set of ring resonators in which the distance between the bus waveguide and ring resonator was gradually increased, with the smallest value for waveguide 1 and biggest for waveguide 8.

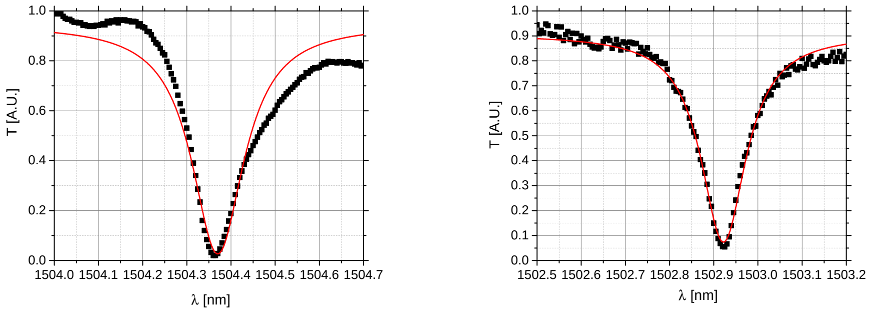

(a) Waveguide 1

(b) Waveguide 2

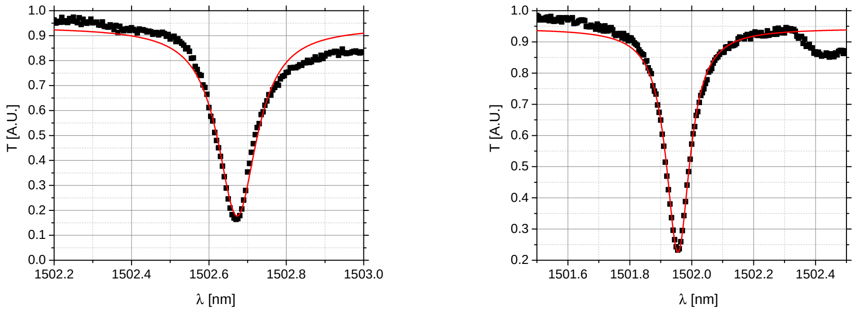

(c) Waveguide 3

(d) Waveguide 4

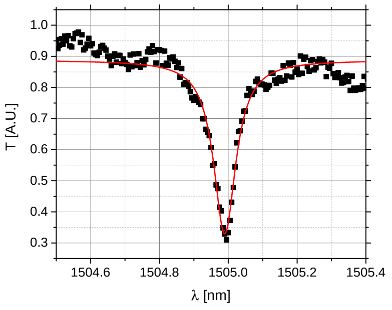

(e) Waveguide 5

Figure A.2: Multi Mode Ring Resonators (20 μm radius). Resonance spectra of a set of ring resonators in which the distance between the bus waveguide and ring resonator was gradually increased, with the smallest value for waveguide 1 and biggest for waveguide 5.

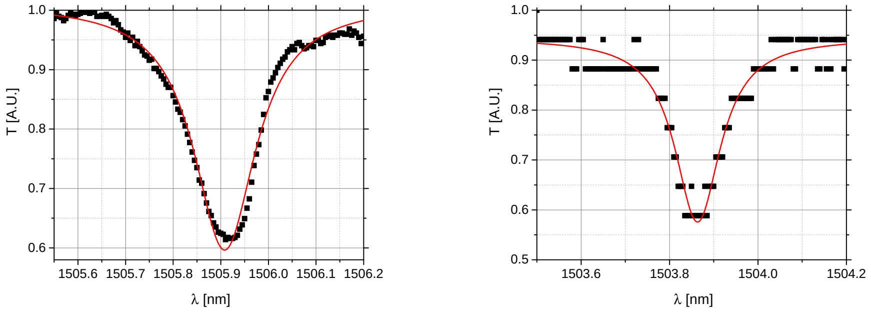

(a) Waveguide 1

(b) Waveguide 2

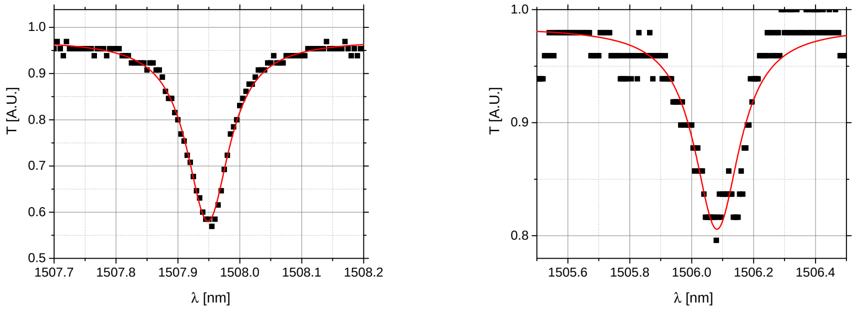

(c) Waveguide 3

(d) Waveguide 4

Figure A.3: Multi Mode Ring Resonators (10 μm radius). Resonance spectra of a set of ring resonators in which the distance between the bus waveguide and ring resonator was gradually increased, with the smallest value for waveguide 1 and biggest for waveguide 4.

Appendix B

Algorithm for apodization of SiC grating coupler

In this Appendix is reported the source code to implement the genetical algorithm for the apodization of grating coupler in Lumerical.

Step 2

```
######################################################################################
############################Optimization############################################
#######################################################################################

size_post=matrix(n_periods+2,1);
size_post1=matrix(n_periods+2,1);

T_1550=0;
deltaW=2e-9;
deltaP=2e-9;
costraingroove=50e-9;
costrainpost=120e-9;

#switchtolayout;
select("Ap_grating");
delete;
addstructuregroup;
set("name","Ap_grating");
position_post=0;

for(ii=0:n_periods){

    size_post1(ii+1,1)=fill(ii+1,1)*Pperiods1(ii+1,1);

    #[x,y] points
    V(1,1:2)=[-size_post1(ii+1,1),0];
    V(2,1:2)=[-size_post1(ii+1,1)+a,z_span_grating];
    V(3,1:2)=[-a,z_span_grating];
    V(4,1:2)=[0,0];
```

```
    #add grating
    position_post=position_post+Pperiods1(ii+1,1);
    addpoly;
    set("name","post");
    set("x",position_post);
    set("y",0);
    set("z span",width);
    set("vertices",V);
    set("material",mat_grating);
    if(get("material")=="<Object defined dielectric>")
      { set("index",index_grating); }
     addtogroup("Ap_grating");
}
select("Ap_grating");
set("x",0);
set("y",0);

for(iii=0:1300){

   #calculate the T_avg_new
    run;
    T = getresult("waveguide","expansion for T");
    Tfund = -T.getattribute("T_backward");
    lambda = T.lambda;
    T_avg_new = integrate(Tfund,1,lambda)/integrate(matrix(length(lambda))+1,1,lambda);

    index=find(lambda,1550e-9);
    lambda_1550=lambda(index);
    T_1550_new=Tfund(index);

   #compare with the best and update if necesary
   if(T_1550_new>=T_1550){
     T_1550=T_1550_new;
     ?T_1550;
      ?iii;

      for(i=0:n_periods){
        size_post(i+1,1)=size_post1(i+1,1);
        Pperiods0(i+1,1)=Pperiods1(i+1,1);
       }
     matlabsave("apod_MM_300nm2nd");
   }

   #mutate from the best
   switchtolayout;
   select("Ap_grating");
   delete;
   addstructuregroup;
   set("name","Ap_grating");

   position_post=0;

   for(i=0:n_periods){
      randW=rand(-1,1)*deltaW;
      randP=rand(-1,1)*deltaP;
      size_post1(i+1,1)=size_post(i+1,1)+randW;
      Pperiods1(i+1,1)=Pperiods0(i+1,1)+randP;
```

```
      if((Pperiods1(i+1,1)-size_post1(i+1,1))<costraingroove){
       size_post1(i+1,1)=Pperiods1(i+1,1)-costraingroove;

}
      if((size_post1(i+1,1)-2*a)<costrainpost){
       size_post1(i+1,1)=costrainpost+2*a;

}

       #[x,y] points
       V(1,1:2)=[-size_post1(i+1,1),0];
       V(2,1:2)=[-size_post1(i+1,1)+a,z_span_grating];
       V(3,1:2)=[-a,z_span_grating];
       V(4,1:2)=[0,0];

      position_post=position_post+Pperiods1(i+1,1);

      #add grating
       addpoly;
       set("name","post");
       set("x",position_post);
       set("y",0);
       set("z span",width);
       set("vertices",V);
       set("material",mat_grating);
       if(get("material")=="<Object defined dielectric>")
         { set("index",index_grating); }
        addtogroup("Ap_grating");
   }
   select("Ap_grating");
   set("x",0);
   set("y",0);
}

#########################best grating


   select("Ap_grating");
   delete;
   addstructuregroup;
   set("name","Ap_grating");

   position_post=0;

   for(i=0:n_periods){

       #[x,y] points
       V(1,1:2)=[-size_post(i+1,1),0];
       V(2,1:2)=[-size_post(i+1,1)+a,z_span_grating];
       V(3,1:2)=[-a,z_span_grating];
       V(4,1:2)=[0,0];

      position_post=position_post+Pperiods0(i+1,1);

      #add grating
       addpoly;
       set("name","post");
       set("x",position_post);
       set("y",0);
```

```
       set("z span",width);
       set("vertices",V);
       set("material",mat_grating);
       if(get("material")=="<Object defined dielectric>")
         { set("index",index_grating); }
        addtogroup("Ap_grating");
   }
   select("Ap_grating");
   set("x",0);
   set("y",0);
```

Step 3

```
clear;
 matlabload("apod_MM_320nm2nd");

z_span_grating = 330e-9;
T_1550=0;

a=(z_span_grating)/tan(theta);
aa=10e-9/tan(theta);#from the previous
diff=30e-9;#from the previous previous-actual z_span_grating

deltaW=2e-9;
deltaP=2e-9;
addstructuregroup;
set("name","Ap_wg");

addrect;
  set("x",(n_periods+1)*period/2);
  set("y",-(Thickness-z_span_grating)/2);
  set("x span",(n_periods+1)*period);
  set("y span",Thickness-z_span_grating);
  set("z span",width);
  set("material",mat_grating);
  if(get("material")=="<Object defined dielectric>")
    { set("index",index_grating); }
  addtogroup("Ap_wg");

addrect;
  set("x",-(n_periods+1)*period/2);
  set("y span",Thickness);
  set("x span",(n_periods+1)*period);
  set("y",-(Thickness)/2+z_span_grating);
  set("z span",10e-6);
  set("material",mat_grating);
  set("z span",width);
  if(get("material")=="<Object defined dielectric>")
    { set("index",index_grating); }
  addtogroup("Ap_wg");
#initial grating etch
   V(1,1:2)=[2*a,0];
   V(2,1:2)=[a,z_span_grating];
   V(3,1:2)=[-a,z_span_grating];
   V(4,1:2)=[-2*a,0];
  addpoly;
```

```
   set("name","fpost");
   set("x",0);
   set("y",0);
   set("z span",width);
   set("vertices",V);
   set("material",mat_grating);
   if(get("material")=="<Object defined dielectric>")
     { set("index",index_grating); }
   addtogroup("Ap_wg");
######################################################box

   select("Ap_wg");
   set("x",-4*aa);
   set("y",-diff);


   addstructuregroup;
   set("name","Ap_grating");

   position_post=0;
       for(i=0:n_periods){

       #[x,y] points
       size_post(i+1,1)=size_post(i+1,1)+2*aa;
}

   for(i=0:n_periods){

       #[x,y] points
       V(1,1:2)=[-size_post(i+1,1),0];
       V(2,1:2)=[-size_post(i+1,1)+a,z_span_grating];
       V(3,1:2)=[-a,z_span_grating];
       V(4,1:2)=[0,0];

      position_post=position_post+Pperiods0(i+1,1);

      #add grating
       addpoly;
       set("name","post");
       set("x",position_post);
       set("y",0);
       set("z span",width);
       set("vertices",V);
       set("material",mat_grating);
       if(get("material")=="<Object defined dielectric>")
         { set("index",index_grating); }
        addtogroup("Ap_grating");
   }
   select("Ap_grating");
   set("x",3*aa);
   set("y",-diff);

T_1550=0;
for(iii=0:6000){

   #calculate the T_avg_new
    run;
    T = getresult("waveguide","expansion for T");
    Tfund = -T.getattribute("T_backward");
```

```
    lambda = T.lambda;
    T_avg_new = integrate(Tfund,1,lambda)/integrate(matrix(length(lambda))+1,1,lambda);

    index=find(lambda,1550e-9);
    lambda_1550=lambda(index);
    T_1550_new=Tfund(index);

   #compare with the best and update if necesary
   if(T_1550_new>=T_1550){
     T_1550=T_1550_new;
     ?T_1550;
      ?iii;

      for(i=0:n_periods){
        size_post(i+1,1)=size_post1(i+1,1);
        Pperiods0(i+1,1)=Pperiods1(i+1,1);
       }
     matlabsave("apod_MM_330nm2nd");
   }

   #mutate from the best
   switchtolayout;
   select("Ap_grating");
   delete;
   addstructuregroup;
   set("name","Ap_grating");

   position_post=0;

   for(i=0:n_periods){
      randW=rand(-1,1)*deltaW;
      randP=rand(-1,1)*deltaP;
      size_post1(i+1,1)=size_post(i+1,1)+randW;
      Pperiods1(i+1,1)=Pperiods0(i+1,1)+randP;

      if((Pperiods1(i+1,1)-size_post1(i+1,1))<costraingroove){
       size_post1(i+1,1)=Pperiods1(i+1,1)-costraingroove;

}
      if((size_post1(i+1,1)-2*a)<costrainpost){
       size_post1(i+1,1)=costrainpost+2*a;

}

       #[x,y] points
       V(1,1:2)=[-size_post1(i+1,1),0];
       V(2,1:2)=[-size_post1(i+1,1)+a,z_span_grating];
       V(3,1:2)=[-a,z_span_grating];
       V(4,1:2)=[0,0];

      position_post=position_post+Pperiods1(i+1,1);

      #add grating
       addpoly;
       set("name","post");
       set("x",position_post);
       set("y",0);
       set("z span",width);
       set("vertices",V);
```

```
        set("material",mat_grating);
        if(get("material")=="<Object defined dielectric>")
          { set("index",index_grating); }
         addtogroup("Ap_grating");
   }
   select("Ap_grating");

}

#########################best grating


   select("Ap_grating");
   delete;
   addstructuregroup;
   set("name","Ap_grating");

   position_post=0;

   for(i=0:n_periods){

        #[x,y] points
        V(1,1:2)=[-size_post(i+1,1),0];
        V(2,1:2)=[-size_post(i+1,1)+a,z_span_grating];
        V(3,1:2)=[-a,z_span_grating];
        V(4,1:2)=[0,0];

      position_post=position_post+Pperiods0(i+1,1);

      #add grating
        addpoly;
        set("name","post");
        set("x",position_post);
        set("y",0);
        set("z span",width);
        set("vertices",V);
        set("material",mat_grating);
        if(get("material")=="<Object defined dielectric>")
          { set("index",index_grating); }
         addtogroup("Ap_grating");
   }
```

Appendix C

Fabrication of SiC photonic crystals

In this appendix are reported fabrication results for the development of SiC photonic crystal. The in-depth description of fabrication of photonics components in 3C SiC is reported in Chap.2.

In a similar way of waveguides, the fabrication of photonic crystal requires low roughness and high resolution. In addition to these, the sidewall angle plays a fundamental role to achieve high quality factor cavities (Chap.6). One of the main cause of reduction of sidewall angle and a main problem for the photonic crystal fabrication, is the shrinking of the mask during the slab etch.

As starting point for the fabrication of SiC photonic crystal, I took recipe of etch developed for the ICP RIE as result of the Plackett-Burman design of experiment (Sec.2.3). The PB etch parameter consisted in: 800 W of ICP power, 280 W of forward power, 0.7

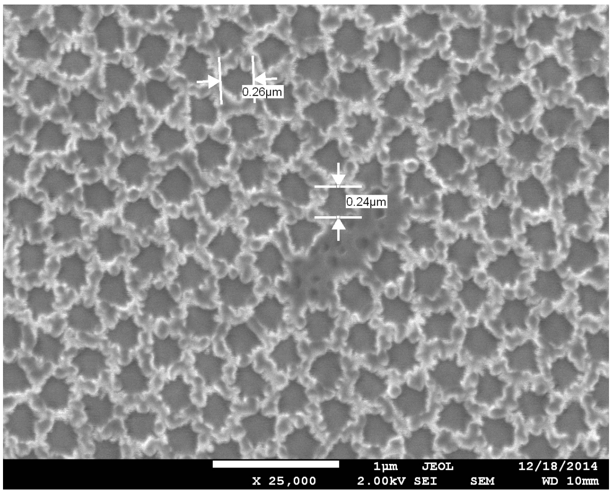

Figure C.1: SiC layer after the PB etch made with 250nm-SiO_2 hardmask. The hardmask was removed in HF after the SiC etch.

mT of pressure , 5 sccm of SF_6 flow, 2 sccm Ar flow and 20°C of plate temperature. In order to complete the process development, both an electron beam lithography (EBL) resist and a hardmask, capable to withstand the powerful SiC etch, have to be defined. The geometry of photonic crystal cavities makes a positive EBL resist well-suited for the their patterning, since it is less time-consuming to expose the holes rather than the surrounding area. Therefore, I chose CSAR62 since it provides good etching resistance together with high resolution.

In order to have high resolution in patterning, the EBL resist was spun between 200nm and 400nm, depending on the selectivity with the hard mask. These thickness are not enough to etch SiC for the desired amount of 300nm and therefore an hard mask is needed.

The first hardmask I implemented consisted of PECVD SiO_2 since it is widely used for Si photonics fabrication. As reported in Fig.C.1, the resulting SiC layer is affected from the inhomogeneous SiO_2-film deposited with the PECVD tool. The thickness of the hardmask was 250nm and the selectivity with the etch was close to 1:1.

Since SiO_2 can be grown directly atop of SiC, I oxidized the SiC layer in order to achieve a hardmask thickness of 200nm. The homogeneity of the film was improved (Fig.C.2) with the respect to PECVD film (Fig.C.1). However, as can be seen from the 60 degree view of the sample (Fig.C.2.b), there are two main problem with the SiO_2 hardmask: 1) a shrinking problem of the hardmask that increases the hole size; 2) the presence of preferential etch sites that causes the formation of tips in SiC. The latter can be attributed to the charging of the SiO_2 layer.

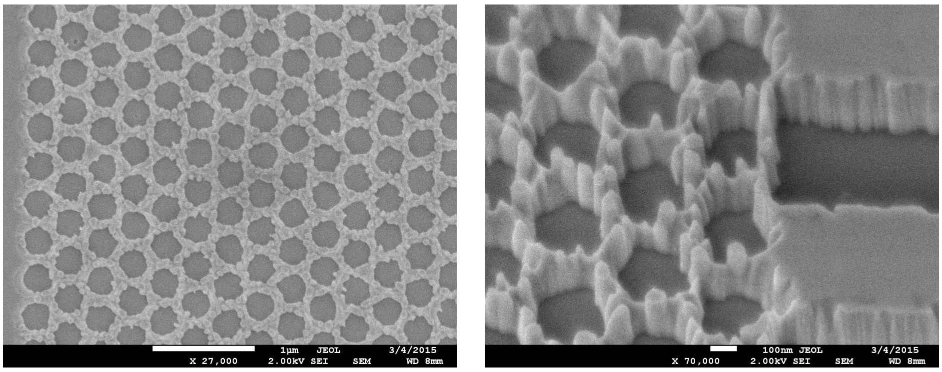

(a) (b)

Figure C.2: SiC photonic crystal made using 200nm of thermal SiO_2 and the PB etch. a) Top view b) 60 degree view.

Due to the difficulties with SiO_2, I tried aluminium (Al) since it was already used for the fabrication of SiC photonics and it offer high resistance with SF_6-based etch. Furthermore, Al can be used to achieve high resolution in patterning as reported in Fig.C.3.(a), where 100nm-thick Al layer deposited via electron beam deposition is etched using an ICP RIE and a HBr-Cl_2 chemistry. However, the PB etch of SiC, using the pattern of Fig.C.3.(a), results in holes with low verticality. This is due to the shrinking of the

Al hardmask during the SiC etch (Fig.C.3.b), consisting of a low etch resistance of the patterned Al edge. This is further shown in Fig.C.4.(a), where there is not contrast in slopes between Al and SiC even though the high etch selectivity. By carrying a short SiC etch (20s), it is possible to notice a change of slope in the SiC sidewall (Fig.C.4.b) resulting from two etch phases: 1) in the initial part of the etch, the Al edge is not consumed and the SiC sidewall is vertical; 2) once the edge of the Al are completely etched, the SiC sidewall verticality decreases.

One approach to avoid the shrinking problem is to increase the hardmask thickness in

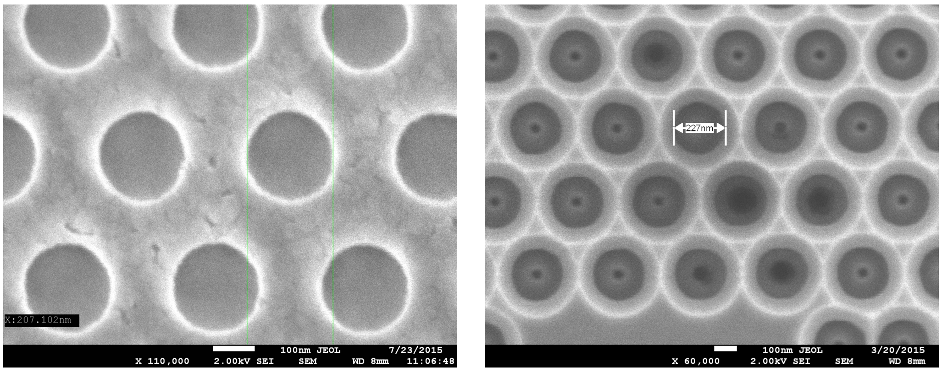

(a) (b)

Figure C.3: a)100nm-thick Al hardmask etched using CSAR62. b) after PB etch of SiC.

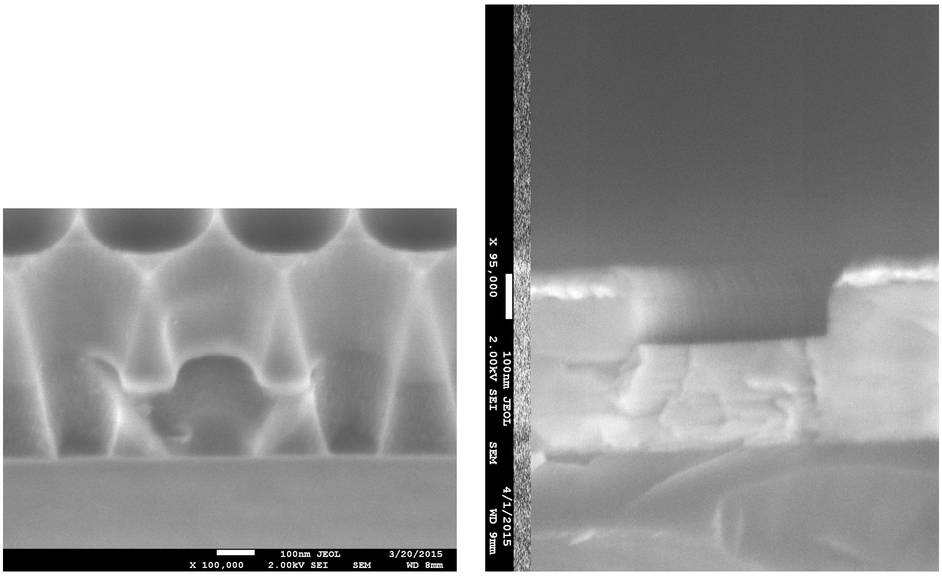

(a) (b)

Figure C.4: a) 45 degree view of the SiC photonic crystal with on top the Al hardmask. b) Cross-section of a SiC feature showing the Al and the SiC. The changes of slopes indicates the Al shrinking.

order to maintain high verticality of the SiC sidewall throughout the etch. In Fig.C.5, SiC was etched using the PB recipe with 300nm-thick Al hardmask. Even though SiC sidewall are vertical (Fig.C.5.b), sputtering of the Al layer produced micromasking (Fig.C.5.a) and residues (Fig.C.5.a) on the SiC sidewall. Both effects considerably worsen the sidewall quality and making the use of a thicker hardmask not valuable.

Another approach to avoid the hardmask shrinking is to reduce the physical sputtering of the PB SIC etch. This can be achieved either reducing the forward plasma power (Fig.C.6.a) or by increasing the pressure of gas precursors inside the plasma chamber (Fig.C.6.b) in order to reduce the line-of-sight of ions and consequently their impact energy. Both paths have the effect of increasing the selectivity between Al and SiC, since it is favoured the chemical aspect of the etch. This resulted in a decrease of sidewall verticality and an increase of roughness.

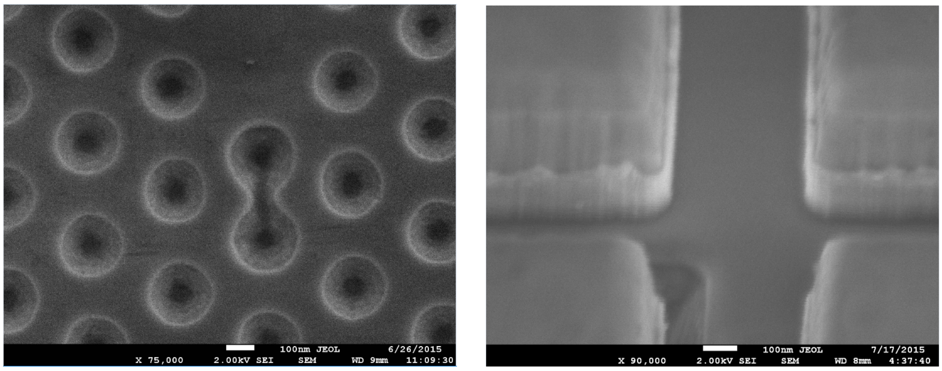

(a) (b)

Figure C.5: PB etch of SiC using 300nm-thick Al hardmask. a) top view after Al removal, showing micromasking on the SiC sidewall; b) 45 degree view of a SiC marker with on top Al hardmask, showing a vertical SiC sidewall and the presence of Al residues.

The amount of physical etch plays a central role in the SiC sidewall angle. For low

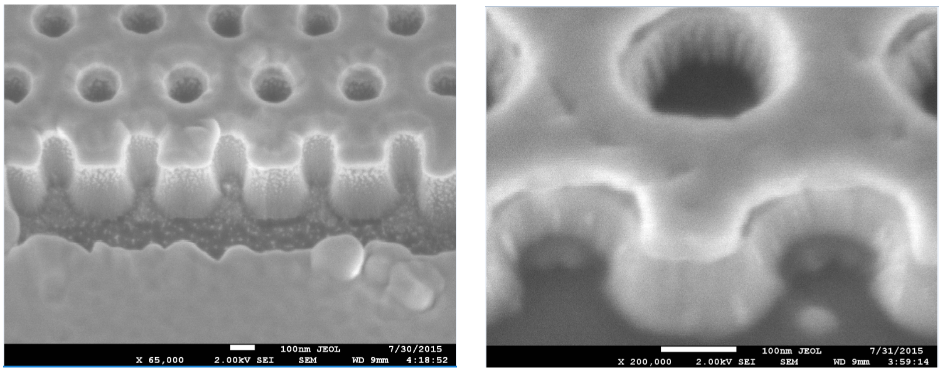

(a) (b)

Figure C.6: 30 degree view of SiC photonic crystal fabricated using 100nm-thick Al hardmask (still on top). a)50 W of forward power of the etch (instead of 280 W); b) 5 mTorr of pressure (instead of 0.7 mTorr).

RF power (Fig.C.6.a) the etch does not provide enough power to achieve vertical sidewall meanwhile for high RF power the hardmask edges are destroyed causing a loss in anisotropy. A trade-off can be achieved between the two conditions as shown in Fig.C.7, where a RF power of 100W was used.

In the holes of the photonic crystal reported in Fig.C.7 there is an effect of micromasking that increases the sidewall roughness. This is consequence of the soft nature of Al that is sputtered and rideposited on the SiC sidewall. Hardmask more resistant to the SiC physical etch can be used to overcome this problem. In Fig.C.8 is reported the SiC photonic crystal fabricated using Al_2O_3 as hardmask. Even though the low RF power of 70W (Fig.C.8.a), the hardmask suffered from shrinking meanwhile SiC was etched inhomogeneously. The latter problem is more evident in Fig.C.8.(b), where the pressure was raised to 5 mTorr.

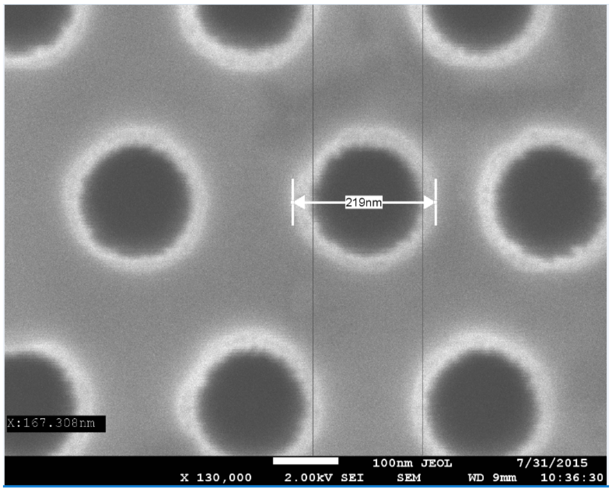

Figure C.7: Top view of SiC photonic crystal fabricated using 100nm-thick Al hardmask (removed in the picture) and 100 W as forward power.

The reduction of forward power could be implemented even for SiO_2 with the aim to

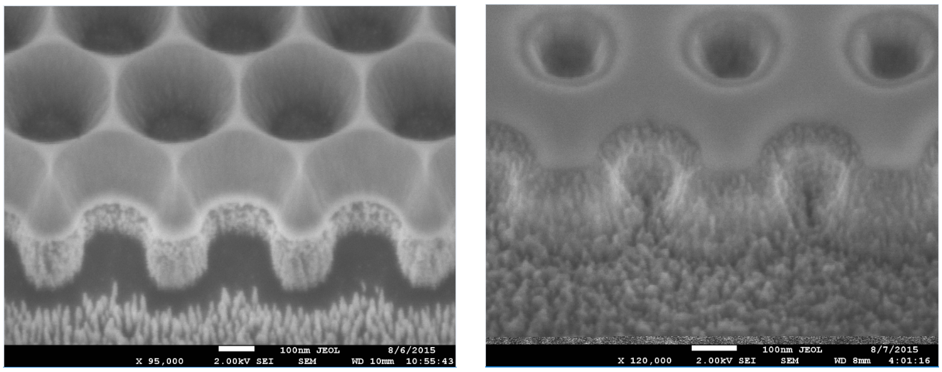

(a) (b)

Figure C.8: Side view of SiC photonic crystal fabricated using 50nm-thick Al_2O_3 hardmask, grown by atomic layer deposition. a) 70 W as forward power; b) 5 mTorr chamber pressure.

achieve the same benefits as for the Al case (Fig.C.7). In FigC.9 is reported the side view of SiC photonic crystal fabricated using 340nm-thick SiO_2 hardmask, grown by thermal oxidization. Even though the RF was dropped to 100W, the shrinking problem still persists, making the use of this hardmask useful only for small thickness of SiC.

The presence of the remaining residues and micromasking (Fig.C.7) were additionally attributed to the oxidization of the Al and to the inhomogeneous etch in air due to the presence of Cl_2 on the resist sidewall after the Al etch. In order to prevent oxidization, 5nm of Titanium (Ti) were deposited right after the Al deposition by electron beam evaporation. The residues Cl_2 molecules were nullified using a short C_4F_8 RIE plasma right after the Al etch. The reduction of RF power together with the removal of the Ar chemistry, contributed to the elimination of the residues that were present at the end of the process. In Fig.C.10.(a) is reported a 3C SiC cavity with a shifted position of the holes adjacent to the cavity in order to increment the quality factor. This sample was fabricated using a tailored etch timing in order to prevent the sputtering of the hardmask edges, that could cause Al redeposition.. Even though some designs required considerable shrunk holes that could eventually cause a worsening of the etch, the process seems not to be affected by this as showed in Fig.C.10.(b).

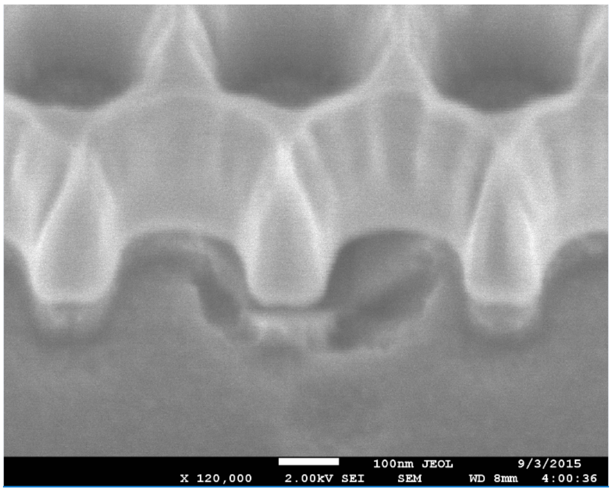

Figure C.9: Side view of SiC photonic crystal fabricated using 340nm-thick SiO_2 hardmask, grown by thermal oxidization

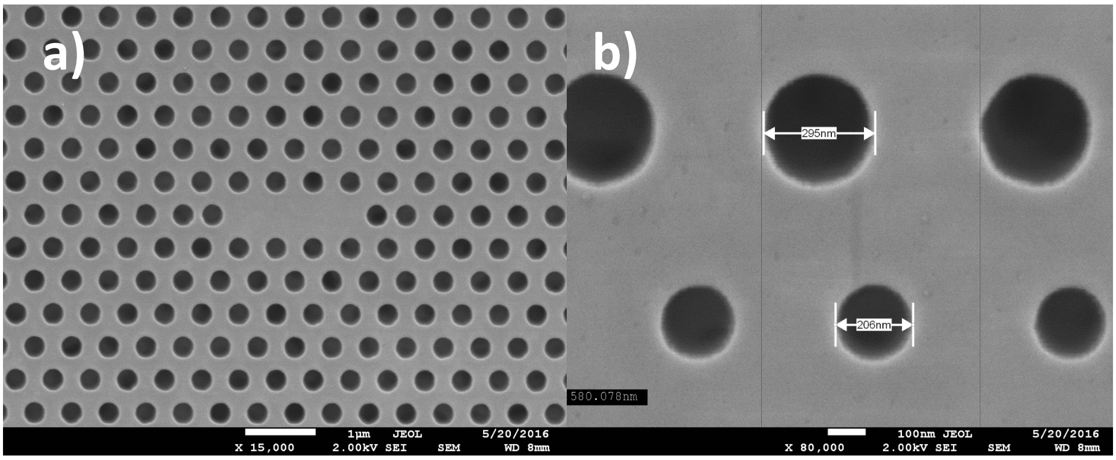

Figure C.10: a)SEM picture of the realized photonic crystal cavity. b) Particular of the fabricated holes showing a near vertical etch.

References

[1] M. Nielsen and I. Chuang, *Quantum computation and quantum information.* Cambridge University Press, 2010.

[2] "Fiber absorption CISCO," http://www.cisco.com/c/en/us/td/docs/optical/15000r7_0/dwdm/planning/guide/70epg/d7ovw.html, accessed: 2017-07-29.

[3] S. Nishino, H. Suhara, H. Ono, and H. Matsunami, "Epitaxial growth and electric characteristics of cubic sic on silicon," *Journal of Applied Physics*, vol. 61, no. 10, pp. 4889–4893, 1987. [Online]. Available: http://dx.doi.org/10.1063/1.338355

[4] M. Portail, M. Zielinski, T. Chassagne, S. Roy, and M. Nemoz, "Comparative study of the role of the nucleation stage on the final crystalline quality of (111) and (100) silicon carbide films deposited on silicon substrates." *Journal of Applied Physics*, vol. 105, no. 8, p. 083505, 2009. [Online]. Available: http://dx.doi.org/10.1063/1.3089215

[5] R. Anzalone, G. D'Arrigo, M. Camarda, C. Locke, S. E. Saddow, and F. L. Via, "Advanced residual stress analysis and fem simulation on heteroepitaxial 3c-sic for mems application," *Journal of Microelectromechanical Systems*, vol. 20, no. 3, pp. 745–752, June 2011.

[6] P. Y. A. Yariv, *Phoonics.*

[7] M. Fox, *Quantum optics: an introduction.* OUP Oxford, 2006, vol. 15.

[8] J. D. Caldwell, O. J. Glembocki, Y. Francescato, N. Sharac, V. Giannini, F. J. Bezares, J. P. Long, J. C. Owrutsky, I. Vurgaftman, J. G. Tischler, V. D. Wheeler, N. D. Bassim, L. M. Shirey, R. Kasica, and S. a. Maier, "Low-loss, extreme subdiffraction photon confinement via silicon carbide localized surface phonon polariton resonators." *Nano letters*, vol. 13, no. 8, pp. 3690–7, aug 2013. [Online]. Available: http://www.ncbi.nlm.nih.gov/pubmed/23815389

[9] "Optical excitation of surface phonon polaritons in silicon carbide by a hole array fabricated by a focused ion beam," *Optical Materials*, vol. 30, no. 2, pp. 328 – 333, 2007. [Online]. Available: http://www.sciencedirect.com/science/article/pii/S0925346706004435", author="HermanHgstrmandSimaValizadehandCarlGustafRibbing

[10] C. R. Gubbin, F. Martini, A. Politi, S. A. Maier, and S. De Liberato, "Strong and Coherent Coupling between Localized and Propagating Phonon Polaritons," *Physical Review Letters*, vol. 116, no. 24, p. 246402, jun 2016. [Online]. Available: http://arxiv.org/abs/1509.09074http://link.aps.org/doi/10.1103/PhysRevLett.116.246402

[11] F. Martini and A. Politi, "Linear integrated optics in 3c silicon carbide," *Opt. Express*, vol. 25, no. 10, pp. 10 735–10 742, May 2017. [Online]. Available: http://www.opticsexpress.org/abstract.cfm?URI=oe-25-10-10735

[12] ——, "3c silicon carbide nanophotonics," in *Frontiers in Optics*. Optical Society of America, 2016, pp. FTh4G–6.

[13] F. Martini and A. Politi, "Four wave mixing in 3C SiC Ring Resonators," *ArXiv e-prints*, Jul. 2017.

[14] R. P. Feynman, "Simulating physics with computers," *International Journal of Theoretical Physics*, vol. 21, no. 6, pp. 467–488, Jun 1982. [Online]. Available: http://dx.doi.org/10.1007/BF02650179

[15] P. W. Shor, "Algorithms for quantum computation: discrete logarithms and factoring," in *Proceedings 35th Annual Symposium on Foundations of Computer Science*, Nov 1994, pp. 124–134.

[16] L. K. Grover, "A fast quantum mechanical algorithm for database search," in *Proceedings of the Twenty-eighth Annual ACM Symposium on Theory of Computing*, ser. STOC '96. New York, NY, USA: ACM, 1996, pp. 212–219. [Online]. Available: http://doi.acm.org/10.1145/237814.237866

[17] D. Deutsch, "Quantum theory, the church-turing principle and the universal quantum computer," *Proceedings of the Royal Society of London A: Mathematical, Physical and Engineering Sciences*, vol. 400, no. 1818, pp. 97–117, 1985. [Online]. Available: http://rspa.royalsocietypublishing.org/content/400/1818/97

[18] D. P. DiVincenzo *et al.*, "The physical implementation of quantum computation," *arXiv preprint quant-ph/0002077*, 2000.

[19] J. I. Cirac and P. Zoller, "Quantum computations with cold trapped ions," *Phys. Rev. Lett.*, vol. 74, pp. 4091–4094, May 1995. [Online]. Available: https://link.aps.org/doi/10.1103/PhysRevLett.74.4091

[20] D. J. Wineland, C. Monroe, W. M. Itano, D. Leibfried, B. E. King, and D. M. Meekhof, “Experimental issues in coherent quantum-state manipulation of trapped atomic ions,” *Journal of Research of the National Institute of Standards and Technology*, vol. 103, no. 3, p. 259, 1998.

[21] R. Blatt and D. Wineland, “Entangled states of trapped atomic ions,” *Nature*, vol. 453, no. 7198, pp. 1008–1015, 2008.

[22] J. Clarke and F. K. Wilhelm, “Superconducting quantum bits,” *Nature*, vol. 453, no. 7198, pp. 1031–1042, 2008.

[23] J. E. Mooij, T. P. Orlando, L. Levitov, L. Tian, C. H. van der Wal, and S. Lloyd, “Josephson persistent-current qubit,” *Science*, vol. 285, no. 5430, pp. 1036–1039, 1999. [Online]. Available: http://science.sciencemag.org/content/285/5430/1036

[24] D. Loss and D. P. DiVincenzo, “Quantum computation with quantum dots,” *Phys. Rev. A*, vol. 57, pp. 120–126, Jan 1998. [Online]. Available: https://link.aps.org/doi/10.1103/PhysRevA.57.120

[25] A. Imamog¯lu, D. D. Awschalom, G. Burkard, D. P. DiVincenzo, D. Loss, M. Sherwin, and A. Small, “Quantum information processing using quantum dot spins and cavity qed,” *Phys. Rev. Lett.*, vol. 83, pp. 4204–4207, Nov 1999. [Online]. Available: https://link.aps.org/doi/10.1103/PhysRevLett.83.4204

[26] M. V. G. Dutt, L. Childress, L. Jiang, E. Togan, J. Maze, F. Jelezko, A. S. Zibrov, P. R. Hemmer, and M. D. Lukin, “Quantum register based on individual electronic and nuclear spin qubits in diamond,” *Science*, vol. 316, no. 5829, pp. 1312–1316, 2007. [Online]. Available: http://science.sciencemag.org/content/316/5829/1312

[27] P. Neumann, N. Mizuochi, F. Rempp, P. Hemmer, H. Watanabe, S. Yamasaki, V. Jacques, T. Gaebel, F. Jelezko, and J. Wrachtrup, “Multipartite entanglement among single spins in diamond,” *Science*, vol. 320, no. 5881, pp. 1326–1329, 2008. [Online]. Available: http://science.sciencemag.org/content/320/5881/1326

[28] J. L. O’Brien, A. Furusawa, and J. Vučković, “Photonic quantum technologies,” *Nature Photonics*, vol. 3, no. 12, pp. 687–695, dec 2009. [Online]. Available: http://www.nature.com/doifinder/10.1038/nphoton.2009.229

[29] W. Gao, A. Imamoglu, H. Bernien, and R. Hanson, “Coherent manipulation, measurement and entanglement of individual solid-state spins using optical fields,” *Nature Photonics*, vol. 9, no. 6, pp. 363–373, 2015.

[30] T. D. Ladd, F. Jelezko, R. Laflamme, Y. Nakamura, C. Monroe, and J. L. OBrien, “Quantum computers,” *Nature*, vol. 464, no. 7285, pp. 45–53, 2010.

[31] C. H. Bennett and G. Brassard, “Quantum cryptography: Public key distribution and con tos5,” 1984.

[32] N. Gisin and R. Thew, “Quantum communication,” *Nature Photonics*, vol. 1, no. 3, pp. 165–171, 2007.

[33] H. Takenaka, A. Carrasco-Casado, M. Fujiwara, M. Kitamura, M. Sasaki, and M. Toyoshima, “Satellite-to-ground quantum-limited communication using a 50-kg-class microsatellite,” *Nature Photonics*, 2017.

[34] V. Giovannetti, S. Lloyd, and L. Maccone, “Quantum-enhanced measurements: Beating the standard quantum limit,” *Science*, vol. 306, no. 5700, pp. 1330–1336, 2004. [Online]. Available: http://science.sciencemag.org/content/306/5700/1330

[35] A. N. Boto, P. Kok, D. S. Abrams, S. L. Braunstein, C. P. Williams, and J. P. Dowling, “Quantum interferometric optical lithography: Exploiting entanglement to beat the diffraction limit,” *Phys. Rev. Lett.*, vol. 85, pp. 2733–2736, Sep 2000. [Online]. Available: https://link.aps.org/doi/10.1103/PhysRevLett.85.2733

[36] T. Rudolph, “Why i am optimistic about the silicon-photonic route to quantum computing,” *APL Photonics*, vol. 2, no. 3, p. 030901, 2017. [Online]. Available: http://dx.doi.org/10.1063/1.4976737

[37] C. K. Hong, Z. Y. Ou, and L. Mandel, “Measurement of subpicosecond time intervals between two photons by interference,” *Physical Review Letters*, vol. 59, no. 18, pp. 2044–2046, nov 1987. [Online]. Available: http://link.aps.org/doi/10.1103/PhysRevLett.59.2044

[38] M. T. Rakher, L. Ma, O. Slattery, X. Tang, and K. Srinivasan, “Quantum transduction of telecommunications-band single photons from a quantum dot by frequency upconversion,” *Nature Photonics*, vol. 4, no. 11, pp. 786–791, oct 2010. [Online]. Available: http://dx.doi.org/10.1038/nphoton.2010.221http://www.nature.com/doifinder/10.1038/nphoton.2010.221

[39] A. Kuhn, M. Hennrich, and G. Rempe, “Deterministic single-photon source for distributed quantum networking,” *Phys. Rev. Lett.*, vol. 89, p. 067901, Jul 2002. [Online]. Available: https://link.aps.org/doi/10.1103/PhysRevLett.89.067901

[40] I. Aharonovich, D. Englund, and M. Toth, “Solid-state single-photon emitters,” *Nature Photonics*, vol. 10, no. 10, pp. 631–641, 2016.

[41] X. Ding, Y. He, Z.-C. Duan, N. Gregersen, M.-C. Chen, S. Unsleber, S. Maier, C. Schneider, M. Kamp, S. Höfling, C.-Y. Lu, and J.-W. Pan, “On-demand single photons with high extraction efficiency and near-unity indistinguishability from a resonantly driven quantum dot in a micropillar,” *Phys. Rev. Lett.*, vol. 116, p. 020401, Jan 2016. [Online]. Available: https://link.aps.org/doi/10.1103/PhysRevLett.116.020401

[42] N. Somaschi, V. Giesz, L. De Santis, J. Loredo, M. P. Almeida, G. Hornecker, S. L. Portalupi, T. Grange, C. Anton, J. Demory *et al.*, "Near optimal single photon sources in the solid state," *arXiv preprint arXiv:1510.06499*, 2015.

[43] M. A. Versteegh, M. E. Reimer, K. D. Jöns, D. Dalacu, P. J. Poole, A. Gulinatti, A. Giudice, and V. Zwiller, "Observation of strongly entangled photon pairs from a nanowire quantum dot," *Nature communications*, vol. 5, 2014.

[44] M. Müller, S. Bounouar, K. D. Jöns, M. Glässl, and P. Michler, "On-demand generation of indistinguishable polarization-entangled photon pairs," *Nature Photonics*, vol. 8, no. 3, pp. 224–228, 2014.

[45] R. M. Stevenson, C. L. Salter, J. Nilsson, A. J. Bennett, M. B. Ward, I. Farrer, D. A. Ritchie, and A. J. Shields, "Indistinguishable entangled photons generated by a light-emitting diode," *Phys. Rev. Lett.*, vol. 108, p. 040503, Jan 2012. [Online]. Available: https://link.aps.org/doi/10.1103/PhysRevLett.108.040503

[46] O. Gazzano, S. M. De Vasconcellos, C. Arnold, A. Nowak, E. Galopin, I. Sagnes, L. Lanco, A. Lemaître, and P. Senellart, "Bright solid-state sources of indistinguishable single photons," *Nature communications*, vol. 4, p. 1425, 2013.

[47] T. Schröder, S. L. Mouradian, J. Zheng, M. E. Trusheim, M. Walsh, E. H. Chen, L. Li, I. Bayn, and D. Englund, "Quantum nanophotonics in diamond

invited

," *J. Opt. Soc. Am. B*, vol. 33, no. 4, pp. B65–B83, Apr 2016. [Online]. Available: http://josab.osa.org/abstract.cfm?URI=josab-33-4-B65

[48] I. Bayn, E. H. Chen, M. E. Trusheim, L. Li, T. Schrder, O. Gaathon, M. Lu, A. Stein, M. Liu, K. Kisslinger, H. Clevenson, and D. Englund, "Generation of ensembles of individually resolvable nitrogen vacancies using nanometer-scale apertures in ultrahigh-aspect ratio planar implantation masks," *Nano Letters*, vol. 15, no. 3, pp. 1751–1758, 2015, pMID: 25621759. [Online]. Available: http://dx.doi.org/10.1021/nl504441m

[49] Z. Huang, W.-D. Li, C. Santori, V. M. Acosta, A. Faraon, T. Ishikawa, W. Wu, D. Winston, R. S. Williams, and R. G. Beausoleil, "Diamond nitrogen-vacancy centers created by scanning focused helium ion beam and annealing," *Applied Physics Letters*, vol. 103, no. 8, p. 081906, 2013. [Online]. Available: http://dx.doi.org/10.1063/1.4819339

[50] Y.-C. Chen, P. S. Salter, S. Knauer, L. Weng, A. C. Frangeskou, C. J. Stephen, S. N. Ishmael, P. R. Dolan, S. Johnson, B. L. Green *et al.*, "Laser writing of coherent colour centres in diamond," *Nature Photonics*, 2016.

[51] A. Sipahigil, K. D. Jahnke, L. J. Rogers, T. Teraji, J. Isoya, A. S. Zibrov, F. Jelezko, and M. D. Lukin, "Indistinguishable photons from separated silicon-vacancy centers in diamond," *Phys. Rev. Lett.*, vol. 113, p. 113602, Sep 2014. [Online]. Available: https://link.aps.org/doi/10.1103/PhysRevLett.113.113602

[52] L. Rogers, K. Jahnke, T. Teraji, L. Marseglia, C. Müller, B. Naydenov, H. Schauffert, C. Kranz, J. Isoya, L. McGuinness *et al.*, "Multiple intrinsically identical single-photon emitters in the solid state," *Nature Communications*, vol. 5, 2014.

[53] A. Sipahigil, M. L. Goldman, E. Togan, Y. Chu, M. Markham, D. J. Twitchen, A. S. Zibrov, A. Kubanek, and M. D. Lukin, "Quantum interference of single photons from remote nitrogen-vacancy centers in diamond," *Phys. Rev. Lett.*, vol. 108, p. 143601, Apr 2012. [Online]. Available: https://link.aps.org/doi/10.1103/PhysRevLett.108.143601

[54] T. Zhong, J. M. Kindem, E. Miyazono, and A. Faraon, "Nanophotonic coherent light-matter interfaces based on rare-earth-doped crystals," *Nature communications*, vol. 6, 2015.

[55] J. J. Longdell, E. Fraval, M. J. Sellars, and N. B. Manson, "Stopped light with storage times greater than one second using electromagnetically induced transparency in a solid," *Phys. Rev. Lett.*, vol. 95, p. 063601, Aug 2005. [Online]. Available: https://link.aps.org/doi/10.1103/PhysRevLett.95.063601

[56] J. C. Howell, R. S. Bennink, S. J. Bentley, and R. W. Boyd, "Realization of the einstein-podolsky-rosen paradox using momentum- and position-entangled photons from spontaneous parametric down conversion," *Phys. Rev. Lett.*, vol. 92, p. 210403, May 2004. [Online]. Available: https://link.aps.org/doi/10.1103/PhysRevLett.92.210403

[57] D. Bouwmeester, J.-W. Pan, K. Mattle, M. Eibl, H. Weinfurter, and A. Zeilinger, "Experimental quantum teleportation," *Nature*, vol. 390, no. 6660, pp. 575–579, 1997.

[58] D. Boschi, S. Branca, F. De Martini, L. Hardy, and S. Popescu, "Experimental Realization of Teleporting an Unknown Pure Quantum State via Dual Classical and Einstein-Podolsky-Rosen Channels," *Physical Review Letters*, vol. 80, no. 6, pp. 1121–1125, feb 1998. [Online]. Available: http://link.aps.org/doi/10.1103/PhysRevLett.80.1121

[59] A. Furusawa, "Unconditional Quantum Teleportation," *Science*, vol. 282, no. 5389, pp. 706–709, oct 1998. [Online]. Available: http://www.ncbi.nlm.nih.gov/pubmed/9784123http://www.sciencemag.org/content/282/5389/706.shorthttp://www.sciencemag.org/cgi/doi/10.1126/science.282.5389.706

[60] L.-A. Wu, H. Kimble, J. Hall, and H. Wu, "Generation of Squeezed States by Parametric Down Conversion," *Physical Review Letters*, vol. 57, no. 20, pp. 2520–2523, nov 1986. [Online]. Available: http://link.aps.org/doi/10.1103/PhysRevLett.57.2520http://journals.aps.org/prl/abstract/10.1103/PhysRevLett.57.2520

[61] M. J. Collins, C. Xiong, I. H. Rey, T. D. Vo, J. He, S. Shahnia, C. Reardon, T. F. Krauss, M. Steel, A. S. Clark *et al.*, "Integrated spatial multiplexing of heralded single-photon sources," *Nature communications*, vol. 4, 2013.

[62] E. Knill, R. Laflamme, and G. J. Milburn, "A scheme for efficient quantum computation with linear optics." *Nature*, vol. 409, no. 6816, pp. 46–52, jan 2001. [Online]. Available: http://www.ncbi.nlm.nih.gov/pubmed/11343107

[63] D. Gottesman and I. L. Chuang, "Demonstrating the viability of universal quantumcomputation using teleportation and single-qubit operations," *Nature*, vol. 402, p. 390, 1999. [Online]. Available: http://www.nature.com/nature/journal/v402/n6760/abs/402390a0.htmlhttp://arxiv.org/abs/quant-ph/9908010

[64] Q. A. Turchette, C. J. Hood, W. Lange, H. Mabuchi, and H. J. Kimble, "Measurement of conditional phase shifts for quantum logic," *Phys. Rev. Lett.*, vol. 75, pp. 4710–4713, Dec 1995. [Online]. Available: https://link.aps.org/doi/10.1103/PhysRevLett.75.4710

[65] A. Rauschenbeutel, G. Nogues, S. Osnaghi, P. Bertet, M. Brune, J. M. Raimond, and S. Haroche, "Coherent operation of a tunable quantum phase gate in cavity qed," *Phys. Rev. Lett.*, vol. 83, pp. 5166–5169, Dec 1999. [Online]. Available: https://link.aps.org/doi/10.1103/PhysRevLett.83.5166

[66] I. Fushman, D. Englund, A. Faraon, N. Stoltz, P. Petroff, and J. Vučković, "Controlled phase shifts with a single quantum dot," *Science*, vol. 320, no. 5877, pp. 769–772, 2008. [Online]. Available: http://science.sciencemag.org/content/320/5877/769

[67] T. Volz, A. Reinhard, M. Winger, A. Badolato, K. J. Hennessy, E. L. Hu, and A. Imamolu, "Ultrafast all-optical switching by single photons," *Nature Photonics*, vol. 6, no. 9, pp. 607–611, aug 2012. [Online]. Available: http://www.nature.com/doifinder/10.1038/nphoton.2012.181

[68] A. Sipahigil, R. E. Evans, D. D. Sukachev, M. J. Burek, J. Borregaard, M. K. Bhaskar, C. T. Nguyen, J. L. Pacheco, H. A. Atikian, C. Meuwly *et al.*, "Single-photon switching and entanglement of solid-state qubits in an integrated nanophotonic system," *arXiv preprint arXiv:1608.05147*, 2016.

[69] P. Lodahl, S. Mahmoodian, and S. Stobbe, "Interfacing single photons and single quantum dots with photonic nanostructures," *Rev. Mod. Phys.*, vol. 87,

pp. 347–400, May 2015. [Online]. Available: https://link.aps.org/doi/10.1103/RevModPhys.87.347

[70] H. Kim, R. Bose, T. C. Shen, G. S. Solomon, and E. Waks, "A quantum logic gate between a solid-state quantum bit and a photon," *Nature Photonics*, vol. 7, no. 5, pp. 373–377, 2013.

[71] C. Dory, K. A. Fischer, K. Müller, K. G. Lagoudakis, T. Sarmiento, A. Rundquist, J. L. Zhang, Y. Kelaita, and J. Vučković, "Complete coherent control of a quantum dot strongly coupled to a nanocavity," *Scientific reports*, vol. 6, 2016.

[72] S. Sun, H. Kim, G. S. Solomon, and E. Waks, "A quantum phase switch between a single solid-state spin and a photon," *Nature Nanotechnology*, vol. 11, no. 6, pp. 539–544, 2016.

[73] C. M. Wilkes, X. Qiang, J. Wang, R. Santagati, S. Paesani, X. Zhou, D. A. B. Miller, G. D. Marshall, M. G. Thompson, and J. L. O'Brien, "60db high-extinction auto-configured mach–zehnder interferometer," *Opt. Lett.*, vol. 41, no. 22, pp. 5318–5321, Nov 2016. [Online]. Available: http://ol.osa.org/abstract.cfm?URI=ol-41-22-5318

[74] F. Marsili, V. B. Verma, J. A. Stern, S. Harrington, A. E. Lita, T. Gerrits, I. Vayshenker, B. Baek, M. D. Shaw, R. P. Mirin *et al.*, "Detecting single infrared photons with 93% system efficiency," *Nature Photonics*, vol. 7, no. 3, pp. 210–214, 2013.

[75] A. Divochiy, F. Marsili, D. Bitauld, A. Gaggero, R. Leoni, F. Mattioli, A. Korneev, V. Seleznev, N. Kaurova, O. Minaeva, G. Gol'tsman, K. G. Lagoudakis, M. Benkhaoul, F. Lévy, and A. Fiore, "Superconducting nanowire photon-number-resolving detector at telecommunication wavelengths," *Nature Photonics*, vol. 2, no. 5, pp. 302–306, apr 2008. [Online]. Available: http://www.nature.com/doifinder/10.1038/nphoton.2008.51

[76] J. P. Sprengers, A. Gaggero, D. Sahin, S. Jahanmirinejad, G. Frucci, F. Mattioli, R. Leoni, J. Beetz, M. Lermer, M. Kamp, S. Hfling, R. Sanjines, and A. Fiore, "Waveguide superconducting single-photon detectors for integrated quantum photonic circuits," *Applied Physics Letters*, vol. 99, no. 18, p. 181110, 2011. [Online]. Available: http://dx.doi.org/10.1063/1.3657518

[77] W. H. Pernice, C. Schuck, O. Minaeva, M. Li, G. Goltsman, A. Sergienko, and H. Tang, "High-speed and high-efficiency travelling wave single-photon detectors embedded in nanophotonic circuits," *Nature communications*, vol. 3, p. 1325, 2012.

[78] S. Bogdanov, M. Y. Shalaginov, A. Boltasseva, and V. M. Shalaev, "Material platforms for integrated quantum photonics," *Opt. Mater. Express*, vol. 7, no. 1,

pp. 111–132, Jan 2017. [Online]. Available: http://www.osapublishing.org/ome/abstract.cfm?URI=ome-7-1-111

[79] J. W. Silverstone, D. Bonneau, J. L. OBrien, and M. G. Thompson, "Silicon quantum photonics," *IEEE Journal of Selected Topics in Quantum Electronics*, vol. 22, no. 6, pp. 390–402, Nov 2016.

[80] C. M. Gentry, J. M. Shainline, M. T. Wade, M. J. Stevens, S. D. Dyer, X. Zeng, F. Pavanello, T. Gerrits, S. W. Nam, R. P. Mirin, and M. A. Popović, "Quantum-correlated photon pairs generated in a commercial 45  nm complementary metal-oxide semiconductor microelectronic chip," *Optica*, vol. 2, no. 12, pp. 1065–1071, Dec 2015. [Online]. Available: http://www.osapublishing.org/optica/abstract.cfm?URI=optica-2-12-1065

[81] S. Azzini, D. Grassani, M. Galli, D. Gerace, M. Patrini, M. Liscidini, P. Velha, and D. Bajoni, "Stimulated and spontaneous four-wave mixing in silicon-on-insulator coupled photonic wire nano-cavities," *Applied Physics Letters*, vol. 103, no. 3, p. 031117, 2013. [Online]. Available: http://scitation.aip.org/content/aip/journal/apl/103/3/10.1063/1.4812640

[82] S. Azzini, D. Grassani, M. J. Strain, M. Sorel, L. G. Helt, J. E. Sipe, M. Liscidini, M. Galli, and D. Bajoni, "Ultra-low power generation of twin photons in a compact silicon ring resonator," *Opt. Express*, vol. 20, no. 21, pp. 23 100–23 107, Oct 2012. [Online]. Available: http://www.opticsexpress.org/abstract.cfm?URI=oe-20-21-23100

[83] D. Grassani, S. Azzini, M. Liscidini, M. Galli, M. J. Strain, M. Sorel, J. E. Sipe, and D. Bajoni, "Micrometer-scale integrated silicon source of time-energy entangled photons," *Optica*, vol. 2, no. 2, p. 88, feb 2015. [Online]. Available: http://www.opticsinfobase.org/optica/abstract.cfm?URI=optica-2-2-88https://www.osapublishing.org/abstract.cfm?URI=optica-2-2-88

[84] J. W. Silverstone, D. Bonneau, K. Ohira, N. Suzuki, H. Yoshida, N. Iizuka, M. Ezaki, C. M. Natarajan, M. G. Tanner, R. H. Hadfield, V. Zwiller, G. D. Marshall, J. G. Rarity, J. L. O'Brien, and M. G. Thompson, "On-chip quantum interference between silicon photon-pair sources," *Nature Photonics*, vol. 8, no. 2, pp. 104–108, dec 2013. [Online]. Available: http://arxiv.org/abs/1304.1490http://www.nature.com/doifinder/10.1038/nphoton.2013.339

[85] A. Bozzola, L. Carroll, D. Gerace, I. Cristiani, and L. C. Andreani, "Optimising apodized grating couplers in a pure soi platform to -0.5 db coupling efficiency," *Opt. Express*, vol. 23, no. 12, pp. 16 289–16 304, Jun 2015. [Online]. Available: http://www.opticsexpress.org/abstract.cfm?URI=oe-23-12-16289

[86] W. S. Zaoui, A. Kunze, W. Vogel, M. Berroth, J. Butschke, F. Letzkus, and J. Burghartz, "Bridging the gap between optical fibers and silicon photonic

integrated circuits." *Optics express*, vol. 22, no. 2, pp. 1277–86, jan 2014. [Online]. Available: http://www.ncbi.nlm.nih.gov/pubmed/24515133

[87] C. A. Husko, A. S. Clark, M. J. Collins, A. De Rossi, S. Combrié, G. Lehoucq, I. H. Rey, T. F. Krauss, C. Xiong, and B. J. Eggleton, "Multi-photon absorption limits to heralded single photon sources." *Scientific reports*, vol. 3, p. 3087, jan 2013. [Online]. Available: http://www.pubmedcentral.nih.gov/articlerender.fcgi?artid=3816289{&}tool=pmcentrez{&}rendertype=abstract

[88] E. Engin, D. Bonneau, C. M. Natarajan, A. S. Clark, M. G. Tanner, R. H. Hadfield, S. N. Dorenbos, V. Zwiller, K. Ohira, N. Suzuki, H. Yoshida, N. Iizuka, M. Ezaki, J. L. O'Brien, and M. G. Thompson, "Photon pair generation in a silicon micro-ring resonator with reverse bias enhancement." *Optics express*, vol. 21, no. 23, pp. 27 826–34, nov 2013. [Online]. Available: http://www.ncbi.nlm.nih.gov/pubmed/24514299

[89] J. W. Silverstone, R. Santagati, D. Bonneau, M. J. Strain, M. Sorel, J. L. OBrien, and M. G. Thompson, "Qubit entanglement between ring-resonator photon-pair sources on a silicon chip," *Nature communications*, vol. 6, 2015.

[90] M. Gould, T. Baehr-Jones, R. Ding, S. Huang, J. Luo, A. K.-Y. Jen, J.-M. Fedeli, M. Fournier, and M. Hochberg, "Silicon-polymer hybrid slot waveguide ring-resonator modulator," *Opt. Express*, vol. 19, no. 5, pp. 3952–3961, Feb 2011. [Online]. Available: http://www.opticsexpress.org/abstract.cfm?URI=oe-19-5-3952

[91] A. Politi, M. J. Cryan, J. G. Rarity, S. Yu, and J. L. O'Brien, "Silica-on-silicon waveguide quantum circuits." *Science (New York, N.Y.)*, vol. 320, no. 5876, pp. 646–9, may 2008. [Online]. Available: http://www.ncbi.nlm.nih.gov/pubmed/18369104

[92] A. Politi, J. C. F. Matthews, and J. L. O'Brien, "Shor's quantum factoring algorithm on a photonic chip." *Science (New York, N.Y.)*, vol. 325, no. 5945, p. 1221, sep 2009. [Online]. Available: http://www.ncbi.nlm.nih.gov/pubmed/19729649

[93] G. Corrielli, A. Crespi, R. Geremia, R. Ramponi, L. Sansoni, A. Santinelli, P. Mataloni, F. Sciarrino, and R. Osellame, "Rotated waveplates in integrated waveguide optics," *Nature communications*, vol. 5, 2014.

[94] J. B. Spring, P. L. Mennea, B. J. Metcalf, P. C. Humphreys, J. C. Gates, H. L. Rogers, C. Söller, B. J. Smith, W. S. Kolthammer, P. G. R. Smith, and I. A. Walmsley, "Chip-based array of near-identical, pure, heralded single-photon sources," *Optica*, vol. 4, no. 1, pp. 90–96, Jan 2017. [Online]. Available: http://www.osapublishing.org/optica/abstract.cfm?URI=optica-4-1-90

[95] M. Kues, C. Reimer, P. Roztocki, L. R. Cortés, S. Sciara, B. Wetzel, Y. Zhang, A. Cino, S. T. Chu, B. E. Little, D. J. Moss, L. Caspani, J. Azaña, and R. Morandotti, "On-chip generation of high-dimensional entangled quantum states and their coherent control," *Nature*, vol. 546, no. 7660, pp. 622–626, Jun 2017, letter. [Online]. Available: http://dx.doi.org/10.1038/nature22986

[96] C. Reimer, M. Kues, P. Roztocki, B. Wetzel, F. Grazioso, B. E. Little, S. T. Chu, T. Johnston, Y. Bromberg, L. Caspani, D. J. Moss, and R. Morandotti, "Generation of multiphoton entangled quantum states by means of integrated frequency combs," *Science*, vol. 351, no. 6278, pp. 1176–1180, 2016. [Online]. Available: http://science.sciencemag.org/content/351/6278/1176

[97] S. Ramelow, A. Farsi, S. Clemmen, D. Orquiza, K. Luke, M. Lipson, and A. L. Gaeta, "Silicon-nitride platform for narrowband entangled photon generation," *arXiv preprint arXiv:1508.04358*, 2015.

[98] M. Poot and H. X. Tang, "Characterization of optical quantum circuits using resonant phase shifts," *Applied Physics Letters*, vol. 109, no. 13, p. 131106, 2016. [Online]. Available: http://dx.doi.org/10.1063/1.4962902

[99] G.-R. Lin, S.-P. Su, C.-L. Wu, Y.-H. Lin, B.-J. Huang, H.-Y. Wang, C.-T. Tsai, C.-I. Wu, and Y.-C. Chi, "Si-rich sinx based kerr switch enables optical data conversion up to 12 gbit/s," *Scientific reports*, vol. 5, 2015.

[100] C. Xiong, W. H. P. Pernice, and H. X. Tang, "Low-loss, silicon integrated, aluminum nitride photonic circuits and their use for electro-optic signal processing," *Nano Letters*, vol. 12, no. 7, pp. 3562–3568, 2012, pMID: 22663299. [Online]. Available: http://dx.doi.org/10.1021/nl3011885

[101] X. Guo, C.-L. Zou, and H. X. Tang, "Second-harmonic generation in aluminum nitride microrings with 2500%/w conversion efficiency," *Optica*, vol. 3, no. 10, pp. 1126–1131, Oct 2016. [Online]. Available: http://www.osapublishing.org/optica/abstract.cfm?URI=optica-3-10-1126

[102] X. Guo, C.-L. Zou, H. Jung, and H. X. Tang, "On-chip strong coupling and efficient frequency conversion between telecom and visible optical modes," *Phys. Rev. Lett.*, vol. 117, p. 123902, Sep 2016. [Online]. Available: https://link.aps.org/doi/10.1103/PhysRevLett.117.123902

[103] X. Guo, C.-l. Zou, C. Schuck, H. Jung, R. Cheng, and H. X. Tang, "Parametric down-conversion photon pair source on a nanophotonic chip," *arXiv preprint arXiv:1603.03726*, 2016.

[104] C. P. Dietrich, A. Fiore, M. G. Thompson, M. Kamp, and S. Höfling, "Gaas integrated quantum photonics: Towards compact and multi-functional quantum photonic integrated circuits," *Laser & Photonics Reviews*, 2016.

[105] M. Arcari, I. Söllner, A. Javadi, S. Lindskov Hansen, S. Mahmoodian, J. Liu, H. Thyrrestrup, E. H. Lee, J. D. Song, S. Stobbe, and P. Lodahl, "Near-unity coupling efficiency of a quantum emitter to a photonic crystal waveguide," *Phys. Rev. Lett.*, vol. 113, p. 093603, Aug 2014. [Online]. Available: https://link.aps.org/doi/10.1103/PhysRevLett.113.093603

[106] I. Söllner, S. Mahmoodian, S. L. Hansen, L. Midolo, A. Javadi, G. Kiršanskė, T. Pregnolato, H. El-Ella, E. H. Lee, J. D. Song *et al.*, "Deterministic photon–emitter coupling in chiral photonic circuits," *Nature nanotechnology*, vol. 10, no. 9, pp. 775–778, 2015.

[107] G. Leo, V. Berger, C. OwYang, and J. Nagle, "Parametric fluorescence in oxidized algaas waveguides," *J. Opt. Soc. Am. B*, vol. 16, no. 9, pp. 1597–1602, Sep 1999. [Online]. Available: http://josab.osa.org/abstract.cfm?URI=josab-16-9-1597

[108] A. Orieux, A. Eckstein, A. Lemaître, P. Filloux, I. Favero, G. Leo, T. Coudreau, A. Keller, P. Milman, and S. Ducci, "Direct bell states generation on a iii-v semiconductor chip at room temperature," *Phys. Rev. Lett.*, vol. 110, p. 160502, Apr 2013. [Online]. Available: https://link.aps.org/doi/10.1103/PhysRevLett.110.160502

[109] J. Wang, A. Santamato, P. Jiang, D. Bonneau, E. Engin, J. W. Silverstone, M. Lermer, J. Beetz, M. Kamp, S. Hfling, M. G. Tanner, C. M. Natarajan, R. H. Hadfield, S. N. Dorenbos, V. Zwiller, J. L. OBrien, and M. G. Thompson, "Gallium arsenide (gaas) quantum photonic waveguide circuits," *Optics Communications*, vol. 327, pp. 49 – 55, 2014, special Issue on Nonlinear Quantum Photonics. [Online]. Available: http://www.sciencedirect.com/science/article/pii/S0030401814001874

[110] T. Teraji, T. Taniguchi, S. Koizumi, K. Watanabe, M. Liao, Y. Koide, and J. Isoya, "Chemical vapor deposition of 12 c isotopically enriched polycrystalline diamond," *Japanese Journal of Applied Physics*, vol. 51, no. 9R, p. 090104, 2012. [Online]. Available: http://stacks.iop.org/1347-4065/51/i=9R/a=090104

[111] G. Balasubramanian, P. Neumann, D. Twitchen, M. Markham, R. Kolesov, N. Mizuochi, J. Isoya, J. Achard, J. Beck, J. Tissler *et al.*, "Ultralong spin coherence time in isotopically engineered diamond," *Nature materials*, vol. 8, no. 5, p. 383, 2009.

[112] E. Togan, Y. Chu, a. S. Trifonov, L. Jiang, J. R. Maze, L. Childress, M. V. G. Dutt, A. S. Sørensen, P. R. Hemmer, A. S. Zibrov, and M. D. Lukin, "Quantum entanglement between an optical photon and a solid-state spin qubit." *Nature*, vol. 466, no. 7307, pp. 730–4, aug 2010. [Online]. Available: http://www.ncbi.nlm.nih.gov/pubmed/20686569

[113] W. Pfaff, B. Hensen, H. Bernien, S. B. van Dam, M. S. Blok, T. H. Taminiau, M. J. Tiggelman, R. N. Schouten, M. Markham, D. J. Twitchen *et al.*, "Unconditional

quantum teleportation between distant solid-state quantum bits," *Science*, vol. 345, no. 6196, pp. 532–535, 2014.

[114] B. Hensen, H. Bernien, a. E. Dréau, A. Reiserer, N. Kalb, M. S. Blok, J. Ruitenberg, R. F. L. Vermeulen, R. N. Schouten, C. Abellán, W. Amaya, V. Pruneri, M. W. Mitchell, M. Markham, D. J. Twitchen, D. Elkouss, S. Wehner, T. H. Taminiau, and R. Hanson, "Loophole-free Bell inequality violation using electron spins separated by 1.3 kilometres," *Nature*, vol. 526, no. 7575, pp. 682–686, oct 2015. [Online]. Available: http://www.nature.com/doifinder/10.1038/nature15759

[115] S. Yang, Y. Wang, D. D. B. Rao, T. Hien Tran, A. S. Momenzadeh, MarkhamM., T. J., P. Wang, W. Yang, R. Stöhr, P. Neumann, H. Kosaka, and J. Wrachtrup, "High-fidelity transfer and storage of photon states in a single nuclear spin," *Nat Photon*, vol. 10, no. 8, pp. 507–511, Aug 2016, letter. [Online]. Available: http://dx.doi.org/10.1038/nphoton.2016.103

[116] A. Sipahigil, R. E. Evans, D. D. Sukachev, M. J. Burek, J. Borregaard, M. K. Bhaskar, C. T. Nguyen, J. L. Pacheco, H. A. Atikian, C. Meuwly, R. M. Camacho, F. Jelezko, E. Bielejec, H. Park, M. Lončar, and M. D. Lukin, "An integrated diamond nanophotonics platform for quantum-optical networks," *Science*, vol. 354, no. 6314, pp. 847–850, 2016. [Online]. Available: http://science.sciencemag.org/content/354/6314/847

[117] M. J. Burek, Y. Chu, M. S. Z. Liddy, P. Patel, J. Rochman, S. Meesala, W. Hong, Q. Quan, M. D. Lukin, and M. Lončar, "High quality-factor optical nanocavities in bulk single-crystal diamond," *Nature communications*, vol. 5, p. 5718, aug 2014. [Online]. Available: http://arxiv.org/abs/1408.5973

[118] B. J. M. Hausmann, B. Shields, Q. Quan, P. Maletinsky, M. McCutcheon, J. T. Choy, T. M. Babinec, A. Kubanek, A. Yacoby, M. D. Lukin, and M. Loncar, "Integrated diamond networks for quantum nanophotonics," *Nano Letters*, vol. 12, no. 3, pp. 1578–1582, 2012, pMID: 22339606. [Online]. Available: http://dx.doi.org/10.1021/nl204449n

[119] B. J. M. Hausmann, I. Bulu, V. Venkataraman, P. Deotare, and M. Lončar, "Diamond nonlinear photonics," *Nature Photonics*, vol. 8, no. 5, pp. 369–374, apr 2014. [Online]. Available: http://www.nature.com/doifinder/10.1038/nphoton.2014.72

[120] J. Riedrich-Möller, L. Kipfstuhl, C. Hepp, E. Neu, C. Pauly, F. Mücklich, A. Baur, M. Wandt, S. Wolff, M. Fischer, S. Gsell, M. Schreck, and C. Becher, "One- and two-dimensional photonic crystal microcavities in single crystal diamond," *Nature nanotechnology*, vol. 7, no. 1, pp. 69–74, jan 2012. [Online]. Available: http://www.ncbi.nlm.nih.gov/pubmed/22081214

[121] S. Niedermeier, H. Schillinger, R. Sauerbrey, B. Adolph, and F. Bechstedt, "Second-harmonic generation in silicon carbide polytypes," *Applied Physics Letters*, vol. 75, no. 5, p. 618, 1999. [Online]. Available: http://adsabs.harvard.edu/abs/1999ApPhL..75..618Nhttp://scitation.aip.org/content/aip/journal/apl/75/5/10.1063/1.124459

[122] L. G. Helt, M. Liscidini, and J. E. Sipe, "How does it scale? comparing quantum and classical nonlinear optical processes in integrated devices," *J. Opt. Soc. Am. B*, vol. 29, no. 8, pp. 2199–2212, Aug 2012. [Online]. Available: http://josab.osa.org/abstract.cfm?URI=josab-29-8-2199

[123] X. Tang, K. G. Irvine, D. Zhang, and M. G. Spencer, "Linear electro-optic effect in cubic silicon carbide," *Applied Physics Letters*, vol. 59, no. 16, p. 1938, 1991. [Online]. Available: http://scitation.aip.org/content/aip/journal/apl/59/16/10.1063/1.106165

[124] A. Vonsovici, G. T. Reed, and A. G. Evans, "β-SiC-on insulator waveguide structures for modulators and sensor systems," *Materials Science in Semiconductor Processing*, vol. 3, no. 5-6, pp. 367–374, oct 2000. [Online]. Available: http://linkinghub.elsevier.com/retrieve/pii/S1369800100000603

[125] S. Nishino, H. Suhara, H. Ono, and H. Matsunami, "Epitaxial growth and electric characteristics of cubic sic on silicon," *Journal of applied physics*, vol. 61, no. 10, pp. 4889–4893, 1987.

[126] J. Cardenas, M. Yu, Y. Okawachi, C. B. Poitras, R. K. Lau, A. Dutt, A. L. Gaeta, and M. Lipson, "Optical nonlinearities in high-confinement silicon carbide waveguides," *Optics letters*, vol. 40, no. 17, pp. 4138–4141, 2015.

[127] A. Lohrmann, B. Johnson, J. McCallum, and S. Castelletto, "A review on single photon sources in silicon carbide," *Reports on Progress in Physics*, vol. 80, no. 3, p. 034502, 2017.

[128] A. L. Falk, B. B. Buckley, G. Calusine, W. F. Koehl, V. V. Dobrovitski, A. Politi, C. a. Zorman, P. X.-L. Feng, and D. D. Awschalom, "Polytype control of spin qubits in silicon carbide." *Nature communications*, vol. 4, no. May, p. 1819, jan 2013. [Online]. Available: http://www.pubmedcentral.nih.gov/articlerender.fcgi?artid=3674240{&}tool=pmcentrez{&}rendertype=abstract

[129] F. Fuchs, V. a. Soltamov, S. Väth, P. G. Baranov, E. N. Mokhov, G. V. Astakhov, and V. Dyakonov, "Silicon carbide light-emitting diode as a prospective room temperature source for single photons." *Scientific reports*, vol. 3, p. 1637, jan 2013. [Online]. Available: http://www.pubmedcentral.nih.gov/articlerender.fcgi?artid=3622138{&}tool=pmcentrez{&}rendertype=abstract

[130] S. Castelletto, B. C. Johnson, V. Ivády, N. Stavrias, T. Umeda, a. Gali, and T. Ohshima, "A silicon carbide room-temperature single-photon source." *Nature materials*, vol. 13, no. 2, pp. 151–6, feb 2014. [Online]. Available: http://www.ncbi.nlm.nih.gov/pubmed/24240243

[131] V. Bratus', R. Melnik, S. Okulov, V. Rodionov, B. Shanina, and M. Smoliy, "A new spin one defect in cubic SiC," *Physica B: Condensed Matter*, vol. 404, no. 23-24, pp. 4739–4741, dec 2009. [Online]. Available: http://dx.doi.org/10.1016/j.physb.2009.08.124http://www.sciencedirect.com/science/article/pii/S092145260900917Xhttp://linkinghub.elsevier.com/retrieve/pii/S092145260900917X

[132] N. T. Son, E. Sorman, W. M. Chen, M. Singh, C. Hallin, O. Kordina, B. Monemar, E. Janzen, and J. L. Lindstrom, "Dominant recombination center in electron-irradiated 3C SiC," *Journal of Applied Physics*, vol. 79, no. 7, p. 3784, 1996. [Online]. Available: http://scitation.aip.org/content/aip/journal/jap/79/7/10.1063/1.361214

[133] J. R. Gao, M. Hajenius, F. D. Tichelaar, T. M. Klapwijk, B. Voronov, E. Grishin, G. Goltsman, C. A. Zorman, and M. Mehregany, "Monocrystalline nbn nanofilms on a 3c-sicsi substrate," *Applied Physics Letters*, vol. 91, no. 6, p. 062504, 2007. [Online]. Available: http://dx.doi.org/10.1063/1.2766963

[134] X. Tang, K. Wongchotigul, and M. G. Spencer, "Optical waveguide formed by cubic silicon carbide on sapphire substrates," *Applied Physics Letters*, vol. 58, no. 9, p. 917, 1991. [Online]. Available: http://scitation.aip.org/content/aip/journal/apl/58/9/10.1063/1.104476

[135] Z. Yang, P. Chak, A. D. Bristow, H. M. van Driel, R. Iyer, J. S. Aitchison, A. L. Smirl, and J. E. Sipe, "Enhanced second-harmonic generation in AlGaAs microring resonators." *Optics letters*, vol. 32, no. 7, pp. 826–8, apr 2007. [Online]. Available: http://www.ncbi.nlm.nih.gov/pubmed/17339950

[136] F. Xia, M. Rooks, L. Sekaric, and Y. Vlasov, "Ultra-compact high order ring resonator filters using submicron silicon photonic wires for on-chip optical interconnects," *Optics express*, vol. 15, no. 19, pp. 11 934–11 941, 2007.

[137] Q. Xu, B. Schmidt, S. Pradhan, and M. Lipson, "Micrometre-scale silicon electro-optic modulator." *Nature*, vol. 435, no. 7040, pp. 325–7, may 2005. [Online]. Available: http://www.ncbi.nlm.nih.gov/pubmed/15902253

[138] P. S. Kuo, J. Bravo-Abad, and G. S. Solomon, "Second-harmonic generation using-quasi-phasematching in a gaas whispering-gallery-mode microcavity," *Nature communications*, vol. 5, 2014.

[139] X. Lu, J. Y. Lee, P. X.-L. Feng, and Q. Lin, "Silicon carbide microdisk resonator." *Optics letters*, vol. 38, no. 8, pp. 1304–6, apr 2013. [Online]. Available: http://www.ncbi.nlm.nih.gov/pubmed/23595466

[140] J. Cardenas, M. Zhang, C. T. Phare, S. Y. Shah, C. B. Poitras, B. Guha, and M. Lipson, "High q sic microresonators," *Optics express*, vol. 21, no. 14, pp. 16 882–16 887, 2013.

[141] G. Pandraud, P. French, and P. Sarro, "Fabrication and characteristics of a pecvd sic evanescent wave optical sensor," *Sensors and Actuators A: Physical*, vol. 142, no. 1, pp. 61–66, 2008.

[142] G. Pandraud, E. Margallo-Balbas, C.-K. Yang, and P. J. French, "Experimental characterization of roughness induced scattering losses in pecvd sic waveguides," *Journal of Lightwave Technology*, vol. 29, no. 5, pp. 744–749, 2011.

[143] M. Gnan, S. Thoms, D. Macintyre, R. De La Rue, and M. Sorel, "Fabrication of low-loss photonic wires in silicon-on-insulator using hydrogen silsesquioxane electron-beam resist," *Electronics Letters*, vol. 44, no. 2, pp. 115–116, 2008.

[144] W. H. P. Pernice, C. Schuck, O. Minaeva, M. Li, G. N. Goltsman, A. V. Sergienko, and H. X. Tang, "High-speed and high-efficiency travelling wave single-photon detectors embedded in nanophotonic circuits," *Nature communications*, vol. 3, p. 1325, jan 2012. [Online]. Available: http://www.pubmedcentral.nih.gov/articlerender.fcgi?artid=3535416{&}tool=pmcentrez{&}rendertype=abstracthttp://www.nature.com/ncomms/journal/v3/n12/abs/ncomms2307.html

[145] H. Tsang and Y. Liu, "Nonlinear optical properties of silicon waveguides," *Semiconductor Science and Technology*, vol. 23, no. 6, p. 064007, 2008.

[146] V. Kovalyuk, W. Hartmann, O. Kahl, N. Kaurova, a. Korneev, G. Goltsman, and W. H. P. Pernice, "Absorption engineering of NbN nanowires deposited on silicon nitride nanophotonic circuits." *Optics express*, vol. 21, no. 19, pp. 22 683–92, sep 2013. [Online]. Available: http://www.ncbi.nlm.nih.gov/pubmed/24104155

[147] C. Schuck, X. Guo, L. Fan, X.-S. Ma, M. Poot, and H. X. Tang, "Quantum interference in heterogeneous superconducting-photonic circuits on a silicon chip," *ArXiv*, pp. 1–11, nov 2015. [Online]. Available: http://arxiv.org/abs/1511.07081

[148] J. S. Levy, A. Gondarenko, M. a. Foster, A. C. Turner-Foster, A. L. Gaeta, and M. Lipson, "CMOS-compatible multiple-wavelength oscillator for on-chip optical interconnects," *Nature Photonics*, vol. 4, no. 1, pp. 37–40, dec 2009. [Online]. Available: http://www.nature.com/doifinder/10.1038/nphoton.2009.259

[149] C. Xiong, X. Zhang, A. Mahendra, J. He, D.-Y. Choi, C. Chae, D. Marpaung, A. Leinse, R. Heideman, M. Hoekman *et al.*, "Compact and reconfigurable silicon nitride time-bin entanglement circuit," *Optica*, vol. 2, no. 8, pp. 724–727, 2015.

[150] J. Carolan, C. Harrold, C. Sparrow, E. Martín-López, N. J. Russell, J. W. Silverstone, P. J. Shadbolt, N. Matsuda, M. Oguma, M. Itoh, G. D. Marshall, M. G. Thompson, J. C. F. Matthews, T. Hashimoto, J. L. O'Brien, and A. Laing, "Universal linear optics," *Science*, vol. 349, no. 6249, pp. 711–716, 2015. [Online]. Available: http://science.sciencemag.org/content/349/6249/711

[151] B. Calkins, P. L. Mennea, A. E. Lita, B. J. Metcalf, W. S. Kolthammer, A. Lamas-Linares, J. B. Spring, P. C. Humphreys, R. P. Mirin, J. C. Gates, P. G. R. Smith, I. A. Walmsley, T. Gerrits, and S. W. Nam, "High quantum-efficiency photon-number-resolving detector for photonic on-chip information processing," *Opt. Express*, vol. 21, no. 19, pp. 22 657–22 670, Sep 2013. [Online]. Available: http://www.opticsexpress.org/abstract.cfm?URI=oe-21-19-22657

[152] J. B. Spring, P. S. Salter, B. J. Metcalf, P. C. Humphreys, M. Moore, N. Thomas-Peter, M. Barbieri, X.-M. Jin, N. K. Langford, W. S. Kolthammer, M. J. Booth, and I. A. Walmsley, "On-chip low loss heralded source of pure single photons," *Opt. Express*, vol. 21, no. 11, pp. 13 522–13 532, Jun 2013. [Online]. Available: http://www.opticsexpress.org/abstract.cfm?URI=oe-21-11-13522

[153] C. Xiong, W. H. Pernice, X. Sun, C. Schuck, K. Y. Fong, and H. X. Tang, "Aluminum nitride as a new material for chip-scale optomechanics and nonlinear optics," *New Journal of Physics*, vol. 14, no. 9, p. 095014, 2012.

[154] W. Pernice, C. Xiong, C. Schuck, and H. Tang, "Second harmonic generation in phase matched aluminum nitride waveguides and micro-ring resonators," *Applied Physics Letters*, vol. 100, no. 22, p. 223501, 2012.

[155] J. P. Sprengers, A. Gaggero, D. Sahin, S. Jahanmirinejad, G. Frucci, F. Mattioli, R. Leoni, J. Beetz, M. Lermer, M. Kamp, S. Hofling, R. Sanjines, and A. Fiore, "Waveguide superconducting single-photon detectors for integrated quantum photonic circuits," *Applied Physics Letters*, vol. 99, no. 18, p. 181110, 2011. [Online]. Available: http://link.aip.org/link/APPLAB/v99/i18/p181110/s1{&}Agg=doi

[156] A. Sipahigil, R. E. Evans, D. D. Sukachev, M. J. Burek, J. Borregaard, M. K. Bhaskar, C. T. Nguyen, J. L. Pacheco, H. A. Atikian, C. Meuwly, R. M. Camacho, F. Jelezko, E. Bielejec, H. Park, M. Lončar, and M. D. Lukin, "Single-Photon Switching and Entanglement of Solid-State Qubits in an Integrated Nanophotonic System," *ArXiv*, aug 2016. [Online]. Available: http://arxiv.org/abs/1608.05147

[157] P. Rath, O. Kahl, S. Ferrari, F. Sproll, G. Lewes-Malandrakis, D. Brink, K. Ilin, M. Siegel, C. Nebel, and W. Pernice, “Superconducting single-photon detectors integrated with diamond nanophotonic circuits,” *Light Sci Appl*, vol. 4, p. e338, Oct 2015, original Article. [Online]. Available: http://dx.doi.org/10.1038/lsa.2015.111

[158] A. Severino, “3c-sic epitaxial growth on large area silicon: thin films,” *Silicon Carbide Epitaxy*, p. 145, 2012.

[159] S. Nishino, J. A. Powell, and H. A. Will, “Production of largearea singlecrystal wafers of cubic sic for semiconductor devices,” *Applied Physics Letters*, vol. 42, no. 5, pp. 460–462, 1983. [Online]. Available: http://dx.doi.org/10.1063/1.93970

[160] H. Nagasawa, K. Yagi, and T. Kawahara, “3c-sic hetero-epitaxial growth on undulant si (001) substrate,” *Journal of crystal growth*, vol. 237, pp. 1244–1249, 2002.

[161] F. Namavar, P. Colter, N. Planes, B. Fraisse, J. Pernot, S. Juillaguet, and J. Camassel, “Investigation of porous silicon as a new compliant substrate for 3c-sic deposition,” *Materials Science and Engineering: B*, vol. 61, pp. 571–575, 1999.

[162] Y. Abe, J. Komiyama, S. Suzuki, and H. Nakanishi, “Sic epitaxial growth on si (001) substrates using a bp buffer layer,” *Journal of crystal growth*, vol. 283, no. 1, pp. 41–47, 2005.

[163] Novasic. [Online]. Available: www.novasic.com

[164] G. Calusine, A. Politi, and D. D. Awschalom, “Silicon carbide photonic crystal cavities with integrated color centers,” *Applied Physics Letters*, vol. 105, no. 1, p. 011123, jul 2014. [Online]. Available: http://scitation.aip.org/content/aip/journal/apl/105/1/10.1063/1.4890083http://arxiv.org/abs/1405.4539

[165] A. Addamiano and J. Sprague, “buffer-layertechnique for the growth of single crystal sic on si,” *Applied Physics Letters*, vol. 44, no. 5, pp. 525–527, 1984.

[166] H. Kim, R. Davis, X. Cox, and R. Linton, “Physical and chemical nature of films formed on si (100) surfaces subjected to c 2 h 4 at elevated temperatures,” *Journal of The Electrochemical Society*, vol. 134, no. 9, pp. 2269–2275, 1987.

[167] G. Ferro, Y. Monteil, H. Vincent, V. Thevenot, M. D. Tran, F. Cauwet, and J. Bouix, “Atomic force microscopy growth modeling of sic buffer layers on si(100) and quality optimization,” *Journal of Applied Physics*, vol. 80, no. 8, pp. 4691–4702, 1996. [Online]. Available: http://dx.doi.org/10.1063/1.363453

[168] F. Khan, B. Roof, L. Zhou, and I. Adesida, “Etching of silicon carbide for device fabrication and through via-hole formation,” *Journal of electronic materials*, vol. 30, no. 3, pp. 212–219, 2001.

[169] N. Plank, M. Blauw, E. Van der Drift, and R. Cheung, "The etching of silicon carbide in inductively coupled sf6/o2 plasma," *Journal of Physics D: Applied Physics*, vol. 36, no. 5, p. 482, 2003.

[170] F. Khan and I. Adesida, "High rate etching of sic using inductively coupled plasma reactive ion etching in sf 6-based gas mixtures," *Applied physics letters*, vol. 75, no. 15, pp. 2268–2270, 1999.

[171] J. Choi, L. Latu-Romain, E. Bano, F. Dhalluin, T. Chevolleau, and T. Baron, "Fabrication of sic nanopillars by inductively coupled sf6/o2 plasma etching," *Journal of Physics D: Applied Physics*, vol. 45, no. 23, p. 235204, 2012.

[172] L. Hiller, T. Stauden, R. M. Kemper, J. K. Lindner, D. J. As, and J. Pezoldt, "Ecr-ectching of submicron and nanometer sized 3c-sic (100) mesa structures," in *Materials Science Forum*, vol. 717. Trans Tech Publ, 2012, pp. 901–904.

[173] S. Ahn, S. Han, J. Lee, J. Moon, and B. Lee, "A study on the reactive ion etching of sic single crystals using inductively coupled plasma of sf6-based gas mixtures," *Metals and Materials International*, vol. 10, no. 1, pp. 103–106, 2004.

[174] L. Jiang and R. Cheung, "Impact of ar addition to inductively coupled plasma etching of sic in sf¡ sub¿ 6¡/sub¿/o¡ sub¿ 2¡/sub¿," *Microelectronic engineering*, vol. 73, pp. 306–311, 2004.

[175] R. Padiyath, R. L. Wright, M. Chaudhry, and S. Babu, "Reactive ion etching of monocrystalline, polycrystalline, and amorphous silicon carbide in cf4/o2 mixtures," *Applied physics letters*, vol. 58, no. 10, pp. 1053–1055, 1991.

[176] F. Khan, L. Zhou, V. Kumar, and I. Adesida, "Low-damage etching of silicon carbide in cl2-based plasmas," *Journal of The Electrochemical Society*, vol. 149, no. 7, pp. G420–G423, 2002.

[177] L. Jiang, N. Plank, M. Blauw, R. Cheung, and E. van der Drift, "Dry etching of sic in inductively coupled cl2/ar plasma," *Journal of Physics D: Applied Physics*, vol. 37, no. 13, p. 1809, 2004.

[178] G. Calusine, A. Politi, and D. D. Awschalom, "Silicon carbide photonic crystal cavities with integrated color centers," *arXiv preprint arXiv:1405.4539*, 2014.

[179] B.-S. Song, S. Yamada, T. Asano, and S. Noda, "Demonstration of two-dimensional photonic crystals based on silicon carbide." *Optics express*, vol. 19, no. 12, pp. 11 084–9, jun 2011. [Online]. Available: http://www.ncbi.nlm.nih.gov/pubmed/21716336

[180] X. Lu, J. Y. Lee, P. X. L. Feng, and Q. Lin, "High Q silicon carbide microdisk resonator," *Applied Physics Letters*, vol. 104, p. 181103, 2014.

[181] K. Yung, J. Wang, S. Huang, C. Lee, and T. Yue, “Modeling the etching rate and uniformity of plasma-aided manufacturing using statistical experimental design,” *Materials and Manufacturing processes*, vol. 21, no. 8, pp. 899–906, 2006.

[182] Nist/sematech e-handbook of statistical methods. [Online]. Available: http://www.itl.nist.gov/div898/handbook/

[183] R. L. Plackett and J. P. Burman, “The design of optimum multifactorial experiments,” *Biometrika*, pp. 305–325, 1946.

[184] C. Fung and J. Kopanski, “Thermal oxidation of 3c silicon carbide single-crystal layers on silicon,” *Applied Physics Letters*, vol. 45, no. 7, pp. 757–759, 1984.

[185] I. Vickridge, J. Ganem, Y. Hoshino, and I. Trimaille, “Growth of sio2 on sic by dry thermal oxidation: mechanisms,” *Journal of Physics D: Applied Physics*, vol. 40, no. 20, p. 6254, 2007.

[186] K. Yee, “Numerical solution of initial boundary value problems involving maxwell’s equations in isotropic media,” *IEEE Transactions on Antennas and Propagation*, vol. 14, no. 3, pp. 302–307, May 1966.

[187] Z. Zhu and T. G. Brown, “Full-vectorial finite-difference analysis of microstructured optical fibers,” *Opt. Express*, vol. 10, no. 17, pp. 853–864, Aug 2002. [Online]. Available: http://www.opticsexpress.org/abstract.cfm?URI=oe-10-17-853

[188] Y. Vlasov and S. McNab, “Losses in single-mode silicon-on-insulator strip waveguides and bends,” *Optics express*, vol. 12, no. 8, pp. 1622–1631, 2004.

[189] P. K. Tien, “Light waves in thin films and integrated optics,” *Appl. Opt.*, vol. 10, no. 11, pp. 2395–2413, Nov 1971. [Online]. Available: http://ao.osa.org/abstract.cfm?URI=ao-10-11-2395

[190] K. K. Lee, D. R. Lim, L. C. Kimerling, J. Shin, and F. Cerrina, “Fabrication of ultralow-loss Si/SiO(2) waveguides by roughness reduction.” *Optics letters*, vol. 26, no. 23, pp. 1888–90, dec 2001. [Online]. Available: http://www.ncbi.nlm.nih.gov/pubmed/18059727

[191] G. A. Porkolab, P. Apiratikul, B. Wang, S. H. Guo, and C. J. K. Richardson, “Low propagation loss algaas waveguides fabricated with plasma-assisted photoresist reflow,” *Opt. Express*, vol. 22, no. 7, pp. 7733–7743, Apr 2014. [Online]. Available: http://www.opticsexpress.org/abstract.cfm?URI=oe-22-7-7733

[192] M. Borselli, T. Johnson, and O. Painter, “Beyond the Rayleigh scattering limit in high-Q silicon microdisks: theory and experiment.” *Optics express*, vol. 13, no. 5, pp. 1515–30, mar 2005. [Online]. Available: http://www.ncbi.nlm.nih.gov/pubmed/19495027

[193] X. Ji, F. A. Barbosa, S. P. Roberts, A. Dutt, J. Cardenas, Y. Okawachi, A. Bryant, A. L. Gaeta, and M. Lipson, "Breaking the loss limitation of on-chip high-confinement resonators," *arXiv preprint arXiv:1609.08699*, 2016.

[194] E. Marcatili, "Bends in optical dielectric guides," *Bell System Technical Journal*, vol. 48, no. 7, pp. 2103–2132, 1969.

[195] A. G. Griffith, R. K. Lau, J. Cardenas, Y. Okawachi, A. Mohanty, R. Fain, Y. H. D. Lee, M. Yu, C. T. Phare, C. B. Poitras, A. L. Gaeta, and M. Lipson, "Silicon-chip mid-infrared frequency comb generation," *Nature Communications*, vol. 6, p. 6299, feb 2015. [Online]. Available: http://www.nature.com/doifinder/10.1038/ncomms7299

[196] A. Yariv, "Universal relations for coupling of optical power between microresonators and dielectric waveguides," *Electronics Letters*, vol. 36, no. 4, pp. 321–322, Feb 2000.

[197] ——, "Critical coupling and its control in optical waveguide-ring resonator systems," *IEEE Photonics Technology Letters*, vol. 14, no. 4, pp. 483–485, 2002.

[198] W. Bogaerts, P. De Heyn, T. Van Vaerenbergh, K. De Vos, S. Kumar Selvaraja, T. Claes, P. Dumon, P. Bienstman, D. Van Thourhout, and R. Baets, "Silicon microring resonators," *Laser & Photonics Reviews*, vol. 6, no. 1, pp. 47–73, 2012. [Online]. Available: http://dx.doi.org/10.1002/lpor.201100017

[199] P. Rabiei, W. Steier, C. Zhang, and L. Dalton, "Polymer micro-ring filters and modulators," *Journal of Lightwave Technology*, vol. 20, no. 11, pp. 1968–1975, 2002.

[200] T. Shoji, T. Tsuchizawa, T. Watanabe, K. Yamada, and H. Morita, "Low loss mode size converter from 0.3 μm square si wire waveguides to singlemode fibres," *Electronics Letters*, vol. 38, no. 25, pp. 1669–1670, 2002.

[201] V. R. Almeida, R. R. Panepucci, and M. Lipson, "Nanotaper for compact mode conversion," *Opt. Lett.*, vol. 28, no. 15, pp. 1302–1304, Aug 2003. [Online]. Available: http://ol.osa.org/abstract.cfm?URI=ol-28-15-1302

[202] B. Schmid, A. Petrov, and M. Eich, "Optimized grating coupler with fully etched slots," *Opt. Express*, vol. 17, no. 13, pp. 11 066–11 076, Jun 2009. [Online]. Available: http://www.opticsexpress.org/abstract.cfm?URI=oe-17-13-11066

[203] S. K. Selvaraja, D. Vermeulen, M. Schaekers, E. Sleeckx, W. Bogaerts, G. Roelkens, P. Dumon, D. V. Thourhout, and R. Baets, "Highly efficient grating coupler between optical fiber and silicon photonic circuit," in *2009 Conference on Lasers and Electro-Optics and 2009 Conference on Quantum electronics and Laser Science Conference*, June 2009, pp. 1–2.

[204] F. Van Laere, T. Claes, J. Schrauwen, S. Scheerlinck, W. Bogaerts, D. Taillaert, L. O'Faolain, D. Van Thourhout, and R. Baets, "Compact focusing grating couplers for silicon-on-insulator integrated circuits," *IEEE Photonics Technology Letters*, vol. 19, no. 23, pp. 1919–1921, 2007.

[205] K. M. Jackson, J. Dunning, C. A. Zorman, M. Mehregany, and W. N. Sharpe, "Mechanical properties of epitaxial 3c silicon carbide thin films," *Journal of microelectromechanical systems*, vol. 14, no. 4, pp. 664–672, 2005.

[206] F. Payne and J. Lacey, "A theoretical analysis of scattering loss from planar optical waveguides," *Optical and Quantum Electronics*, vol. 26, no. 10, pp. 977–986, 1994.

[207] F. Grillot, L. Vivien, S. Laval, D. Pascal, and E. Cassan, "Size influence on the propagation loss induced by sidewall roughness in ultrasmall soi waveguides," *IEEE Photonics Technology Letters*, vol. 16, no. 7, pp. 1661–1663, July 2004.

[208] T. Barwicz, C. W. Holzwarth, P. T. Rakich, M. A. Popovi, E. P. Ippen, and H. I. Smith, "Optical loss in silicon microphotonic waveguides induced by metallic contamination," *Applied Physics Letters*, vol. 92, no. 13, p. 131108, 2008. [Online]. Available: http://dx.doi.org/10.1063/1.2903714

[209] R. W. Boyd, "Nonlinear optics," 2008.

[210] I. Wu and G. Guo, "Second-harmonic generation and linear electro-optical coefficients of SiC polytypes and nanotubes," *Physical Review B*, vol. 78, no. 3, p. 035447, jul 2008. [Online]. Available: http://link.aps.org/doi/10.1103/PhysRevB.78.035447

[211] M. Fejer, G. Magel, D. H. Jundt, and R. Byer, "Quasi-phase-matched second harmonic generation: tuning and tolerances," *Quantum Electronics, IEEE Journal of*, vol. 28, no. 11, pp. 2631–2654, Nov 1992.

[212] S. Yamada, B.-S. Song, S. Jeon, J. Upham, Y. Tanaka, T. Asano, and S. Noda, "Second-harmonic generation in a silicon-carbide-based photonic crystal nanocavity," *Optics letters*, vol. 39, no. 7, pp. 1768–1771, 2014.

[213] Z. Yang, P. Chak, A. D. Bristow, H. M. van Driel, R. Iyer, J. S. Aitchison, A. L. Smirl, and J. Sipe, "Enhanced second-harmonic generation in algaas microring resonators," *Optics letters*, vol. 32, no. 7, pp. 826–828, 2007.

[214] W. H. P. Pernice, C. Xiong, C. Schuck, and H. X. Tang, "Second harmonic generation in phase matched aluminum nitride waveguides and micro-ring resonators," *Applied Physics Letters*, vol. 100, no. 22, p. 223501, 2012. [Online]. Available: http://dx.doi.org/10.1063/1.4722941

[215] C. Xiong, W. Pernice, K. K. Ryu, C. Schuck, K. Y. Fong, T. Palacios, and H. X. Tang, "Integrated gan photonic circuits on silicon (100) for second harmonic

generation," *Opt. Express*, vol. 19, no. 11, pp. 10 462–10 470, May 2011. [Online]. Available: http://www.opticsexpress.org/abstract.cfm?URI=oe-19-11-10462

[216] S. Mariani, A. Andronico, A. Lemaître, I. Favero, S. Ducci, and G. Leo, "Second-harmonic generation in AlGaAs microdisks in the telecom range." *Optics letters*, vol. 39, no. 10, pp. 3062–5, may 2014. [Online]. Available: http://www.ncbi.nlm.nih.gov/pubmed/24978274

[217] A. Rao, M. Malinowski, A. Honardoost, J. R. Talukder, R. Rabiei, P. Delfyett, and S. Fathpour, "Second-harmonic generation in periodically-poled thin film lithium niobate wafer-bonded on silicon," *ArXiv*, p. 1609.09117, sep 2016. [Online]. Available: http://arxiv.org/abs/1609.09117

[218] P. S. Kuo and G. S. Solomon, "On- and off-resonance second-harmonic generation in gaas microdisks," *Opt. Express*, vol. 19, no. 18, pp. 16 898–16 918, Aug 2011. [Online]. Available: http://www.opticsexpress.org/abstract.cfm?URI=oe-19-18-16898

[219] A. C. Turner, M. A. Foster, A. L. Gaeta, and M. Lipson, "Ultra-low power parametric frequency conversion in a silicon microring resonator," *Opt. Express*, vol. 16, no. 7, pp. 4881–4887, Mar 2008. [Online]. Available: http://www.opticsexpress.org/abstract.cfm?URI=oe-16-7-4881

[220] P. P. Absil, J. V. Hryniewicz, B. E. Little, P. S. Cho, R. A. Wilson, L. G. Joneckis, and P.-T. Ho, "Wavelength conversion in gaas micro-ring resonators," *Opt. Lett.*, vol. 25, no. 8, pp. 554–556, Apr 2000. [Online]. Available: http://ol.osa.org/abstract.cfm?URI=ol-25-8-554

[221] M. A. Foster, A. C. Turner, R. Salem, M. Lipson, and A. L. Gaeta, "Broad-band continuous-wave parametric wavelength conversion in silicon nanowaveguides," *Opt. Express*, vol. 15, no. 20, pp. 12 949–12 958, Oct 2007. [Online]. Available: http://www.opticsexpress.org/abstract.cfm?URI=oe-15-20-12949

[222] M. A. Foster, A. C. Turner, J. E. Sharping, B. S. Schmidt, M. Lipson, and A. L. Gaeta, "Broad-band optical parametric gain on a silicon photonic chip," *Nature*, vol. 441, no. 7096, pp. 960–963, 2006.

[223] R. H. Stolen and C. Lin, "Self-phase-modulation in silica optical fibers," *Phys. Rev. A*, vol. 17, pp. 1448–1453, Apr 1978. [Online]. Available: https://link.aps.org/doi/10.1103/PhysRevA.17.1448

[224] J. Leuthold, C. Koos, and W. Freude, "Nonlinear silicon photonics," *Nature Photonics*, vol. 4, no. 8, p. 535, 2010.

[225] H. Jung, C. Xiong, K. Y. Fong, X. Zhang, and H. X. Tang, "Optical frequency comb generation from aluminum nitride microring resonator,"

Opt. Lett., vol. 38, no. 15, pp. 2810–2813, Aug 2013. [Online]. Available: http://ol.osa.org/abstract.cfm?URI=ol-38-15-2810

[226] X. Lu, J. Y. Lee, S. Rogers, and Q. Lin, "Optical kerr nonlinearity in a high-q silicon carbide microresonator," *Opt. Express*, vol. 22, no. 25, pp. 30 826–30 832, Dec 2014. [Online]. Available: http://www.opticsexpress.org/abstract.cfm?URI=oe-22-25-30826

[227] F. De Leonardis, R. A. Soref, and V. M. Passaro, "Dispersion of nonresonant third-order nonlinearities in silicon carbide," *Scientific reports*, vol. 7, p. 40924, 2017.

[228] Q. Lin, O. J. Painter, and G. P. Agrawal, "Nonlinear optical phenomena in silicon waveguides: Modeling and applications," *Opt. Express*, vol. 15, no. 25, pp. 16 604–16 644, Dec 2007. [Online]. Available: http://www.opticsexpress.org/abstract.cfm?URI=oe-15-25-16604

[229] J. Hansryd, P. A. Andrekson, M. Westlund, J. Li, and P. O. Hedekvist, "Fiber-based optical parametric amplifiers and their applications," *IEEE Journal of Selected Topics in Quantum Electronics*, vol. 8, no. 3, pp. 506–520, May 2002.

[230] M. A. Foster, A. C. Turner, M. Lipson, and A. L. Gaeta, "Nonlinear optics in photonic nanowires," *Optics Express*, vol. 16, no. 2, p. 1300, 2008. [Online]. Available: http://www.opticsinfobase.org/abstract.cfm?uri=OE-16-2-1300http://www.opticsinfobase.org/abstract.cfm?URI=oe-16-2-1300https://www.osapublishing.org/oe/abstract.cfm?uri=oe-16-2-1300

[231] K. Karch, P. Pavone, W. Windl, O. Schütt, and D. Strauch, "Ab initio," *Phys. Rev. B*, vol. 50, pp. 17 054–17 063, Dec 1994. [Online]. Available: https://link.aps.org/doi/10.1103/PhysRevB.50.17054

[232] R. Anzalone, G. D'arrigo, M. Camarda, C. Locke, S. Saddow, and F. La Via, "Advanced residual stress analysis and fem simulation on heteroepitaxial 3c–sic for mems application," *Journal of Microelectromechanical Systems*, vol. 20, no. 3, pp. 745–752, 2011.

[233] I. D. Rukhlenko, M. Premaratne, and G. P. Agrawal, "Effective mode area and its optimization in silicon-nanocrystal waveguides," *Opt. Lett.*, vol. 37, no. 12, pp. 2295–2297, Jun 2012. [Online]. Available: http://ol.osa.org/abstract.cfm?URI=ol-37-12-2295

[234] L. G. Helt, Z. Yang, M. Liscidini, and J. E. Sipe, "Spontaneous four-wave mixing in microring resonators," *Opt. Lett.*, vol. 35, no. 18, pp. 3006–3008, Sep 2010. [Online]. Available: http://ol.osa.org/abstract.cfm?URI=ol-35-18-3006

[235] M. S. Z. Marlan O. Scully, *Quantum Optics*.

[236] X. Li, J. Chen, P. Voss, J. Sharping, and P. Kumar, "All-fiber photon-pair source for quantum communications: Improved generation of correlated photons," *Opt. Express*, vol. 12, no. 16, pp. 3737–3744, Aug 2004. [Online]. Available: http://www.opticsexpress.org/abstract.cfm?URI=oe-12-16-3737

[237] K.-I. Harada, H. Takesue, H. Fukuda, T. Tsuchizawa, T. Watanabe, K. Yamada, Y. Tokura, and S.-I. Itabashi, "Frequency and Polarization Characteristics of Correlated Photon-Pair Generation Using a Silicon Wire Waveguide," *IEEE Journal of Selected Topics in Quantum Electronics*, vol. 16, no. 1, pp. 325–331, 2010. [Online]. Available: http://ieeexplore.ieee.org/lpdocs/epic03/wrapper.htm?arnumber=5325708

[238] S. Yang, Y. Zhang, T. Baehr-Jones, and M. Hochberg, "High efficiency germanium-assisted grating coupler," *Opt. Express*, vol. 22, no. 25, pp. 30 607–30 612, Dec 2014. [Online]. Available: http://www.opticsexpress.org/abstract.cfm?URI=oe-22-25-30607

[239] C. Xiong, B. Bell, and B. J. Eggleton, "Cmos-compatible photonic devices for single-photon generation," *Nanophotonics*, vol. 5, no. 3, pp. 427–439, 2016.

[240] D. Stucki, N. Walenta, F. Vannel, R. T. Thew, N. Gisin, H. Zbinden, S. Gray, C. R. Towery, and S. Ten, "High rate, long-distance quantum key distribution over 250km of ultra low loss fibres," *New Journal of Physics*, vol. 11, no. 7, p. 075003, 2009. [Online]. Available: http://stacks.iop.org/1367-2630/11/i=7/a=075003

[241] C. Gobby, Z. L. Yuan, and A. J. Shields, "Quantum key distribution over 122 km of standard telecom fiber," *Applied Physics Letters*, vol. 84, no. 19, pp. 3762–3764, 2004. [Online]. Available: http://dx.doi.org/10.1063/1.1738173

[242] F. Marsili, V. B. Verma, J. a. Stern, S. Harrington, a. E. Lita, T. Gerrits, I. Vayshenker, B. Baek, M. D. Shaw, R. P. Mirin, and S. W. Nam, "Detecting single infrared photons with 93% system efficiency," *Nature Photonics*, vol. 7, no. 3, pp. 210–214, feb 2013. [Online]. Available: http://www.nature.com/doifinder/10.1038/nphoton.2013.13

[243] A. W. Elshaari, I. E. Zadeh, K. D. Jns, and V. Zwiller, "Thermo-optic characterization of silicon nitride resonators for cryogenic photonic circuits," *IEEE Photonics Journal*, vol. 8, no. 3, pp. 1–9, June 2016.

[244] "Idquantique ID100 Silicon Avalanche Photodiode," http://www.idquantique.com/photon-counting/photon-counting-modules/id100/, accessed: 2017-07-22.

[245] E. Saglamyurek, N. Sinclair, J. Jin, J. A. Slater, D. Oblak, F. Bussières, M. George, R. Ricken, W. Sohler, and W. Tittel, "Broadband waveguide quantum memory for entangled photons," *Nature*, vol. 469, no. 7331, pp. 512–5, jan

2011. [Online]. Available: http://www.nature.com/nature/journal/v469/n7331/abs/nature09719.htmlhttp://www.ncbi.nlm.nih.gov/pubmed/21228775

[246] J. Jin, M. Grimau Puigibert, L. Giner, J. A. Slater, M. R. E. Lamont, V. B. Verma, M. D. Shaw, F. Marsili, S. W. Nam, D. Oblak, and W. Tittel, "Entanglement swapping with quantum-memory-compatible photons," *Phys. Rev. A*, vol. 92, p. 012329, Jul 2015. [Online]. Available: https://link.aps.org/doi/10.1103/PhysRevA.92.012329

[247] K. F. Reim, J. Nunn, V. O. Lorenz, B. J. Sussman, K. C. Lee, N. K. Langford, D. Jaksch, and I. A. Walmsley, "Towards high-speed optical quantum memories," *Nature Photonics*, vol. 4, no. 4, pp. 218–221, mar 2010. [Online]. Available: http://www.nature.com/nphoton/journal/v4/n4/abs/nphoton.2010.30.htmlhttp://www.nature.com/doifinder/10.1038/nphoton.2010.30

[248] Y.-N. Xu and W. Y. Ching, "Electronic structure and optical properties of α and β phases of silicon nitride, silicon oxynitride, and with comparison to silicon dioxide," *Phys. Rev. B*, vol. 51, pp. 17 379–17 389, Jun 1995. [Online]. Available: https://link.aps.org/doi/10.1103/PhysRevB.51.17379

[249] C. Reimer, M. Kues, P. Roztocki, B. Wetzel, F. Grazioso, B. E. Little, S. T. Chu, T. Johnston, Y. Bromberg, L. Caspani, D. J. Moss, and R. Morandotti, "Generation of multiphoton entangled quantum states by means of integrated frequency combs," *Science*, vol. 351, no. 6278, pp. 1176–1180, mar 2016. [Online]. Available: http://science.sciencemag.org/content/351/6278/1176.abstracthttp://www.sciencemag.org/cgi/doi/10.1126/science.aad8532

[250] Z. Vernon, M. Liscidini, and J. E. Sipe, "No free lunch: the tradeoff between heralding rate and efficiency in microresonator-based heralded single photon sources," *Optics letters*, vol. 41, no. 4, pp. 788–791, 2016. [Online]. Available: http://arxiv.org/abs/1512.04879

[251] P. Berman, *Cavity quantum electrodynamics.* Academic Press, Inc., Boston, MA (United States), Dec 1994.

[252] C. Gerry and P. Knight, *Introductory Quantum Optics.* Cambridge University Press, 2005. [Online]. Available: https://books.google.co.uk/books?id=CgByyoBJJwgC

[253] J. R. Weber, W. F. Koehl, J. B. Varley, a. Janotti, B. B. Buckley, C. G. Van de Walle, and D. D. Awschalom, "Quantum computing with defects." *Proceedings of the National Academy of Sciences of the United States of America*, vol. 107, no. 19, pp. 8513–8, may 2010. [Online]. Available: http://www.pubmedcentral.nih.gov/articlerender.fcgi?artid=2889300{&}tool=pmcentrez{&}rendertype=abstract

[254] D. J. Christle, A. L. Falk, P. Andrich, P. V. Klimov, J. ul Hassan, N. T. Son, E. Janzén, T. Ohshima, and D. D. Awschalom, "Isolated electron spins in silicon carbide with millisecond coherence times," *Nature Materials*, vol. 14, no. 2, pp. 160–163, dec 2014. [Online]. Available: http://arxiv.org/abs/1406.7325http://www.ncbi.nlm.nih.gov/pubmed/25437259http://www.nature.com/doifinder/10.1038/nmat4144

[255] W. F. Koehl, B. B. Buckley, F. J. Heremans, G. Calusine, and D. D. Awschalom, "Room temperature coherent control of defect spin qubits in silicon carbide." *Nature*, vol. 479, no. 7371, pp. 84–7, nov 2011. [Online]. Available: http://www.nature.com/doifinder/10.1038/nature10562http://www.ncbi.nlm.nih.gov/pubmed/22051676

[256] E. Yablonovitch, "Inhibited Spontaneous Emission in Solid-State Physics and Electronics," *Physical Review Letters*, vol. 58, no. 20, pp. 2059–2062, may 1987. [Online]. Available: http://link.aps.org/doi/10.1103/PhysRevLett.58.2059

[257] S. John, "Strong localization of photons in certain disordered dielectric superlattices," *Phys. Rev. Lett.*, vol. 58, pp. 2486–2489, Jun 1987. [Online]. Available: https://link.aps.org/doi/10.1103/PhysRevLett.58.2486

[258] Y. Akahane, T. Asano, B.-s. Song, and S. Noda, "High-Q photonic nanocavity in a two-dimensional photonic crystal." *Nature*, vol. 425, no. 6961, pp. 944–7, oct 2003. [Online]. Available: http://www.ncbi.nlm.nih.gov/pubmed/14586465

[259] B.-S. Song, S. Noda, T. Asano, and Y. Akahane, "Ultra-high-Q photonic double-heterostructure nanocavity," *Nature Materials*, vol. 4, no. 3, pp. 207–210, feb 2005. [Online]. Available: http://www.nature.com/doifinder/10.1038/nmat1320

[260] H. Raether, *Surface plasmons on smooth and rough surfaces and on gratings.* Springer, 2006, vol. 111.

[261] J. D. Caldwell, L. Lindsay, V. Giannini, I. Vurgaftman, T. L. Reinecke, S. A. Maier, and O. J. Glembocki, "Low-loss, infrared and terahertz nanophotonics using surface phonon polaritons," *Nanophotonics*, vol. 4, no. 1, pp. 44–68, 2015.

[262] Pitman, K. M., Hofmeister, A. M., Corman, A. B., and Speck, A. K., "Optical properties of silicon carbide for astrophysical applications* - i. new laboratory infrared reflectance spectra and optical constants," *A&A*, vol. 483, no. 2, pp. 661–672, 2008. [Online]. Available: https://doi.org/10.1051/0004-6361:20078468

[263] J. Le Gall, M. Olivier, and J.-J. Greffet, "Experimental and theoretical study of reflection and coherent thermal emissionby a sic grating supporting a surface-phonon polariton," *Phys. Rev. B*, vol. 55, pp. 10 105–10 114, Apr 1997. [Online]. Available: https://link.aps.org/doi/10.1103/PhysRevB.55.10105

[264] J. B. Khurgin and G. Sun, “Scaling of losses with size and wavelength in nanoplasmonics and metamaterials,” *Applied Physics Letters*, vol. 99, no. 21, p. 211106, 2011.

[265] Y. Chen, Y. Francescato, J. D. Caldwell, V. Giannini, T. W. W. Ma, O. J. Glembocki, F. J. Bezares, T. Taubner, R. Kasica, M. Hong, and S. A. Maier, “Spectral tuning of localized surface phonon polariton resonators for low-loss mid-ir applications,” *ACS Photonics*, vol. 1, no. 8, pp. 718–724, 2014. [Online]. Available: http://dx.doi.org/10.1021/ph500143u

[266] A. Konrad, A. M. Kern, M. Brecht, and A. J. Meixner, “Strong and coherent coupling of a plasmonic nanoparticle to a subwavelength fabryprot resonator,” *Nano Letters*, vol. 15, no. 7, pp. 4423–4428, 2015, pMID: 26061892. [Online]. Available: http://dx.doi.org/10.1021/acs.nanolett.5b00766

[267] H.-I. Kuo, C. A. Zorman, and M. Mehregany, “Fabrication and testing of single crystalline 3c-sic devices using a novel sic-on-insulator substrate,” in *TRANSDUCERS, Solid-State Sensors, Actuators and Microsystems, 12th International Conference on, 2003*, vol. 1. IEEE, 2003, pp. 742–745.